

Journal of *Donghua University* (English Edition)

Former *Journal of China Textile University*

Vol. 42 No. 2

April 30, 2025

Editorial Board

Journal of Donghua University (English Edition) (ISSN 1672-5220, CN 31-1920/TS) is published bimonthly and started in 1984.

Aims and Scope *Journal of Donghua University (English Edition)* draws together many aspects of science and technology of textiles and other related disciplines, from fundamental research and development to industrial application. Subject areas covered include: textiles, materials, clothing, chemistry, biomedical engineering, mechanical engineering, computer science, applied physics, management engineering, etc.

Subscription Information *Journal of Donghua University (English Edition)* is published 6 times a year. Volume 42 (6 issues) will be published in 2025. For information on subscription rates please contact Journal Center of Donghua University, 1882 West Yan'an Road, Shanghai 200051, China.

Director of Journal Center

WANG Kebin

Executive Editors

GAO Yu YANG Jianxia WU Yarong

Director of Editorial Board

LIU Shuhui

Vice Director of Editorial Board

ZHU Meifang

Editor-in-Chief

ZHU Meifang

Associate Executive Editor-in-Chief

CHEN Zhigang

Editorial Board Members

CHEN Biqiong	CHEN Nanliang	CHEN Zhigang	CUI Wenguo
DING Bin	DONG Kai	FANG Jian	FU Jiajia
GONG Jixian	GU Bohong	JIANG Jinhua	JIN Jianyong
KANG Yanming	LI Diansen	LI Fang	LI Jingchao
LIAO Guangfu	LIAO Yaozu	LIU Shuhui	LIU Wanjun
LIU Xuqing	LIU Yanan	LIU Yanbo	LIU Zunfeng
LUO Yan	MAO Jifu	MENG Weidong	PAN Ruru
PENG Yitian	QIN Xiaohong	REN Yuanlin	SHEN Bo
SI Yang	SONG Hui	SUN Gang	SUN Zhihong
TIAN Mingwei	WANG Chunrui	WANG Hongzhi	WANG Huaping
WANG Run	WANG Xianfeng	WANG Yunyi	WU Tong
XI Peng	XIN Binjie	XING Yanjun	XU Fujun
XU Yang	YAN Jianhua	YANG Jian	YI Tao
YOU Zhengwei	ZHANG Guanglin	ZHANG Kun	ZHANG Qinghua
ZHANG Qingsong	ZHANG Ruiyun	ZHAO Huijing	ZHU Meifang
ZHUANG Xupin			

Youth Editorial Committee Members

CAO Xinwang	FANG Yinchun	GUAN Fuwang	HUANG Xin
LIN Huiting	LIU Baojiang	NIU Yaolan	TANG Chunxia
YAN Jing	ZHANG Changhuan	ZHENG Xianhong	

Contents

Advanced Functional Materials

- 107 Triboelectric Nanogenerators Based on Polyimide Membranes Doped with Barium Titanate Nanoparticles and Multi-Walled Carbon Nanotubes LIU Jingjing, AFZAL Syed Umer, WANG Kaibo, YAN Jing
- 116 Improving Tensile Properties of Flexible Conductive Polyacrylonitrile@Carbon Nanotube Nanofiber Membrane by Cellulose Nanocrystal ZHANG Changhuan, WANG Liuyao, WANG Haowen, MA Tao, SUN Hongyangzi, HUANG Yi, TONG Yiting, CHEN Yang, ZHANG Liran
- 124 Effect of Heat Treatment on Molecular Mass and Thermal Properties of Thermotropic Liquid Crystal Polyesters... DONG Shihang, CHEN Yufeng, WAN Hai, LIANG Yuan, HUANG Shuhan, WANG Yanping, XIA Yumin

Textile Processing and Application

- 136 Reactive Dyeing of Wool Fabric Using Recycled Dyeing Wastewater WANG Bingxin, HAN Bo, ZHANG Xinyuan, LI Wanxin, XU Jia, SHU Dawu

Resource, Ecology and Environment

- 144 Effectiveness and Concentration Distribution of Negative Air Ions on Human Health in Indoor Environment DENG Xiaoni, AN Yuhui, YANG Xuebin, ZHANG Ruidan, XIONG Chen

Information Technology and Artificial Intelligence

- 156 Personal Style Guided Outfit Recommendation with Multi-Modal Fashion Compatibility Modeling WANG Kexin, ZHANG Jie, ZHANG Peng, SUN Kexin, ZHAN Jiamei, WEI Meng
- 168 Design of Dual-Wavelength Bifocal Metalens Based on Generative Adversarial Network Model LIU Gangcheng, WANG Junkai, LIN Sen, WU Binhe, WANG Chunrui, ZHOU Jian, SUN Hao
- 177 Context-Aware Visual Entailment Driven by Specific Instructions HAN Yufeng, HAO Kuangrong, TANG Xuesong, WEI Bing
- 187 An Efficient Temporal Decoding Module for Action Recognition HUANG Qiubo, MEI Jianmin, ZHAO Wupeng, LU Yiru, WANG Mei, CHEN Dehua

Intelligent Detection and Control

- 197 Calculating Sound Absorption Coefficients of Sound-Absorbing Materials Using Flow Resistivity ZHU Congyun, SHAO Zhenya, DING Guofang
- 204 Corneal Topographic Restoration Imaging Based on Placido Disc WAN Xuanrun, WANG Chaoxing, HU Jun, JIANG Jian, LI Kangmei

Fundamental Science

- 213 Leader-Following Consensus for a Class of Nonlinear Cascaded Multi-Agent Systems LI Xianda, KANG Jianling

DOI: 10.19884/j.1672-5220.202405014

Triboelectric Nanogenerators Based on Polyimide Membranes Doped with Barium Titanate Nanoparticles and Multi-Walled Carbon Nanotubes

LIU Jingjing, AFZAL Syed Umer, WANG Kaibo, YAN Jing*

School of Textile Science and Engineering, Tiangong University, Tianjin 300387, China

Abstract: High performance is always the research objective in developing triboelectric nanogenerators (TENGs) for future versatile applications. In this study, flexible triboelectric membranes were prepared based on polyimide (PI) membranes doped with barium titanate (BTO) nanoparticles and multi-walled carbon nanotubes (MWCNTs). The piezoelectric BTO nanoparticles were incorporated to boost the electric outputs by the synergistic effect of piezoelectricity and triboelectricity and MWCNTs were incorporated to provide a microcapacitor structure for enhancing the performance of TENGs. When the mass fraction of the BTO nanoparticle was 10% and the mass fraction of the MWCNT was 0.1%, the corresponding TENG achieved optimum electric outputs (an open-circuit voltage of around 65 V, a short-circuit current of about 20.0 μ A and a transferred charge of about 25.0 nC), much higher than those of the TENG with a single PI membrane. The TENG is potentially used to supply energy for commercial light-emitting diodes and as self-powered sensors to monitor human physical training conditions. This research provides a guideline for developing TENGs with high performance, which is crucial for their long-term use.

Keywords: triboelectric nanogenerator (TENG); energy harvesting; multi-walled carbon nanotube (MWCNT); barium titanate (BTO); polyimide (PI)

CLC number: TB332

Document code: A

Article ID: 1672-5220(2025)02-0107-09

Open Science Identity
(OSID)



0 Introduction

In recent years, wearable electronic devices have completely changed fitness tracking, physical training and entertainment, but due to the limitations of traditional batteries, their energy supply has become the critical issue which needs to be addressed^[1]. The triboelectric nanogenerator (TENG) is a contemporary nanopower solution that effectively converts mechanical power into electric power through triboelectricity and electrostatic induction, providing a promising opportunity^[2]. The TENG has attracted attention for its versatility in

managing various substances and its function as a self-powered sensor, constantly tracking the behavior of external power sources^[3-4]. Despite significant progress, there is still room for development in the overall output performance of the TENG to meet numerous utility needs, highlighting the importance of ongoing research and innovation in advancing the TENG technology^[5].

Common choices of triboelectric materials for TENGs include polyimide (PI), polytetrafluoroethylene (PTFE) and polydimethylsiloxane (PDMS) due to their electronegativity^[6]. PI is favored for TENGs due to its blend durability, chemical resistance, ease of production and ability to withstand wear. By adding particles such as ZnO^[7], SrTiO₃^[8], ZnSnO₃^[9] and barium titanate (BTO)^[10] into polymer materials, the output of the TENG can be enhanced by combining the advantages of piezoelectric and triboelectric effects, and then a specialized layer called a piezoelectric-trioboelectric layer is introduced^[11]. Among them, BTO nanoparticles have attracted a great interest due to their piezoelectric and dielectric properties, as well as their cost-effectiveness. For example, Yang et al.^[12] proposed a TENG enhanced with BTO merging silicone rubber, and the TENG achieved good output performance and flexibility.

Moreover, adding conductive fillers to the triboelectric polymer matrix plays an important role in improving the overall output performance of TENGs by providing a microcapacitor for storing more electrons. In previous researches, various conductive materials, including MXene^[13], multi-walled carbon nanotubes (MWCNTs)^[14], graphene^[15] and silver nanoparticles^[16], have been used. Among these materials, MWCNTs stand out not only for their durability and flexibility, but also for their excellent mechanical and thermal properties^[17-18]. The microcapacitor, which relies on its high surface area due to its tubular structure and nanoscale dimensions, enables efficient charge trapping and storage, thereby improving the overall output performance of TENGs under specific external pressures^[19-20]. In previous studies, BTO nanoparticles are used as the piezoelectric

Received date: 2024-05-23

Foundation item: National Natural Science Foundation of China (No. 52103267)

* Correspondence should be addressed to YAN Jing, email: yanjing@tiangong.edu.cn

Citation: LIU J J, AFZAL S U, WANG K B, et al. Triboelectric nanogenerators based on polyimide membranes doped with barium titanate nanoparticles and multi-walled carbon nanotubes[J]. *Journal of Donghua University (English Edition)*, 2025, 42(2): 107-115.

material to enhance the property, and MWCNTs are used to build the microcapacitor structure within the polymer matrix for performance enhancement.

In this study, a TENG is developed based on nanocomposite membranes of the PI matrix, BTO nanoparticles and MWCNTs (BTO/MWCNT/PI membranes) to combine the piezoelectric effect, microcapacitor effect and triboelectric effect. BTO nanoparticles are incorporated to enhance the combined effects of piezoelectric and triboelectric mechanisms. Furthermore, MWCNTs are used to improve both the current and voltage output through the microcapacitor structure. BTO/MWCNT/PI membranes are prepared by the solution casting method, and their tensile properties, dielectric properties and triboelectric performance are discussed considering BTO and MWCNT mass fractions. High-performance triboelectric materials are expected to be obtained through the study.

1 Materials and Methods

1.1 Materials

BTO nanoparticles with an average diameter of 100 nm were bought from Macklin, China. MWCNTs with a mass fraction of 98%, a diameter of 10–20 nm and a length of around 10–30 μm were bought from Chengdu Organic Chemicals Co., Ltd., China. 4,4'-Oxydianiline (ODA) and 1,2,4,5-pyromellitic dianhydride (PMDA) were purchased from Tianjin Zhongtai Chemical Technology Co., Ltd., China. *N,N*-Dimethylformamide (DMF) was purchased from Aladdin, China.

1.2 Preparation of BTO/MWCNT/PI membranes

BTO nanoparticles were subjected to the annealing process at 1 000 °C for 10 h to attain the tetragonal crystal structure. The BTO/MWCNT/PI membrane was made by the solution casting method. Firstly, BTO nanoparticles at mass fractions of 5%, 10%, 15% and 20% were added to the ODA/DMF solvent to make a homogenous solution. Secondly, PMDA was added to the solution to get a uniform mixture solution. Thirdly, the mixture solution was scraped onto a clean glass plate to obtain BTO/polyamic acid (PAA) membranes, and then the membranes were put into a muffle oven for thermal imidization at 300 °C to obtain BTO/PI membranes (5BTO/PI, 10BTO/PI, 15BTO/PI and 20BTO/PI). Then, BTO/MWCNT/PI membranes were made by adding BTO at a mass fraction of 10% and MWCNTs at mass fractions of 0.1%, 0.2%, 0.3% and 0.4%, which were termed as BTO/0.1MWCNT/PI,

BTO/0.2MWCNT/PI, BTO/0.3MWCNT/PI and BTO/0.4MWCNT/PI, respectively. Finally, the nanocomposite membrane was fabricated to get the vertical contact-separation TENG with the working area of 2 cm × 2 cm for testing and characterization.

1.3 Characterization

The structures of BTO/MWCNT/PI membranes were examined by using a field emission scanning electron microscope (Gemini SEM500 ZEISS, Germany). Tensile properties were evaluated by using a universal testing machine (Model 3369, Instron, USA). For dielectric property measurements within the range of 1– 1×10^7 Hz at room temperature, a high-performance frequency analyzer from NoVo Control Technologies in Germany was utilized. During testing procedures, samples were placed between electrodes (a diameter of 2 cm) to form a microcapacitor structure. An oscilloscope (MDO3014, Tektronix, China) was used to measure the voltage and an electrometer (6517B, Keithley, China) was used to measure the current. The vibrator (JZK10, Sinocera Piezoirronics Inc., China) provided pressures at various frequencies.

2 Results and Discussion

2.1 Structure and performance of BTO/PI membranes

As can be seen from Fig. 1(a), the cross-sectional scanning electron microscopy (SEM) image of the PI membrane shows a smooth structure. 5BTO/PI has some increase in the bulges from the cross-sectional view, as shown in Fig. 1(b). For 10BTO/PI, the bulges spread out through the cross-section, as shown in Fig. 1(c). 15BTO/PI and 20BTO/PI exhibit more pronounced agglomerates compared to 10BTO/PI, as shown in Figs. 1(d) and 1(e). The increase of the BTO mass fraction leads to excessive clustering or agglomeration^[21].

The stress-strain curves of PI and BTO/PI membranes are shown in Fig. 2. As can be seen, the PI membrane has the strength of about 110 MPa and the fracture strain of nearly 60%. By adding BTO nanoparticles at mass fractions of 5%, 10%, 15% and 20%, the strengths of BTO/PI membranes decrease to the values lower than 80 MPa, and the fracture strains are lower than 30%. This is because the PI chain movement is prohibited by the BTO nanoparticles, and then the BTO/PI membranes are less flexible and prone to break under strains. In addition, excess BTO nanoparticles would cause non-uniform stress distribution in the PI matrix^[11].

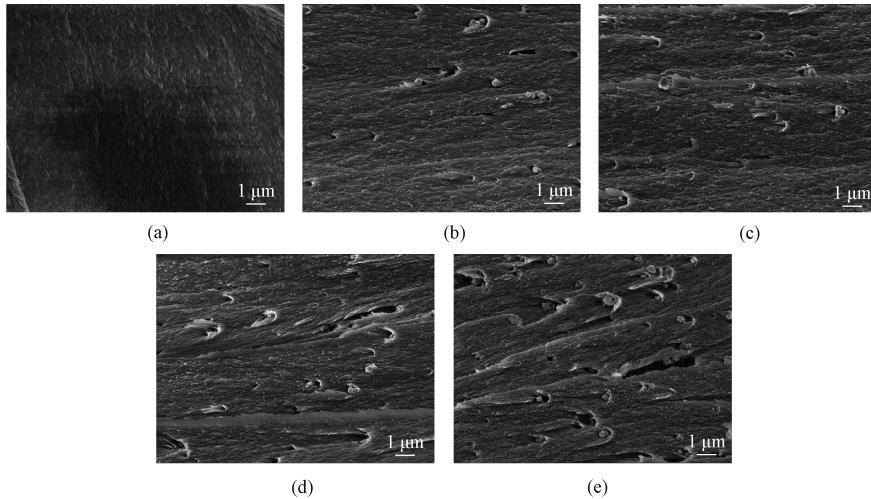


Fig. 1 Cross-sectional SEM images of PI and BTO/PI membranes: (a) PI; (b) 5BTO/PI; (c) 10BTO/PI; (d) 15BTO/PI; (e) 20BTO/PI

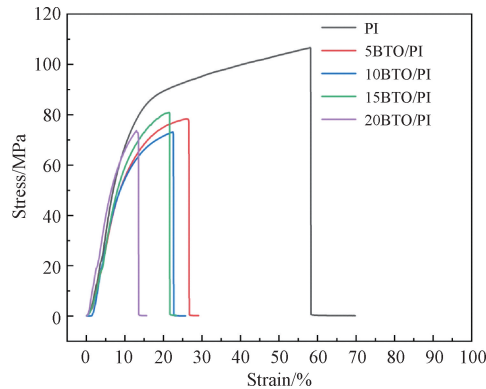


Fig. 2 Tensile properties of PI and BTO/PI membranes

The dielectric properties and conductive properties of PI and BTO/PI membranes are shown in Fig. 3, where δ is the loss angle and $\tan \delta$ is used to characterize the dielectric loss. The dielectric constant of the PI membrane is 1.5, and that of 20BTO/PI increases to 2.8 due to the high dielectric constant of BTO nanoparticles. Additionally, the presence of BTO nanoparticles may introduce relaxation within the material^[22]. This leads to the dielectric loss being about 0.040. As BTO nanoparticles are non-conductive, the conductivity displays non-significant changes by adding BTO nanoparticles.

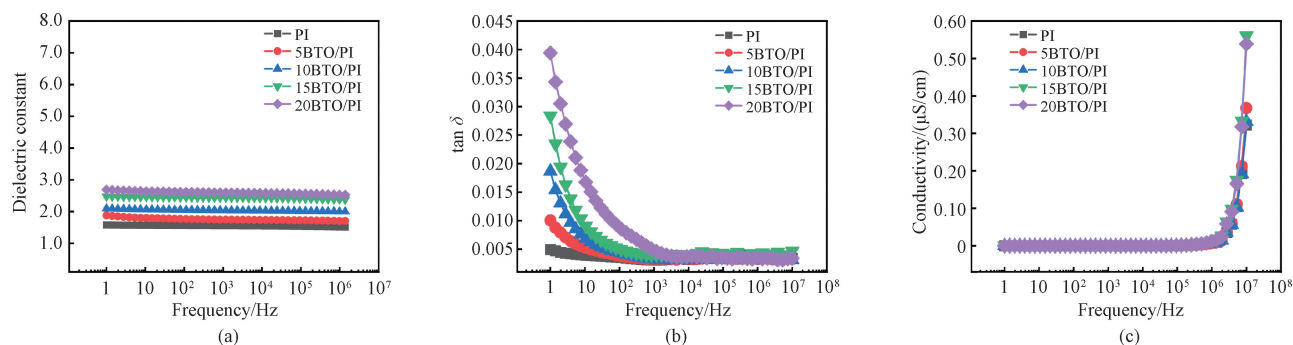


Fig. 3 Dielectric properties and conductive properties of PI and BTO/PI membranes: (a) dielectric constant; (b) dielectric loss; (c) conductivity

To evaluate the effect of BTO mass fractions on the output performance of TENGs, the open-circuit voltage V_{oc} , the short-circuit current I_{sc} and the transferred charge Q_{sc} of TENGs based on BTO/PI membranes at different BTO mass fractions are shown in Fig. 4. There is an initial increase in V_{oc} and I_{sc} as the BTO mass fraction increases. Specifically, at a BTO mass fraction of 10%, V_{oc} and I_{sc} are the highest, being 40 V and

9.9 μ A, respectively. It indicates that this mixture offers optimum triboelectric performance. Moreover, the TENG based on 10BTO/PI exhibits the highest Q_{sc} of 14.9 nC. However, a decline in the output performance is observed for the TENG based on BTO/PI membranes at BTO mass fractions higher than 10%, which is attributed to the aggregation of BTO nanoparticles confirmed by their SEM images.

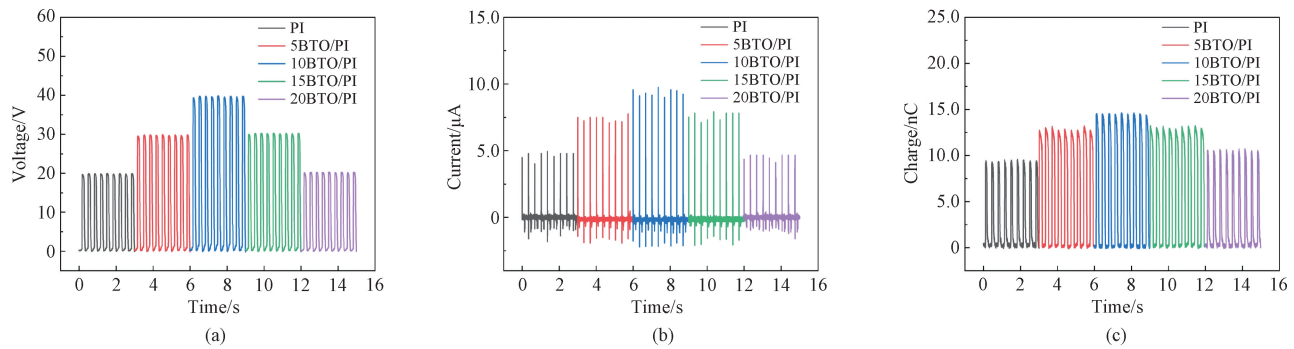


Fig. 4 Output performance of TENGs based on PI and BTO/PI membranes: (a) open-circuit voltage; (b) short-circuit current; (c) transferred charge

2.2 Structure and performance of BTO/MWCNT/PI membranes

For investigating the morphological structure of the membranes, cross-sectional SEM images of BTO/MWCNT/PI membranes were taken. As shown in Fig. 5(a), BTO nanoparticles and MWCNTs are uniformly dispersed in the PI matrix and there is no agglomeration. Figure 5(b) shows the co-existence of BTO nanoparticles and MWCNTs on BTO/0.2 MWCNT/PI. When the MWCNT mass fraction increases to 0.3% and 0.4%, the agglomerates become more prominent in BTO/MWCNT/PI membranes as shown in Figs. 5(c) and 5(d), which is also confirmed in Ref. [23].

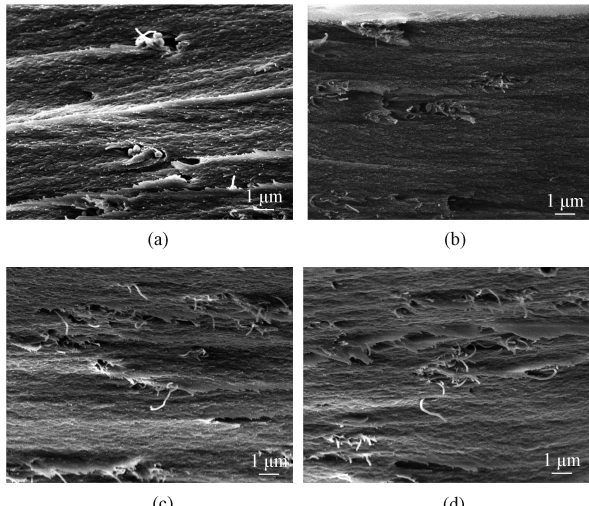


Fig. 5 Cross-sectional SEM images of BTO/MWCNT/PI membranes: (a) BTO/0.1MWCNT/PI; (b) BTO/0.2MWCNT/PI; (c) BTO/0.3MWCNT/PI; (d) BTO/0.4MWCNT/PI

To investigate the tensile properties of the triboelectric layers, the tensile properties of the BTO/MWCNT/PI membranes were tested. The results are shown in Fig. 6. The strength of BTO/0.1 MWCNT/PI is up to 83 MPa, slightly higher than that of 10BTO/PI. The increase in the strength of the BTO/MWCNT/PI membranes by adding MWCNTs can be explained by the

fact that MWCNTs are well-known inorganic materials with good tensile properties. However, the strength does not further increase when the MWCNT mass fraction increases. As for the fracture strain, the addition of MWCNTs results in a continuous increase.

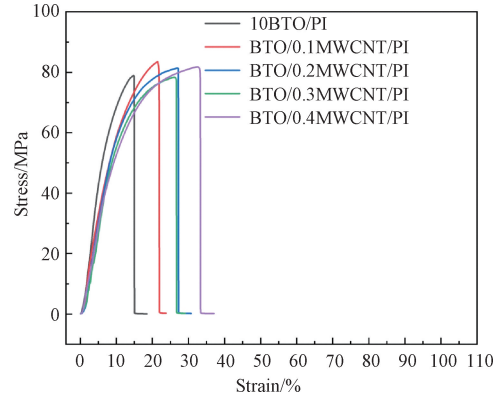


Fig. 6 Tensile properties of 10BTO/PI and BTO/MWCNT/PI membranes

Compared with the PI membrane, BTO/MWCNT/PI membranes have better dielectric properties as shown in Fig. 7. There is a gradual increase in the dielectric constant from 2.0 to 2.7, the dielectric loss from 0.01 to 0.06, and the conductivity from 0.50 μS/cm to 0.75 μS/cm. The reason is that MWCNTs disperse more firmly in the membrane and can form multiple microcapacitors. This network, where MWCNTs act as electrodes with a thin dielectric layer, substantially improves the charge storage capacity. Each microcapacitor provides an exceptionally high capacitance, which can be attributed to the significant increase in the dielectric constant^[24]. This suggests that BTO nanoparticle addition further enhances the dielectric properties of the membranes. The dielectric loss of BTO/MWCNT/PI membranes increases with the increase of MWCNT mass fractions because of current leakage caused by the high conductivity of MWCNTs. The presence of MWCNTs improves the conductivity because of their inherent conductive properties.

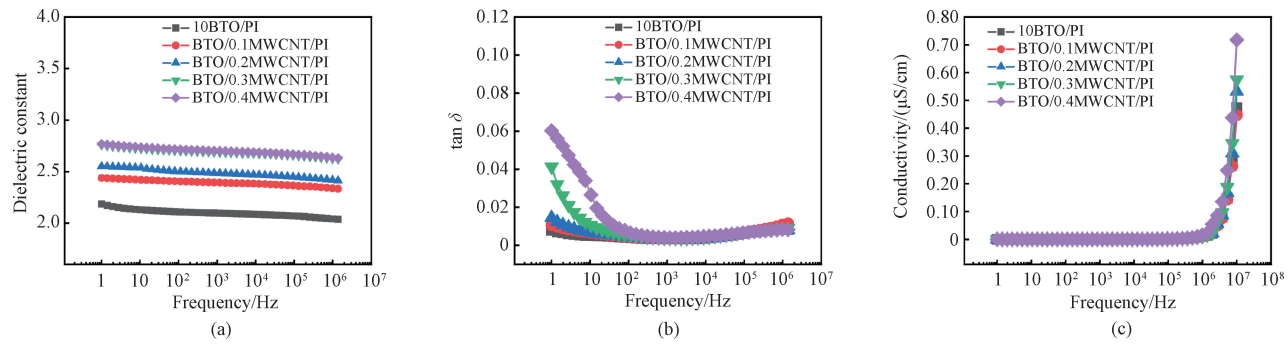


Fig. 7 Dielectric properties and conductive properties of 10BTO/PI and BTO/MWCNT/PI membranes; (a) dielectric constant; (b) dielectric loss; (c) conductivity

Output performance of TENGs based on BTO/MWCNT/PI membranes was tested. The results are shown in Fig. 8. BTO/0.1 MWCNT/PI shows the highest open-circuit voltage of around 65 V, short-circuit current of about 20.0 μA and transferred charge of about 25.0 nC because of the synergies between piezoelectric

and triboelectric effects as well as the microcapacitor structure formed by MWCNTs^[24]. When the mass fraction of MWCNTs further increases, the output performance of the TENG decreases, which may be attributed to the agglomeration of nanofillers or excessive charge loss caused by MWCNTs.

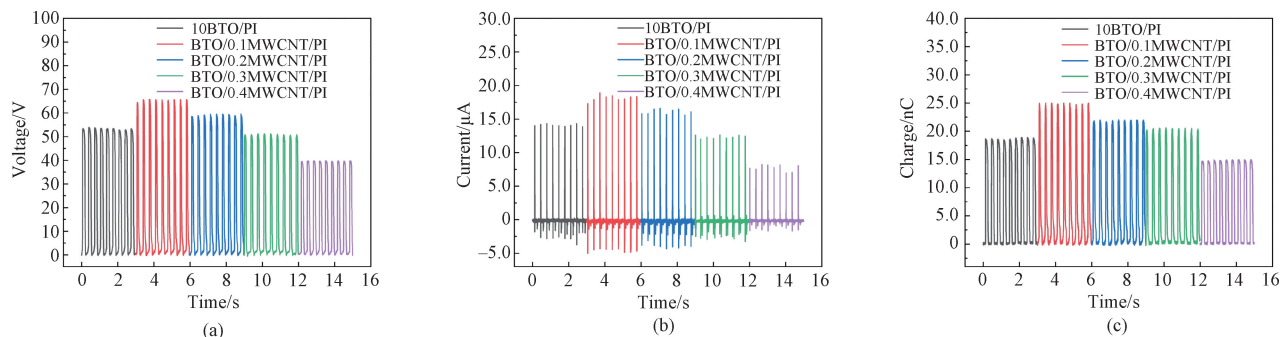
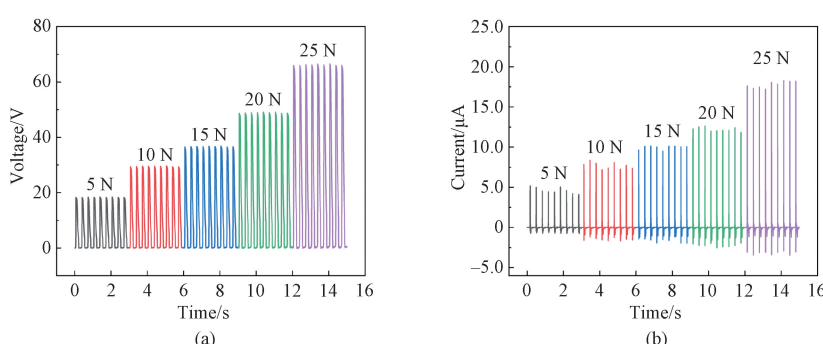


Fig. 8 Output performance of TENGs based on 10BTO/PI and BTO/MWCNT/PI membranes; (a) open-circuit voltage; (b) short-circuit current; (c) transferred charge

2.3 Applications of TENGs based on BTO/MWCNT/PI membranes

To evaluate the output performance of TENGs based on BTO/MWCNT/PI membranes under different conditions, the outputs at different pressures or frequencies were studied. The results are shown in Fig. 9. When the pressure increases from 5 N to 25 N at a frequency of 3.0 Hz, as shown in Figs. 9(a) and 9(b), V_{oc} increases from 18 V to 66 V and I_{sc} increases from 5.0 μA to 18.0 μA . This is because the surface charges on the friction layer are determined by the

capacitance and piezoelectric effects. If a higher pressure is applied, the contact between the two friction layers becomes more efficient in helping the generation of charges. When the pressure is 25 N and the frequency varies from 1.0 Hz to 3.0 Hz, V_{oc} presents no significant change because of the unchangeable electrical potential difference, while I_{sc} increases continuously, as shown in Figs. 9(c) and 9(d). Because the increasing frequency accelerates the charge transfer speed, the output current, which depends on the charge transfer speed, increases accordingly.



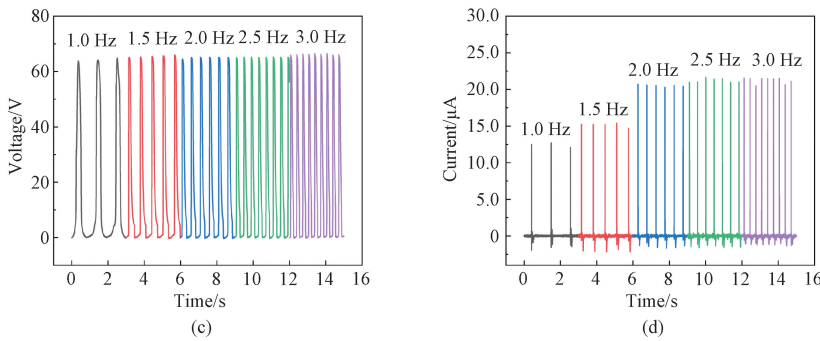


Fig. 9 Output performance of TENGs under different conditions: (a) open-circuit voltage at different pressures; (b) short-circuit current at different pressures; (c) open-circuit voltage at different frequencies; (d) short-circuit current at different frequencies

In order to supply power to microelectronic devices, V_{oc} and I_{sc} of TENGs were measured at a frequency of 3.0 Hz, a pressure of 25 N and an external load resistance R from $1 \times 10^4 \Omega$ to $1 \times 10^{10} \Omega$. The results are shown in Fig. 10. With the increase of R , V_{oc} increases but I_{sc} decreases.

The power density P of the BTO/MWCNT/PI membrane is calculated based on

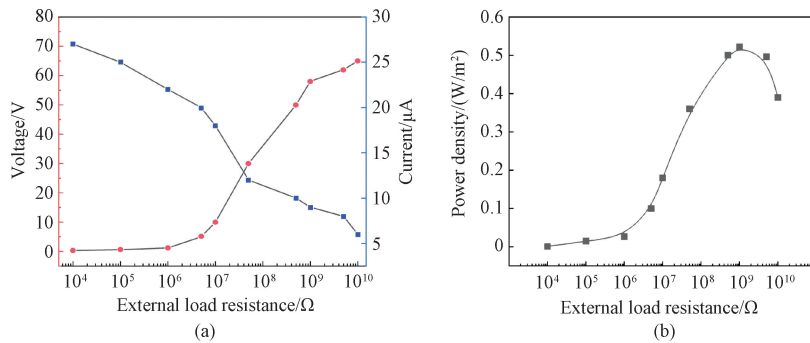


Fig. 10 Output performance of TENGs at different external load resistances: (a) open-circuit voltage and short-circuit current; (b) power density

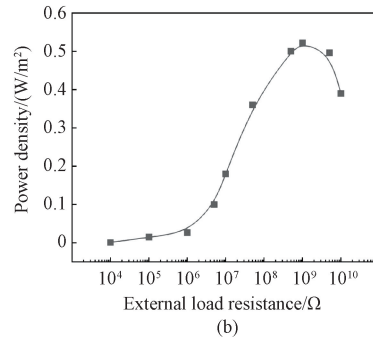
In order to harness ambient power for sustainable applications, the integration of TENG-based sensors into wearable electronics was studied. The BTO/MWCNT/PI membrane-based TENG can charge different microcapacitors with capacitances of 0.22, 1.00 and 4.70 μF in terms of voltages, as shown in Fig. 11(a). It is indicated that the TENG can be used to store charges which would then be used for lighting up different light-emitting diodes (LEDs) as shown in Fig. 11(b). This novel method allows the seamless integration of TENG-based sensors into diverse wearable devices, such as smartwatches, health trackers and fitness monitors.

Figure 11(c) illustrates the generation of charges through pressure changes on the TENG-based sensor by the movement of feet. The black and red lines represent the output performance of TENGs on the heel and toes in

$$P = \frac{U^2}{RA},$$

where U is the instantaneous peak voltage; A is the working area.

As R increases, P increases gradually first and then decreases. The peak power density is about 0.5 W/m^2 at R of $1 \times 10^9 \Omega$ ^[23].



1.0 s, respectively. TENG-based sensors can detect gestures or commands when the TENG at the foot strikes the ground, generating a detectable current. Similarly, while the pressure is on the toe area, the TENG on the toes would generate signals, and the TENG on the heel would show released pressures. For walking, the speed of the foot movement is low, so the TENG on the toes shows a low current, and the TENG on the heel is landed on the ground and shows a high current. Conversely, for running, the TENG on the toes shows a high current but the TENG on the heel still shows a current higher than that for walking, which shows that the frequency of foot movement increases and implies the state of running. This would be implemented in digital reality applications, or as a hands-unfastened interface for controlling digital devices, and could help in the gesture recognition.

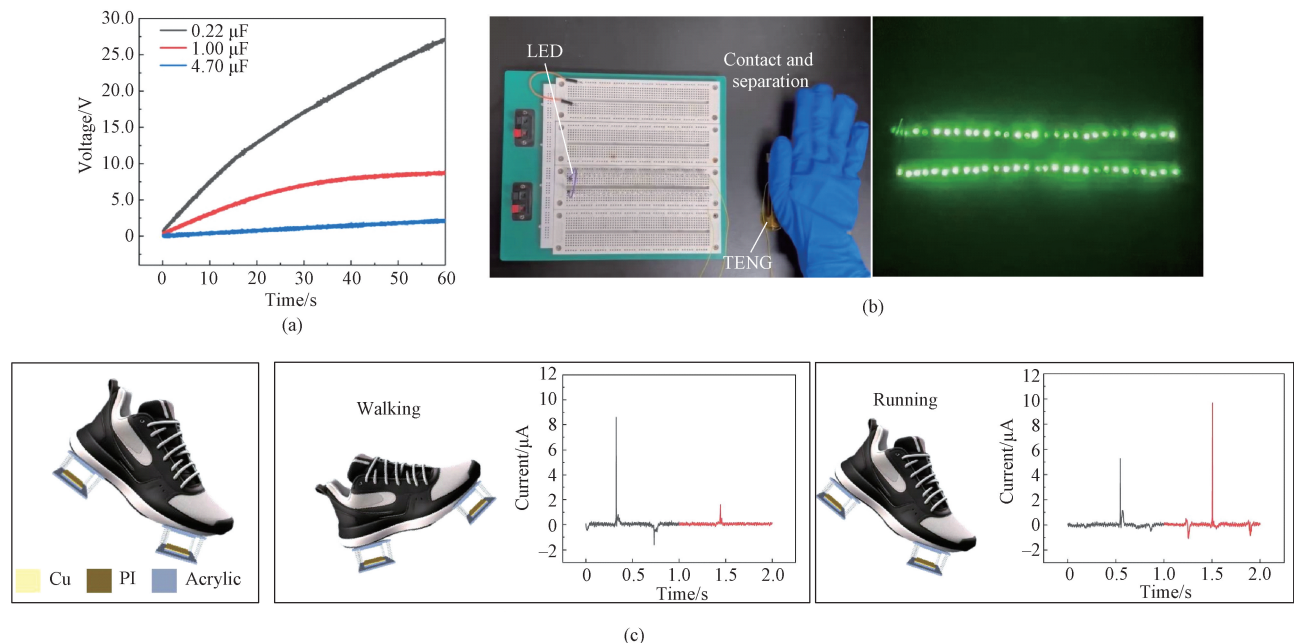


Fig. 11 TENG actual power supply capacity and application: (a) charging process for commercial capacitors; (b) commercial LEDs; (c) motion sensing

3 Conclusions

The integration of flexible PI membranes with BTO nanoparticles and MWCNTs has demonstrated significant advancements in the performance of the TENG. Systematic testing at different compositions determines that a membrane comprising BTO nanoparticles (a mass fraction of 10%) and MWCNTs (a mass fraction of 0.1%) within the PI matrix yields optimal results. The TENG shows remarkable tensile properties with a strength of 83 MPa, and an enhanced electric output (an open-circuit voltage of around 65 V, a short-circuit current of about 20.0 μA and a transferred charge of about 25.0 nC). The high performance of the TENG holds significant promise for a multitude of versatile applications. Specifically, the potential to power commercial LEDs and microelectronics highlights the viability of using TENGs as sustainable energy sources. Additionally, the capacity for self-powered sensors to monitor human physical training conditions signifies a valuable application in wearable fitness technology and can be used for the detection of various body health issues, such as body imbalances, foot misalignment and falls. Such advancements are crucial for ensuring the long-term viability and widespread adoption of the TENG technology across diverse fields, ranging from consumer electronics to healthcare and environmental monitoring.

References

- [1] FANG J L, DU J X. Classification of preparation methods and wearability of smart textiles [J].

- Journal of Donghua University (English Edition)*, 2022, 39(4) : 379-391.
 [2] WU C S, WANG A C, DING W B, et al. Triboelectric nanogenerator: a foundation of the energy for the new era [J]. *Advanced Energy Materials*, 2019, 9(1) : 1802906.
 [3] XU X, OUYANG Y T, LU S R, et al. Highly flexible and recyclable F-SiO₂/MPU composites for self-powered active motion sensors [J]. *Composites Science and Technology*, 2021, 216: 109068.
 [4] YU D M, LIU L F, YU J Y, et al. Enhancing piezoelectric output via constrained phase separation on single nanofibers: harnessing endogenous triboelectricity [J]. *Journal of Donghua University (English Edition)*, 2025, 42 (1) : 12-19.
 [5] MA J, QI X W, ZHAO Y L, et al. Polyimide/mesoporous silica nanocomposites: characterization of mechanical and thermal properties and tribochemistry in dry sliding condition [J]. *Materials & Design*, 2016, 108: 538-550.
 [6] LEE J W, YE B U, BAIK J M. Research update: recent progress in the development of effective dielectrics for high-output triboelectric nanogenerator [J]. *APL Materials*, 2017, 5(7) : 073802.
 [7] SINGH H H, KHARE N. Improved performance of ferroelectric nanocomposite flexible film based triboelectric nanogenerator by controlling surface morphology, polarizability, and hydrophobicity [J]. *Energy*, 2019, 178: 765-771.
 [8] CHEN J, GUO H Y, HE X M, et al. Enhancing

- performance of triboelectric nanogenerator by filling high dielectric nanoparticles into sponge PDMS film [J]. *ACS Applied Materials & Interfaces*, 2016, 8(1) : 736-744.
- [9] PARIA S, SI S K, KARAN S K, et al. A strategy to develop highly efficient TENGs through the dielectric constant, internal resistance optimization, and surface modification [J]. *Journal of Materials Chemistry A*, 2019, 7(8) : 3979-3991.
- [10] ZHANG P, ZHANG W K, DENG L, et al. A triboelectric nanogenerator based on temperature-stable high dielectric BaTiO₃-based ceramic powder for energy harvesting[J]. *Nano Energy*, 2021, 87: 106176.
- [11] YAN J, LV M D, QIN Y B, et al. Triboelectric nanogenerators based on membranes comprised of polyurethane fibers loaded with ethyl cellulose and barium titanate nanoparticles [J]. *ACS Applied Nano Materials*, 2023, 6 (7) : 5675-5684.
- [12] YANG C J, HE J, GUO Y H, et al. Highly conductive liquid metal electrode based stretchable piezoelectric-enhanced triboelectric nanogenerator for harvesting irregular mechanical energy [J]. *Materials & Design*, 2021, 201: 109508.
- [13] SOHEL RANA S M, RAHMAN M T, SALAUDDIN M, et al. Electrospun PVDF-TrFE/MXene nanofiber mat-based triboelectric nanogenerator for smart home appliances [J]. *ACS Applied Materials & Interfaces*, 2021, 13 (4) : 4955-4967.
- [14] LIU Z Q, MUHAMMAD M, CHENG L, et al. Improved output performance of triboelectric nanogenerators based on polydimethylsiloxane composites by the capacitive effect of embedded carbon nanotubes [J]. *Applied Physics Letters*, 2020, 117(14) : 143903.
- [15] REN C J, BAI Z Q, LIU X J, et al. Preparation and actuated strain properties of functionalized graphene modified polyurethane materials [J]. *Journal of Donghua University (Natural Science)*, 2022, 48(6) : 21-28, 35. (in Chinese)
- [16] XIA X N, CHEN J, GUO H Y, et al. Embedding variable micro-capacitors in polydimethylsiloxane for enhancing output power of triboelectric nanogenerator [J]. *Nano Research*, 2017, 10(1) : 320-330.
- [17] YUE L P, ZHANG X Y, LI W D, et al. RETRACTED: a transparent pressure-sensitive adhesive with high electrical conductivity based on water-soluble nano core-shell hollow composite [J]. *Composites Science and Technology*, 2018, 160: 119-126.
- [18] SUI J L, DU M Z, JING Y Y, et al. Enhancing accuracy of flexible piezoresistive pressure sensors by suppressing Seebeck effect [J]. *Journal of Donghua University (English Edition)* , 2021, 38 (6) : 498-503.
- [19] KHAN S A, ZHANG H L, XIE Y H, et al. Flexible triboelectric nanogenerator based on carbon nanotubes for self-powered weighing[J]. *Advanced Engineering Materials*, 2017, 19(3) : 1600710.
- [20] ZHU Y B, YANG B, LIU J Q, et al. A flexible and biocompatible triboelectric nanogenerator with tunable internal resistance for powering wearable devices [J]. *Scientific Reports* , 2016, 6: 22233.
- [21] LI Z H, WANG X L, HU Y Q, et al. Triboelectric properties of BaTiO₃/polyimide nanocomposite film [J]. *Applied Surface Science*, 2022, 572: 151391.
- [22] DOU L Y, LIN Y H, NAN C W. An overview of linear dielectric polymers and their nanocomposites for energy storage [J]. *Molecules*, 2021, 26(20) : 6148.
- [23] WANG H X, YANG J W, UMER S, et al. Robust multi-walled carbon nanotubes @ thermoplastic polyurethane porous films with conductive fabrics for wearable triboelectric nanogenerators[J]. *Polymer Composites*, 2024, 45(2) : 1208-1217.
- [24] YAN J, WANG K B, WANG Y Q, et al. Polyimide nanofiber-based triboelectric nanogenerators using piezoelectric carbon nanotube@barium titanate nanoparticles[J]. *ACS Applied Nano Materials*, 2024, 7(11) : 13156-13165.

基于钛酸钡纳米颗粒和多壁碳纳米管掺杂聚酰亚胺膜的摩擦纳米发电机

刘晶晶, AFZAL Syed Umer, 王凯博, 闫 静*

天津工业大学 纺织科学与工程学院, 天津 300387

摘要: 开发高性能摩擦纳米发电机 (triboelectric nanogenerator, TENG) 以满足未来多功能应用需求始终是该领域的研究目标。该文通过掺杂钛酸钡 (barium titanate, BTO) 纳米颗粒和多壁碳纳米管 (multi-walled carbon nanotube, MWCNT) 制备聚酰亚胺 (polyimide, PI) 柔性摩擦电膜: 引入压电 BTO 纳米颗粒, 通过压电效应和摩擦电效应的协同作用来提高电输出; 引入 MWCNT 来构建微电容结构以增强 TENG 的性能。当 BTO 纳米颗粒的质量分数为 10% 且 MWCNT 的质量分数为 0.1% 时, TENG 可获得约 65 V、20.0 μ A 和 25.0 nC 的最佳摩擦电输出性能, 远高于纯 PI 膜的 TENG。该 TENG 可为商用发光二级管供电, 也可作为自供电传感器来监测人体活动状况。该研究为开发高性能 TENG 奠定了基础, 对其长期使用具有重要意义。

关键词: 摩擦纳米发电机; 能源采集; 多壁碳纳米管; 钛酸钡; 聚酰亚胺

DOI: 10.19884/j.1672-5220.202501015

Improving Tensile Properties of Flexible Conductive Polyacrylonitrile @ Carbon Nanotube Nanofiber Membrane by Cellulose Nanocrystal

ZHANG Changhuan, WANG Liuyao, WANG Haowen, MA Tao, SUN Hongyangzi*, HUANG Yi, TONG Yiting, CHEN Yang, ZHANG Liran*

School of Materials Design & Engineering, Beijing Institute of Fashion Technology, Beijing 100029, China

Abstract: The flexible conductive nanofiber membrane is widely used in the field of wearable electronics. High tensile properties of electrospun nanofiber membranes are essential for their successful commercial application. With cellulose nanocrystal (CNC) as the reinforcement, the flexible conductive polyacrylonitrile (PAN)/CNC@carbon nanotube (CNT) nanofiber membrane is electrospun from the PAN solution containing suspended CNC and impregnated with the CNT solution. The structure and properties of nanofiber membranes are studied. The results show that with the increase of the PAN mass fraction, the viscosity of the electrospinning solution increases, leading to an increase in the nanofiber diameter. When the mass fraction of PAN is 12%, PAN/CNC nanofiber membranes at different CNC mass fractions are successfully prepared. The structure and properties of PAN/CNC nanofiber membranes are affected by the addition of CNC. As the CNC mass fraction increases, the nanofibers become thicker, the nanofiber diameter distribution widens, and the tensile strength first increases and then decreases. When the mass ratio of PAN to CNC is 4:1, the tensile strength of the PAN/CNC nanofiber membrane is the highest, and it is higher than that of the PAN nanofiber membrane. After impregnating the PAN/CNC nanofiber membrane with CNTs, the tensile strength of the nanofiber membrane increases to 3.12 MPa and the surface resistivity is $64 \Omega/\text{cm}^2$. The flexible conductive nanofiber membranes would be used in energy storage and sensing fields, and the study might provide a strong base for their future development.

Keywords: cellulose nanocrystal (CNC); flexible conductive nanofiber membrane; tensile property; carbon nanotube (CNT); electrospinning; polyacrylonitrile (PAN)

CLC number: TS102

Document code: A

Article ID: 1672-5220(2025)02-0116-08

Open Science Identity
(OSID)



0 Introduction

Flexible and stretchable wearable electronics have

significant application potential in various fields, such as bioelectronics^[1-2], human-computer interaction^[3-4], smart living^[5-6], electronic skin^[7-8] and healthcare^[9]. However, conventional microelectronics manufacturing processes brittle semiconductor materials and is not suitable for the fabrication of flexible and stretchable wearable electronics^[10]. Electrospinning, a simple, universal and low-cost technology, emerges as a versatile and cost-effective solution and is used for preparing continuous nanofibers^[11]. Electrospun flexible nanofiber membranes have been extensively used in biomedicine, filtration and protection, energy storage and energy catalyst^[12-14]. Li et al.^[15] prepared the biocompatible poly(lactic acid)/wool keratin/carbon nanotube (CNT) @ CNT fiber membrane via electrospinning and immersion for a pressure electronic sensor with flexibility and conductivity. CNTs have excellent properties, such as high conductivities and high elastic moduli. Zhang et al.^[13] prepared the polyacrylonitrile (PAN)/LiFePO₄ precursor/CNT membrane via electrospinning, and the membrane was used as the cathode of the lithium-ion battery after heat treatment. PAN membranes have gained significant attention due to their exceptional properties. They are synthesized via fabrication techniques such as phase inversion and electrospinning, and possess excellent mechanical properties, thermal stability and chemical resistance. PAN membranes have been extensively studied for various applications like oil-water separation, heavy metal ion removal, water purification, hemodialysis and lithium-ion batteries^[16].

Cellulose nanocrystal (CNC) is extracted from plant fibers and has received a tremendous amount of interest in recent years due to its unique properties and potential applications^[17-18]. CNC is a class of fascinating bio-based nanoscale materials, and possesses high strengths, rigidity, high moduli, adaptable surface chemistry, low

Received date: 2025-01-21

Foundation items: Beijing Municipal Education Commission, China (Nos. KM202210012009 and 202410012002); National Natural Science Foundation of China (No. 52202015); Project of Constructing the Emerging Interdisciplinary Platform Based on “Clothing Science” of Beijing Institute of Fashion Technology, China (No. 11000024T000003073871); XXX Key Laboratory of China (No. HTKJ2024KL703002)

* Correspondence should be addressed to SUN Hongyangzi, email: 20190031@bift.edu.cn; ZHANG Liran, email: 20180022@bift.edu.cn

Citation: ZHANG C H, WANG L Y, WANG H W, et al. Improving tensile properties of flexible conductive polyacrylonitrile@carbon nanotube nanofiber membrane by cellulose nanocrystal [J]. *Journal of Donghua University (English Edition)*, 2025, 42(2): 116-123.

densities, bio-compatibility and renewability, making it an attractive nanomaterial for use in various fields such as renewable energy, electronics, biomedical engineering and pharmaceuticals^[19-24]. Specifically, CNC is a needle-shaped or rod-like nanoparticle, and exhibits a high aspect ratio and high tensile strength. Surface hydroxyl groups on CNC could provide active sites for hydrogen bonding with the hydroxyl groups of hydrophilic polymer matrices and physical interlocking with the non-polar matrices, to induce the reinforcing effect in the polymer. The large interfacial area and strong interactions between the reinforcement and the polymer matrix would enhance nano-confinement effects that substantially improve mechanical properties^[25-27]. CNC has been successfully used to reinforce various electrospun polymer nanofibers. Dong et al.^[28] produced uniform fibers composed of poly(methyl methacrylate) (PMMA) and CNC by electrospinning. Xiang et al.^[29] improved the tensile strength of the electrospun nanofiber membrane by the incorporation of CNC into poly(lactic acid). Besides, the abundant hydroxyl groups on the CNC surface enable the material to possess high reactivity, contributing to the possibility of extensive chemical modification^[27].

In this study, based on the principle of electrospinning, CNC reinforced PAN (PAN/CNC) nanofiber membranes are prepared. After CNT impregnation, the flexible conductive PAN/CNC@CNT nanofiber membranes are prepared. The effects of CNC addition and CNT impregnation on the structure and properties of electrospun nanofiber membranes are studied.

1 Materials and Methods

1.1 Materials

PAN (the weight-average molecular mass is 150 000 g/mol) was provided by Sigma Aldrich, USA. N,N-Dimethylformamide (DMF) was provided by Shanghai Richjoint Chemical Reagents Co., Ltd., China. CNC was provided by Shansi Technology Co., Ltd., China. CNTs were provided by Nanjing XFNANO Materials Technology Co., Ltd., China. Sodium dodecylbenzene sulfonate (SDBS) was provided by Beijing Tong Guang Fine Chemicals Company, China.

1.2 Sample preparation

1.2.1 Preparation of electrospinning solution

PAN electrospinning solutions at PAN mass fractions of 10%, 12% and 14% in DMF were prepared at 60 °C with magnetic stirring by an S10-3 stirrer (Shanghai Sile Instrument Co., Ltd., China) for 24 h.

PAN/CNC electrospinning solutions at PAN/CNC mass ratios of 2:1, 3:1, 4:1 and 5:1 were prepared as follows by adjusting CNC mass fractions. CNC solutions in DMF were prepared by a KQ-500DE ultrasonic device

(Kunshan Ultrasonic Instrument Co., Ltd., China) for 2 h, and then stirred by the S10-3 stirrer for 2 h. The PAN solution (a mass fraction of 12%) was mixed with the CNC solution by the VORTEX3 vortex mixer (IKA, Germany).

1.2.2 Preparation of electrospun nanofiber membranes

PAN and PAN/CNC nanofiber membranes were prepared by using high-voltage electrospinning. The electrospinning solution was loaded into a 10 mL syringe with a capillary tip (a diameter of 0.51 mm). The flow rate of the solution was 1 mL/h. A variable high-voltage power supply (EST804A, Tianjin Dongwen, China) was used to provide an electric potential of around 15 kV. The tip-to-collector distance was 15 cm. The nanofibers were collected on a flat and nonstick release paper. The nanofiber membrane was removed from the release paper and then dried in a DHG-9035A oven (Shanghai Yiheng Technology Instrument Co., Ltd., China) to remove the residual solvent.

1.2.3 Preparation of flexible conductive PAN/CNC@CNT nanofiber membranes

The electrospun PAN/CNC nanofiber membrane was impregnated in the CNT solution to obtain the flexible conductive PAN/CNC@CNT nanofiber membrane.

1) Preparation of the CNT solution. The electrospun nanofiber membrane of a certain size was prepared and weighed. Deionized water was weighed according to a certain bath ratio (1:100 and 1:50). The mixed solution of SDBS (100 mg/mL) and CNT (2 mg/mL) was prepared with the KQ-500DE ultrasonic device for 1 h and then mixed on the VORTEX3 vortex mixer to form a homogeneous solution.

2) Functionalization of the electrospun nanofiber membrane. The prepared electrospun nanofiber membrane was fixed on the tin paper with a long-tailed clip. The nanofiber membrane was placed near the nozzle of the plasma. The plasma treatment was carried out on the front and back sides of the nanofiber membrane.

3) CNT impregnation. The plasma-treated electrospun nanofiber membrane was placed in the CNT solution for 1-h ultrasonic processing, and then put into the oven at 80 °C for drying.

1.3 Testing and characterization

1.3.1 Morphology

The morphology of electrospun nanofiber membranes before and after CNT impregnation was evaluated by a JSM-6701F scanning electron microscope (JEOL Ltd., Japan). The voltage was 5 kV, and the current was 10 μA.

1.3.2 Nanofiber diameter

The nanofiber diameter of the electrospun nanofiber membrane was analyzed by using the ImageJ software (American National Institutes of Health, USA) according to the scanning electron microscopy (SEM) images.

1.3.3 Membrane thickness

The thickness of the electrospun nanofiber membrane was measured by an SD-201-1 thickness gauge (Dongguan Shenliang Measuring Instrument Co., Ltd., China).

1.3.4 Tensile property

The tensile properties of electrospun nanofiber membranes before and after CNT impregnation were tested by using an LT350 tensile testing platform (Linkam Scientific, UK).

1.3.5 Conductivity

The conductivity of electrospun nanofiber membranes before and after CNT impregnation was tested by using an RTS-9 four-probe tester (Guangzhou Four Probe Technology Co., Ltd., China). The parameters of the tester were set to be a square resistance with a current

of 10 mA.

2 Results and Discussion

2.1 Morphology and nanofiber diameter of PAN nanofiber membranes

SEM images and the corresponding nanofiber diameter distribution of PAN nanofiber membranes are shown in Fig. 1. It can be seen that PAN nanofibers can be successfully electrospun from PAN solutions. The diameters of the nanofibers are relatively uniform and consistent. There is no beading or sticking. All nanofibers are continuous and straight, forming three-dimensional porous network structures. The diameters of nanofibers increase gradually with the increase of the PAN mass fraction in the electrospinning solution.

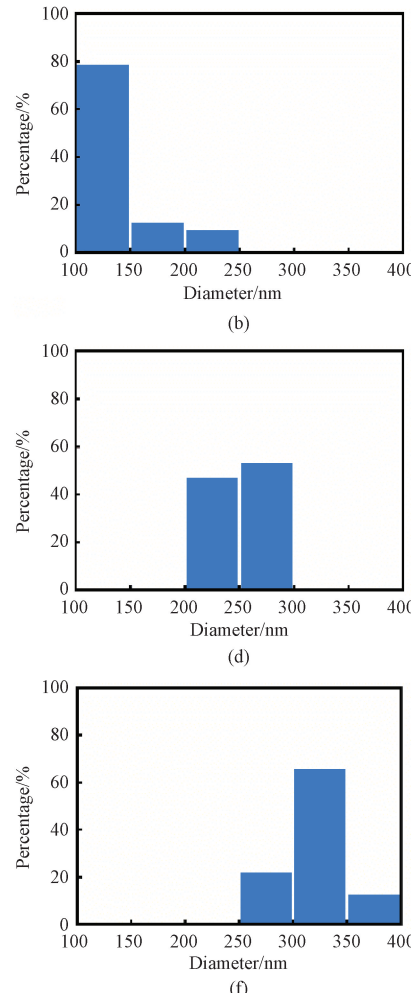
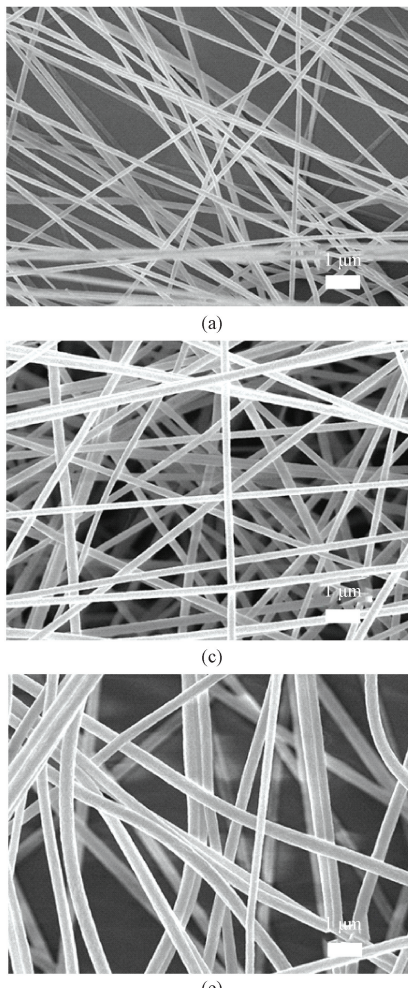


Fig. 1 SEM images and corresponding nanofiber diameter distribution of PAN nanofiber membranes at different PAN mass fractions: (a)-(b) 10%; (c)-(d) 12%; (e)-(f) 14%

The relationship between the average nanofiber diameter and the PAN mass fraction is shown in Fig. 2, where R^2 reflects the degree of the linear correlation between the average nanofiber diameter y_1 and the PAN mass fraction x_1 . R^2 is close to 1, indicating a linear relationship between the average nanofiber diameter and the PAN mass fraction.

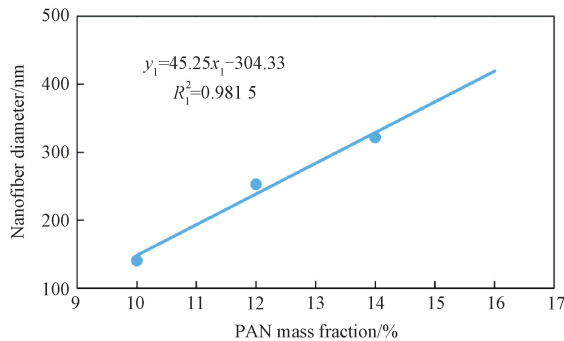


Fig. 2 Relationship between average nanofiber diameter and PAN mass fraction of PAN nanofiber membranes

When the PAN mass fraction is 10%, 12% and 14%, the average nanofiber diameter is 141, 253 and 322 nm, respectively. The nanofiber diameter increases with the increase of the PAN mass fraction.

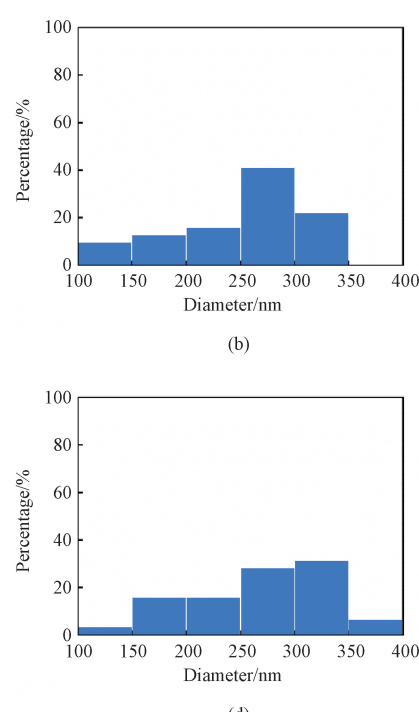
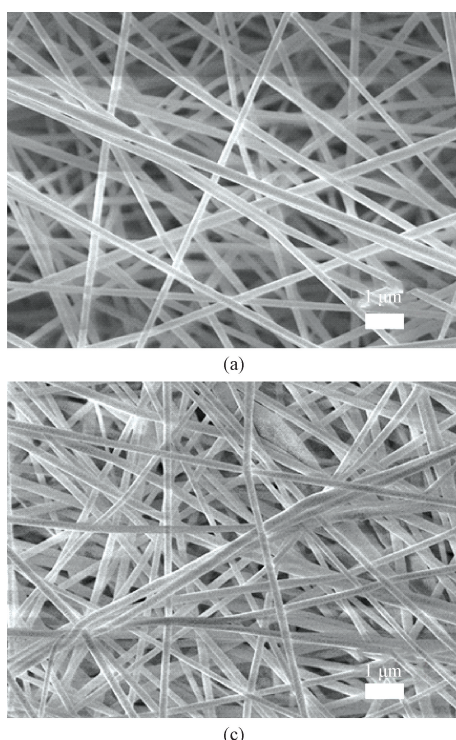
In theory, the tensile strength of the electrospun nanofiber membrane does not increase with the increase of the PAN mass fraction. Thicker nanofibers may increase the contact area between nanofibers, enhancing friction forces, which could improve the tensile strength of the electrospun nanofiber membrane. However, thicker nanofibers are generally less flexible and more prone to

stress concentration during stretching, which could lead to a decrease in the tensile strength. Besides, the nano-reinforcement CNC would be added to the electrospinning solution. The addition of CNC greatly affects the solution viscosity and the electrospinning process. Adding a small amount of CNC would make the electrospinning process difficult when the PAN mass fraction is too high. When the PAN mass fraction is too low, CNC addition would easily lead to the poor nanofiber diameter uniformity. Thus, in the follow-up study, the PAN mass fraction is set to be 12% to electrospin the nanofiber membrane.

2.2 Morphology and nanofiber diameter of PAN/CNC nanofiber membranes

SEM images and the corresponding nanofiber diameter distribution of PAN/CNC nanofiber membranes are shown in Fig. 3. The nano-reinforcement CNC can be well wrapped by the PAN nanofiber. The PAN/CNC nanofibers at different CNC mass fractions are uniform, and there is no serious beading, filament or adhesion phenomenon. The nanofiber membrane also exhibits a three-dimensional porous network structure. As the CNC mass fraction increases, the difficulty of electrospinning increases.

The addition of CNC could affect the nanofiber diameter. The nanofiber diameter of the PAN nanofiber membrane (a PAN mass fraction of 12%) without CNC addition is distributed in 200–300 nm. After the CNC addition, the diameter uniformity of the nanofibers becomes poor, and the nanofiber diameter distribution becomes wide. With the increase of CNC mass fraction, the nanofiber diameter has an increasing tendency.



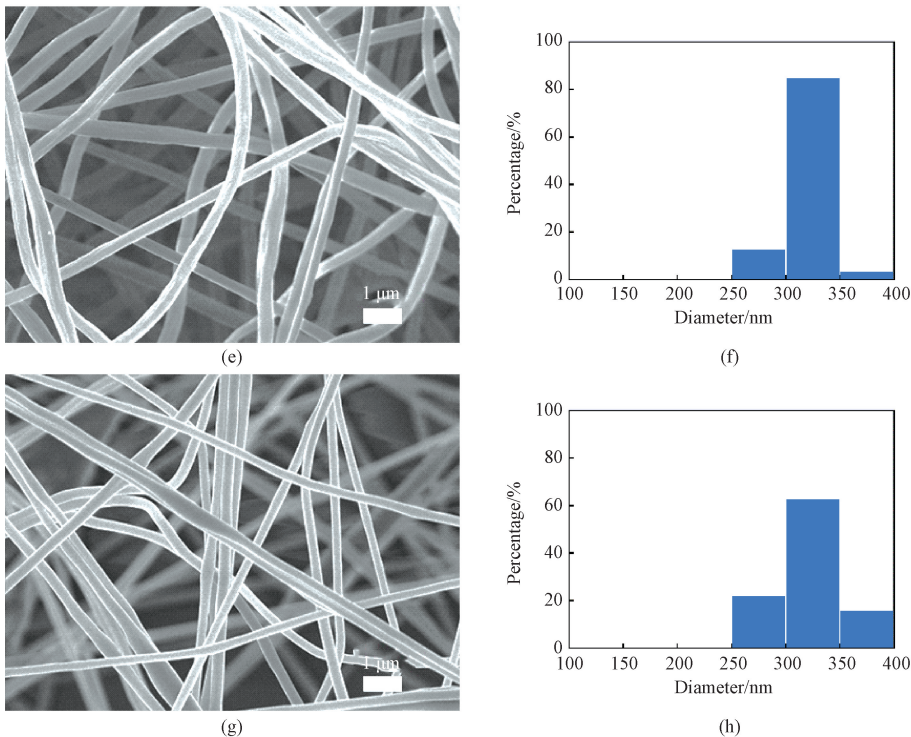


Fig. 3 SEM images and corresponding nanofiber diameter distribution of PAN/CNC nanofiber membranes at different PAN/CNC mass ratios; (a)-(b) 5:1; (c)-(d) 4:1; (e)-(f) 3:1; (g)-(h) 2:1

Table 1 shows the average nanofiber diameters of PAN/CNC nanofiber membranes. The nanofiber diameter increases after the addition of CNC. When CNC is added with a low content, there is little effect on the diameter of the nanofibers. The average nanofiber diameter is 255 nm when the mass ratio of PAN to CNC is 5:1. The average nanofiber diameter tends to increase significantly as the mass fraction of CNC increases. This may be due to that the addition of CNC affects the properties of the electrospinning solution and thereby affects the nanofiber diameter.

Table 1 Average nanofiber diameters of PAN/CNC nanofiber membranes at different PAN/CNC mass ratios

PAN/CNC mass ratio	Average nanofiber diameter/nm
5:1	255
4:1	272
3:1	316
2:1	325

2.3 Effect of electrospinning time on thickness of PAN/CNC nanofiber membranes

With the speed, voltage and distance from the needle to the collection all being fixed, the relationship between the thickness of the PAN/CNC nanofiber membrane (a PAN mass fraction of 12% and a PAN/CNC mass ratio of 4:1) and the electrospinning time is shown in Fig. 4, where R^2 reflects the degree of the linear correlation between the nanofiber membrane thickness y_2 and the

electrospinning time x_2 .

When the electrospinning time is shorter, the membrane is thinner. When the electrospinning time is extended from 4 h to 5 h, the thickness of the PAN/CNC nanofiber membrane increases from 0.040 mm to 0.085 mm by 112.5%. When the electrospinning time is extended from 4 h to 8 h, the thickness of the PAN/CNC nanofiber membrane increases from 0.040 mm to 0.411 mm by 927.5%. R^2 is close to 1, indicating an approximately linear relationship between the membrane thickness and the electrospinning time.

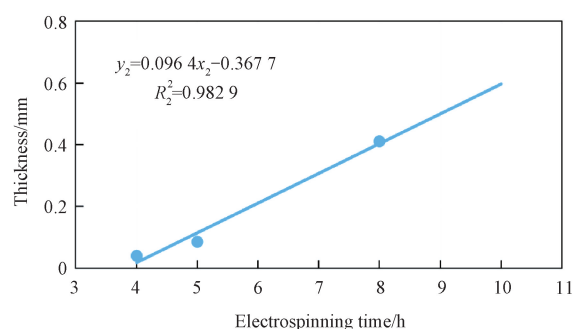


Fig. 4 Relationship between membrane thickness and electrospinning time of PAN/CNC nanofiber membranes

2.4 Morphology of PAN/CNC @ CNT nanofiber membranes

SEM images of PAN/CNC and PAN/CNC @ CNT nanofiber membranes at a PAN/CNC mass ratio of 4:1

are shown in Fig. 5. It is evident that CNTs can be effectively loaded onto the electrospun nanofiber

membrane. CNTs contribute to the stable conductive network, and improve the conductive performance.

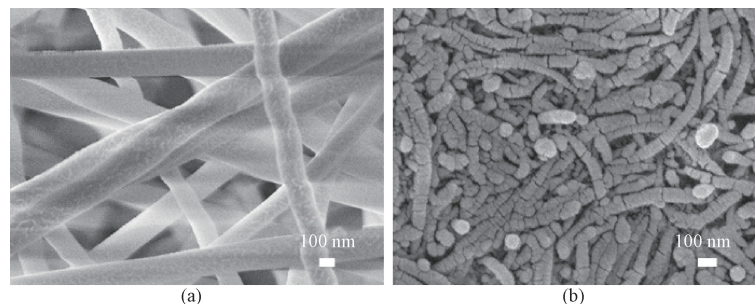


Fig. 5 SEM images of nanofiber membranes: (a) PAN/CNC; (b) PAN/CNC@CNT

2.5 Tensile properties of PAN, PAN/CNC and PAN/CNC@CNT nanofiber membranes

The tensile stress-strain curves of PAN, PAN/CNC and PAN/CNC@CNT nanofiber membranes are shown in Fig. 6. The tensile strength of the PAN nanofiber membrane is 0.81 MPa. The addition of CNC affects the tensile properties of the PAN nanofiber membrane. With the increase of the CNC mass fraction, the tensile strength of the PAN/CNC nanofiber membrane first increases and then decreases. When the mass ratio of PAN to CNC is 4:1, the tensile strength reaches the maximum, which is 2.13 MPa. The result shows that the addition of CNC could enhance the tensile strength of nanofiber membranes. The strong interfacial interaction between CNC and the compatible polymer results from hydrogen bonding and enables the effective stress/load transfer between the reinforcement and the matrix, resulting in high stretching resistance as well as high performance of nanocomposites^[26, 30]. The tensile strength of the PAN/CNC@CNT nanofiber membrane at a PAN/CNC mass ratio of 4:1 increases to 3.12 MPa. Compared with that of the PAN nanofiber membrane, the tensile strength of the PAN/CNC@CNT nanofiber membrane increases by about 285%. This indicates that CNTs can further improve the tensile properties of PAN/CNC nanofiber membranes due to the high elastic modulus and tensile strength of CNTs.

2.6 Conductivity of PAN/CNC and PAN/CNC@CNT nanofiber membranes

The surface resistivity of PAN/CNC and PAN/CNC@CNT nanofiber membranes at a PAN/CNC mass ratio of 4:1 is shown in Table 2. PAN is an insulating material, and CNC is also an insulating or semiconducting material. The PAN/CNC nanofiber membrane has a very low conductivity and it may not be measurable by the four-point probe method. After CNT impregnation, the surface resistivity changes to $64 \Omega/\text{cm}^2$. This is because the surface of the PAN/CNC nanofiber membrane is loaded with a certain amount of CNTs which have a high conductivity. Therefore, the flexible PAN/CNC@CNT nanofiber membrane has a higher conductivity.

Table 2 Surface resistivity of PAN/CNC and PAN/CNC@CNT nanofiber membranes

Nanofiber membrane	Surface resistivity/(Ω/cm^2)
PAN/CNC	—
PAN/CNC@CNT	64

3 Conclusions

CNC reinforced PAN nanofiber membranes were successfully prepared by electrospinning. Flexible conductive PAN/CNC@CNT nanofiber membranes were successfully prepared by impregnating PAN/CNC nanofiber membranes with CNTs. With the increase of the PAN mass fraction, the viscosity of the electrospinning solution increases and the nanofiber diameter becomes larger. The PAN/CNC nanofiber membranes can be successfully prepared with the addition of nano-reinforcement CNC at a PAN mass fraction of 12%. The addition of CNC affects the structure and properties of electrospun nanofiber membranes. With the addition of CNC, the nanofiber diameter increases and the nanofiber diameter distribution widens. When the mass ratio of PAN to CNC is 4:1, the tensile strength of the PAN/CNC nanofiber membrane is the highest, and it is higher than that of the PAN nanofiber membrane. After CNT impregnation, the tensile strength of the flexible conductive PAN/CNC@CNT nanofiber membrane

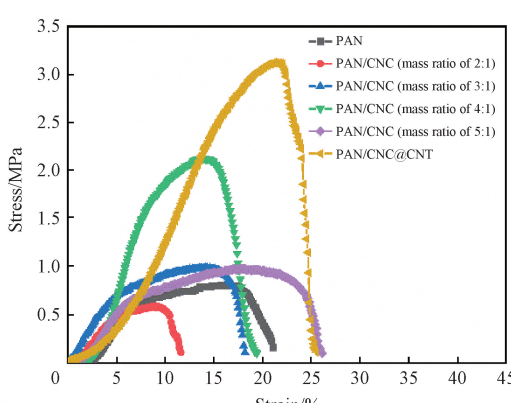


Fig. 6 Tensile stress-strain curves of electrospun nanofiber membranes

increases from 2.13 MPa to 3.12 MPa, and the surface resistivity changes to $64 \Omega/cm^2$. The flexible conductive nanofiber membranes could be used in energy storage and sensing fields, and this study might provide a strong base for their future development.

References

- [1] HOU Y, YANG Y, WANG Z Y, et al. Whole fabric-assisted thermoelectric devices for wearable electronics [J]. *Advanced Science*, 2022, 9(1) : e2103574.
- [2] JIA L H, LI Y H, REN A B, et al. Degradable and recyclable hydrogels for sustainable bioelectronics [J]. *ACS Applied Materials & Interfaces*, 2024, 16(26) : 32887-32905.
- [3] ZHANG L R, WU H, CHEN Y, et al. Biocompatible reduced graphene oxide ink hybridized by wool keratin for flexible strain sensor electronics [J]. *ACS Applied Electronic Materials*, 2024, 6(2) : 793-805.
- [4] LI T L, SU Y F, CHEN F Y, et al. Bioinspired stretchable fiber-based sensor toward intelligent human-machine interactions [J]. *ACS Applied Materials & Interfaces*, 2022, 14(19) : 22666-22677.
- [5] ZENG R J, WANG W J, CHEN M M, et al. CRISPR-Cas12a-driven MXene-PEDOT: PSS piezoresistive wireless biosensor [J]. *Nano Energy*, 2021, 82 : 105711.
- [6] LI H, CHEN J W, CHANG X H, et al. A highly stretchable strain sensor with both an ultralow detection limit and an ultrawide sensing range [J]. *Journal of Materials Chemistry A*, 2021, 9(3) : 1795-1802.
- [7] CHEN Y, SUN Y L, WEI Y Y, et al. How far for the electronic skin: from multifunctional material to advanced applications [J]. *Advanced Materials Technologies*, 2023, 8(8) : 2201352.
- [8] FROYEN A A F, SCHENNING A P H J. A multifunctional structural coloured electronic skin monitoring body motion and temperature [J]. *Soft Matter*, 2023, 19(3) : 361-365.
- [9] LIU Y T, LUO T T, DING C B, et al. Progress in the application of flexible and wearable electrochemical sensors in monitoring biomarkers of athletes [J]. *Advanced Materials Technologies*, 2024, 9(23) : 2400619.
- [10] CORZO D, TOSTADO-BLÁZQUEZ G, BARAN D. Flexible electronics: status, challenges and opportunities [J]. *Frontiers in Electronics*, 2020, 1 : 594003.
- [11] QUAN Z Z, ZU Y, LEI S, et al. Parametric effects on length of stable section of electrospinning jet [J]. *Journal of Donghua University (English Edition)*, 2021, 38 (5) : 417-423.
- [12] GAO T T, ZHENG J M, WANG D Y. Fabrication of high-efficiency polyvinyl alcohol nanofiber membranes for air filtration based on principle of stable electrospinning [J]. *Journal of Donghua University (English Edition)*, 2023, 40 (2) : 142-148.
- [13] ZHANG C H, YAO L, QIU Y P. Synthesis and characterization of LiFePO₄-carbon nanofiber-carbon nanotube composites prepared by electrospinning and thermal treatment as a cathode material for lithium-ion batteries [J]. *Journal of Applied Polymer Science*, 2016, 133(9) : 43001.
- [14] ZHANG C H, LIANG Y Z, YAO L, et al. Effect of thermal treatment on the properties of electrospun LiFePO₄-carbon nanofiber composite cathode materials for lithium-ion batteries [J]. *Journal of Alloys and Compounds*, 2015, 627 : 91-100.
- [15] LI X X, SONG X H, ZHANG L R, et al. Biocompatible polylactic acid/wool keratin/carbon nanotubes fibers via electrospinning as a flexible pressure electronic sensor [J]. *ACS Applied Electronic Materials*, 2024, 6(8) : 6131-6139.
- [16] MASKE V A, KOKATE A M, MORE P A, et al. A comprehensive review of polyacrylonitrile membranes: modifications and applications [J]. *Polymer Bulletin*, 2024, 81(18) : 16415-16455.
- [17] JIANG L, LI K, YANG H Y, et al. Improving mechanical properties of electrospun cellulose acetate nanofiber membranes by cellulose nanocrystals with and without polyvinylpyrrolidone [J]. *Cellulose*, 2020, 27(2) : 955-967.
- [18] LU H L, CEN X M, LI F Y, et al. Facile synthesis of highly elastic and antibacterial hydrogels based on rosin-modified cellulose nanocrystals [J]. *Journal of Materials Science*, 2025, 60(4) : 2118-2130.
- [19] TRACHE D, HUSSIN M H, MOHAMAD HAAFIZ M K, et al. Recent progress in cellulose nanocrystals: sources and production [J]. *Nanoscale*, 2017, 9(5) : 1763-1786.
- [20] AROCKIASAMY F S, MANOHARAN B, SANTHI V M, et al. Navigating the nano-world future: harnessing cellulose nanocrystals from green sources for sustainable innovation [J]. *Heliyon*, 2025, 11(1) : e41188.
- [21] YAN Y, ZU M M, YI Y J, et al. Research progress of green and low consumption preparation method of cellulose nanocrystal and its application [J/OL]. *Acta Materiae Compositae Sinica* (2024-09-19) [2025-01-03]. <https://doi.org/10.13801/j.cnki.fhclxb.20240919.003>. (in Chinese)
- [22] ASADNIA M, SADAT-SHOJAI M. Recent perspective of synthesis and modification strategies of cellulose nanocrystals and cellulose nanofibrils and their beneficial impact in scaffold-

- based tissue engineering: a review [J]. *International Journal of Biological Macromolecules*, 2025, 293: 139409.
- [23] LI Z X, FENG D L, ZHANG Z, et al. Palladium hexagonal nanoparticles/carbon nanotubes/cellulose nanocrystals integrated over paper for wearable hydrogen sensing with fast response by bridging behavior [J]. *Sensors and Actuators B: Chemical*, 2025, 427: 137153.
- [24] LIU X, ZHENG H R, CHEN Q, et al. Cellulose nanocrystals-doped hybrid matrix membranes for vanadium flow battery [J/OL]. *CIESC Journal* (2024-12-30) [2025-01-20]. <https://link.cnki.net/urlid/11.1946>. (in Chinese)
- [25] MOON R J, MARTINI A, NAIRN J, et al. Cellulose nanomaterials review: structure, properties and nanocomposites [J]. *Chemical Society Reviews*, 2011, 40(7): 3941-3994.
- [26] NG H M, SIN L T, TEE T T, et al. Extraction of cellulose nanocrystals from plant sources for application as reinforcing agent in polymers [J]. *Composites Part B: Engineering*, 2015, 75: 176-200.
- [27] RANA A K, FROLLINI E, THAKUR V K. Cellulose nanocrystals: pretreatments, preparation strategies, and surface functionalization [J]. *International Journal of Biological Macromolecules*, 2021, 182: 1554-1581.
- [28] DONG H, STRAWHECKER K E, SNYDER J F, et al. Cellulose nanocrystals as a reinforcing material for electrospun poly(methyl methacrylate) fibers: formation, properties and nanomechanical characterization [J]. *Carbohydrate Polymers*, 2012, 87(4): 2488-2495.
- [29] XIANG C H, JOO Y L, FREY M W. Nanocomposite fibers electrospun from poly(lactic acid)/cellulose nanocrystals [J]. *Journal of Biobased Materials and Bioenergy*, 2009, 3(2): 147-155.
- [30] REBOUILLET S, PLA F. State of the art manufacturing and engineering of nanocellulose: a review of available data and industrial applications [J]. *Journal of Biomaterials and Nanobiotechnology*, 2013, 4: 165-188.

纤维素纳米晶提高柔性导电聚丙烯腈@碳纳米管纳米纤维膜的拉伸性能

张长欢，王刘瑶，王浩文，马 涛，孙宏洋子^{*}，黄 易，童依婷，陈 洋，张力冉^{*}
北京服装学院 材料设计与工程学院，北京 100029

摘要：柔性导电纳米纤维膜在可穿戴电子设备领域的应用非常广泛，而良好的拉伸性能是静电纺纳米纤维膜商业化的必备性能之一。以纤维素纳米晶（cellulose nanocrystal, CNC）为增强材料，通过对含 CNC 的 PAN 溶液的静电纺丝及碳纳米管（carbon nanotube, CNT）水分散液的浸渍处理，成功制备了柔性导电聚丙烯腈（polyacrylonitrile, PAN）/CNC@CNT 纳米纤维膜。对该纳米纤维膜的结构和性能进行研究。结果表明：随着纺丝液中 PAN 质量分数的增加，纺丝液的黏度增加，纤维直径增加。当 PAN 质量分数为 12% 时，可成功制备不同 CNC 质量分数的 PAN/CNC 纳米纤维膜。CNC 的添加对 PAN/CNC 纳米纤维膜的结构和性能产生了影响。随着 CNC 质量分数的增加，纤维直径增加，直径分布范围变宽，拉伸强度先提高后降低。当 PAN 与 CNC 的质量比为 4:1 时，PAN/CNC 纳米纤维膜的拉伸强度最高，明显高于 PAN 纳米纤维膜。经过 CNT 水分散液浸渍处理得到的 PAN/CNC@CNT 纳米纤维膜的拉伸强度增加至 3.12 MPa，表面电阻率为 64 Ω/cm²。柔性导电纳米纤维膜有望广泛应用于储能、传感等领域，该研究结果可为上述领域的研究提供一定的基础。

关键词：纤维素纳米晶；柔性导电纳米纤维膜；拉伸性能；碳纳米管；静电纺丝；聚丙烯腈

DOI: 10.19884/j.1672-5220.202405016

Effect of Heat Treatment on Molecular Mass and Thermal Properties of Thermotropic Liquid Crystal Polyesters

DONG Shihang¹, CHEN Yufeng¹, WAN Hai¹, LIANG Yuan², HUANG Shuohan¹, WANG Yanping¹, XIA Yumin^{1*}

1. Key Laboratory of High Performance Fibers & Products, Ministry of Education, College of Materials Science and Engineering, Donghua University, Shanghai 201620, China

2. College of Physics, Donghua University, Shanghai 201620, China

Abstract: The thermotropic liquid crystal polyester (TLCP) fiber is an increasingly important strategic high-performance fiber. In this paper, the TLCP was prepared by two-step melt polymerization using 4-hydroxybenzoic acid (HBA) and 6-hydroxy-2-naphthoic acid (HNA) as comonomers at a molar ratio of 7:3. The structure of TLCP was confirmed by the Fourier transform infrared (FTIR) spectrometer and nuclear magnetic resonance (NMR) spectrometer. The thermal and rheological properties of TLCP before and after heat treatment were analyzed systematically by the differential scanning calorimeter (DSC), dynamic mechanical analyzer (DMA) and high-temperature rotational rheometer. The results revealed that the melting temperature, glass transition temperature and melt viscosity of the TLCP increased significantly after heat treatment. It indicates that the crystallization of the TLCP is perfect, and solid-phase condensation occurs during heat treatment, which increases its molecular mass. In conclusion, heat treatment at a temperature below but close to the melting temperature can effectively regulate the structure and properties of the TLCP, and the results of this study can provide a reference for the high strengthening of TLCP fibers.

Keywords: thermotropic liquid crystal polyester (TLCP); heat treatment; viscosity; thermal property

CLC number: TG15; TQ323.4 **Document code:** A

Article ID: 1672-5220(2025)02-0124-12

Open Science Identity
(OSID)



0 Introduction

Thermotropic liquid crystalline polyesters (TLCPs) have attracted significant research and commercial attention due to their outstanding thermal stability, mechanical strength and chemical resistance, and low linear thermal expansion coefficient^[1-9]. However, their molecular structure, which lacks flexible segments and exhibits a rigid rod-like configuration, leads to strong intermolecular forces, increasing brittle fractures or

fatigue cracks. Furthermore, these polyesters have high melting temperatures, posing challenges for processing and limiting their applications^[10-12]. To overcome these challenges, several methods have been explored to lower the melting temperature of TLCPs, aiming to strike a balance between the performance and processing temperature. These methods include introducing substituents and flexible groups to mesogenic units, as well as incorporating nonlinear monomers into the molecular chains. For example, poly(hydroxybenzoic acid) (P-HBA), synthesized from a rigid main chain represented by 4-hydroxybenzoic acid (HBA), exhibits an extremely high melting temperature and undergoes decomposition before melting. Conversely, 6-hydroxy-2-naphthoic acid (HNA), a nonlinear monomer with a kinked structure resembling a naphthalene ring, can be copolymerized with HBA to lower the melting temperature and prevent chain stacking^[13-24]. By employing these methods, it becomes possible to achieve a balance between the performance and processing temperature in TLCPs, thereby expanding their potential applications.

Melt polymerization is a method of polymerizing monomers at high temperatures, where the polymerization reaction occurs above the melting temperature of both the monomer and the polymer. This process offers advantages such as the reduced energy consumption, the shortened processing time and the improved production efficiency. However, it requires precise control over the ratio and extent of functional groups among monomers. Due to the challenge of precisely controlling the quantity of monomers during polymerization, polydisperse polymers with a wide molecular mass distribution are often produced. Heat treatment can be utilized to enhance the crystallinity and orientation of polymers, thereby improving their performance^[25-29]. Reyes et al.^[30] reported that molecular rearrangement during heat treatment could effectively adjust the physical properties of TLCPs by controlling their microstructure. The results

Received date: 2024-05-27

Foundation item: National Key Research and Development Program of China (No. 2021YFB3700105)

* Correspondence should be addressed to XIA Yumin, email: xym@dh.edu.cn

Citation: DONG S H, CHEN Y F, WAN H, et al. Effect of heat treatment on molecular mass and thermal properties of thermotropic liquid crystal polyesters[J]. *Journal of Donghua University (English Edition)*, 2025, 42(2): 124-135.

indicate an increase in the melting temperature, crystallinity and tensile modulus of TLCPs. These findings provide valuable insights for further optimizing the performance and processing of TLCPs.

This study utilized a two-step melt polymerization method to prepare the TLCP at a molar ratio of HBA to HNA of 7:3 (denoted as B70-N30). Firstly, the structures of the monomers before and after acetylation and the synthesized TLCP were compared using the Fourier transform infrared (FTIR) spectrometer, nuclear magnetic resonance (NMR) spectrometer and differential scanning calorimeter (DSC). Secondly, solid-phase condensation was conducted on the TLCP at different heat treatment temperatures of 240, 250 and 260 °C, and at different heat treatment times of 2, 4, 6, 8 and 10 h. Finally, the effects of the heat treatment temperature and time on the melting temperature, glass transition temperature and molecular mass of the TLCP were analyzed using the DSC, dynamic mechanical analyzer (DMA) and high-temperature rotational rheometer.

1 Materials and Methods

1.1 Materials

HBA and HNA were supplied by Zhejiang Shengxiao Chemical Company (Quzhou, China). Acetic anhydride was purchased from Shanghai Titan Technology Company (Shanghai, China).

1.2 Preparation

The TLCP at a molar ratio of 7:3 of HBA to HNA was prepared by a two-step melt polymerization method, as shown in Fig. 1. In the acetylation reaction step, HBA

and HNA were separately added to a round-bottom flask equipped with a mechanical stirrer and a condenser. An excess amount of acetic anhydride was added for the acetylation of monomers having hydroxyl groups. The acetylation was carried out at 150 °C for 3 h, after which the acetylated monomers, 4-acetoxy-benzoic acid (ABA) and 6-acetoxy-2-naphthalic acid (ANA), were rapidly cooled in a water bath and fully dried in a vacuum oven. The acetylated monomers and catalyst were added together into a three-neck round-bottom flask equipped with a mechanical stirrer, an N₂ inlet and a condenser. The reaction was performed under a constant flow of N₂. The process commenced with a gradual linear heating of the mixture from 260 °C to 280 °C, where it underwent reaction for 3.0 h. Subsequently, the temperature was incrementally raised to 300 °C and sustained for 1.5 h. Following this phase, the temperature was further elevated to 320 °C at which the reaction was maintained for an additional 1.5 h. Finally, to ensure thorough polymerization, the reaction mixture was subjected to a vacuum environment for 0.5 h. To characterize the structure, thermal and mechanical properties, the TLCP was injection molded into three different shapes of specimens: dumbbell-shaped (75 mm × 12.5 mm × 2.0 mm, with a narrow section in the middle measuring 25 mm × 4 mm × 2.0 mm), rectangular (50 mm × 7 mm × 2.0 mm), and cylindrical (Φ25 mm × 2.0 mm, where Φ represents the diameter). For solid-phase condensation, the TLCP powder and injection molded samples were subjected to heat treatment at different temperatures (240, 250 and 260 °C) and times (2, 4, 6, 8 and 10 h) using a DSC.

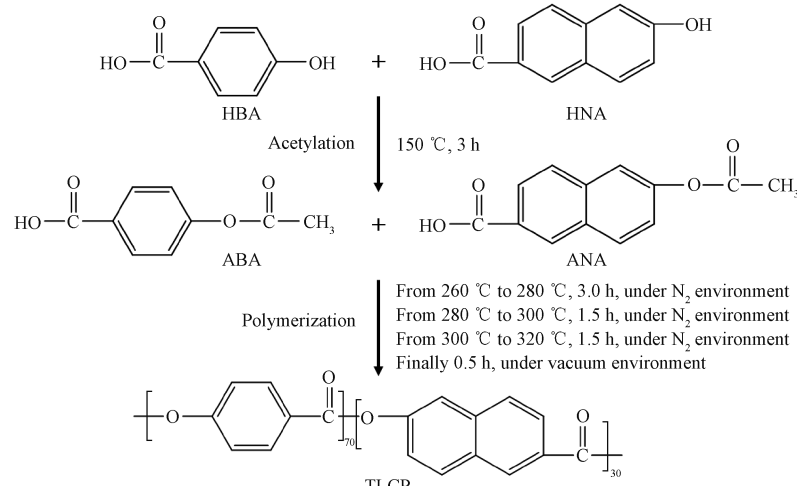


Fig. 1 Reaction route of TLCP

1.3 Characterization

The monomers were analyzed by using an FTIR spectrometer (Nicolet iS10, Thermo Fisher Scientific, Germany) to investigate any changes before and after acetylation. The spectra were acquired in a wavenumber range of 4 000 cm⁻¹ to 400 cm⁻¹.

The ¹H-NMR spectra of the monomers were obtained using an NMR spectrometer (ADVANCE400, Bruker Corporation, Germany) to analyze their chemical compositions.

The thermal properties of the TLCP were analyzed using a DSC (214 Polyma, NETZSCH-Gerätebau GmbH,

Germany) in a temperature range of 20 °C to 350 °C under N₂ environment. The heating and cooling rates were set at 20 °C/min. The monomers were analyzed using a DSC before and after acetylation. The temperature ranges were set at 20–230 °C and 20–260 °C, respectively, with two heating and cooling cycles.

The rectangular samples of the injection-molded TLCP were analyzed using a DMA (DMA8000, PerkinElmer, USA). The samples were heat-treated at temperatures of 240, 250 and 260 °C for 2 h, respectively, before testing. The measurement system employed a single cantilever test method in a testing temperature range of -100 °C to 200 °C at a heating rate of 0.5 °C/min, a static force of 0.05 N, an elongation of 0.002 mm, a data acquisition interval of 0.5 s, and a frequency of 1 Hz. Liquid nitrogen purging was utilized at a flow rate of 20 mL/min.

The melt rheology of the cylindrical injection-molded TLCP specimens under an oscillatory dynamic shear was analyzed with the aid of a rheometer (MCR702, Anton Paar, Austria) with parallel plate geometry. Dynamic frequency sweep tests were carried out in a frequency range of 0.001 rad/s to 100 rad/s.

2 Results and Discussion

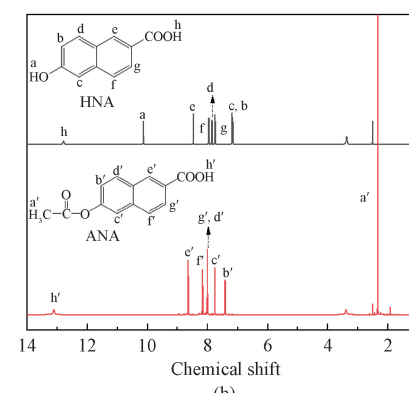
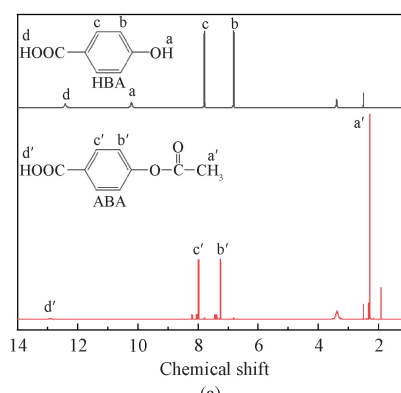
2.1 Analysis of chemical structure

Figure 2 illustrates the ¹H-NMR spectra of the monomers before and after acetylation. In the ¹H-NMR spectrum of HBA (Fig. 2(a)), the peak at chemical shift of 7.80 corresponds to the hydrogen atom adjacent to the carboxyl group on the benzene ring, while the peak at 6.80 represents the hydrogen atom adjacent to the hydroxyl group on the benzene ring. Additionally, the peak at 10.20 corresponds to the hydrogen atom in the hydroxyl group of HBA, and the peak at 12.40 corresponds to the hydrogen atom in the carboxyl group of HBA. In the ¹H-NMR spectrum of HNA (Fig. 2(b)), the peak at 12.80 represents the hydrogen atom in the carboxyl group, while the peaks at 8.46, 7.94 and 7.75 correspond to the hydrogen atoms near the carboxyl group on the naphthalene ring. The peaks at 7.85, 7.18 and 7.15

represent the hydrogen atoms near the hydroxyl group on the naphthalene ring. The peak at 10.13 corresponds to the hydrogen atom on the hydroxyl group of HNA. The ¹H-NMR spectra of ABA and ANA reveal that the peaks at position “a” disappear, and the peaks related to the acetyl group emerge at 2.30. This observation confirms that HBA and HNA have been fully acetylated.

Figures 2(c) and 2(d) show the DSC curves for the four monomers: HBA, HNA, ABA and ANA in the first (denoted as HBA-1, HNA-1, ABA-1 and ANA-1, respectively) and second heating cycles (denoted as HBA-2, HNA-2, ABA-2 and ANA-2, respectively). During the second heating cycle, the melting temperatures of ABA and ANA are determined to be 187.4 °C and 219.8 °C, respectively. These values are consistent with the commercially available samples' melting temperatures.

The acetylation process of the monomers was investigated by using the FTIR spectrometer, and the results are presented in Fig. 2(e). The peak at 3380 cm⁻¹ is associated with the stretching vibration of the O—H in the monomer. The peaks at 1370 and 1760 cm⁻¹ are attributed to the stretching vibrations of the C—H and C=O within the acetoxy group, respectively. Upon the acetylation of HBA and HNA, the O—H absorption peak vanishes, and two new absorption peaks appear, corresponding to the C=O and C—H in the acetoxy group. These peaks disappear following polymerization. Figure 2(f) reveals an absorption peak at 3070 cm⁻¹, attributed to the stretching vibration of the C—H on the aromatic ring, and a strong absorption peak at 1730 cm⁻¹, assigned to the vibration of the C=O in the ester group. As shown in the magnified region from 1300 cm⁻¹ to 1650 cm⁻¹ in Fig. 2(f), the peaks at 1413, 1505 and 1600 cm⁻¹ correspond to the stretching vibrations of the C=C on the benzene ring, aligning with the FTIR spectrum of ABA; whereas the peaks at 1340, 1470 and 1630 cm⁻¹ are associated with the naphthalene ring structural units, matching the FTIR spectrum of ANA. The presence of these functional group characteristic absorption peaks confirms the successful preparation of the TLCP.



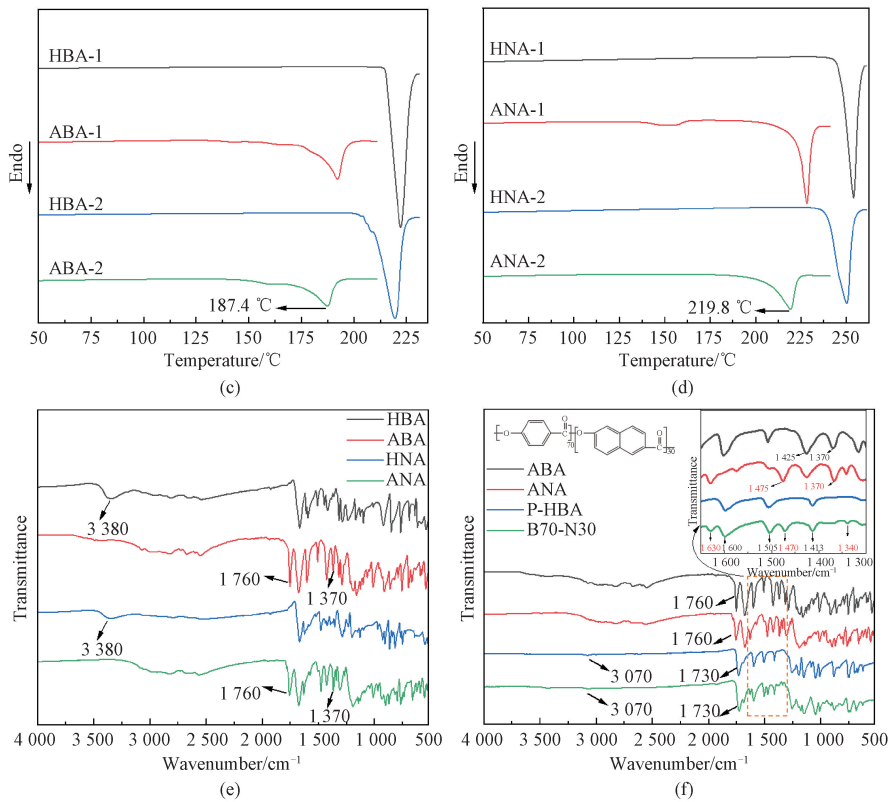


Fig. 2 Chemical structure analysis of monomers and TLCP: (a) ¹H-NMR spectra of HBA and ABA; (b) ¹H-NMR spectra of HNA and ANA; (c) DSC curves of HBA and ABA during heating; (d) DSC curves of HNA and ANA during heating; (e) FTIR spectra of monomers before and after acetylation; (f) FTIR spectra of TLCP

2.2 Effect of heat treatment on melting and crystallization temperatures

Figure 3 shows the DSC curves of the TLCP during the second heating and cooling cycle, with results summarized in Table 1. The melting temperature T_{m2} and crystallization temperature T_{c2} of the TLCP during the second heating and cooling cycle increase significantly. The crystallization temperature of the TLCP increases from 220.3 °C to a maximum of 223.7 °C. Moreover, the crystallization temperature is positively proportional to the heat treatment time. After heat treatment, the molecular chains of the TLCP align in an orderly manner. This alignment enhances the cohesion and directionality of molecular interactions, thereby forming a more complete crystal structure. The increase in the crystallization temperature is correlated with a higher crystallinity, which enhances its stability and heat resistance in high-temperature environments^[31-32]. It can be seen that after eliminating the thermal history, treating the TLCP at 240 °C for 8 h increases the melting temperature from 260.9 °C to 264.1 °C. Similarly, treating the TLCP at 250 °C for 8 h increases the melting temperature to 264.9 °C, and treating it at 260 °C for

4 h raises the melting temperature to 264.6 °C. Therefore, it can be concluded that increasing the heat treatment temperature is beneficial to the solid-phase condensation reaction^[33-34]. With the increase in the heat treatment temperature, the reactivity of end groups in the amorphous region and the diffusion rate of small molecules increase, promoting solid-phase condensation. However, further extending the treatment time for solid-phase condensation leads to a decrease in the melting temperature of the TLCP. This is due to the occurrence of not only condensation reactions involving end functional groups but also chain exchange reactions in the solid-phase condensation process, resulting in the recombination of chain structural units. On the one hand, the reaction between end functional groups can increase the molecular mass, while chain exchange reactions do not necessarily lead to an increase in the molecular mass and sometimes result in a decrease. On the other hand, the slower diffusion of small molecules due to the adhesive linkage of granular samples leads to an increase in by-products within the granular samples, resulting in a lower melting temperature.

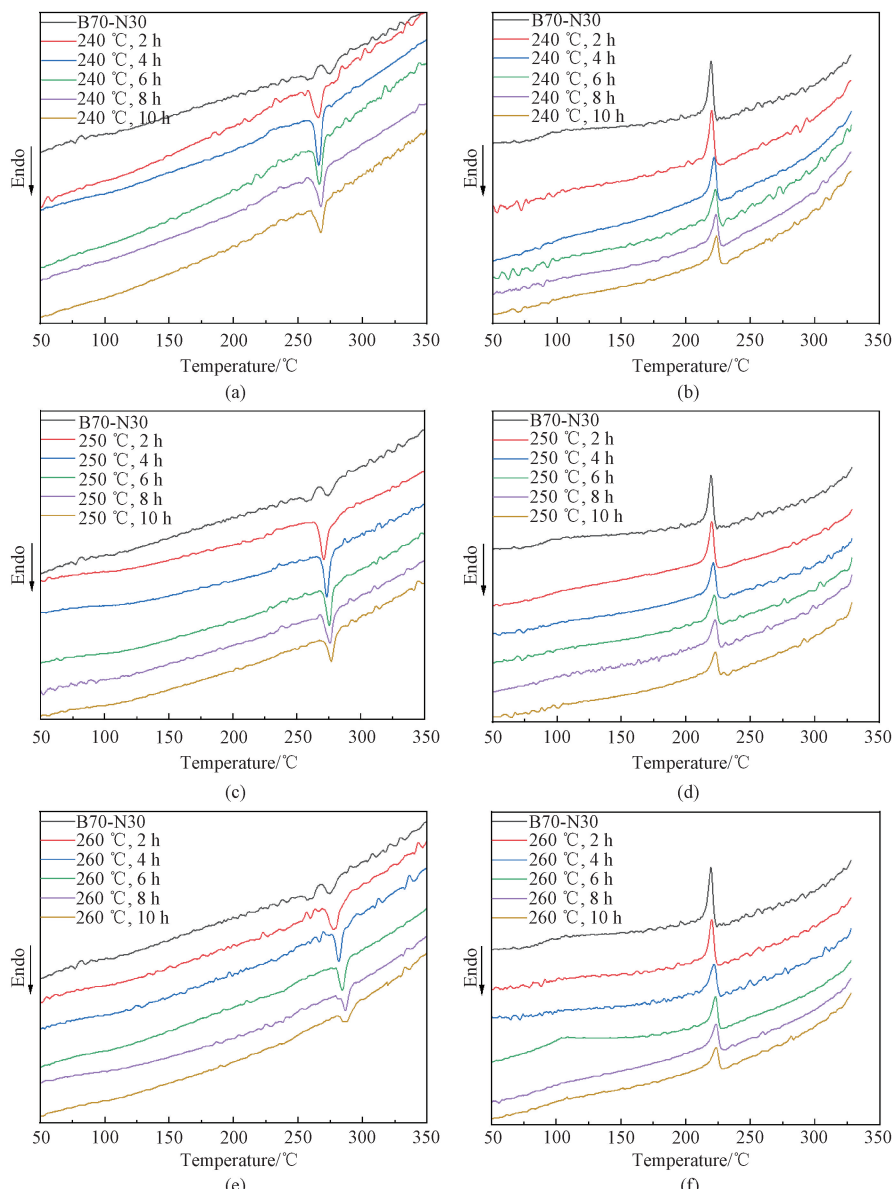


Fig. 3 DSC curves of TLCP: (a) DSC heating curves of TLCP after heat treatment at 240 °C for different times; (b) DSC cooling curves of TLCP after heat treatment at 240 °C for different times; (c) DSC heating curves of TLCP after heat treatment at 250 °C for different times; (d) DSC cooling curves of TLCP after heat treatment at 250 °C for different times; (e) DSC heating curves of TLCP after heat treatment at 260 °C for different times; (f) DSC cooling curves of TLCP after heat treatment at 260 °C for different times

Table 1 Thermal properties of TLCP after heat treatment for different times

Treatment temperature/°C	Treatment time/h	Thermal property	
		$T_{c2}/^{\circ}\text{C}$	$T_m/^{\circ}\text{C}$
240	0	220.3	260.9
	2	220.9	261.9
	4	222.4	263.6
	6	223.0	263.7
	8	223.4	264.1
	10	223.5	262.9

(Table 1 continued)

Treatment temperature/°C	Treatment time/h	Thermal property	
		$T_{c2}/^{\circ}\text{C}$	$T_{m2}/^{\circ}\text{C}$
250	0	220.3	260.9
	2	220.6	261.7
	4	221.7	263.8
	6	222.2	264.2
	8	223.3	264.9
	10	223.4	263.1
260	0	220.3	260.9
	2	221.0	262.6
	4	222.1	264.6
	6	223.2	264.2
	8	223.6	263.4
	10	223.7	263.3

2.3 Effect of heat treatment on glass transition temperature

The DMA curves of the injection-molded TLCP samples are presented in Fig. 4. The storage modulus exhibits a continuous decrease with the increase of the temperature (E' represents the storage modulus, E'' denotes the loss modulus, and $\tan \delta$ reflects the material's viscoelastic behavior). The mechanical damping curves, both before and after heat treatment,

exhibit three distinct relaxation transitions at approximately -50 , 30 and 100 $^{\circ}\text{C}$. These transitions are commonly denoted as α , β and γ , from high to low temperatures. The α relaxation process corresponds to the molecular chain movement, which is associated with the glass transition temperature. The β and γ relaxation processes are attributed to multiple transitions resulting from the movement of structural units smaller than the chain segments.

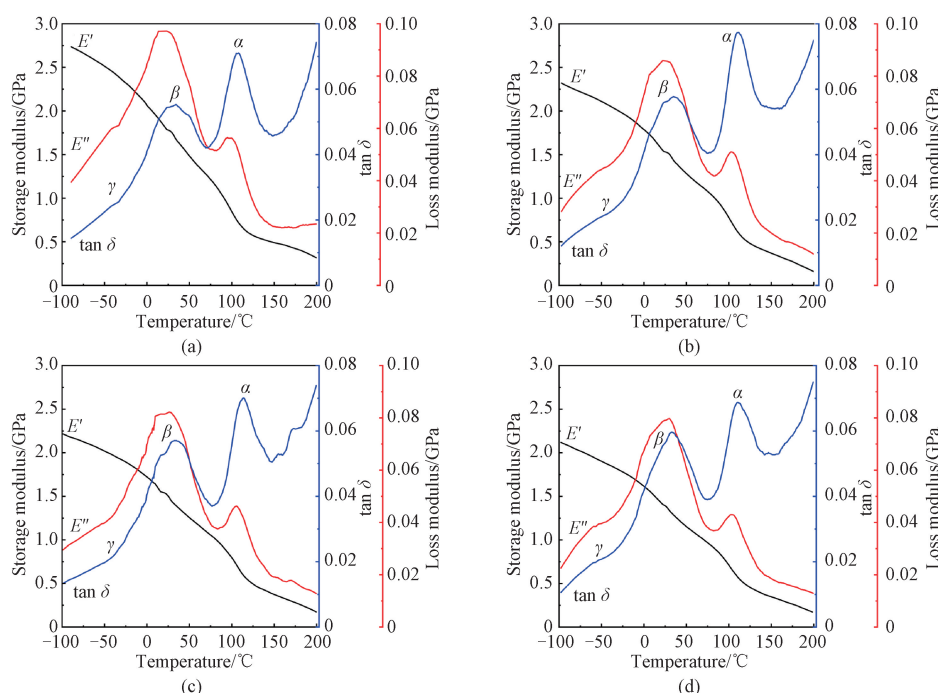


Fig. 4 DMA curves of TLCP; (a) untreated injection parts; (b) injection parts treated at 240 $^{\circ}\text{C}$ for 10 h; (c) injection parts treated at 250 $^{\circ}\text{C}$ for 10 h; (d) injection parts treated at 260 $^{\circ}\text{C}$ for 10 h

Figure 5 presents the relationship between the heat treatment time and $\tan \delta$ at different temperatures for the TLCP. Table 2 shows the correlation between the

relaxation temperatures and the heat treatment time and temperature. It can be observed that after the heat treatment, the α relaxation transition shifts towards higher

temperatures, leading to varying degrees of increased glass transition temperatures^[35]. However, there is no direct proportional relationship between the heat treatment time and the glass transition temperature. The maximum value of the glass transition temperature after a heat treatment at 240 °C is 110.0 °C, while it reaches 111.6 °C after a heat treatment at 250 °C, and the maximum value after a heat treatment at 260 °C is 110.9 °C. The experiment results demonstrate that raising the heat treatment temperature enhances the glass transition temperature of the TLCP. However, prolonging the heat treatment time may marginally decrease this temperature. Nonetheless, the glass transition temperature remains higher compared to that of untreated samples. The impact of heat treatment time and temperature on the internal structure of the TLCP is intricate. Appropriate heat treatment facilitates the optimization and organization

of the molecular structure of polyesters, concurrently alleviating internal stresses and defects. Extending heat treatment time might increase the molecular mobility and induce reorganization, potentially influencing the glass transition temperature of the TLCP. Additionally, with increasing heat treatment temperature and time, the intensity of the β relaxation process increases, while the intensity of the α relaxation process decreases. Heat treatment above the glass transition temperature of semi-crystalline polymers allows for the movement of the smallest molecular units, leading to the formation of a more perfect crystalline phase. During solid-phase condensation, the TLCP tends to exhibit improved crystallization, and condensation between functional groups further increases the molecular mass. As a result, after heat treatment, the glass transition temperature of the TLCP shifts towards higher temperatures^[36].

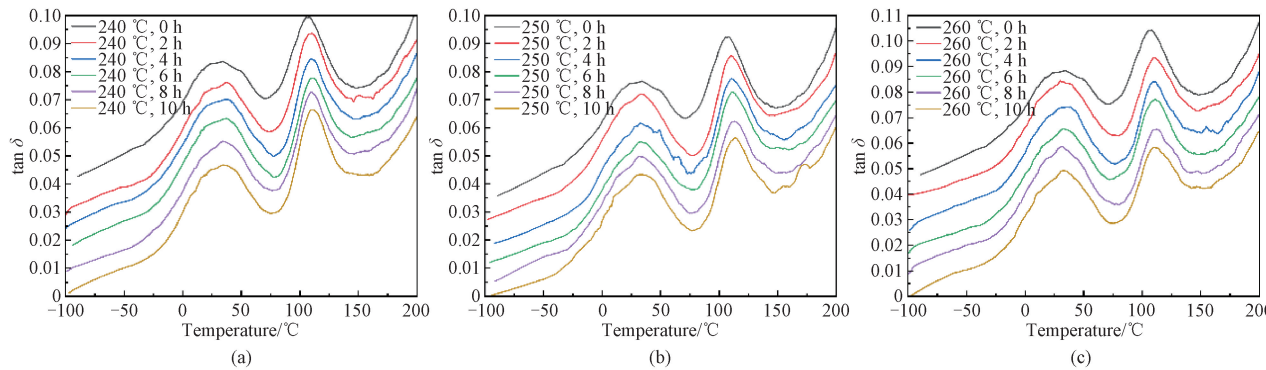


Fig. 5 Evolution of $\tan \delta$ with heat treatment time at frequency of 1 Hz and different temperatures: (a) 240 °C; (b) 250 °C; (c) 260 °C

Table 2 Correlation between relaxation temperatures and heat treatment time and temperature

Treatment temperature/°C	Treatment time/h	Relaxation temperature/°C	
		β	α
240	0	34.2	108.0
	2	36.3	108.3
	4	35.4	109.8
	6	34.8	110.0
	8	34.3	109.8
	10	34.6	109.4
250	0	34.2	108.0
	2	32.6	110.0
	4	32.6	110.6
	6	31.5	111.0
	8	31.6	110.6
	10	32.3	111.6
260	0	34.2	108.0
	2	30.0	110.0
	4	30.5	109.5
	6	32.8	110.9
	8	31.5	109.2
	10	32.9	109.9

2.4 Effect of heat treatment on molecular mass

TLCPs are a type of anisotropic non-Newtonian fluids. The most significant difference between TLCPs and conventional polymer fluids is the presence of orientational characteristics, which leads to distinct rheological behavior. The viscosity-shear rate flow curve of TLCPs can be divided into three flow regions; region I represents the shear-thinning region at low shear rates, where the apparent viscosity decreases rapidly with increasing of the shear rate; region II is the quasi-Newtonian region with the nearly constant viscosity; region III corresponds to shear-thinning at high shear rates. However, not all TLCPs exhibit these three flow regions.

Figure 6 illustrates the relationship between the melt viscosity and shear rate of the TLCP at different shear temperatures. At low shear rates, the viscosity increases slightly with the increase in the shear rate. This is because the molecular chains of the cylindrical samples obtained by injection molding are highly oriented. At 280 °C, the highly oriented cylindrical samples experience some entanglement at lower shear forces, leading to a slight increase in the viscosity. As the shear rate increases, the TLCP exhibits shear-thinning characteristics. The samples subjected to high shear forces also have highly oriented molecular chains. When the temperature rises to 285 °C, even at lower shear forces, some entanglement occurs, leading to an increase in the viscosity. As the temperature increases, the viscosity of the TLCP exhibits a significant decrease, indicating a strong temperature dependence of the viscosity. At 280 °C and 285 °C, the viscosity of the TLCP decreases by three orders of magnitude with the increasing shear rate, and as the temperature continues to rise, the decreasing trend of the viscosity becomes less pronounced. The increase in the viscosity at lower shear rates may be related to the liquid crystalline state of the polyester. Additionally, no distinct three flow regions are observed on the flow curve of the TLCP. Within a certain range of shear rates, it exhibits the characteristic of shear-thinning.

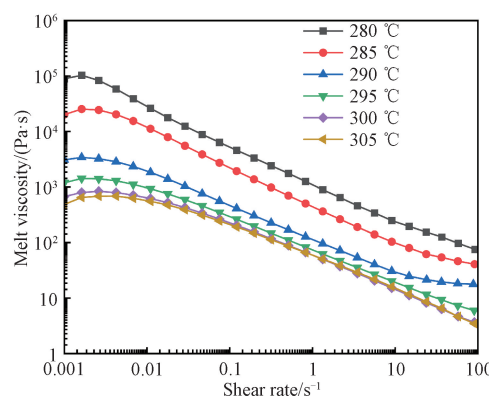


Fig. 6 Relationship between melt viscosity and shear rate of TLCP at different shear temperatures

Figures 7 – 9 illustrate the viscosity curves of the TLCP subjected to heat treatment at different shear temperatures for different times. The viscosity of the samples tends to decrease as the shear temperature increases. Additionally, at a constant temperature, the viscosity demonstrates the shear-thinning behavior with an increase in the shear rate. In the case of TLCPs, the rigid chains exhibit local orientation at low shear rates. However, with increasing of the shear rates, the rigid chains rapidly develop a broader range of orientations. Moreover, due to the strong intermolecular forces of the rigid chain structure, once orientation occurs, it is difficult to reverse. The extensive orientation range hinders the transfer of momentum between flow layers, leading to a significant reduction in the interlayer drag force and subsequently decreasing the melt viscosity.

Romo-Uribe et al.^[37] reported that the dependence of the viscosity on the molecular mass for nematic copolymers without flexible spacers could be represented as $\eta_0 \propto M^{4.1}$ (η_0 represents the zero shear viscosity, and M represents the viscosity-average molecular mass). This value (4.1) is distinctly different from the value of 3.4 for conventional polymer melts but lies within the range of values reported for nematic polymers with flexible spacers. The molecular mass of the TLCP correlates positively with the viscosity^[38-39]. The viscosity curves of samples subjected to heat treatment at 240 °C for different times overlapped almost completely, indicating that there is no significant increase in the molecular mass after heat treatment at 240 °C. However, the viscosity curves of samples subjected to heat treatment at 250 °C for different times start to disperse. At shear temperatures of 280, 285, 290 and 295 °C, the viscosity of heat-treated samples is higher than that of untreated samples, suggesting an increase in the molecular mass of the TLCP due to heat treatment at 250 °C. When the heat treatment temperature elevates to 260 °C, the viscosity curves for different heat treatment times show greater dispersion, indicating a more pronounced increase in viscosity and a further improvement in the molecular mass of the TLCP. Additionally, the molecular mass of the samples subjected to heat treatment at 250 °C and 260 °C at a shear temperature of 280 °C increases with longer heat treatment time^[40]. These results indicate that solid-phase condensation reactions are difficult at lower temperatures, while they are accelerated at higher temperatures, leading to a rapid increase in the molecular mass. Therefore, to obtain a higher molecular mass of the TLCP, a higher heat treatment temperature and longer treatment time should be selected.

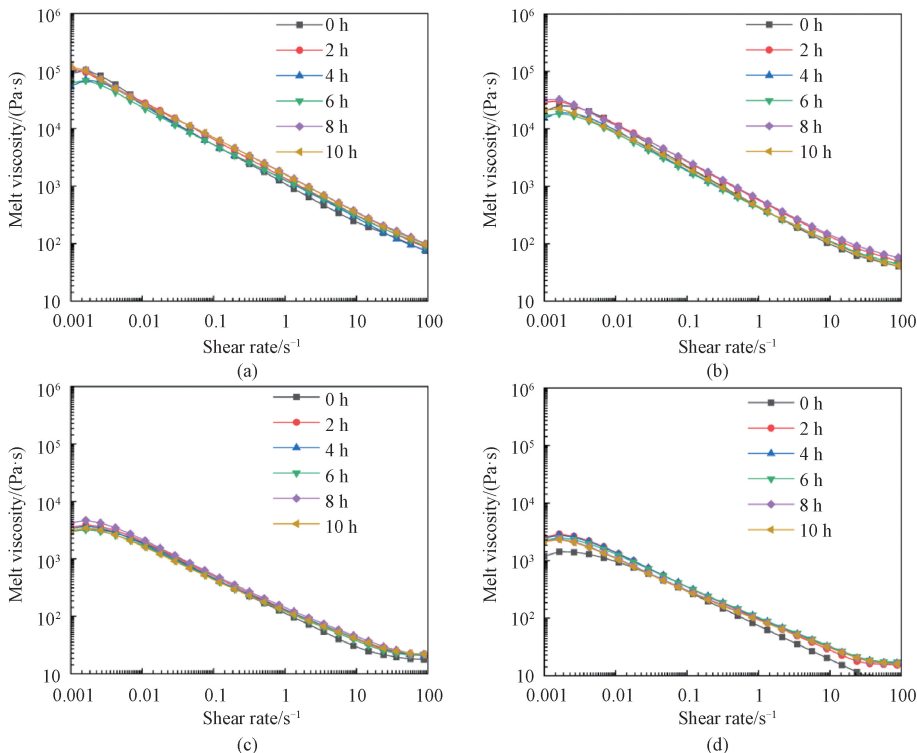


Fig. 7 Viscosity curves of TLCP after heat treatment at 240 °C for different times at specific shear temperature; (a) 280 °C; (b) 285 °C; (c) 290 °C; (d) 295 °C

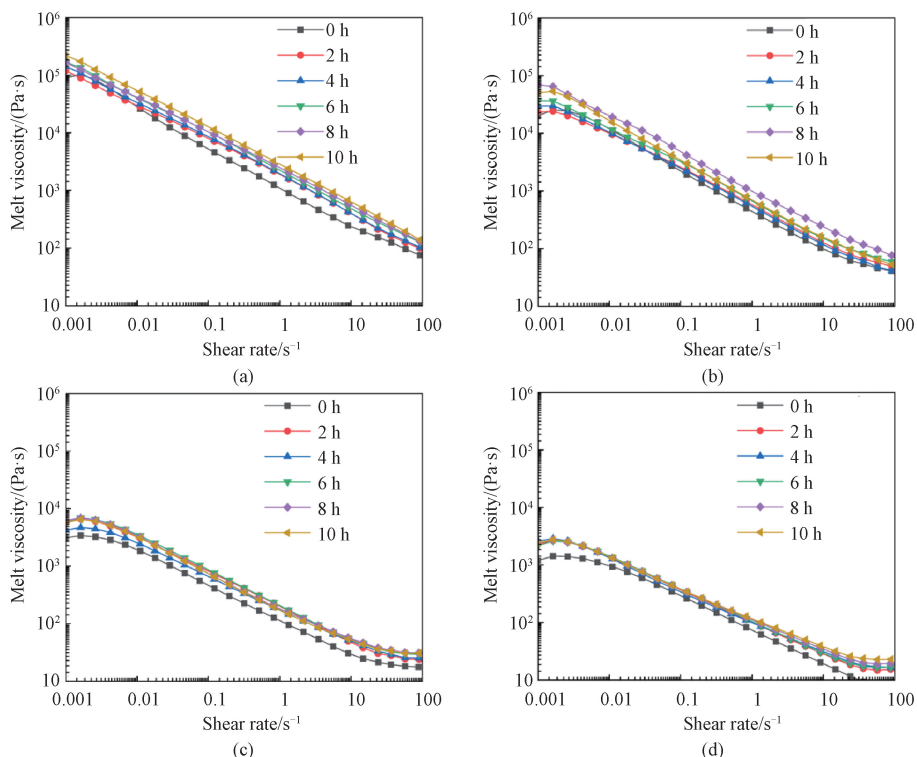


Fig. 8 Viscosity curves of TLCP after heat treatment at 250 °C for different times at specific shear temperature; (a) 280 °C; (b) 285 °C; (c) 290 °C; (d) 295 °C

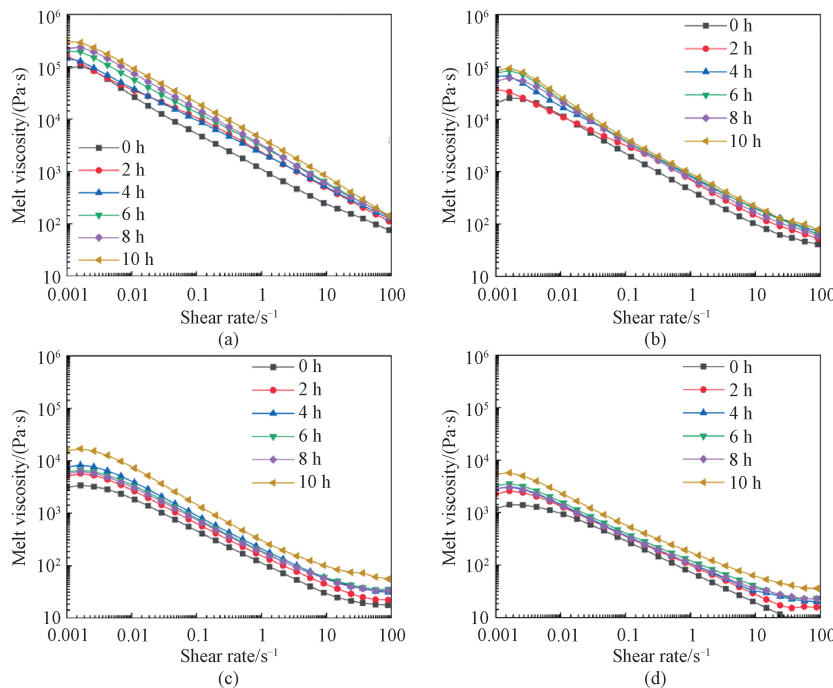


Fig. 9 Viscosity curves of TLCP after heat treatment at 260 °C for different times at specific shear temperature: (a) 280 °C; (b) 285 °C; (c) 290 °C; (d) 295 °C

3 Conclusions

A TLCP at a molar ratio of 7:3 of HBA to HNA was prepared using a two-step melt polymerization method. The TLCP was subjected to solid-phase condensation by using a DSC. Experimental results showed that after eliminating the thermal history, heat treatment at 260 °C for 4 h improved the melting temperature of the TLCP from 260.9 °C to 264.6 °C. However, further extending the heat treatment time resulted in a decrease in the melting temperature. The slower diffusion of small molecules due to the adhesive linkage of granular samples leads to an increase in by-products within the granular samples, resulting in a lower melting temperature. After heat treatment at 250 °C, the glass transition temperature rose from 108.0 °C to 111.6 °C. Observation of the viscosity curves of the TLCP revealed marked changes in the viscosity for different treatment times at 260 °C. At higher temperatures, the reaction rate of solid-phase condensation was faster, leading to rapid growth in the molecular mass. In summary, heat treatment resulted in an enhancement of the melting temperature, glass transition temperature and molecular mass of the TLCP. However, the impact of heat treatment on TLCP is complex and requires a comprehensive consideration of treatment conditions.

References

- [1] LYU X L, XIAO A Q, SHI D, et al. Liquid crystalline polymers: discovery, development,

and the future [J]. *Polymer*, 2020, 202: 122740.

- [2] SCHALLER R, PEIJS T, TERVOORT T A. High-performance liquid-crystalline polymer films for monolithic “composites” [J]. *Composites Part A: Applied Science and Manufacturing*, 2016, 81: 296-304.
- [3] KOMATSU S, WETZEL B, FRIEDRICH K. Novel liquid crystal polymers with tailored chemical structure for high barrier, mechanical and tribological performance [M]. Cham: Springer, 2015: 15-39.
- [4] RAMATHAL H, LAWAL A. Barrier properties of a thermotropic liquid-crystalline polymer [J]. *Journal of Applied Polymer Science*, 2003, 89 (9): 2457-2463.
- [5] WEINKAUF D H, PAUL D R. Gas transport properties of thermotropic liquid-crystalline copolymers. I. The effects of orientation and annealing [J]. *Journal of Polymer Science Part B: Polymer Physics*, 1992, 30(8): 817-835.
- [6] WEI P, LI L L, WANG L, et al. Synthesis and properties of high performance biobased liquid crystal copolymers toward load-bearing bone repair application [J]. *European Polymer Journal*, 2022, 173: 111278.
- [7] WANG S Y, MA S N, LI N, et al. Branched thermotropic liquid crystal polymer with favourable processability and dielectric properties [J]. *European Polymer Journal*, 2023, 196: 112302.
- [8] THOMPSON D C, TANTOT O, JALLAGEAS

- H, et al. Characterization of liquid crystal polymer (LCP) material and transmission lines on LCP substrates from 30 to 110 GHz [J]. *IEEE Transactions on Microwave Theory and Techniques*, 2004, 52(4): 1343-1352.
- [9] GUAN Q B, LU X, CHEN Y Y, et al. High-performance liquid crystalline polymer for intrinsic fire-resistant and flexible triboelectric nanogenerators [J]. *Advanced Materials*, 2022, 34(34): e2204543.
- [10] PARK G T, CHANG J H, LIM A R. Thermotropic liquid crystalline polymers with various alkoxy side groups: thermal properties and molecular dynamics [J]. *Polymers*, 2019, 11(6): 992.
- [11] CHOI E J, LEE S J, JEONG Y G. Effects of mesogenic cycloaliphatic units on the microstructure and properties of thermotropic liquid crystalline polyesters [J]. *ChemistrySelect*, 2023, 8(1): e202203131.
- [12] SONG B S, LEE J Y, JANG S H, et al. Fiber formation and structural development of HBA/HNA thermotropic liquid crystalline polymer in high-speed melt spinning [J]. *Polymers*, 2021, 13(7): 1134.
- [13] DONG D W, JIANG S C, NI Y S, et al. Syntheses and properties of thermotropic copolymers of *p*-hydroxybenzoic acid [J]. *European Polymer Journal*, 2001, 37(3): 611-617.
- [14] LI X G, ZHOU Z L, WU X G, et al. Structure and properties of liquid crystalline naphthalenediol copolymers [J]. *Journal of Applied Polymer Science*, 1994, 51(11): 1913-1921.
- [15] KRIGBAUM W R, HAKEMI H, KOTEK R. Nematicogenic polymers having rigid chains. 1. Substituted poly(*p*-phenylene terephthalates) [J]. *Macromolecules*, 1985, 18(5): 965-973.
- [16] WEI P, CAKMAK M, CHEN Y W, et al. Aromatic liquid crystalline copolymers with low T_m and high T_g : synthesis, characterization, and properties [J]. *Journal of Applied Polymer Science*, 2014, 131(13): 40487.
- [17] WEI P, CAKMAK M, CHEN Y W, et al. The influence of bisphenol AF unit on thermal behavior of thermotropic liquid crystal copolymers [J]. *Thermochimica Acta*, 2014, 586: 45-51.
- [18] LENZ R W. Synthesis and properties of thermotropic liquid crystal polymers with main chain mesogenic units [J]. *Polymer Journal*, 1985, 17(1): 105-115.
- [19] WEI P, LOU H J, YAN J F, et al. Synthesis and properties of high performance aromatic thermotropic liquid crystal copolymers based on naphthalene ring structure [J]. *Polymer*, 2022, 240: 124472.
- [20] BALLAUFF M, SCHMIDT G F. Rigid rod polymers with flexible side chains. 2. Observation of a novel type of layered mesophase [J]. *Die Makromolekulare Chemie, Rapid Communications*, 1987, 8(2): 93-97.
- [21] PAN Z Y, GAO S X, ZHAO Y F, et al. Processability-enhanced aromatic thermotropic liquid crystalline copolymers via the introduction of the unsymmetrical units [J]. *Journal of Applied Polymer Science*, 2023, 140(13): e53659.
- [22] WEI P, WANG L, WANG X H, et al. Nonisothermal and isothermal oxidative degradation behavior of thermotropic liquid crystal polyesters containing kinked bisphenol AF and bisphenol A units [J]. *High Performance Polymers*, 2014, 26(8): 935-945.
- [23] JACKSON W J Jr. Liquid crystalline polymers. 5. Liquid crystalline polyesters containing naphthalene rings [J]. *Macromolecules*, 1983, 16(7): 1027-1033.
- [24] LANGELAAN H C, DE BOER A P. Crystallization of thermotropic liquid crystalline HBA/HNA copolymers [J]. *Polymer*, 1996, 37(25): 5667-5680.
- [25] PARK S, NA Y J, KIM A Y, et al. Annealing effect of thermotropic liquid crystalline copolyester fibers on thermo-mechanical properties and morphology [J]. *Scientific Reports*, 2022, 12: 13100.
- [26] SARLIN J, TÖRMÄLÄ P. Heat treatment studies of a TLCP fiber [J]. *Journal of Applied Polymer Science*, 1993, 50(7): 1225-1231.
- [27] SARLIN J, TÖRMÄLÄ P. Isothermal heat treatment of a thermotropic LCP fiber [J]. *Journal of Polymer Science Part B: Polymer Physics*, 1991, 29(4): 395-405.
- [28] KIM Y C, ECONOMY J. The mechanical properties of thermally treated 73/27 HBA/HNA copolyester [J]. *Polymers for Advanced Technologies*, 1999, 10(8): 493-500.
- [29] LEE W J, KWAC L K, KIM H G, et al. Thermotropic liquid crystalline copolyester fibers according to various heat treatment conditions [J]. *Scientific Reports*, 2021, 11: 11654.
- [30] REYES-MAYER A, ROMO-URIBE A, JAFFE M. Structure evolution of thermotropic polymers by thermal annealing. A light and X-ray scattering study [J]. *MRS Online Proceedings Library*, 2015, 1765(1): 65-70.
- [31] SCHNEGGENBURGER L A, OSENAR P, ECONOMY J. Direct evidence for sequence ordering of random semicrystalline copolymers during high-temperature annealing [J]. *Macromolecules*, 1997, 30(13): 3754-3758.
- [32] KAITO A, KYOTANI M, NAKAYAMA K. Effects of draw-down ratio and annealing

- treatment on structure formation in extruded strands of a thermotropic liquid crystalline copolyester [J]. *Journal of Macromolecular Science, Part B*, 1995, 34(1/2) : 105-118.
- [33] ROMO-URIBE A, REYES-MAYER A, SARMIENTO-BUSTOS E, et al. Synchrotron scattering and nanoindentation of heat treated high performance thermotropic polymer [J]. *MRS Advances*, 2018, 3(62) : 3709-3714.
- [34] KIM Y C, ECONOMY J. The degradation process observed during step annealing of 73/27 HBA/HNA copolyester [J]. *Macromolecules*, 1999, 32(9) : 2855-2860.
- [35] ROMO-URIBE A, REYES-MAYER A, CALIXTO RODRIGUEZ M, et al. On the influence of thermal annealing on molecular relaxations and structure in thermotropic liquid crystalline polymer [J]. *Polymer*, 2022, 240: 124506.
- [36] REYES-MAYER A, ALVARADO-TENORIO B, ROMO-URIBE A, et al. SALS, WAXS and mechanical properties of heat-treated thermotropic polymers [J]. *Polymers for Advanced Technologies*, 2013, 24(12) : 1029-1039.
- [37] ROMO-URIBE A, WINDLE A H. Melt viscosity of main-chain thermotropic liquid crystalline polymers without flexible spacers [J]. *Macromolecules*, 1995, 28(21) : 7085-7087.
- [38] HEBERER D P, ODELL J A, PERCEC V. Rheology and flow-induced liquid crystal phase transitions in thermotropic polyethers [J]. *Journal of Materials Science*, 1994, 29 (13) : 3477-3483.
- [39] KAITO A, KYOTANI M, NAKAYAMA K. Effects of annealing on the structure formation in a thermotropic liquid crystalline copolyester [J]. *Macromolecules*, 1990, 23(4) : 1035-1040.
- [40] WARNER S B, LEE J. Towards understanding the increase in strength of thermotropic polyesters with heat treatment [J]. *Journal of Polymer Science Part B: Polymer Physics*, 1994, 32 (10) : 1759-1769.

热处理工艺对热致液晶聚芳酯分子量及热性能的影响

董世航¹, 陈宇锋¹, 万海¹, 梁源², 黄铄涵¹, 王燕萍¹, 夏于曼^{1*}

1. 东华大学 高性能纤维及制品教育部重点实验室, 材料科学与工程学院, 上海 201620

2. 东华大学 物理学院, 上海 201620

摘要: 热致液晶聚芳酯 (thermotropic liquid crystal polyester, TLCP) 纤维是一种重要的战略性高性能纤维。该文以 4-羟基苯甲酸 (HBA) 和 6-羟基-2-萘甲酸 (HNA) 作为共聚单体 (摩尔比为 7:3), 通过两步熔融缩聚法制备了 TLCP。通过傅里叶变换红外光谱和核磁共振波谱确认了 TLCP 的结构。利用差示扫描量热仪、动态热机械分析仪和高温旋转流变仪分析了热处理前后 TLCP 的热性能和流变学特性。结果表明, 经过热处理后, TLCP 的熔点、玻璃化转变温度和熔体黏度显著增加, 这表明 TLCP 的结晶更加完善, 并且在热处理过程中发生了固相缩聚反应, 增加了其分子量。总之, 在低于但接近熔点的温度条件下进行热处理可以有效调节 TLCP 的结构和性能, 该研究结果可为 TLCP 纤维的高强化提供参考。

关键词: 热致液晶聚芳酯; 热处理; 黏度; 热性能

Reactive Dyeing of Wool Fabric Using Recycled Dyeing Wastewater

WANG Bingxin, HAN Bo, ZHANG Xinyuan, LI Wanxin, XU Jia, SHU Dawu*

College of Textile and Garments, Hebei University of Science and Technology, Shijiazhuang 050018, China

Abstract: Aiming to solve the problem of large discharge and severe pollution of reactive dyeing wastewater for wool fabrics, peroxodisulfate (SPS) was used for the degradation and recycling of dyeing wastewater containing reactive dye Lanasol Red CE. The process of degrading the reactive dye was determined by using the dye residual rate as the evaluation index. The feasibility of reactive dyeing of wool fabrics using recycled dyeing wastewater was confirmed by measuring the dye uptake, exhaustion and fixation rates, as well as color parameters and fastness of the dyed fabrics. The results showed that the appropriate conditions for degrading Lanasol Red CE were 0.2 g/L SPS, an initial pH value of 3 and 100 °C for 30 min. Under these conditions, the dye degradation rate was as high as 93.14%. When the recycled dyeing wastewater was used for dyeing of wool fabrics, the exhaustion rate of Lanasol Red CE exceeded 99%, and the fixation rate was higher than that achieved by the conventional dyeing process. Under the same dyeing conditions, the recycled-dyed fabrics appeared darker. When the number of cycles was fewer than five, the effect on color fastness was not obvious. Although the color fastness to rubbing and washing of the fabrics dyed in the 10th cycle decreased by half a grade and 1 grade, respectively, compared to that of the fabrics dyed with the conventional dyeing process, they still met the production requirements.

Keywords: wool fabric; reactive dye; dyeing wastewater; recycling; dyeing

CLC number: X791

Article ID: 1672-5220(2025)02-0136-08

Document code: A

Open Science Identity
(OSID)



0 Introduction

Wool products are highly regarded by consumers because of their exceptional elasticity, luxurious feel and excellent moisture absorption properties^[1]. Wool reactive dye is designed specifically for wool fibers, offering advantages such as vibrant colors, easy application, uniform dyeing and excellent fastness^[2]. However, the wool fiber dyeing process generates substantial amounts

of dyeing wastewater, causing severe environmental pollution.

Printing and dyeing wastewater exhibits deep color, high alkalinity, high organic pollutant contents, and significant variations in water quality, making it one of the most challenging types of industrial wastewater to treat^[3-4]. To meet the requirements for the reuse of printing and dyeing wastewater, the primary treatment targets include reducing chemical oxygen demand (COD), biochemical oxygen demand (BOD) and chromaticity^[5]. Three main treatment technologies are employed for dealing with dyes in printing and dyeing wastewater: physical methods (such as adsorption, membrane separation and coagulation-flocculation), chemical methods (including chemical oxidation, photocatalytic oxidation and electrochemical processes), and biological methods (comprising anaerobic, aerobic and combined anaerobic-aerobic treatments)^[6-7].

Current methods for treating printing and dyeing wastewater include adsorption, membrane separation and advanced oxidation^[8]. The adsorption method can capture various toxic and hazardous substances, making it suitable for treating different types of printing and dyeing wastewater^[9-10]. Additionally, the cost of preparing adsorbents is relatively low. Nevertheless, adsorbents need periodic replacement, and the waste adsorbents can cause secondary pollution. The research demonstrated that activated carbon adsorption treatment of printing and dyeing wastewater achieved a COD removal rate of 66% with a theoretical adsorption capacity of 2.11 mg/g after static adsorption for 30 min^[11]. However, this method exhibits poor adsorption effects for water-soluble dyes and low regeneration rates. The membrane separation method is simple to operate and can recover reusable substances^[12-14]. Sun et al.^[15] prepared a thiourea-modified graphene oxide membrane and investigated its removal efficiency of methyl orange, rhodamine B and methylene blue, which reached 94.01%, 87.07% and 99.67%, respectively. However, in practice, membranes are prone to clogging due to contaminants and incur high production cost.

Received date: 2024-06-28

Foundation items: Youth Foundation of Hebei Province Department of Education Fund, China (No. QN2023090); Opening Project of Textile Ecological Dyeing and Finishing Key Laboratory of Sichuan Province (Chengdu Textile College), China (No. 2024DF-AO2); Innovation and Entrepreneurship Training Program for College Students, China (No. 202410082023)

* Correspondence should be addressed to SHU Dawu, email: shudawu@126.com

Citation: WANG B X, HAN B, ZHANG X Y, et al. Reactive dyeing of wool fabric using recycled dyeing wastewater[J]. *Journal of Donghua University (English Edition)*, 2025, 42(2): 136-143.

The advanced oxidation method exhibits high oxidation potential, rapid degradation rates, high efficiency in degradation and minimal secondary pollution, making it a standout method for treating printing and dyeing wastewater^[16]. Advanced oxidation is the degradation of dye molecules in printing and dyeing wastewater with the help of oxidation techniques such as Fenton oxidation, ozone oxidation and persulfate oxidation^[17]. Among these oxidation techniques, Fenton oxidation offers mild and efficient reaction conditions and is relatively easy to operate. However, it requires the use of large amounts of H₂O₂. Additionally, the side reaction between Fe²⁺ and H₂O₂ reduces the utilization of H₂O₂, and the high cost of H₂O₂ adds to the overall expense^[18]. Although ozone can effectively remove organic matter and color from printing and dyeing wastewater, it struggles to achieve deep treatment effects or to meet reuse standards when used alone^[19-20]. Persulfate oxidation produces free radicals with strong oxidizing ability during the reaction process, which decomposes pollutants with complex structures that are difficult to degrade into CO₂, H₂O and inorganic salts^[21-23]. The generated inorganic salts can serve as dyeing promoters, but the relevant studies on recycling them from dyeing wastewater for reuse in wool fabric dyeing have rarely been reported.

This paper focuses on the degradation and recycling treatment of dyeing wastewater containing Lanasol Red CE through the thermal activation of peroxodisulfate (SPS). The effects of three factors, namely the temperature, pH value and SPS mass concentration on the dye degradation were discussed. Subsequently, the recycled dyeing wastewater was used as a dyeing medium for wool fabric dyeing. The dye uptake, exhaustion and fixation rates, color parameters and color fastness of the

dyed fabrics were compared with those of the fabrics dyed with the conventional dyeing process.

1 Materials and Methods

1.1 Materials

Lanasol Red CE was purchased from Huntsman Chemical Co., Ltd. (Shanghai, China). Glacial acetic acid (analytic reagent) was purchased from Tianjin Oubokai Chemical Co., Ltd. (Tianjin, China). Anhydrous sodium carbonate (analytic reagent) was purchased from Tianjin Baishi Chemical Co., Ltd. (Tianjin, China). Soap flakes were obtained from Shanghai Textile Industry Technical Supervision Institute (Shanghai, China). SPS was purchased from Tesco Chemical Co., Ltd. (Hubei, China). Other chemicals were purchased from Sinopharm Chemical Reagent Co., Ltd. (Shanghai, China). Wool fabrics with an area density of 280 g/m² were provided by Shandong Ruyi Woolen Garment Group Co., Ltd. (Shandong, China).

1.2 Experimental methods

1.2.1 Preparation of simulated dyeing wastewater

Simulated dyeing wastewater was prepared using Lanasol Red CE at a mass concentration of 0.05 g/L. The simulated dyeing wastewater (100 mL) was used to investigate the effects of various reaction conditions on the dye residual rate by varying the degradation temperatures (25 °C to 100 °C), pH values (3 to 11) and SPS mass concentrations (0.2 g/L to 0.4 g/L).

1.2.2 Reactive dyeing process of wool fabrics

The dyeing process of wool fabrics was carried out according to the process curve shown in Fig. 1, with a dye dosage of 2% (on the mass of fabrics) and a bath ratio of 1:40.

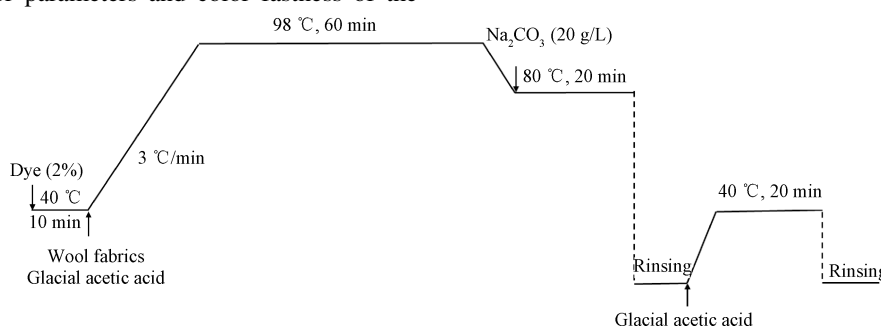


Fig. 1 Dyeing process of wool fabrics with Lanasol Red CE

Wool fabrics were dyed using an AS-I rotary room-temperature dyeing machine (Guangdong Heshan Hongfa Dyeing & Finishing Machinery Manufacturing Co., Ltd., China). After the dyeing process, dyeing wastewater was heated to 100 °C, and SPS (0.2 g/L) was added and treated the dyeing wastewater for 30 min to obtain reusable water. Subsequently, Lanasol Red CE was added to prepare the dyeing solution for the next round of dyeing. The above process was repeated for 10 cycles, with the wastewater of each dyeing cycle collected

separately. The color parameters of the dyed fabrics were measured after each dyeing cycle, and the exhaustion and fixation rates were determined after each dyeing cycle.

1.3 Analyses and measurements

1.3.1 Degradation of dyeing wastewater

According to Lambert-Beer's law, the absorbance A of a parallel beam of monochromatic light passing through a uniform, non-scattering and light-absorbing substance is directly proportional to the mass concentration C of the substance and the thickness of the absorbing layer.

Therefore, with a constant thickness, A is proportional to C . Hence, the dye residual rate S and the first-order dye degradation rate constant k are

$$S = \frac{C_{t_1}}{C_0} \times 100\% = \frac{A_{t_1}}{A_0} \times 100\%, \quad (1)$$

$$k = -\ln(C_{t_1}/C_0)/t_1, \quad (2)$$

where t_1 is the degradation time; C_{t_1} and A_{t_1} represent the mass concentration and absorbance of the dyeing solution at time t_1 , respectively; C_0 and A_0 represent the mass concentration and absorbance of the original dyeing solution, respectively.

1.3.2 Dye uptake measurement

The absorbance of the original dyeing solution and the residual dyeing solution was measured separately. The dye uptake D of the reactive dye is

$$D = \frac{A_0 - A_{t_2}}{A_0} \times 100\%, \quad (3)$$

where t_2 is the dyeing time; A_{t_2} represents the absorbance of the residual dyeing solution at time t_2 .

1.3.3 Exhaustion rate and fixation rate measurements

The exhaustion rate E of the reactive dye is

$$E = \frac{A_0 - A_e}{A_0} \times 100\%, \quad (4)$$

where A_e represents the absorbance of the residual dyeing solution at the end of the dyeing process.

The dyed fabrics were washed at a bath ratio of 1:50 with soap flakes (2 g/L) to get the soaped residue liquor. Absorbance measurements were performed on the soaped residue liquor, the residue dyeing solution and the original dyeing solution. The fixation rate F of the reactive dye is

$$F = \left(1 - \frac{A_e + A_2}{A_0}\right) \times 100\%, \quad (5)$$

where A_2 represents the absorbance of the soaped residue liquor.

1.3.4 Color performance analysis

The color parameters of the fabric samples were measured using a Color i5 colorimeter (Datacolor Corporation, USA) at a 10° viewing angle with D₆₅ illumination. The measured L^* , a^* , b^* , C^* , h and K/S values were averaged. L^* , a^* , b^* , C^* , h and K/S are the brightness, red-green index, yellow-blue index, color saturation value, hue value and apparent color depth value of the dyed fabrics, respectively.

The color difference ΔE^* of the dyed fabrics is

$$\Delta E^* = \sqrt{(\Delta L^*)^2 + (\Delta a^*)^2 + (\Delta b^*)^2}, \quad (6)$$

where ΔL^* is the difference of the brightness; Δa^* is the difference of the red-green index; Δb^* is the difference of the yellow-blue index.

1.3.5 Color fastness measurement

The color fastness of dyed fabrics to dry and wet rubbing was tested according to GB/T 3920—2008 Textiles—tests for color fastness—color fastness to rubbing. Color fading and staining were assessed using a gray scale to measure the color change. Washing fastness was tested according to GB/T 3921—2008 Textiles—tests for color fastness—color fastness to washing, using a washing color fastness tester (Wenzhou Darong Textile Instrument Co., Ltd., China) under the following conditions: 5 g/L soap flakes, 40 °C, 30 min, and a bath ratio of 1:50.

1.3.6 Determination of SPS mass concentration

The standard curve of SPS mass concentration vs. absorbance was plotted by potassium iodide chromatography, and the absorbance was then calculated to obtain the mass concentration of the remaining SPS in the dyeing wastewater. An SPS solution with a mass concentration of 250.000 mg/L was prepared and successively diluted to obtain SPS standard solutions with mass concentrations of 125.000, 62.500, 31.250 and 15.625 mg/L. Then, the SPS standard solutions (1 mL) were taken and reacted with potassium iodide solution (100 g/L) for 15 min. Subsequently, the absorbance was measured at 400 nm using a UV-3200 UV-Vis spectrophotometer (Shanghai Mapada Instrument Co., Ltd., China) and the standard curve was plotted as shown in Fig. 2 (y represents the SPS mass concentration, x represents the absorbance, and R represents the correlation coefficient).

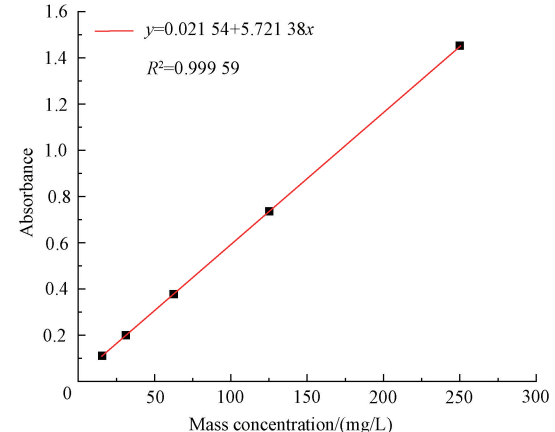


Fig. 2 Standard curve of SPS mass concentration vs. absorbance

Figure 2 illustrates a strong correlation between SPS mass concentration and absorbance, indicating that absorbance can serve as a reliable metric for quantifying the SPS mass concentration.

2 Results and Discussion

There are two prerequisites for recycling dyeing wastewater from the reactive dyeing of wool fabrics: one is the efficient treatment of colored wastewater and the other is the application of recycled wastewater to dyeing

without affecting the dyeing behavior of the dye. Dyeing wastewater contains hydrolyzed dye, inorganic salts and alkali, and may impact the effectiveness of wastewater treatment^[24]. Therefore, the dye residual rate was used as the evaluation index to explore the impact of the degradation temperature, pH value and SPS mass concentration on the degradation of the reactive dye.

2.1 Influencing factors of dye degradation

2.1.1 Degradation temperature

To investigate the effect of the degradation temperature on the treatment of dyeing wastewater, experiments were conducted under neutral conditions. The mass concentration of SPS was set at 0.8 g/L, and the degradation temperatures were set at 25, 50, 80, 90 and 100 °C, respectively, for degradation time ranging from 0 to 30 min. The dye residual rate and the first-order dye degradation rate constant of Lanasol Red CE are shown in Fig. 3.

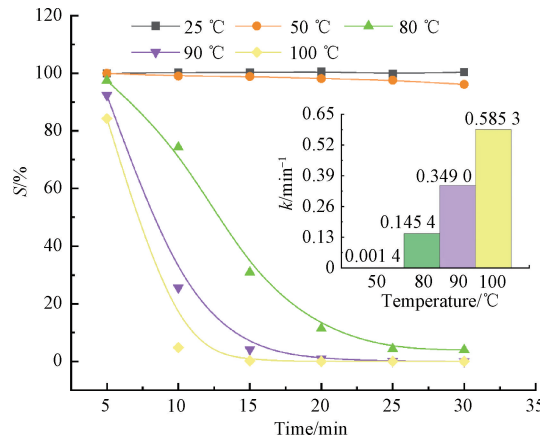


Fig. 3 Effect of degradation temperature on dye residual rate

As shown in Fig. 3, when the degradation temperatures are set at 25 °C and 50 °C, the dye residual rates are higher than 96.0% even after treating the dyeing wastewater for 30 min, which means that dye degradation could not be achieved using SPS below 50 °C. When the degradation temperature increases to 80 °C and the degradation time extends from 5 min to 30 min, the dye residual rate gradually decreases from 97.5% to 4.0%. When the degradation temperature exceeds 80 °C, the dye residual rate decreases significantly. This suggests that at the same degradation time, higher degradation temperatures result in lower dye residual rates, indicating more dye degradation. In addition, from the effect of temperature on the dye degradation rate constant in Fig. 3, it can be seen that when the degradation temperature increases from 50 °C to 100 °C, the dye degradation rate constant increases from 0.0014 min⁻¹ to 0.5853 min⁻¹, indicating that increasing the temperature is favorable for the degradation of the dye by SPS. The mentioned phenomenon is attributed to the fact that increasing the temperature activates SPS, which generates a large number of free radicals ($\cdot\text{OH}$ and $\text{SO}_4^{\cdot-}$) and destroys

the structure of Lanasol Red CE. To ensure the complete degradation of the reactive dye, the degradation temperature is set at 100 °C in subsequent experiments.

2.1.2 Initial pH value

To reveal the influence of the initial pH value on the degradation of dyeing wastewater, the pH value was adjusted to 3, 7 and 11, respectively. The mass concentration of SPS was maintained at 0.8 g/L, and the degradation was conducted at 100 °C for 0–30 min. The dye residual rate and the first-order dye degradation rate constant of Lanasol Red CE are shown in Fig. 4.

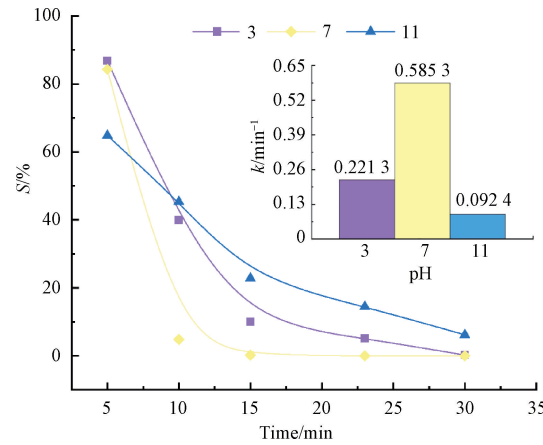
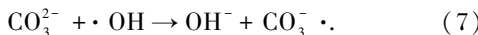


Fig. 4 Effect of initial pH value on dye residual rate

As shown in Fig. 4, when the pH value is 7, the dye residual rate decreases with degradation time, indicating that the majority of the reactive dye has been degraded. When the pH value is adjusted to 11 with Na_2CO_3 solution, the dye degradation rate slows down. The result suggests that a longer degradation time is necessary under the alkaline condition to completely degrade the reactive dye. When the pH value is 3, the dye residual rate decreases to 10.01%. As illustrated in Fig. 4, the dye degradation rate constant increases from 0.0924 min⁻¹ to 0.5853 min⁻¹ when the pH value decreases from 11 to 7. Then, it subsequently decreases to 0.2213 min⁻¹ when the pH value is further adjusted to 3. However, the degradation rate is excessively rapid under neutral conditions, making it challenging to control the reaction process. Considering the complete degradation of the reactive dye and the reuse of dyeing wastewater as a medium for dyeing wool fabrics, the initial pH value is set at 3 for subsequent experiments.

Wool fabric dyeing does not necessitate the addition of salt, resulting in dyeing wastewater that is free of salt. The addition of Na_2CO_3 to the dyeing wastewater affects not only the rate of dye degradation but also the residual rate corresponding to 30 min of degradation. This effect is attributed to the scavenging action of CO_3^{2-} in Na_2CO_3 on hydroxyl radicals in the solution. When CO_3^{2-} is present in the dyeing wastewater, it competes with dye molecules for hydroxyl radicals ($\cdot\text{OH}$) in the solution,

reacting to form carbonate radicals ($\text{CO}_3^{2-} \cdot$)^[25]:



Thus the number of active radicals is reduced, leading to a significant decrease in degradation effect.

2.1.3 SPS mass concentration

During the dye degradation process, the number of free radicals determines the dye degradation effect, and the SPS mass concentration is closely related to the number of free radicals. To identify the minimum effective SPS mass concentration that achieves efficient dye degradation while maintaining cost effectiveness, a lower SPS mass concentration of 0.2–0.4 g/L was used at a pH value of 3, and the degradation was carried out at 100 °C for 30 min. The effect of SPS mass concentration on dye residual rate and the first-order dye degradation rate constant of Lanasol Red CE is shown in Fig. 5.

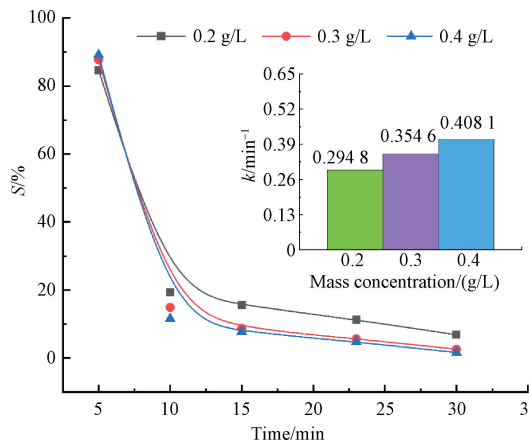


Fig. 5 Effect of SPS mass concentration on dye residual rate

As shown in Fig. 5, Lanasol Red CE degrades rapidly in the first 10 min. After 10 min, the dye residual rate decreases slowly with the prolongation of the degradation time. The higher the mass concentration of SPS, the lower the dye residual rate at the same treatment time. The dye residual rate decreases from 6.86% to 1.65% when the SPS mass concentration increases from 0.2 g/L to 0.4 g/L, and the dye degradation rate constant increases from 0.2948 min^{-1} to 0.4081 min^{-1} . At the end of the degradation, the dyeing wastewater is clarified and transparent, which can achieve a good degradation effect and can be used for subsequent recycled dyeing. Excessive mass concentration of SPS may lead to its incomplete decomposition, and SPS will remain in the dye solution, affecting the subsequent dyeing. Therefore, 0.2 g/L SPS was chosen for the subsequent experiments.

2.2 Recycling reactive dyeing of wool fabrics

SPS is converted to sodium sulfate salt, which remains in the degradation solution. Meanwhile, thermally activated reactive dyes are degraded into small

molecules. The dyeing behavior of Lanasol Red CE may be affected by the use of recycled dyeing wastewater. To reveal the dyeing behavior of reactive dye for wool fabrics, cycle dyeing experiments were conducted.

2.2.1 Dye uptake

To adequately degrade the reactive dye in the dyeing wastewater, the dyeing wastewater was treated with 0.2 g/L SPS at 100 °C for 30 min. Subsequently, the dyeing of wool fabrics was carried out following the dyeing method outlined in the experimental section. The results of the dye uptake are shown in Fig. 6.

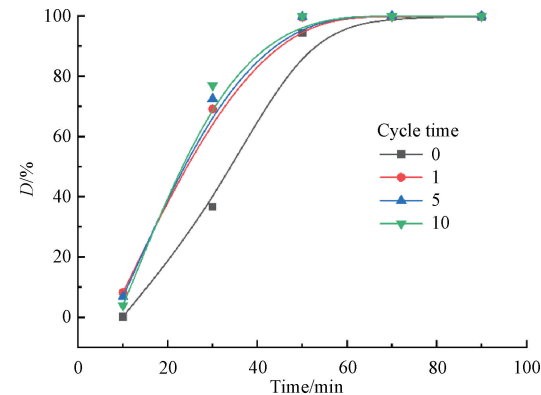


Fig. 6 Effect of cycle times on dye uptake

In the conventional dyeing process (cycle time 0), dye uptake increases slowly with the dyeing time, which reaches 94.39% at 50 min and eventually stabilizes at 99.62% at 70 min. When the dyeing wastewater is used for dyeing, the dye uptake increases compared to that of the conventional dyeing process, and the increase becomes more noticeable with each subsequent cycle. Taking dyeing for 30 min as an example, the dye uptake is 36.65% when dyeing with a conventional dyeing process. The dye uptakes of 1, 5 and 10 cycle times are 69.07%, 72.55% and 76.92%, respectively. Although the cycle time changes the dye uptake, it does not impact the final exhaustion rate. Compared to conventional dyeing process, the dyeing wastewater contains inorganic salts. These salts facilitate the dye molecules to detach from the dye solution and penetrate into the wool fiber, leading to a high dye uptake at the beginning of the dyeing process^[26].

2.2.2 Exhaustion rate and fixation rate

Figure 7 shows that the exhaustion rate of Lanasol Red CE is almost unaffected by the cycle times, reaching over 99.00%, while the fixation rate shows a trend of initially increasing and then stabilizing. The fixation rate of conventional dyeing is 82.90%, which is lower than that of the recycling dyeing. The fixation rate suggests that using recycled dyeing wastewater for wool fabric dyeing can achieve higher fixation rates.

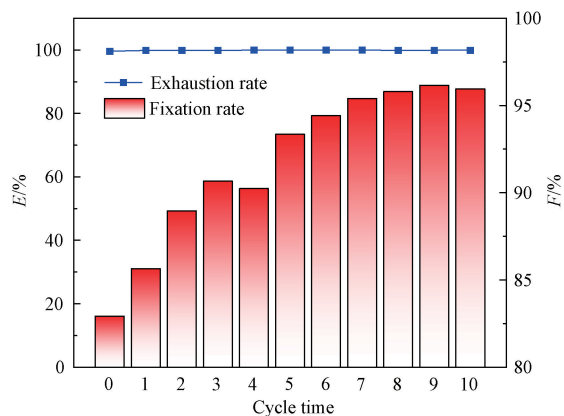


Fig. 7 Exhaustion rate and fixation rate of Lanasol Red CE

2.2.3 Color parameters and color fastness

To investigate the dyeing effect of Lanasol Red CE in two different dyeing media, the color parameters of the dyed fabrics were tested. The results are shown in Table 1. The brightness value L^* of the dyed fabrics

using the recycled dyeing wastewater decreases. This indicates that the dyed fabrics are darker, which coincides with the increase in the apparent color depth K/S value by 0.47 to 2.43. The increase in the red-green index a^* , yellow-blue index b^* , color saturation value C^* and hue value h indicates that the color of the cycle-dyed fabrics exhibits enhanced reddish, bluish and bright hues. At the same dye dosage, the apparent color depth K/S value of the dyed fabrics increases, indicating that the dyed fabrics have higher color yields, which coincides with the higher color fixation rate shown in Fig. 7. Compared to that of the conventional dyeing process, the color differences ΔE^* for the 1st, 5th and 10th dyeing cycles are 0.93, 2.25 and 4.02, respectively. This indicates that the color difference increases with the increasing dyeing cycle times. The dyed fabric with ΔE^* between 2.00 and 5.00 is considered as a conditionally accepted product. Although there are slight color variations, the color consistently matches that of the conventional dyeing process. The color parameters are slightly different but can be corrected by adjusting the dyeing process variables^[27].

Table 1 Color parameters of dyed fabric

Cycle time	L^*	a^*	b^*	C^*	h	K/S	ΔE^*	Color block of picture pattern
0	40.69	59.13	12.36	60.41	11.80	18.50	—	
1	40.36	58.78	13.16	60.02	11.67	18.97	0.93	
5	40.67	59.39	14.59	61.16	13.79	20.16	2.25	
10	40.07	59.57	16.31	61.77	15.31	20.93	4.02	

The color fastness to rubbing and washing of the dyed fabrics is presented in Table 2. The color fastness to rubbing is the same as that of conventional dyeing when the cycle times are less than 5, while the color fastness to

washing shows a decrease of half a grade. The color fastness to rubbing and washing of the 10th cycle dyed fabrics decreases by half a grade and 1 grade, respectively, but all of them meet the production requirements.

Table 2 Color fastness to rubbing and washing of dyed fabrics

Cycle time	Rubbing fastness		Washing fastness		
	Dry	Wet	Dyed fabric discoloration	Wool fabric stained	Cotton fabric stained
0	4	4	4-5	4-5	4-5
1	4	4	4	4	4
5	4	4	4	4	4
10	3-4	3-4	3-4	3-4	3-4

3 Conclusions

As for the dyeing wastewater of Lanasol Red CE, the appropriate degradation conditions were 0.2 g/L SPS, an initial pH value of 3 and 100 °C for 30 min. The

dye degradation rate reached as high as 93.14%. Compared with conventional dyeing, when using recycled dyeing wastewater for wool fabric dyeing, the dye exhaustion rate exceeded 99.00%, and the fixation rate was higher than that achieved by the conventional dyeing process. The K/S value of wool fabrics dyed using the

recycled dyeing wastewater increased by 0.47 to 2.43. The rubbing and washing fastness of the 10th cycle dyed fabrics were reduced by half a grade and 1 grade, respectively, but all of them met the production requirements.

References

- [1] HOSSEINNEZHAD M, GHARANJIG K, IMANI H, et al. Green dyeing of wool yarns with yellow and black myrobalan extract as biomordant with natural dyes [J]. *Journal of Natural Fibers*, 2022, 19(10) : 3893-3915.
- [2] XU S Y, SHANG Q M, WANG Y. Reactive dyes for wool [J]. *China Dyeing & Finishing*, 2012, 49(6) : 1-7. (in Chinese)
- [3] SHU D W, FANG K J, LIU X M, et al. Influence of fabric heating rate on salt-free pad-steam dyeing of reactive dye [J]. *Journal of Textile Research*, 2018, 39(2) : 106-111. (in Chinese)
- [4] BAO J S, WU T, LI J. Potentials and challenges of carbon knowledge graph in sustainable textile production for carbon traceability: a review [J]. *Journal of Donghua University (English Edition)*, 2024, 41(4) : 349-364.
- [5] ZHOU K Y. Printing and dyeing wastewater reuse technology [J]. *Energy Environmental Protection*, 2012, 26 (4) : 35-36, 40. (in Chinese)
- [6] EWUZIE U, SALIU O D, DULTA K, et al. A review on treatment technologies for printing and dyeing wastewater (PDW) [J]. *Journal of Water Process Engineering*, 2022, 50: 103273.
- [7] SAMSAMI S, MOHAMADIZANIANI M, SARRAFAZADEH M H, et al. Recent advances in the treatment of dye-containing wastewater from textile industries: overview and perspectives [J]. *Process Safety and Environmental Protection*, 2020, 143: 138-163.
- [8] SOLAYMAN H M, HOSSEN M A, ABD AZIZ A, et al. Performance evaluation of dye wastewater treatment technologies: a review [J]. *Journal of Environmental Chemical Engineering*, 2023, 11(3) : 109610.
- [9] INGRASSIA E B, LEMOS E S, ESCUDERO L B. Treatment of textile wastewater using carbon-based nanomaterials as adsorbents: a review [J]. *Environmental Science and Pollution Research*, 2023, 30(40) : 91649-91675.
- [10] LI W, MU B N, YANG Y Q. Feasibility of industrial-scale treatment of dye wastewater via bio-adsorption technology [J]. *Bioresource Technology*, 2019, 277: 157-170.
- [11] QIAO H, ZHANG L, LI W, et al. Activated carbon adsorption treatment of printing and dyeing wastewater and regeneration research [J]. *New Chemical Materials*, 2022, 50: 422-426. (in Chinese)
- [12] JEGATHEESAN V, PRAMANIK B K, CHEN J Y, et al. Treatment of textile wastewater with membrane bioreactor: a critical review [J]. *Bioresource Technology*, 2016, 204: 202-212.
- [13] ZHANG Y Q, SHAAD K, VOLLMER D, et al. Treatment of textile wastewater using advanced oxidation processes: a critical review [J]. *Water*, 2021, 13(24) : 3515.
- [14] MIRZA N R, HUANG R, DU E D, et al. A review of the textile wastewater treatment technologies with special focus on advanced oxidation processes (AOPs), membrane separation and integrated AOP-membrane processes [J]. *Desalination and Water Treatment*, 2020, 206: 83-107.
- [15] SUN W P, ZHANG H P, LIU X, et al. Ability and mechanism of modified graphene oxide membrane for treatment of printing and dyeing wastewater [J]. *Fine Chemicals*, 2024, 41(6) : 1372-1381, 1392. (in Chinese)
- [16] VINAYAGAM V, PALANI K N, GANESH S, et al. Recent developments on advanced oxidation processes for degradation of pollutants from wastewater with focus on antibiotics and organic dyes [J]. *Environmental Research*, 2024, 240: 117500.
- [17] PRIYADARSHINI M, DAS I, GHANGREKAR M M, et al. Advanced oxidation processes: performance, advantages, and scale-up of emerging technologies [J]. *Journal of Environmental Management*, 2022, 316: 115295.
- [18] XIONG Z. A review of advanced oxidation techniques for the treatment of organic wastewater [J]. *Shanghai Dyestuffs*, 2024, 52(3) : 23-25. (in Chinese)
- [19] REKHATE C V, SRIVASTAVA J K. Recent advances in ozone-based advanced oxidation processes for treatment of wastewater: a review [J]. *Chemical Engineering Journal Advances*, 2020, 3: 100031.
- [20] JIANG T H. Discussion on key technologies for deep treatment and reuse of printing and dyeing wastewater [J]. *Resource Conservation and Environmental Protection*, 2018(2) : 71-72.
- [21] NIDHEESH P V, DIVYAPRIYA G, EZZAHRA TITCHOU F, et al. Treatment of textile wastewater by sulfate radical based advanced oxidation processes [J]. *Separation and Purification Technology*, 2022, 293: 121115.
- [22] BHARGAVA N, BAHADUR N, KANSAL A. Techno-economic assessment of integrated photochemical AOPs for sustainable treatment of textile and dyeing wastewater [J]. *Journal of Water Process Engineering*, 2023, 56: 104302.
- [23] XU X Y, TANG Y. Research status of advanced

- oxidation process based on free radicals in printing and dyeing wastewater treatment [J]. *Guangdong Chemical Industry*, 2024, 51(1): 86-88. (in Chinese)
- [24] HAN B, WANG Y L, SHU D W, et al. Reactive dyeing using recycled dyeing wastewater [J]. *Journal of Textile Research*, 2023, 44(8): 151-157. (in Chinese)
- [25] TIAN K, HU L M, LI L T, et al. Recent advances in persulfate-based advanced oxidation processes for organic wastewater treatment [J]. *Chinese Chemical Letters*, 2022, 33(10): 4461-4477.
- [26] CAO W Z, PEI L J, ZHANG H J, et al. Sustainable wool fabric pad dyeing using reactive dyes in silicone non-aqueous medium [J]. *Environmental Chemistry Letters*, 2021, 19(1): 737-741.
- [27] SHU D W, HAN B, AN F F, et al. Sustainable coloration of cotton fabrics in the recycled residual dyeing liquor [J]. *Sustainable Chemistry and Pharmacy*, 2024, 41: 101716.

回用染色废水用于羊毛织物活性染料染色

王冰欣，韩博，张馨元，李万新，许佳，舒大武*

河北科技大学 纺织服装学院，河北 石家庄 050018

摘要：针对毛用活性染料染色废水排放量大、污染严重的问题，利用过二硫酸钠（SPS）对毛用活性染料兰纳素红CE染色残液进行降解处理和循环再利用。以染料残留率为评价指标，确定了毛用活性染料降解工艺。通过测试循环染色过程中的染料上染率、固色率及染色织物颜色参数和色牢度，证实了利用活性染料染色废水实现羊毛织物循环染色的可行性。结果表明：处理毛用活性染料兰纳素红CE所适宜的条件是0.2 g/L SPS，初始pH值为3，100 °C处理30 min，此时染料降解率高达93.14%。在利用降解后的染色废水进行循环染色时，染料上染率均高于99.00%，固色率较传统染色工艺高。在染色条件相同的情况下，循环染色织物表观颜色更深。循环次数低于5次时，对色牢度影响不明显。尽管第10次循环染色织物的耐摩擦色牢度和耐洗色牢度分别降低半级和1级，但织物仍能满足生产要求。

关键词：羊毛织物；活性染料；染色废水；循环利用；染色

Effectiveness and Concentration Distribution of Negative Air Ions on Human Health in Indoor Environment

DENG Xiaomi¹, AN Yuhui², YANG Xuebin^{1*}, ZHANG Ruidan¹, XIONG Chen¹

1. College of Environmental Science and Engineering, Donghua University, Shanghai 201620, China

2. Marine Design and Research Institute of China, Shanghai 200011, China

Abstract: Negative air ions (NAIs) in indoor environments have been suggested to positively impact human health by effectively reducing particulate contamination and gaseous pollutants, as well as inhibiting the growth of microorganisms, bacteria and viruses. This study investigates the common ionizers with different module types, and the mechanism of NAIs for enhancing indoor air quality, as well as the positive and negative impacts on human health. The association between NAI concentrations and human health outcomes is examined, and alternative measures to balance beneficial and unavailing effects are investigated. While NAIs demonstrate efficacy in removing particulate pollutants, alleviating depression, enhancing cognitive function and even stimulating sympathetic activity, it is pertinent to acknowledge the presence of contradictory findings concerning their effects on cardiac autonomic function and respiratory physiology. To address this complexity, it is imperative to consider alternative measures that strike a balance between the beneficial and unavailing effects of NAIs. These measures can encompass a general assessment of the characteristics of particulate pollutants, a strategic selection of ionizer technologies, and adherence to the recommended optimal concentration thresholds of NAIs.

Keywords: indoor environment; negative air ion (NAI); human health; particle removal; alternative measure

CLC number: TU83

Document code: A

Article ID: 1672-5220(2025)02-0144-12

Open Science Identity
(OSID)



0 Introduction

Negative air ions (NAIs), often referred to as “air vitamins”, are significant factors in assessing air quality. In natural environments such as forests, waterfalls and torrential rains, NAIs are abundant. NAIs are typically found in molecular clusters, with concentrations ranging from approximately 5.0×10^3 to 1.0×10^5 ion/cm³^[1]. High NAI concentrations can be found as high as 0.5×10^5 ion/cm³ near waterfalls, while in urban areas and indoor environments, it drops to several hundreds or

lower^[2]. Artificial methods can produce higher concentrations of NAIs^[3], thus providing substantially higher energy compared to naturally generated NAIs. This is achieved by using ionizing radiation or high-voltage potentials, which supply sufficient energy to either remove electrons from neutral air molecules or allow these molecules to gain electrons, leading to the formation of ions^[4-5].

NAIs have been widely applied in air purification to remove particulate pollutants in indoor environments^[6-7], to induce the decomposition of indoor organic pollutants^[8], and to enable effective disinfection of aerosolized *Escherichia coli*, *Salmonella typhimurium* and *Staphylococcus epidermidis* air microorganisms^[9-11]. An environment favorable for human living should correspond to the following requirements^[12]: air ion concentration within $4.0 \times 10^2 - 5.0 \times 10^4$ ion/cm³, and unipolarity coefficient *K* within 0.4 – 1.0. That is to say, the concentration of NAIs should be at least equal to or greater than the concentration of the positive air ions (PAIs).

In aerosol airborne, NAIs and PAIs inevitably coexist with particulate contamination, gaseous pollutants, microorganisms, bacteria and viruses, etc. Some of them are directly or indirectly harmful to human health. For example, each 10.0 μg/m³ increase in chronic exposure to fine particulate matter 2.5 (PM_{2.5}) is associated with a significant rise in the risks of major cardiovascular and pulmonary events, ranging from 8% to over 20%^[13]. Exposure to PM_{2.5} can induce an increase in lipid peroxidation, vascular inflammation, endothelial cell injury initiation, respiratory diseases, and coronary and carotid atherosclerosis. PM_{2.5} can also cause atherosclerotic vascular plaque rupture myocardial infarction, and stroke by activating metalloproteinase.

The most significant contribution of this study is to summarize the effectiveness and concentration level of NAIs on human health, especially in enclosed environments. Section 1 introduces the common ionizers with different module types. Section 2 presents the

Received date: 2024-02-23

Foundation item: Research Project of Marine Design and Research Institute of China

* Correspondence should be addressed to YANG Xuebin, email: xbyang@dhu.edu.cn

Citation: DENG X N, AN Y H, YANG X B, et al. Effectiveness and concentration distribution of negative air ions on human health in indoor environment [J]. *Journal of Donghua University (English Edition)*, 2025, 42(2): 144-155.

mechanism of NAIs for improving indoor air environments. Section 3 collects the direct and indirect effects of NAIs on human health. Section 4 discusses the NAI concentration distribution, and provides the alternative measures to balance the beneficial and unavailing effects of NAIs.

1 Common Ionizers with Different Module Types

To improve air quality and to enhance a healthy environment, ionizers are frequently utilized in residences, workplaces, medical institutions and public areas. Currently, there is a vast array of ionizers available on the market, each with unique design, performance and efficiency features. This variety stems

from changes in consumer demands and technological advancements. The ionizer information about various module types and ion generation rates has been gathered from Amazon.com to thoroughly grasp the functionality and variety of uses of ionizers.

Table 1 presents the variable density of common ionizers with different module types. Their ion outputs are in the range of 2.0×10^9 ion/s to 1.2×10^{13} ion/s. The ion concentration is different at varying distances from emitting electrodes. The ion concentration gradually decays with the increasing distance. Taking the ion output with 1.0×10^{13} ion/s as an example, there is an attenuation of the order of approximately one-tenth that occurs at a distance of 3.0 cm. The rated voltages of the tabulated ionizers are in the kilovolt level, and the rated powers are less than 1.0 W.

Table 1 Variable density of common ionizers with different module types

Module type	Ion type	Image	Ion output/ (ion/s)	Ion concentration/(ion/cm ³)	Voltage/kV
TFB-YA178	NAI		1.0×10^{13}	$C_{\text{NAI}} > 1.1 \times 10^{12}$ (2.9 cm from emitter)	NV: -7.5
TFB-YA1102	BAI		—	$C_{\text{PAI}} > 1.5 \times 10^8$; $C_{\text{NAI}} > 2.0 \times 10^{12}$ (15.0 cm from emitter)	PV: 2.0 ± 0.5 ; NV: -2.5 ± 0.5
TFB-YD1278	BAI		—	$C_{\text{PAI}} > 4.0 \times 10^{10}$; $C_{\text{NAI}} > 8.0 \times 10^{10}$ (15.0 cm from emitter)	PV: 3.0 ± 0.5 NV: -3.0 ± 0.5
XHJ-D12F	NAI		—	$C_{\text{NAI}} > 1.9 \times 10^{12}$ (2.9 cm from emitter)	NV: -9.5
TFB-YD12102DJ1	NAI		—	$C_{\text{NAI}} > 1.0 \times 10^6$ (15.0 cm from emitter)	NV: -7.5 ± 0.5
MIG-ION-12V-NP	NAI		1.2×10^{13}	$C_{\text{NAI}} > 1.9 \times 10^{12}$ (2.9 cm from emitter)	NV: -9.5
1XDC	NAI		—	$C_{\text{NAI}} > 7.0 \times 10^6$ (10.0 cm from emitter)	NV: -3.8 ± 0.5

Notes: BAI—bipolar air ion; C_{NAI} —concentration of NAIs; C_{PAI} —concentration of PAIs; PV—positive voltage; NV—negative voltage.

2 Mechanisms of Improving Indoor Air Environments

Under NAIs in an indoor environment, there are different mechanisms involved in the removal of aerosol

particles and the decomposition of organic pollutants.

2.1 Removal mechanism of aerosol particles

If the oppositely charged particles are present in an enclosed space aerosol, the electrostatic forces cause the particles to attract each other. This process coagulates ultrafine and fine particles into large particles. The

common filters are generally less efficient at removing ultrafine and fine particles. Fortunately, the coagulation process improves the particle removal efficiency of mechanical air filters. If the aerodynamic diameter of particles formed by coagulation is greater than 1.0 μm , the air filter presents better removal efficiency^[11]. Furthermore, combining ionizers with natural ventilation can greatly improve the removal of aerosol particles^[14].

Ortiz-Grisales et al.^[7] employed a high-voltage booster output to ionize air molecules from stainless steel electrodes, and the particle capture efficiency was as high as 97%. Two devices (5 cm \times 40 cm acrylic chambers) were employed to produce 2.0×10^{13} ion/s, and PM_{2.5} can be reduced from 999 mg/m³ to 0 (in a 40 cm \times 40 cm acrylic chamber) in about 5–7 min.

Pushpawela et al.^[15] examined the particles removed when the ionizer was operated in a closed chamber with a volume of 1 m³, a closed unventilated chamber with a volume of 20 m³, and three forced ventilation chambers with volumes of 32, 45 and 132 m³, respectively. The closed chamber experiment was conducted using ambient particles and smoke. While a small ionizer (Aironic AH-202, Aironic Pty Ltd., Australia) was used, 70% of the particles and smoke are removed within 15 min.

Shi et al.^[16] evaluated the long-term particle collection efficiency of M6-level synthetic filters with and without ionization through field and indoor tests. Ionization treatment increased filtration efficiency by 40% during most operating time. The ionization system was managed by periodically switching the ionizer polarity and the filtration efficiency of aerosol particles was maintained above 50% for half a year. Compared with the F7-level filter, the pressure drop of the ionizer-assisted M6 filter was reduced by 25%–30%.

2.2 Decomposition mechanism of organic pollutants

The NAI active substances (ions or free radicals) play an important role in inducing the decomposition of indoor organic pollutants^[8]. They can trigger a chain reaction and lead to fragmentation and ionization of indoor organic pollutants. Mass spectrometric monitoring of the intermediate shows that NAIs cause the alkyl groups to be cleaved and the alkyl radicals are subsequently replaced with negative electrons. Due to the high activity and selectivity of esters, a small reduction in CO₃⁻ can produce a large number of intermediates during the reaction with esters. Therefore, NAIs have a high degradation efficiency for a variety of esters. The real-time mass spectrometry analyses of intermediates reveal that the interactions between CO₃⁻ and O⁻ on aldehyde groups, alkyl oxidation and ·OH dehydrogenation, and alkyl cleavage are the three main pathways for the

degradation of aldehydes, benzene congeners and esters.

3 Effects on Human Health

NAIs are recognized to improve mental health, productivity and overall well-being, but there is no consistent or reliable evidence for therapeutic effectiveness, and there is controversy regarding antimicrobial benefits^[17].

3.1 Beneficial effects

The published studies on the beneficial effects of NAIs on human health are summarized in Table 2 (the case number + letter (a, b or c) indicates that the studies on the mechanism of action of NAIs are consistent across these studies). NAIs present beneficial effects on human health by improving the internal physiological processes of the human body, and disinfecting bacteria and inactivating viruses.

The beneficial effects of NAIs on human health are obtained by changing amino acid metabolism and promoting energy production^[18], alleviating depression and atypical seasonal affective disorder (SAD) symptoms^[19], benefiting cognitive function^[20], improving respiratory function beneficial to heart rate variability^[21-22], alleviating fatigue caused by muscle overload^[23], being more effective for antidepressant efficacy^[24], being efficacious in chronic depression^[25], reducing depression in dozens of minutes^[26], increasing sympathetic activity and improving cognitive ability^[27], improving thermal comfort and human physiological stress^[28], and so on.

The beneficial effects of NAIs in removing particles, disinfecting bacteria and inactivating viruses are multifaceted. These include enhancing deposition to reduce particulate concentration^[29-31]; inhibiting microorganisms^[17]; facilitating the removal of particles and viruses^[32]; providing an energy-efficient air purification intervention^[33]; offering better disinfection performance^[10]; reducing the airborne *staphylococcus aureus* concentration^[34]; removing contaminant particles^[31], ultrafine particles^[15], submicron particles^[29], fog and smoke^[30], and PM_{2.5}^[35].

NAIs exert biological and therapeutic effects^[36], with the possible mechanism playing biologically and physiologically essential roles such as biochemical reactions, transmembrane transport of a substance, and propagation of the nervous influx. There is also another point that NAIs affect the autonomic nervous system, increase sympathetic activity, and slightly decrease vagal efferent activity^[27].

Table 2 Literature surveys on beneficial effect of NAIs on human health

Case number	Author	Study purpose	Study model	Study object	Ion concentration/ (ion/cm ³)	Primary outcomes of interest
1a	Kolarž et al. ^[32]	Effects of NAIs deposition on removal of aerosolized pathogens from indoor air	Control trial	Atomized NaCl solution aerosol and cigarette smoke aerosol	$C_{\text{NAI}} = 2.0 \times 10^4$	Benefit particle removal such as viruses
1b	Sahay et al. ^[34]	Effects of NAIs and PAIs on building contaminants	Laboratory experiment	<i>Staphylococcus aureus</i> , VOCs, PM _{2.5} , etc.	$C_{\text{NAI}} = 5.9 \times 10^4$ $C_{\text{PAI}} = 9.2 \times 10^4$	Effective in reducing indoor microbes and particulate pollutants
2	Duan et al. ^[33]	Effects of air purification interventions on dosage delivered to small airway	Full-scale experiment using an <i>in vitro</i> airway model	3D-printed human replica (healthy 34-year-old male)	$C_{\text{NAI}} = 1.5 \times 10^5$, 3.0 × 10 ⁵ and 7.0 × 10 ⁵ , respectively	Effective in reducing small airway particle exposure
3	Shiu et al. ^[31]	Contaminant particle removal by ionizer	Closed test chamber	Different distances (30, 50, 70, and 90 cm) from the ionizer	$C_{\text{NAI}} = 6.0 \times 10^5$	Particle removal efficiency was affected by particle size (0.1–0.5 μm)
4	Wu et al. ^[29]	Deposition removal of submicron particles by ionizer	Stainless steel chamber	Air velocity of 0.56, 1.20 and 2.00 m/s, and NaCl particles of 30, 50, 100, 170 and 300 nm	$C_{\text{NAI}} = 1.2 \times 10^6$ –4.3 × 10 ⁶	Air cleaner effectiveness ranged from 57.6% to 96.0%
5	Sawant et al. ^[30]	Effects of NAIs on fog and smoke	Closed dark room	Fog and vehicle smoke under natural decay or with NAI application	$C_{\text{NAI}} = 5.0 \times 10^5$ –2.0 × 10 ⁷	93.0% to 97.0% of particles were removed in glass container
6	Pushpawela et al. ^[15]	Efficiency of ionizer in removing airborne particles	Chambers or rooms with volume of 1, 20, 32, 45 and 132 m ³	Controlled amount of smoke	$C_{\text{NAI}} = 1.0 \times 10^6$	70.0% of particles were removed by ionizer in 15 min
7	Liu et al. ^[35]	Effects of NAIs on cardiopulmonary health	Randomized crossover trial	56 healthy college students (33 males and 23 females)	True purifier: 60 591±12 184; sham purifier: 53 ± 16	Effective in reducing indoor PM _{2.5} concentrations and increasing NAI levels
8a	Jiang et al. ^[17]	Effects on humans, animals and microorganisms	Systematic review of studies on NAIs	263 studies (1960–2018)	$C_{\text{NAI}} > 1000$	Benefit humans and animals, and inhibit microorganisms
8b	Nunayon et al. ^[10]	Air ion disinfection efficacy under different ventilation duct conditions	Steel ventilation duct system	Three bacteria species: <i>Escherichia coli</i> , <i>Salmonella typhimurium</i> and <i>Staphylococcus epidermidis</i>	$C_{\text{NAI}} = 7.5 \times 10^5$ –9.5 × 10 ⁵ ; $C_{\text{PAI}} = 7.5 \times 10^5$ –9.5 × 10 ⁵	Positive ionizer showed better disinfection performance
9	Bowers et al. ^[19]	Effects on depression symptoms of SAD	Parallel-group design; single-blind study	40 subjects with symptoms of seasonal affective disorder	$C_{\text{NAI}} = 2.0 \times 10^3$ –2.0 × 10 ⁶	Alleviate atypical symptoms SAD
10	Bowers et al. ^[19]	Effects on depression symptoms of SAD	Parallel-group design; single-blind study	40 subjects with symptoms of seasonal affective disorder	$C_{\text{NAI}} = 2.0 \times 10^3$ –2.0 × 10 ⁶	Alleviate depression

(Table 2 continued)

Case number	Author	Study purpose	Study model	Study object	Ion concentration/ (ion/cm ³)	Primary outcomes of interest
11a	Flory et al. ^[24]	Evaluating the efficacy of two active treatments	Randomized controlled trial	73 female students and staff (18–51 years)	$C_{\text{NAI}} = 4.0 \times 10^3$ – 2.0×10^6	High-density NAIs have better antidepressant effects
11b	Goel et al. ^[25]	Effects on non-seasonal chronic depression	Randomized controlled trial	32 patients (8 males and 24 females)	C_{NAI} of high-density: $C_{\text{NAI}} = 4.5 \times 10^{14}$; C_{NAI} of low-density: 1.7×10^{11}	Alleviate chronic depression
11c	Goel et al. ^[26]	Effects on mood changes in a student population	Subjects were randomly assigned to one of four conditions	118 subjects (49 males and 69 females)	C_{NAI} of high-density: 4.5×10^{14} ; C_{NAI} of low-density: 1.7×10^{11}	Alleviate depression within 15–30 min
12	Perez et al. ^[36]	Effects on mood and depression	Meta-analysis model	33 studies (1957–2012)	$C_{\text{NAI}} = 1.0 \times 10^3$ – 2.75×10^7	NAIs at the highest level present lower depression scores
13a	Chu et al. ^[20]	Effects on cognitive function	Controlled test	39 non-smoking healthy adults (28 males and 11 females)	$C_{\text{NAI}} = 1489.30 \pm 148.92$	Benefit cognitive function
13b	Xiao et al. ^[18]	Associations between NAI concentration and health effects	Analysis of English-language studies	14 (2013–2023)	—	Benefit health by altering amino acid metabolism and promoting energy production
13c	Enache et al. ^[2]	Effects on living organisms	Environmental determinants	—	Town: < 500; extra-urban areas: 500–1500; modern office: 100–350	Promote environmental friendliness and offer additional therapeutic benefits
14	Wallner et al. ^[27]	Effects on cognitive performance, well-being, lung function and cardiovascular function	Double-blind over trial	20 healthy non-smoking adults (10 males and 10 females)	$C_{\text{NAI}} = 367$ –866	Improve cognitive ability
15	Wallner et al. ^[27]	Effects on cognitive performance, well-being, lung function and cardiovascular function	Double-blind over trial	20 healthy non-smoking adults (10 males and 10 females)	$C_{\text{NAI}} = 367$ –866	Increase sympathetic activity
16	Ho et al. ^[23]	Effects on the functional activities of badminton athletes	Double-blind study	38 badminton players (20 males and 18 females)	$C_{\text{NAI}} = 0$, 300, 3 000 and 30 000, respectively	Alleviate fatigue caused by muscle overload
17	Liu et al. ^[21]	Associations between short-term exposure to forest NAIs and heart rate variability	Repeated-measure panel study	31 healthy adults	C_{NAI} of the median (IQR): 68.11 (138, 20)	Improve HRV, especially to parasympathetic nerve activity
18	Liu et al. ^[22]	Associations between NAIs and cardiorespiratory effect after double-blind purification	Randomized, double-blind crossover study	44 healthy middle school students (24 boys and 20 girls)	$C_{\text{NAI}} = 1.2 \times 10^4$	Improve respiratory function

Notes: HRV—heart rate variability; IQR—interquartile range; VOCs—volatile organic compounds.

3.2 Unavailing effects

The published studies on the unavailing effects of NAIs on human health are summarized in Table 3. The ionizer (NAI concentration is 997 ion/cm^3) could elicit significant benefits to the respiratory system, but is seemingly offset by apparently negative effects on cardiac autonomic function^[37]. Figure 1 illustrates the effect of NAIs on human health summarized from the published literature. NAIs seem to have no influence (NAI concentration is $2\ 194 \text{ ion/cm}^3$ or $1\ 038 \text{ ion/cm}^3$) on lung health or function^[27], unobvious effect (NAI

concentration is $1.6 \times 10^3 - 1.5 \times 10^6 \text{ ion/cm}^3$) on respiratory function and symptoms^[38], no effect (NAI concentration is $(2.2 \pm 0.3) \times 10^5 \text{ ion/cm}^3$) on aerobic metabolism, performance or recovery during exercise^[39], and no effect (NAI concentration is $7.0 \times 10^6 \text{ ion/cm}^3$) on rat health about reproductive function or postnatal growth and development^[40]. Ozone and electroporation, more than NAIs, are the principal causes of cell death amongst the bacteria^[41]. If the unipolarity coefficient K is above 1.0, in combination with air pollution, NAIs might cause even more harm to the human body^[12].

Table 3 Literature surveys on unavailing effect of NAIs on human health

Case number	Author	Study purpose	Study model	Study object	NAI concentration/ (ion/cm ³)	Primary outcomes of interest
19	Dong et al. ^[37]	Effects on children	Randomized and double-blind crossover study	44 healthy middle school students (24 boys and 20 girls)	Real-purification : $12\ 997 \pm 3\ 814$; sham-purification : 12 ± 10	Benefit respiratory system were offset by apparently negative effects on cardiac autonomic function
20	Alexander et al. ^[38]	Effects on respiratory function and symptoms	Literature review on random effects meta-analysis model	23 studies (1933–1993)	$1.6 \times 10^3 - 1.5 \times 10^6$	Unobvious effect
21	Nimmerichter et al. ^[39]	Effects on oxygen uptake kinetics, recovery and performance during exercise	Randomized and double-blind trial	14 trained males	Control group : $1.4 \times 10^6 - 1.6 \times 10^6$; indoor air : $(2.2 \pm 0.3) \times 10^5$	No effect on aerobic metabolism, performance or recovery during exercise

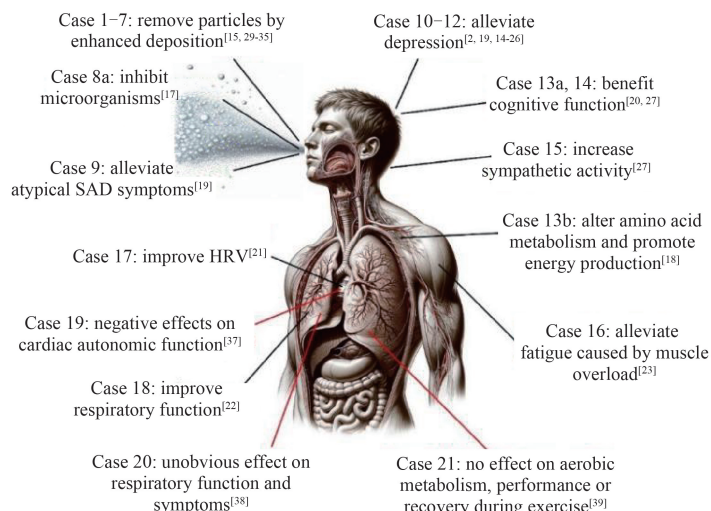


Fig. 1 Effect of NAIs on human health summarized from published literature

Although electrostatic precipitators and ionizers can do the same as high-efficiency particulate air (HEPA) in removing PM_{2.5}, both of them also generate by-products that might be harmful to human health^[35]. An obvious disadvantage of ionizers is the emission of ozone^[42-43], which can seriously harm our health with long-term exposure. Many ionizers emit ozone more or less^[44-46]. At high humidity and voltage, for example, a humidity of 90% and a voltage of -7 kV , the ionizers should

strictly comply with the electrostatic air purifier safety standards, Underwriters Laboratories, Inc. (UL, Northbrook, IL, USA) Standard 867 (UL—867)^[47-48] and the 0.05 mg/L ozone limit specified by the State of California, USA^[49].

Another side effect is that the continuous emission of NAIs into a closed environment can cause charges to build up on the insulating surface, which can then lead to static problems, especially at low humidity^[50].

4 Discussion and Measures

In most natural environments^[2, 51-52], NAI concentrations mainly range from 2.0×10^2 ion/cm³ to 5.0×10^4 ion/cm³. High-density NAI concentrations are commonly found alongside low-density particulate pollutants in natural environments. This clean and favorable air quality provides a beneficial bioactive capacity for human health.

4.1 Concentration distribution of NAIs on human health

Summarized from published literature, the full-

scale and the partial-scale concentration distributions of NAIs on human health are shown in Fig. 2 and Fig. 3, respectively. Full-scale concentration distribution represents the inclusion of all the NAI concentrations involved in the cases, aiming to showcase the NAI concentrations studied in each case and their corresponding effects. Partial-scale concentration distribution primarily displays the cases that fall within the range of NAI concentrations in natural environments, with the maximum value on its horizontal axis equal to the highest concentration of NAIs found in nature.

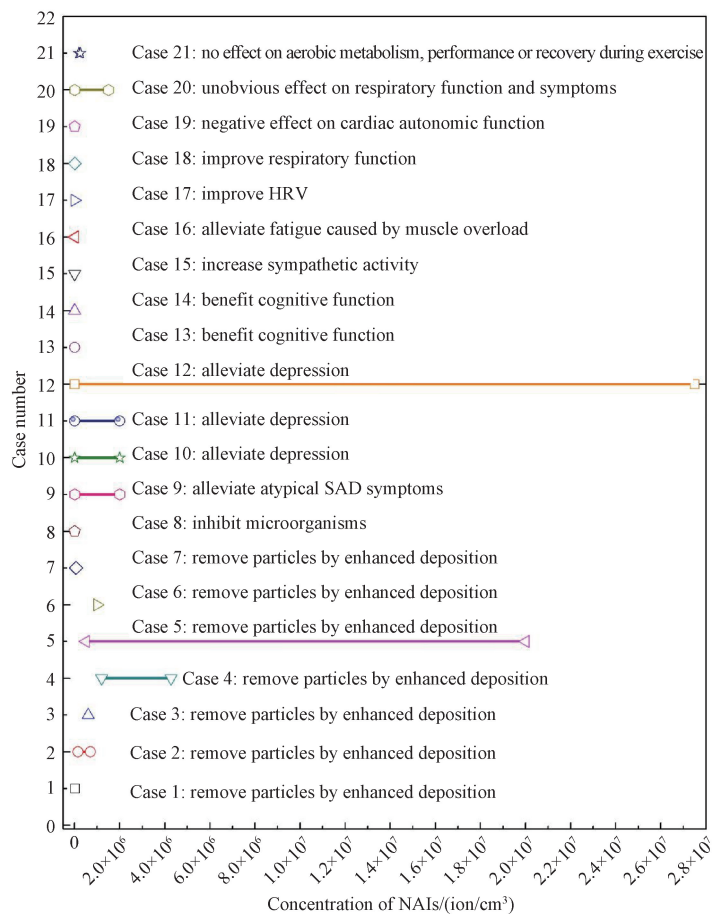


Fig. 2 Full-scale concentration distribution of NAIs on human health summarized from published literature

Out of the 18 cases demonstrating beneficial effects, six cases including Cases 4 – 5 (remove particles by enhanced deposition), Case 9 (alleviate atypical SAD symptoms), and Cases 10 – 12 (alleviate depression), explored NAI concentrations that either included 2.0×10^6 ion/cm³ within the tested range, or reached this value as the maximum concentration. The other 12 cases investigated the NAI concentrations that were lower than

2.0×10^6 ion/cm³. For the three unavailing effect cases (Cases 19–21), their NAI concentrations are all below 2.0×10^6 ion/cm³.

As illustrated in Fig. 3, the NAI concentrations of all partial-scale cases are larger than 2.0×10^2 ion/cm³. Also, the NAI concentrations of nine cases including Case 1, Case 8, and Cases 13–19, are less than 5.0×10^4 ion/cm³.

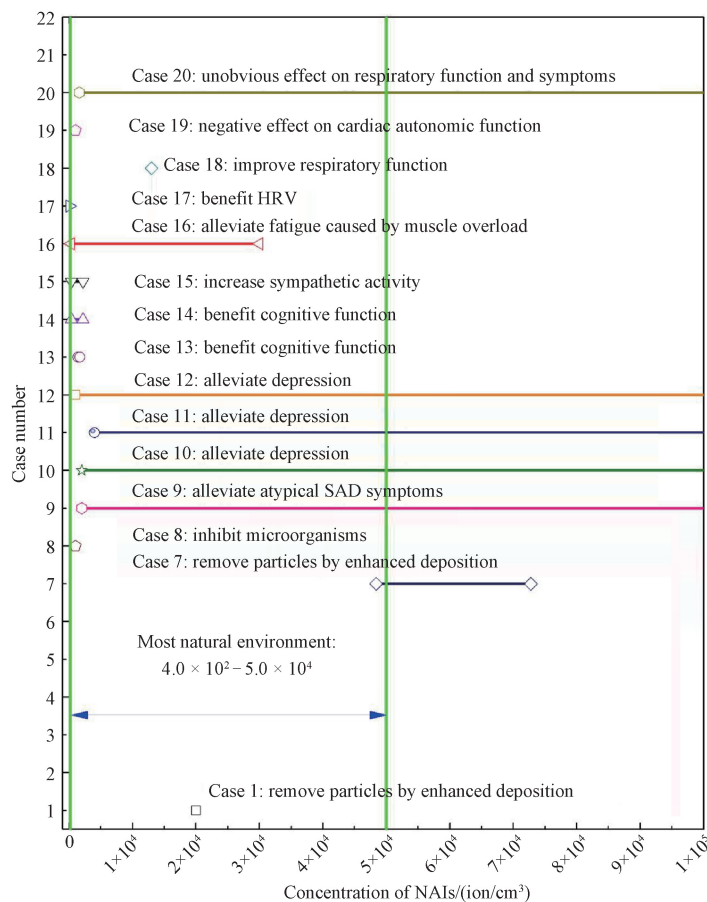


Fig. 3 Partial-scale concentration distribution of NAIs on human health summarized from published literature

Although some cases reported that higher NAI concentrations can provide more effectiveness, no case explores the full-size NAI concentrations for their beneficial or unavailing effect on human health. The relatively higher NAI concentrations seem to present lower depression scores^[36], greater antidepressant efficacy^[24], and efficacious in chronic depression^[25]. However, the increase in NAI concentrations might elevate the levels of systemic oxidative stress^[35]. To avoid adverse effects on human health, all cases seem to select serious and conservative levels of NAI concentrations. Further research is needed to explore whether increasing NAI concentrations beyond current levels could potentially enhance their beneficial effects on human health while ensuring safety.

4.2 Measures to balance beneficial and unavailing effects

Using ionizers as an alternative for enhancing indoor air quality presents certain risks and benefits. Risks include potential respiratory problems due to ozone production by ionizers and a rise in systemic oxidative stress levels that counteract the positive effects on cardiorespiratory function from reduced PM_{2.5}. The benefits of using air ionizers encompass air purification through the adsorption of fine particles such as dust, bacteria and viruses, along with alleviating depression

and atypical SAD symptoms through increased NAI concentrations.

To balance the beneficial and unavailing effects of NAIs, a more extensive and comprehensive scientific investigation should be conducted before employing ionizers as alternative solutions to improve indoor air quality. Taking the enclosed environment as an example, the measures are in the following steps.

1) The type and concentration of particulate pollutants should be generally assessed in advance. This is primarily due to the potential ion-particle interactions between NAIs and particulate pollutants. Furthermore, if ionizers are effective in removing particulate pollutants from the air, the parameters for ionizers need to be adjusted. They no longer represent pure NAI exposure but instead reflect a modified environment where particulate pollutants have been diminished. The coexistence of NAIs with particulate pollutants and gases^[12] (such as CO, NO_x and SO₂) in indoor air may expose occupants to a potentially harmful combination.

2) The selection of ionizers should focus on a few variables that impact the ion concentration, such as the air circulation rate, relative humidity and wall electrostatic characteristics (prevent charging insulating surfaces).

3) The regulation of NAI concentration should be

moderated to ensure safety and efficacy, with adjustments based on specific conditions. This can be accomplished through monitoring NAI levels, modulating ionizer output, and managing operation time, thereby minimizing the production of by-products.

4) The immediate implementation of emergency procedures for ionizers, including discontinuing their use or switching them off, should take place as soon as any individual experiences discomfort or adverse effects.

5 Conclusions

Based on the survey of published literature, this study highlights the mechanism of NAIs for improving the indoor air environment, the beneficial or unavailing effects on human health, and alternative measures to balance beneficial and unavailing effects. The conclusions are drawn in the following three points.

1) Consensus effect of NAIs on human health. There is common consent that NAIs can remove particles by enhanced deposition, inhibit microorganisms, alleviate depression, benefit cognitive function, and even increase sympathetic activity.

2) Contradictory effect of NAIs on human health. Some studies advocate that forest NAIs are beneficial to heart rate variability, but others claim that there are negative effects on cardiac autonomic function. Also, some studies report that NAIs can improve respiratory function, but others elaborate that there are unobvious effects on respiratory function or no effects on aerobic metabolism performance or recovery during exercise. These discrepancies may be caused by differences in research methods and sample selection. The effects of NAIs in forests on human health are inconsistent in some studies, and such differences should be understood and explained from objective and scientific perspectives. Thus, more studies should be further investigated on the effects of NAIs on human health.

3) Desirable NAI concentrations. There is no extensive or complete investigation of the influence of NAI concentrations on human health. This means that there is a lack of sufficient evidence to support the unavailing NAI effects on human health, to provide a full-scale response curve of NAI concentrations on human health, or to maintain moderate NAI concentrations in certain types of indoor environments or for specific occupants. However, the World Health Organization (WHO) considers the air with NAI concentrations between $1\ 000 \text{ ion}/\text{cm}^3$ and $1\ 500 \text{ ion}/\text{cm}^3$ to be clean air^[53]. Some studies have revealed that NAI concentrations above $700 \text{ ion}/\text{cm}^3$ could meet the basic physiological needs of the human body, while NAI concentrations above $1\ 000 \text{ ion}/\text{cm}^3$ could benefit human health^[54]. As mentioned earlier, NAI concentrations in most natural environments range from $2.0 \times 10^2 \text{ ion}/\text{cm}^3$ to $5.0 \times 10^4 \text{ ion}/\text{cm}^3$. The desirable range of NAI concentration is recommended to be $1.0 \times 10^2\text{--}5.0 \times 10^4 \text{ ion}/\text{cm}^3$, which is a noteworthy advancement.

References

- [1] WANG H, WANG B, NIU X, et al. Study on the change of negative air ion concentration and its influencing factors at different spatio-temporal scales [J]. *Global Ecology and Conservation*, 2020, 23: e01008.
- [2] ENACHE L M, BUNESCU I. Air ionization-an environmental factor with therapeutic potential [J]. *GEOREVIEW: Scientific Annals of Stefan cel Mare University of Suceava. Geography Series*, 2019, 29(1): 31-39.
- [3] PATIL V N, PATIL B P, SHIMPI N G, et al. Proposed negative ion generator [J]. *International Journal of Applied Information Systems*, 2012, 3: 44-48.
- [4] YAN X J, WANG H R, HOU Z Y, et al. Spatial analysis of the ecological effects of negative air ions in urban vegetated areas: a case study in Maiji, China [J]. *Urban Forestry & Urban Greening*, 2015, 14(3): 636-645.
- [5] GUO H Y, CHEN J, WANG L F, et al. A highly efficient triboelectric negative air ion generator [J]. *Nature Sustainability*, 2020, 4(2): 147-153.
- [6] HARTMANN A, KRIEGEL M. The influence of air ions on the particle concentration in indoor environments: a systematic literature review [J]. *Results in Engineering*, 2022, 15: 100528.
- [7] ORTIZ-GRISALES P, PATIÑO-MURILLO J, DUQUE-GRISALES E. Comparative study of computational models for reducing air pollution through the generation of negative ions [J]. *Sustainability*, 2021, 13(13): 7197.
- [8] LIN L, LI Y, KHAN M, et al. Real-time characterization of negative air ion-induced decomposition of indoor organic contaminants by mass spectrometry [J]. *Chemical Communications*, 2018, 54(76): 10687-10690.
- [9] NUNAYON S S, ZHANG H H, CHAN V, et al. Study of synergistic disinfection by UVC and positive/negative air ions for aerosolized *Escherichia coli*, *Salmonella typhimurium*, and *Staphylococcus epidermidis* in ventilation duct flow [J]. *Indoor Air*, 2022, 32(1): e12957.
- [10] NUNAYON S S, ZHANG H H, JIN X, et al. Experimental evaluation of positive and negative air ions disinfection efficacy under different ventilation duct conditions [J]. *Building and Environment*, 2019, 158: 295-301.
- [11] ZHOU P, YANG Y, HUANG G S, et al. Numerical and experimental study on airborne disinfection by negative ions in air duct flow [J]. *Building and Environment*, 2018, 127: 204-210.
- [12] SKROMULIS A. Impact of cluster ions and air

- pollution on human health [J]. *Environment Technologies Resources. Proceedings of the International Scientific and Practical Conference*, 2019, 1: 267-271.
- [13] HENNING R J. Particulate matter air pollution is a significant risk factor for cardiovascular disease [J]. *Current Problems in Cardiology*, 2024, 49 (1): 102094.
- [14] REN C, HAGHIGHAT F, FENG Z B, et al. Impact of ionizers on prevention of airborne infection in classroom [J]. *Building Simulation*, 2023, 16(5): 749-764.
- [15] PUSHPAWELA B, JAYARATNE R, NGUY A, et al. Efficiency of ionizers in removing airborne particles in indoor environments [J]. *Journal of Electrostatics*, 2017, 90: 79-84.
- [16] SHI B B, EKBERG L. Ionizer assisted air filtration for collection of submicron and ultrafine particles-evaluation of long-term performance and influencing factors [J]. *Environmental Science & Technology*, 2015, 49(11): 6891-6898.
- [17] JIANG S Y, MA A L, RAMACHANDRAN S. Negative air ions and their effects on human health and air quality improvement [J]. *International Journal of Molecular Sciences*, 2018, 19(10): 2966.
- [18] XIAO S, WEI T J, PETERSEN J D, et al. Biological effects of negative air ions on human health and integrated multiomics to identify biomarkers: a literature review [J]. *Environmental Science and Pollution Research International*, 2023, 30(27): 69824-69836.
- [19] BOWERS B, FLORY R, AMETEPE J, et al. Controlled trial evaluation of exposure duration to negative air ions for the treatment of seasonal affective disorder [J]. *Psychiatry Research*, 2018, 259: 7-14.
- [20] CHU C H, CHEN S R, WU C H, et al. The effects of negative air ions on cognitive function: an event-related potential (ERP) study [J]. *International Journal of Biometeorology*, 2019, 63(10): 1309-1317.
- [21] LIU S, LI C, CHU M T, et al. Associations of forest negative air ions exposure with cardiac autonomic nervous function and the related metabolic linkages: a repeated-measure panel study [J]. *Science of the Total Environment*, 2022, 850: 158019.
- [22] LIU S, HUANG Q Y, WU Y, et al. Metabolic linkages between indoor negative air ions, particulate matter and cardiorespiratory function: a randomized, double-blind crossover study among children [J]. *Environment International*, 2020, 138: 105663.
- [23] HO C S, LEE M C, CHANG C Y, et al. Beneficial effects of a negative ion patch on eccentric exercise-induced muscle damage, inflammation, and exercise performance in badminton athletes [J]. *Chinese Journal of Physiology*, 2020, 63(1): 35-42.
- [24] FLORY R, AMETEPE J, BOWERS B. A randomized, placebo-controlled trial of bright light and high-density negative air ions for treatment of seasonal affective disorder [J]. *Psychiatry Research*, 2010, 177 (1/2): 101-108.
- [25] GOEL N, TERMAN M, TERMAN J S, et al. Controlled trial of bright light and negative air ions for chronic depression [J]. *Psychological Medicine*, 2005, 35(7): 945-955.
- [26] GOEL N, ETWAROO G R. Bright light, negative air ions and auditory stimuli produce rapid mood changes in a student population: a placebo-controlled study [J]. *Psychological Medicine*, 2006, 36(9): 1253-1263.
- [27] WALLNER P, KUNDI M, PANNY M, et al. Exposure to air ions in indoor environments: experimental study with healthy adults [J]. *International Journal of Environmental Research and Public Health*, 2015, 12 (11): 14301-14311.
- [28] LIN W, ZENG C C, NIE W B, et al. Study of the vertical structures, thermal comfort, negative air ions, and human physiological stress of forest walking spaces in summer [J]. *Forests*, 2022, 13(2): 335.
- [29] WU Y Y, CHEN Y C, YU K P, et al. Deposition removal of monodisperse and polydisperse submicron particles by a negative air ionizer [J]. *Aerosol and Air Quality Research*, 2015, 15(3): 994-1007.
- [30] SAWANT V S, MEENA G S, JADHAV D B. Effect of negative air ions on fog and smoke [J]. *Aerosol and Air Quality Research*, 2012, 12(5): 1007-1015.
- [31] SHIUE A, HU S C. Contaminant particles removal by negative air ionic cleaner in industrial minienvironment for IC manufacturing processes [J]. *Building and Environment*, 2011, 46(8): 1537-1544.
- [32] KOLARŽ P, ILIĆA Ž, JANKOVIĆ M, et al. Estimating aerosol particle removal in indoor air by ion-enhanced deposition [J]. *Journal of Aerosol Science*, 2023, 173: 106199.
- [33] DUAN M J, WANG L J, MENG X Y, et al. Negative ion purifier effects on indoor particulate dosage to small airways [J]. *International Journal of Environmental Research and Public Health*, 2021, 19(1): 264.
- [34] SAHAY R, MENDEZ J, WOZNIAK A, et al. Bipolar ionization and its contribution to smart and safe buildings [R]. A CABA White Paper, 2021.
- [35] LIU W, HUANG J, LIN Y, et al. Negative ions

- offset cardiorespiratory benefits of PM_{2.5} reduction from residential use of negative ion air purifiers [J]. *Indoor Air*, 2021, 31(1): 220-228.
- [36] PEREZ V, ALEXANDER D D, BAILEY W H. Air ions and mood outcomes: a review and meta-analysis[J]. *BMC Psychiatry*, 2013, 13: 29.
- [37] DONG W, LIU S, CHU M T, et al. Different cardiorespiratory effects of indoor air pollution intervention with ionization air purifier: findings from a randomized, double-blind crossover study among school children in Beijing [J]. *Environmental Pollution*, 2019, 254: 113054.
- [38] ALEXANDER D D, BAILEY W H, PEREZ V, et al. Air ions and respiratory function outcomes: a comprehensive review[J]. *Journal of Negative Results in Biomedicine*, 2013, 12: 14.
- [39] NIMMERICHTER A, HOLDHAUS J, MEHNEN L, et al. Effects of negative air ions on oxygen uptake kinetics, recovery and performance in exercise: a randomized, double-blinded study [J]. *International Journal of Biometeorology*, 2014, 58(7): 1503-1512.
- [40] YAMAMOTO D, WAKO Y, KUMABE S, et al. Positive and negative ions by air purifier have no effects on reproductive function or postnatal growth and development in rats [J]. *Fundamental Toxicological Sciences*, 2015, 2 (3): 101-110.
- [41] FLETCHER L A, GAUNT L F, BEGGS C B, et al. Bactericidal action of positive and negative ions in air[J]. *BMC Microbiology*, 2007, 7: 32.
- [42] YU K P. Enhancement of the deposition of ultrafine secondary organic aerosols by the negative air ion and the effect of relative humidity [J]. *Journal of the Air & Waste Management Association*, 2012, 62(11): 1296-1304.
- [43] BERRY D, MAINELIS G, FENNELL D. Effect of an ionic air cleaner on indoor/outdoor particle ratios in a residential environment [J]. *Aerosol Science and Technology*, 2007, 41 (3): 315-328.
- [44] WARING M S, SIEGEL J A, CORSI R L. Ultrafine particle removal and generation by portable air cleaners [J]. *Atmospheric Environment*, 2008, 42(20): 5003-5014.
- [45] WU C C, LEE G W M. Oxidation of volatile organic compounds by negative air ions [J]. *Atmospheric Environment*, 2004, 38(37): 6287-6295.
- [46] CHEN L W, GONZE E, ONDARTS M, et al. Electrostatic precipitator for fine and ultrafine particle removal from indoor air environments [J]. *Separation and Purification Technology*, 2020, 247: 116964.
- [47] ZHANG Q, JENKINS P L. Evaluation of ozone emissions and exposures from consumer products and home appliances[J]. *Indoor Air*, 2017, 27 (2): 386-397.
- [48] AFSHARI A, MO J, TIAN E, et al. Testing portable air cleaning units-test methods and standards: a critical review[J]. *REHVA Journal*, 2022, 59(3): 35-46.
- [49] DE L'ANSES A. Identification et analyse des différentes techniques d'épuration d'air intérieur émergentes[R]. 2017.
- [50] LEE B U, YERMAKOV M, GRINSHPUN S A. Removal of fine and ultrafine particles from indoor air environments by the unipolar ion emission[J]. *Atmospheric Environment*, 2004, 38(29): 4815-4823.
- [51] LAZZERINI F T, ORLANDO M T, DE PRA W. Progress of negative air ions in health tourism environments applications[J]. *Boletin Sociedad Espanola Hidrologia Medica*, 2018, 33(1): 27-46.
- [52] PAWAR S D, MEENA G S, JADHAV D B. Air ion variation at poultry-farm, coastal, mountain, rural and urban sites in India[J]. *Aerosol and Air Quality Research*, 2012, 12(3): 444-455.
- [53] SHANG Y Y, WANG H B, TAO Y, et al. Temporal and spatial characteristics of atmospheric negative oxygen ions and the relationship with meteorological factors in Chishui [J]. *Mid-Low Latitude Mountain Meteorology*, 2018, 42(4): 43-48. (in Chinese)
- [54] LI A, LI Q, ZHOU B, et al. Temporal dynamics of negative air ion concentration and its relationship with environmental factors: results from long-term on-site monitoring[J]. *Science of the Total Environment*, 2022, 832: 155057.

室内环境空气负离子对人体健康的功效及浓度分布

邓晓妮¹, 安毓辉², 杨学宾^{1*}, 张瑞丹¹, 熊辰¹

1. 东华大学 环境科学与工程学院, 上海 201620

2. 中国船舶设计研究院, 上海 200011

摘要: 室内环境中存在的空气负离子 (negative air ion, NAI) 可有效减少微粒污染物和气体污染物, 并抑制微生物、细菌和病毒的生长, 从而对人体健康产生积极影响。该综述调查了不同模块类型的常见离子发生器, 分析了 NAI 改善室内空气质量的机制及 NAI 对人体健康的影响。研究还调查了不同的 NAI 浓度对人体健康各方面的影响, 以及平衡有益和不确定影响的替代措施。虽然 NAI 在去除颗粒物、缓解抑郁、增强认知功能甚至刺激交感神经活动方面具有功效, 但在对心脏自律神经功能和呼吸生理的影响方面, 存在着相互矛盾的研究结果。为解决这一复杂问题, 需考虑采取其他措施, 在 NAI 的有益影响和不确定影响之间取得平衡。这些措施包括对颗粒污染物特性的总体评估, 对 NAI 发生器的选择, 以及遵守所推荐的 NAI 最佳浓度阈值。

关键词: 室内环境; 空气负离子; 人体健康; 颗粒去除; 替代措施

Personal Style Guided Outfit Recommendation with Multi-Modal Fashion Compatibility Modeling

WANG Kexin¹, ZHANG Jie^{2*}, ZHANG Peng², SUN Kexin³, ZHAN Jiamei⁴, WEI Meng⁴

1. School of Computer Science and Technology, Donghua University, Shanghai 201620, China

2. Institute of Artificial Intelligence, Donghua University, Shanghai 201620, China

3. College of Mechanical Engineering, Donghua University, Shanghai 201620, China

4. College of Information Science and Technology, Donghua University, Shanghai 201620, China

Abstract: A personalized outfit recommendation has emerged as a hot research topic in the fashion domain. However, existing recommendations do not fully exploit user style preferences. Typically, users prefer particular styles such as casual and athletic styles, and consider attributes like color and texture when selecting outfits. To achieve personalized outfit recommendations in line with user style preferences, this paper proposes a personal style guided outfit recommendation with multi-modal fashion compatibility modeling, termed as PSGNet. Firstly, a style classifier is designed to categorize fashion images of various clothing types and attributes into distinct style categories. Secondly, a personal style prediction module extracts user style preferences by analyzing historical data. Then, to address the limitations of single-modal representations and enhance fashion compatibility, both fashion images and text data are leveraged to extract multi-modal features. Finally, PSGNet integrates these components through Bayesian personalized ranking (BPR) to unify the personal style and fashion compatibility, where the former is used as personal style features and guides the output of the personalized outfit recommendation tailored to the target user. Extensive experiments on large-scale datasets demonstrate that the proposed model is efficient on the personalized outfit recommendation.

Keywords: personalized outfit recommendation; fashion compatibility modeling; style preference; multi-modal representation; Bayesian personalized ranking (BPR); style classifier

CLC number: Z62

Document code: A

Article ID: 1672-5220(2025)02-0156-12

Open Science Identity
(OSID)



0 Introduction

In recent years, there has been a growing interest in personalized outfit recommendations within the fashion

industry^[1-3]. With the advancement of the Internet technology, users can access extensive fashion information online, leading to an ever-expanding choice space. However, this abundance of information also poses challenges for users in filtering out their preferred fashion products. Outfit recommendations are initially generated based on fashion compatibility which quantifies the aesthetic coordination between clothes in terms of colors, styles, fabrics and other multi-modal attributes. A compatible outfit usually conforms to the aesthetic standards of most people. At the same time, personal preferences also influence the recommendation results. Consequently, numerous scholars have dedicated themselves to studying how to recommend outfit combinations that align with both current fashion trends and user style preferences. This trend arises from the increasing emphasis on the personal style and the necessity to tailor recommendation services accordingly. However, most existing fashion outfit recommendations still fall short of fully meeting these personal style needs. Thus, combining fashion styles with user style preferences remains an urgent problem within this field.

One crucial aspect that is often overlooked by current fashion outfit recommendations is users' distinct partiality towards specific styles. A style is a critical element in outfits, represents divergent aesthetic orientations and channels of self-expression, and influences clothing selection. User style preferences are deeply rooted in the individual taste and reflect the desired image projection. By neglecting the personal style, traditional recommendations have shortcomings in providing accurate suggestions that align with user style preferences. Some studies have defined clothing attributes as factors to quantify fashion styles by analyzing the fashion design process, demonstrating a meaningful relationship between clothing attributes and

Received date: 2024-04-30

Foundation items: Shanghai Frontier Science Research Center for Modern Textiles, Donghua University, China; Open Project of Henan Key Laboratory of Intelligent Manufacturing of Mechanical Equipment, Zhengzhou University of Light Industry, China (No. IM202303); National Key Research and Development Program of China (No. 2019YFB1706300)

* Correspondence should be addressed to ZHANG Jie, email: mezhangjie@dhu.edu.cn

Citation: WANG K X, ZHANG J, ZHANG P, et al. Personal style guided outfit recommendation with multi-modal fashion compatibility modeling [J]. *Journal of Donghua University (English Edition)*, 2025, 42(2): 156-167.

fashion styles^[4-5]. Despite these advances, the personalization factor of fashion styles remains a challenge. The complexity of capturing user style preferences from a style perspective highlights the necessity of further exploration and improvement in the current fashion outfit recommendation field. Therefore, this study attempts to explore the role of the personal style in the fashion outfit recommendation.

Fashion compatibility is another essential aspect, and fashion representation serves as the foundation for it. Current studies primarily focus on considering either a single visual or textual modality when it comes to fashion representation, as well as methods that simultaneously take both modalities into account^[6-7]. The importance of the interaction between these two modalities has been proven by numerous research studies^[8-9]. However, existing multi-modal methods that linearly integrate visual and textual modalities, despite recognizing their complementarity, still struggle to reduce redundancy. These linear fusion methods limit the exploration of the diversity of fashion representation and may not fully capture the complex characteristics of fashion trends. Furthermore, the multi-modal information in the fashion representation can be exploited to understand the compatibility between individual fashion items and the whole. Learning fashion compatibility can pave the way for personalized outfit recommendations and enhance the overall consumer experience.

To overcome these challenges, a personal style guided network is proposed that can analyze multi-modal data such as clothing images and textual descriptions related to the outfits favored by users on social media platforms. On the one hand, the multi-modal representation of clothing is modeled to learn the outfit compatibility, that is, the degree of coordination between different items that constitute a set of clothing. On the other hand, the user style preference is extracted and guided to the personalized outfit recommendation.

Primary contributions of this study can be succinctly summarized as follows.

1) A comprehensive personal style guided network for personalized outfit recommendations has been constructed, in which a two-stage style extraction model is used to model the relationship among clothing attributes, outfit styles and personal styles.

2) Multi-modal compatibility of outfits, derived from images and texts, is leveraged to achieve an enhanced representation. Distinct from other studies, the integration of multi-modal features and style features into the Bayesian personalized ranking^[10] (BPR) framework is employed to fulfill the guiding function of the personal style.

3) A range of experiments have confirmed improvement over established baselines and have validated the effectiveness of various components within

the proposed model.

1 Related Works

This study focuses on the personalized outfit recommendation, a field that has been extensively studied^[11-13]. These studies can be divided into two tasks: fashion compatibility modeling and personalized outfit matching. In this section, related studies on these two tasks are reviewed. The personal style in this study is highlighted in comparison to that of prior studies.

1.1 Fashion compatibility modeling

Existing studies on fashion compatibility modeling differ in how they evaluate the compatibility score between two or a set of items. One explicit way is to decompose outfit compatibility into pairwise interactions between items. However, these metric learning approaches^[14-16] rely on pairwise comparisons between item features alone. In contrast, Cucurull et al.^[17] defined the context as a construct that was acknowledged to be compatible with each of these items. They addressed the compatibility prediction problem by employing a graph neural network that learned to generate product embeddings based on their visual features and contextual information. To capture high-order relationships between items, most of the studies treat the outfit as a whole. Lin et al.^[18] utilized multi-instance learning to generate correlation embeddings of individual items and acquired users' attention towards different matching items through an attention mechanism. Lu et al.^[8] leveraged tensor decomposition of the discrete content and sampled from a set of underlying Bernoulli variables to map items and users into binary codes. Among the existing methods, only a few have studied the problem of personalized outfit recommendation. Moreover, most of these studies utilize either a single data mode with limited information^[6] or only superficially combine visual and textual modalities at a low level. They fail to acquire high-level fashion representation knowledge through complementary interaction between the heterogeneous modes. Aligning these complex modes poses a significant challenge for complete fashion representation. Therefore, the proposed model investigates a non-linear multi-modal fusion method to represent fashion items with rich complementary information from images and texts.

1.2 Personalized outfit matching

Another task of personalized outfit recommendations is personalized outfit matching. Some studies have solved this problem from perspectives like multi-instance learning, attention mechanisms and tensor decomposition. Song et al.^[7] modeled overall compatibility modeling and user style preference modeling in personalized outfit recommendations as two separate subtasks. They focused on separating the two subtasks and extracted user style preferences from users' historical

outfit data for personalization. Some studies have modeled attribute-based fashion outfit recommendations from three aspects: attribute representation, attribute explanation and attribute preference modeling. Feng et al.^[19] partitioned embeddings of different attributes into different regions and adopted adversarial prediction networks to ensure independence between attribute embedding regions. This attribute-region embedding method can enhance the distinction between different attribute semantics. Sagar et al.^[9] pre-trained a neural network model for attribute classification and identified harmonious and inharmonious attributes between fashion items to address interpretability in outfit recommendations. This attribute classification-based approach can provide explanations for outfit recommendations. Zhan et al.^[20] constructed an attribute-aware fashion knowledge graph and designed a user-specific relational-aware attention mechanism to predict users' fine-grained preferences over different attributes for personalized outfit recommendations. Wang et al.^[21] defined conditional preferences by dividing user-item interaction data into preference conditions and constructing the conditional weight branch to learn preference degrees. Ding et al.^[22] proposed to integrate coordination knowledge into fashion and define category combinations as templates. Personalization was achieved through learning user style preferences for these templates. Although existing studies have explored personalized outfit recommendations from various perspectives, they overlook the personal style. To this end, the personal style is extracted from users' historical outfit data, and then it is used to guide the outfit recommendation.

Style is defined as a durable and recognizable pattern of aesthetic choices^[23]. De Divitiis et al.^[24] trained a universal style classifier based on the color triplets to investigate how specific color combinations were associated with particular emotions and lifestyles. However, solely relying on color combinations presents subjectivity and makes it challenging to identify more complex styles. Sun et al.^[25] obtained style-conditioned image patches by randomly cropping from apparel images and trained an image encoder in conjunction with textual descriptions to integrate style information with verbal representations. However, this approach is contingent on manual annotation. An et al.^[26] constructed a hybrid style framework to clarify the classification criteria of fashion styles. Banerjee et al.^[27] annotated clothing into eight

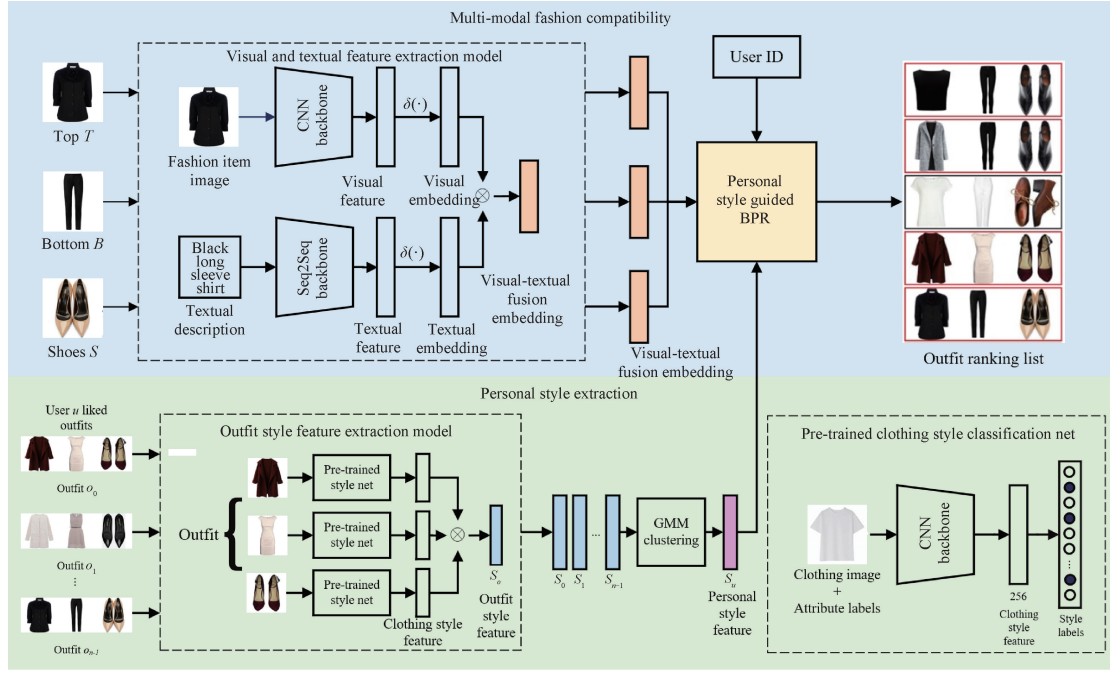
specific styles. Moreover, the style of an outfit is impacted by various attributes, with factors like colors, textures and fabric patterns playing a significant role in determining its style categorization. For instance, soft color collocation represents a gentle style, slim design reveals elegance, and loose version and pockets belong to a casual style. Jeon et al.^[4] redefined fashion attributes and proposed 25 new fashion styles, demonstrating the strong association between these styles and fashion attributes. This brings an important breakthrough to the field of fashion and provides us with new perspectives to understand and master fashion styles. Given these complexities surrounding the personalized outfit recommendation encompassing style preferences and attribute considerations, it becomes evident that how to capture user style preferences remains challenging for current outfit recommendations.

2 Proposed Methods

2.1 Problem formulation

Given sets of existing users $U = \{u_0, u_1, \dots, u_{n_U-1}\}$, tops $T = \{t_0, t_1, \dots, t_{n_T-1}\}$, bottoms $B = \{b_0, b_1, \dots, b_{n_B-1}\}$ and shoes $S = \{s_0, s_1, \dots, s_{n_S-1}\}$. For each user u , there is a set of historical outfits $O_u = \{o_0, o_1, \dots, o_{n_O-1}\}$. Here, n_U, n_T, n_B, n_S and n_O represent the number of elements in sets U, T, B, S and O_u , respectively. Each outfit consists of a top, a bottom and a pair of shoes, denoted as $o = (t_p, b_q, s_r)$, where p, q and r represent indices of items in sets T, B and S , respectively.

The personal style guided network (PSGNet), illustrated in Fig. 1, consists of three main components: a multi-modal fashion compatibility module, a personal style extraction module and a personal style guided BPR framework. The multi-modal fashion compatibility module contains a visual and textual feature extraction model and fashion compatibility evaluation. Visual-textual fusion embeddings are extracted from fashion item images and textual descriptions by the visual and textual feature extraction model. The personal style extraction module is an item-outfit-user three-level structure. By merging item features and personal style features, the personal style guided BPR framework aims to optimize the final outfit preference ranking for users, using positive and negative sample pairs.



CNN—convolutional neural network; GMM—Gaussian mixture model; $\delta(\cdot)$ —sigmoid activation function;

Seq2Seq—sequence-to-sequence.

Fig. 1 Overview of PSGNet

2.2 Personal style extraction

User style preferences refer to types, colors, fabrics and other aspects of clothing they like, which are often contained in users' historical outfit data. The personal style encapsulates a variety of preferences. Specifically, nine personal style categories are delineated across three dimensions: age, line and movement, as detailed in Table 1. By leveraging historical outfit data, it becomes possible to establish a comprehensive understanding of the relationship between users' unique fashion preferences and the personal style. However, the challenge lies in accurately modeling and characterizing the personal style. In response, a method that combines CNNs, specifically the 50-layer residual network^[28] (ResNet50), with the GMM^[29] clustering algorithm is proposed to tackle this issue. The method leverages the strengths of deep learning for feature extraction and the probabilistic nature of GMM for clustering.

The subtle relationship between fashion style representation and user style preferences is studied by establishing the relationship between clothing attributes and individual preferences. This process entails establishing connections between clothing attributes and individual preferences based on an examination of users' historical outfit data. To extract style features at the item level, CNNs that have been pre-trained on large-scale fashion attribute datasets DeepFashion^[5] are employed.

Such networks effectively encode subtle style characteristics, such as silhouettes, colors and texture, into vector representations. Specifically, the pre-trained clothing style classification net is used to extract the fashion style. It utilizes ResNet50 to extract fashion features from clothing images and attribute labels as shown in Fig. 2. For instance, the style features of a top t , denoted as S_t , a bottom b , denoted as S_b and a pair of shoes s , denoted as S_s , are ascertained.

Table 1 Categories and criteria of personal styles

Personal style	Age	Line	Movement
Lively	Youthful	Soft	Dynamic
Sweet	Youthful	Medium	Dynamic
Sporty	Youthful	Sharp	Dynamic
Elegant	Medium	Soft	Medium
Natural	Medium	Medium	Medium
Avant-garde	Medium	Sharp	Medium
Romantic	Mature	Soft	Static
Classic	Mature	Medium	Static
Metropolitan	Mature	Sharp	Static

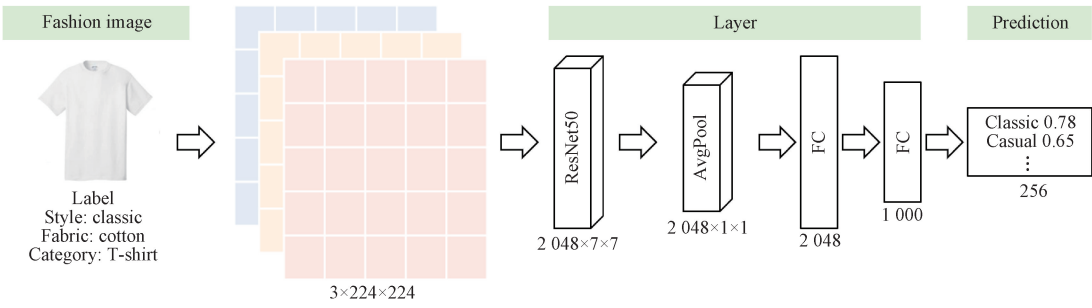


Fig. 2 Schematic diagram of pre-trained clothing style classification net

To capture the overall style of the outfit, an aggregation function is implemented to merge these item-level vectors into a unified vector representation, thus encapsulating the holistic style of the ensemble. This unified vector representation S_o serves as a bridge that connects clothing attributes with personalized preferences in a common embedding space. S_o can be expressed as

$$S_o = S_i \otimes S_b \otimes S_s. \quad (1)$$

To realize user-level style modeling, a hierarchical learning approach is pursued. It begins at the item level, progresses to the outfit level and culminates in the modeling of user style preferences. By concatenating

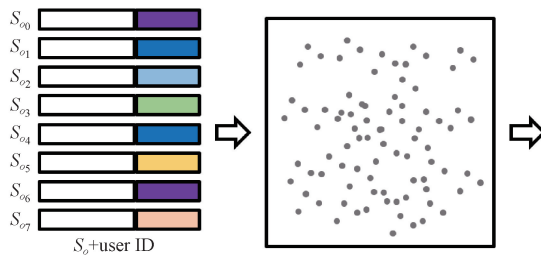


Fig. 3 Process of personal style feature clustering

Consequently, the personal style feature representation S_u for a given user u is aggregated by each outfit o in the users' historical outfit set O_u using adaptive pooling into a user-level style feature:

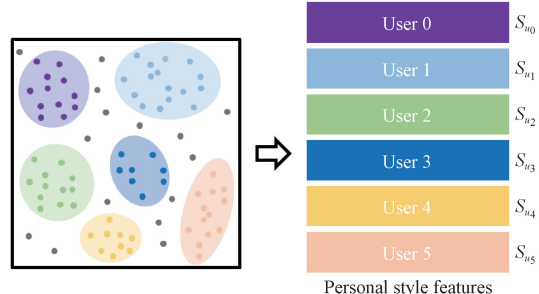
$$S_u = g(\{S_o \mid o \in O_u\}), \quad (2)$$

where $g(\cdot)$ denotes the GMM clustering mechanism being employed to derive user-level style features from outfit-level style representations. This hierarchical modeling approach allows styles to be learned from clothing attributes at the item level, abstracted to the outfit style and finally personalized to user style preferences. Consequently, a data-driven method emerges whereby the personal style of a user can be learned and represented, thereby facilitating the recommendation of complementary outfits tailored to each individual.

2.3 Multi-modal fashion compatibility

In the visual and textual feature extraction model,

outfit style vector representations for each user, clustering algorithms, for example, GMM cluster, can be harnessed to identify user groups exhibiting similar style preferences and patterns. The personal style analysis involves concatenating outfit-level style features for each user and utilizing the user ID as a form of supervision for clustering, as shown in Fig. 3. This process effectively groups users with comparable style preferences, and the cluster assignment for each user characterizes their personalized style signature. GMM cluster groups users with similar fashion styles. Based on the established user clusters, the approach extracts the personal style for each individual.



CNNs are recognized for their ability to learn visual representations, which are instrumental in extracting the deep features of images to depict the visual information of clothing. Seq2Seq models^[30] are adopted in learning textual features, and then are utilized to extract textual features from the textual description of clothing and express semantic information. Using visual and textual embedded features rather than directly visual and textual features is more conducive to learning the potential correlation between the two modalities. Therefore, multilayer perceptron (MLP) is used to convert visual and textual features into latent embeddings. Here, in a given example, the upper clothing is denoted as top t and an MLP is employed to derive the latent visual embedding v_t :

$$v_t = \delta(\omega_t \tilde{v}_t + b_t), \quad (3)$$

where ω_t is the weight parameter; \tilde{v}_t is the visual feature

extracted by the CNN; b_t is the bias parameter. Similarly, latent textual embeddings c_t , can be obtained. Visual-textual fusion embedding for the top t is denoted as z_t :

$$z_t = v_t \otimes c_t, \quad (4)$$

where v_t denotes the latent visual embeddings for the top t . Likewise, the latent visual, textual and visual-textual fusion embeddings for b and s are represented by v_b and v_s , c_b and c_s , z_b and z_s , respectively.

Understanding the compatibility relationships between clothing items for effective collocation is essential for fashion recommendation systems. A method that distinguishes positive and negative outfit samples is proposed, enabling us to capture the essence of compatibility in clothing matching. The similarity and complementarity of visual, textual and visual-textual fusion embeddings are leveraged to design the pairwise compatibility scoring function:

$$\begin{cases} C_{tb} = v_t^T v_b + c_t^T c_b + z_t^T z_b, \\ C_{ts} = v_t^T v_s + c_t^T c_s + z_t^T z_s, \\ C_{bs} = v_b^T v_s + c_b^T c_s + z_b^T z_s, \end{cases} \quad (5)$$

where C_{tb} , C_{ts} and C_{bs} represent the pairwise compatibility scores between t and b , t and s , and b and s , respectively. Equation (5) allows the proposed model to capture the intricate dynamics of clothing compatibility and refine the recommendations that it provides to users.

To determine the outfits with higher compatibility scores, the optimization goal C can be formulated:

$$C \equiv \{(t, b_i, b_j) \mid C_{tb_i} > C_{tb_j}\}, \quad (6)$$

where the subscripts i and j stand for positive samples and negative samples, respectively.

Pairwise compatibility scores among tops, bottoms and shoes are considered, along with the corresponding weights for each type, to calculate the overall compatibility score C_{tbs} of the outfit consisting of t , b and s :

$$C_{tbs} = \rho C_{tb} + \sigma C_{ts} + \tau C_{bs}, \quad (7)$$

where $\rho, \sigma, \tau \in [0, 1]$, and they are non-negative trade-off parameters that control the importance of different pairwise compatibilities for modeling the overall compatibility. By considering these factors, the proposed model can provide more accurate and refined compatibility assessments for users to seek outfit recommendations.

2.4 Personal style guided BPR

At this point, the multi-modal fashion compatibility module provides the fashion representation and learns the compatibility of different modalities, and the personal style extraction module captures the personal style. Naturally, Eqs. (2) and (7) are combined for the

complete fashion representation. The performance score $F_{u, o}$ of o consisting of t , b and s for a user u is

$$F_{u, o} = S_u \vartheta C_{tbs}, \quad (8)$$

where ϑ is a tensor with a fixed dimension.

Through positive and negative sample classification and multi-modal feature extraction, the proposed model can effectively learn the compatibility law of clothing matching to model the compatibility relationship. On this basis, the BPR framework has been modified to optimize personalized outfit recommendation. Given tuples (u, o_i, o_j) , where o_i is the outfit that the user u prefers and o_j is the outfit that the user u does not prefer. Therefore, the optimization goal P is

$$P \equiv \{(u, o_i, o_j) \mid F_{u, o_i} > F_{u, o_j}\}. \quad (9)$$

A rank loss function $\mathcal{L}_{\text{rank}}$ can be expressed as

$$\mathcal{L}_{\text{rank}} = \sum_{(u, o_i, o_j) \in P} \log \{1 + \exp[-(F_{u, o_i} - F_{u, o_j})]\}. \quad (10)$$

By building the compatibility model and the personalized model, the proposed model can effectively leverage the advantages of both to recommend outfits that are personalized and compatible. The personalized sorting mechanism and compatibility constraint learning are the keys to realizing personalized and compatible clothing-matching recommendations.

3 Experiments

The performance of the proposed PSGNet is evaluated through a comparative analysis with state-of-the-art models. Additionally, ablation experiments are conducted to assess the individual contributions of each module.

3.1 Dataset and experiment settings

3.1.1 Outfit dataset

The Polyvore-630 dataset employed in these experiments is a large-scale fashion outfit dataset constructed by Lu et al.^[8], and mines user data from the Polyvore website. This dataset comprises 150 380 outfits created by 630 users, with each outfit consisting of a top, a bottom and a pair of shoes. Unlike the original Polyvore dataset^[31], the Polyvore-630 dataset incorporates abundant historical collocation information from users, making it amenable to personalized outfit recommendations. The dataset includes positive and negative samples for users. Negative samples are generated by replacing an item in a positive outfit with a randomly selected item from a different category. A ratio of one positive outfit to 10 negative outfits is maintained for each user. With its abundance of user preference cues, the Polyvore-630 dataset offers a realistic and comprehensive validation platform for personalized outfit recommendations. The statistics of this dataset are shown

in Table 2.

Table 2 Statistics of Polyvore-630 dataset

Polyvore-630	Number of outfits	Number of items
Training dataset	127 326	159 729
Test dataset	23 054	45 505

3.1.2 Experiment settings

In the experiments, AlexNet^[32] is utilized as the default backbone network for image feature extraction. Following the approach presented in Ref. [8], in order to handle images of arbitrary sizes, the FC layers of AlexNet are replaced with convolutional layers, accompanied by average pooling layers that result in 4 096-dimensional feature vectors. For textual feature extraction from item descriptions, the Seq2Seq model is employed, and yields textual features of dimensionality-2 400. To train the style classifier, ResNet50 is used as the backbone network, augmented with an additional average pooling layer and two FC layers to extract style embeddings of dimensionality-256. The proposed model is implemented using the PyTorch framework. To enhance robustness, the models resample the negative samples in each epoch instead of fixing them during training. The experiments are performed on the tasks of personalized outfit recommendations, and test outfits are ranked for each user based on descending compatibility and personalized scores. The ranking performance is evaluated by using metrics such as the area under the receiver operating characteristic curve (AUC) and normalized discounted cumulative gain (NDCG).

3.2 Personalized outfit recommendation

The proposed model is compared with the following state-of-the-art models.

1) Visual BPR (VBPR)^[6]: apart from capturing the latent factors of user-item interactions, VBPR specifically models the user style preference towards visual factors.

2) General compatibility and personal preference-BPR (GP-BPR)^[7]: GP-BPR incorporates visual and textual modalities of fashion items and user-item data, utilizing both visual and textual information, to create a personalized compatibility model for clothing matching in a linear manner.

3) Personalized attribute-wise interpretable-BPR (PAI-BPR)^[9]: PAI-BPR employs fashion attributes and user-item data to develop an interpretable personalized fashion recommendation scheme that considers attributes on an individual basis.

4) Fashion hash net (FHN)^[8]: FHN proposes a discrete content-based tensor factorization model that maps items and users to binary codes for efficient fashion recommendations.

5) Multi-modal fashion compatibility and conditional preference model (MCCP)^[21]: MCCP

leverages multi-modal features to partition the user-item data into preference conditions and establishes a conditional preference model.

According to the experimental results shown in Table 3, PSGNet performs better than the baseline models in recommending outfits that conform to user style preferences and fashion compatibility. Compared with VBPR only using visual features, GP-BPR performs better, which proves the effectiveness of combining the visual and textual modalities. However, since GP-BPR can only linearly fuse visual and textual features, its performance is inferior to FHN, MCCP and PSGNet. Among these models, MCCP incorporating user conditional preferences performs the second best, highlighting the importance of modeling user style preferences for personalized outfit recommendations. The proposed PSGNet combines the multi-modal and personalized advantages of other models and focuses on learning personal styles, achieving the highest on both evaluation metrics.

Table 3 Results of personalized outfit recommendation performance comparison

Model	AUC	NDCG
VBPR	0.779 6	0.698 6
GB-BPR	0.838 8	0.727 1
PAI-BPR	0.827 8	0.756 6
FHN	0.846 5	0.764 8
MCCP	0.861 2	0.802 2
PSGNet	0.887 6	0.823 1

In Fig. 4, supplementary top-10 recommendation results are presented for a specific user, showcasing the performance of different models. Among them, PSGNet exhibits the best performance, as evidenced by its ability to recommend outfits that are consistent in the style while maintaining a high ranking of positive samples. While VBPR, GP-BPR, PAI-BPR and FHN are capable of recommending partially preferred outfits for users, they also tend to rank negative samples highly. The recommendation results of MCCP and PSGNet align more closely with user style preferences. However, it is worth noting that the recommended outfits by PSGNet exhibit a consistent personal style. These findings underscore the superiority and reliability of the proposed model in capturing and modeling the personal style of the user, thus highlighting its significant potential in the field of personalized outfit recommendations.

In summary, the experimental results validate that the proposed model can promote personalization and fashion compatibility in outfit recommendations by multi-modal fusion feature learning and personal style modeling.



Fig. 4 Top 10 recommendations for user 1: (a) VBPR; (b) GB-BPR; (c) PAI-BPR; (d) FHN; (e) MCCP; (f) PSGNet

3.3 Fashion compatibility matching

Previous experiments have demonstrated the performance of the proposed model on the personalized outfit recommendation task. The results on another task, fashion compatibility matching, are expanded. To demonstrate the ability of the proposed model in fashion compatibility matching, a fill-in-the-blank (FITB) fashion recommendation experiment was conducted by randomly selecting an item as a blank and setting three negative candidates for each clothing item within the test dataset. The categories of the negative candidates are the same as the ground-truth (GT). The accuracy of the proposed model is compared with the following baselines.

1) Bidirectional long short term memory (Bi-LSTM)^[31]: Bi-LSTM treats a fashion outfit as a sequence conditioned on the previous items and sequentially predicts the next item to learn their compatibility relationship.

2) Compatibility scoring network (CSN)^[33]: CSN learns image embeddings that respect item types, and jointly learns notions of item similarity and compatibility in an end-to-end model.

3) Multi-layered comparison network (MCN)^[34]: MCN leverages feature mappings from diverse layers of CNN and global average pooling to construct representations in various aspects. Subsequently, it derives an overall compatibility score through pairwise similarity enumerations across different layers.

4) FHN: FHN utilizes type-dependent hashing modules to generate binary codes for outfits, while employing visual semantic embedding to ensure consistent representation across visual and textual modalities.

As presented in Table 4, superior performance of PSGNet over the baselines highlights the effectiveness of the proposed model in addressing the fashion compatibility matching task. Upon a thorough examination of Table 4, the following accurate results for the evaluation are observed.

1) PSGNet exhibits the highest accuracy in the FITB task. This notable improvement stems from the utilization of both visual and textual features to effectively represent fashion items, resulting in the enhanced accuracy in the compatibility modeling. Conversely, Bi-LSTM and CSN mainly rely on visual features to analyze the compatibility between fashion items, failing to exploit the advantage of integrating visual and textual modalities, thereby leading to subpar performance.

2) While MCN and FHN incorporate visual and textual modalities for modeling fashion compatibility, they fall short in deeply integrating multi-modal information and neglect the compatibility relationships between individual items. Consequently, MCN and FHN exhibit limited predictive performance regarding compatibility relative to PSGNet.

Table 4 Results of fashion compatibility matching performance comparison

Model	FITB accuracy
Bi-LSTM	0.462 7
CSN	0.583 0
MCN	0.641 5
FHN	0.658 3
PSGNet	0.675 9

In Fig. 5, a comparative analysis of individual models is presented by visually examining various test examples of the FITB task. The purpose of including different categories as blank options in these examples is to evaluate the degree to which the model's choice is influenced by the category. The GT option is A, while the negative candidates are options B, C and D. In example 1, it becomes apparent that Bi-LSTM incorrectly selects option B which resembles option A. This outcome suggests that Bi-LSTM is susceptible to visual similarities and disregards the crucial aspect of compatibility. Subsequently, in example 2, it can be observed that the erroneous selection of CSN could be

primarily attributed to its susceptibility to color influences. This observation intimates that CSN might lack the necessary capacity to effectively capture color compatibility due to its limited expression of visual features. Example 3 demonstrates that MCN can successfully identify options compatible with the candidates. However, these choices do not align with the personal style. Example 4 exemplifies the capability of the proposed model to select options that align with the personal style rather than solely focusing on fashion compatibility. These examples underscore the capacity of the proposed model to holistically consider both fashion compatibility and personalized preferences.

Example	Query	A (GT)	Candidate B	C	D	Result
Example 1						Bi-LSTM: B CSN: A MCN: A FHN: A PSGNet: A
Example 2						Bi-LSTM: D CSN: B MCN: A FHN: A PSGNet: A
Example 3						Bi-LSTM: B CSN: C MCN: C FHN: A PSGNet: A
Example 4						Bi-LSTM: D CSN: C MCN: D FHN: D PSGNet: A

Fig. 5 Four examples of FITB query results

It can be affirmed that the proposed model exhibits effective performance in the FITB task, effectively circumventing the impact of diverse categories while simultaneously incorporating compatibility and user style preferences. Consequently, the findings further substantiate the efficacy of the proposed model in fashion compatibility modeling. To summarize, PSGNet achieves optimized fashion compatibility modeling by extensively integrating multi-modal representations and simultaneously addressing the compatibility relationships between fashion items.

3.4 Ablation study of PSGNet

In order to validate the effectiveness of each component in the proposed model, ablation experiments are conducted by involving the removal of specific modules. Based on PSGNet (the full model), various architecture variants have been developed by ablating components, including the personal style feature extraction module, visual feature extraction module and

textual feature extraction module. The experiments have been performed on the Polyvore-630 dataset, with the accuracy, AUC and NDCG serving as the metrics.

To verify the performance improvements facilitated by the personal style guidance and multi-modal information for personalized outfit recommendations, four comparative experiments are designed.

1) **PSGNet**: training a multi-modal clothing matching model using personal style features to guide both visual and textual inputs.

2) **PSGNet-style**: remove personal style features. Calculate compatibility directly, without a personal style feature extraction module.

3) **PSGNet-text**: remove textual features. Train a recommendation model exclusively based on users' historical images and pre-trained style features, while disregarding textual features.

4) **PSGNet-image**: remove visual features. Train a recommendation model solely using users' historical

textual and personal style features without leveraging visual features.

Results of the ablation study are listed in Table 5. After removing the personal style feature extraction module, the overall performance metric of PSGNet-style decreases by about 0.03, indicating that the personal style is important for representing personalized user preferences. Furthermore, the results also demonstrate that the multi-modal module can substantially enhance the accuracy, AUC and NDCG metrics for personalized outfit recommendations, as compared to using only a single modality (either visual or textual modality). This verifies the complementary role of multi-modal information which can provide richer expressions of user style preferences than a unimodal model in personalized scenarios.

Table 5 Results of ablation experiments

Model	Accuracy	AUC	NDCG
PSGNet	0.881 3	0.887 6	0.823 1
PSGNet-style	0.853 4	0.854 3	0.796 4
PSGNet-text	0.865 6	0.861 8	0.802 5
PSGNet-image	0.832 8	0.819 4	0.768 0

Additionally, ablation studies quantify the contribution of each component. Style features encode personalized preferences, while the multi-modal module generates aesthetically compatible matchings. By incorporating these factors in a balanced manner, PSGNet exhibits strong representational power and potential for expansion. The modularized framework also allows convenient ablation of components to isolate their unique contributions.

In summary, the comparative experiments and ablation studies provide compelling quantitative evidence for the utility of the proposed model in improving personalized outfit recommendations.

4 Conclusions

In summary, the proposed model effectively overcomes the limitations of existing personalized outfit recommendations, making significant progress towards more personalized and accurate outfit recommendations. By modeling personal style features, fashion compatibility relationships and integrating multi-modal fashion item representations, these innovations benefit both individuals and fashion businesses. For individuals, it would improve satisfaction with tailored outfit recommendations; for fashion businesses, it would boost customer engagement, clicks and sales. Based on strong empirical results, integrating personal style guidance and multi-modal learning offers promising directions for further enhancing personalized outfit recommendations.

In subsequent research, more factors like target occasions, environmental conditions and style preferences will be explored to better understand user needs.

Furthermore, the proposed model currently falls short in addressing personalized outfit recommendations for new users. To enhance the model's applicability, efforts will focus on solving the user cold-start problem, perhaps by incorporating objective factors and devising targeted strategies to ensure effective generalization.

References

- [1] CHEN H J, SHUAI H H, CHENG W H. A survey of artificial intelligence in fashion [J]. *IEEE Signal Processing Magazine*, 2023, 40(3) : 64-73.
- [2] CHEN X, CHEN H, XU H, et al. Personalized fashion recommendation with visual explanations based on multi-modal attention network: towards visually explainable recommendation [C]// Proceedings of the 42nd International ACM SIGIR Conference on Research and Development in Information Retrieval. New York, USA: ACM, 2019: 765-774.
- [3] CHENG W H, SONG S J, CHEN C Y, et al. Fashion meets computer vision: a survey [EB/OL]. (2021-01-28) [2024-04-01]. <https://arxiv.org/abs/2003.13988>.
- [4] JEON Y, JIN S, HAN K. FANCY: human-centered, deep learning-based framework for fashion style analysis [C]// Proceedings of the Web Conference 2021. New York, USA: ACM, 2021: 2367-2378.
- [5] LIU Z, LUO P, QIU S, et al. DeepFashion: powering robust clothes recognition and retrieval with rich annotations [C]// Proceedings of IEEE Conference on Computer Vision and Pattern Recognition. New York, USA: IEEE, 2016: 1096-1104.
- [6] HE R N, MCAULEY J. VBPR: visual Bayesian personalized ranking from implicit feedback [J]. *Proceedings of the AAAI Conference on Artificial Intelligence*, 2016, 30(1) : 144-150.
- [7] SONG X M, HAN X J, LI Y K, et al. GP-BPR: personalized compatibility modeling for clothing matching [C]// Proceedings of the 27th ACM International Conference on Multimedia. New York, USA: ACM, 2019: 320-328.
- [8] LU Z, HU Y, YU C, et al. Personalized fashion recommendation with discrete content-based tensor factorization [J]. *IEEE Transactions on Multimedia*, 2023, 25: 5053-5064.
- [9] SAGAR D, GARG J, KANSAL P, et al. PAI-BPR: personalized outfit recommendation scheme with attribute-wise interpretability [C]// 2020 IEEE Sixth International Conference on Multimedia Big Data. New York, USA: IEEE, 2020: 221-230.
- [10] RENDLE S, FREUDENTHALER C, GANTNER Z, et al. BPR: Bayesian personalized ranking

- from implicit feedback [C]//Proceedings of the International Conference on Uncertainty in Artificial Intelligence. [S. l.]: AUAI Press, 2009, 452-461.
- [11] GONG W, KHALID L. Aesthetics, personalization and recommendation: a survey on deep learning in fashion [EB/OL]. (2021-01-20) [2024-04-01]. <https://arxiv.org/abs/2101.08301v1>.
- [12] GU X L, GAO F, TAN M, et al. Fashion analysis and understanding with artificial intelligence [J]. *Information Processing & Management*, 2020, 57(5) : 102276.
- [13] DELDJOO Y, NAZARY F, RAMISA A, et al. A review of modern fashion recommender systems [EB/OL]. (2022-02-06) [2024-04-01]. <https://arxiv.org/abs/2202.02757v3>.
- [14] HAN X T, WU Z X, JIANG Y G, et al. Learning fashion compatibility with bidirectional LSTMs [EB/OL]. (2017-07-08) [2024-04-01]. <http://arxiv.org/abs/1707.05691>.
- [15] MCAULEY J, TARGETT C, SHI Q F, et al. Image-based recommendations on styles and substitutes[EB/OL]. (2015-06-15) [2024-04-01]. <https://arxiv.org/abs/1506.04757v1>.
- [16] SONG X M, FENG F L, LIU J H, et al. NeuroStylist: neural compatibility modeling for clothing matching [C]//Proceedings of the 25th ACM International Conference on Multimedia. New York, USA: ACM, 2017: 753-761.
- [17] CUCURULL G, TASLAKIAN P, VAZQUEZ D. Context-aware visual compatibility prediction [C]//2019 IEEE/CVF Conference on Computer Vision and Pattern Recognition. New York, USA: IEEE, 2019: 12609-12618.
- [18] LIN Y S, MOOSAEI M, YANG H. OutfitNet: fashion outfit recommendation with attention-based multiple instance learning [C]//Proceedings of the Web Conference 2020. New York, USA: ACM, 2020: 77-87.
- [19] FENG Z L, YU Z Y, YANG Y Z, et al. Interpretable partitioned embedding for customized fashion outfit composition[EB/OL]. (2018-06-21) [2024-03-28]. <https://arxiv.org/abs/1806.04845>.
- [20] ZHAN H J, LIN J, AK K E, et al. A^3 -FKG: attentive attribute-aware fashion knowledge graph for outfit preference prediction [J]. *IEEE Transactions on Multimedia*, 2022, 24: 819-831.
- [21] WANG Y Z, LIU L, FU X D, et al. MCCP: multi-modal fashion compatibility and conditional preference model for personalized clothing recommendation [J]. *Multimedia Tools and Applications*, 2024, 83(4) : 9621-9645.
- [22] DING Y J, MOK P Y, MA Y S, et al. Personalized fashion outfit generation with user coordination preference learning [J]. *Information Processing & Management*, 2023, 60 (5) : 103434.
- [23] GODART F C. Why is style not in fashion? Using the concept of ‘style’ to understand the creative industries [M]//JONES C, MAORET M, eds. Research in the Sociology of Organizations. [S. l.]: Emerald Publishing Limited, 2018: 103-128.
- [24] DE DIVITIIS L, BECATTINI F, BAECHI C, et al. Style-based outfit recommendation [C]//2021 International Conference on Content-Based Multimedia Indexing. New York, USA: IEEE, 2021: 1-4.
- [25] SUN Z, ZHOU Y H, HE H H, et al. SGDiff: a style guided diffusion model for fashion synthesis [EB/OL]. (2023-08-15) [2023-11-14]. <https://arxiv.org/abs/2308.07605v1>.
- [26] AN H, LEE K Y, CHOI Y, et al. Conceptual framework of hybrid style in fashion image datasets for machine learning [J]. *Fashion and Textiles*, 2023, 10(1) : 18.
- [27] BANERJEE D, DHAKAD L, MAHESHWARI H, et al. Recommendation of compatible outfits conditioned on style [EB/OL]. (2022-03-30) [2023-11-14]. <https://arxiv.org/abs/2203.16161v1>.
- [28] HE K M, ZHANG X Y, REN S Q, et al. Deep residual learning for image recognition [EB/OL]. (2015-12-10) [2023-11-14]. <https://arxiv.org/abs/1512.03385v1>.
- [29] FRALEY C. How many clusters? Which clustering method? Answers via model-based cluster analysis [J]. *The Computer Journal*, 1998, 41(8) : 578-588.
- [30] SUTSKEVER I, VINYALS O, LE Q V. Sequence to sequence learning with neural networks [EB/OL]. (2014-12-14) [2023-11-06]. <https://arxiv.org/abs/1409.3215>.
- [31] HAN X, WU Z, JIANG Y G, et al. Learning fashion compatibility with bidirectional LSTMs [C]//Proceedings of the 25th ACM International Conference on Multimedia. New York, USA: ACM, 2017: 1078-1086.
- [32] KRIZHEVSKY A, SUTSKEVER I, HINTON G E. ImageNet classification with deep convolutional neural networks [J]. *Communications of the ACM*, 2017, 60(6) : 84-90.
- [33] VASILEVA M I, PLUMMER B A, DUSAD K, et al. Learning type-aware embeddings for fashion compatibility [EB/OL]. (2018-03-25) [2024-01-22]. <https://arxiv.org/abs/1803.09196v2>.
- [34] WANG X, WU B, ZHONG Y. Outfit compatibility prediction and diagnosis with multi-layered comparison network [C]//Proceedings of the 27th ACM International Conference on Multimedia. Nice, France: ACM, 2019: 329-337.

结合多模态时尚兼容性建模和个人风格引导的服装搭配推荐

汪可欣¹, 张洁^{2*}, 张朋², 孙可芯³, 占家美⁴, 魏濛⁴

1. 东华大学 计算机科学与技术学院, 上海 201620

2. 东华大学 人工智能研究院, 上海 201620

3. 东华大学 机械工程学院, 上海 201620

4. 东华大学 信息科学与技术学院, 上海 201620

摘要:个性化服装搭配推荐已经成为时尚领域的一个研究热点。然而,现有的推荐方法尚未充分挖掘用户风格偏好。通常情况下,用户在选择服装时,不仅会倾向于特定风格,如休闲风格或运动风格,还会关注服装的颜色、质地等细节特征。为了推荐符合用户风格偏好的个性化服装搭配,该文提出了一种结合多模态时尚兼容性建模和个人风格引导的服装搭配推荐方法,简称 PSGNet。首先,设计一个风格分类器,将不同服装类型和属性的时尚图像划分到不同的风格类别中;其次,建立个人风格预测模块,通过分析历史数据提取用户风格偏好;再次,为了克服单模态表示的局限性并增强时尚兼容性,利用时尚图像和文本数据来同时提取服装的多模态特征;最后,通过贝叶斯个性化排序(Bayesian personalized ranking, BPR)算法来整合这些模块以统一个人风格和时尚兼容性,其中个人风格特征可引导输出推荐结果,为每位目标用户提供量身定制的个性化服装搭配推荐。在大规模数据集上进行广泛实验。结果表明,该文所提出的方法可有效推荐个性化服装搭配。

关键词:个性化服装搭配推荐;时尚兼容性建模;风格偏好;多模态表示;贝叶斯个性化排序;风格分类器

DOI: 10.19884/j.1672-5220.202404001

Design of Dual-Wavelength Bifocal Metalens Based on Generative Adversarial Network Model

LIU Gangcheng¹, WANG Junkai¹, LIN Sen¹, WU Binhe^{1*}, WANG Chunrui¹, ZHOU Jian², SUN Hao^{2*}

1. College of Physics, Donghua University, Shanghai 201620, China

2. Shanghai Institute of Microsystem and Information Technology, Chinese Academy of Sciences, Shanghai 200050, China

Abstract: Multifocal metalenses are of great concern in optical communications, optical imaging and micro-optics systems, but their design is extremely challenging. In recent years, deep learning methods have provided novel solutions to the design of optical planar devices. Here, an approach is proposed to explore the use of generative adversarial networks (GANs) to realize the design of metalenses with different focusing positions at dual wavelengths. This approach includes a forward network and an inverse network, where the former predicts the optical response of meta-atoms and the latter generates structures that meet specific requirements. Compared to the traditional search method, the inverse network demonstrates higher precision and efficiency in designing a dual-wavelength bifocal metalens. The results will provide insights and methodologies for the design of tunable wavelength metalenses, while also highlighting the potential of deep learning in optical device design.

Keywords: generative adversarial network (GAN); metalens; forward network; inverse design

CLC number: O43

Article ID: 1672-5220(2025)02-0168-09

Document code: A

Open Science Identity
(OSID)



0 Introduction

Metasurfaces, the two-dimensional equivalent of metamaterials, are artificially designed planar optical structures^[1]. Metasurfaces are composed of the meta-atoms arranged periodically at subwavelength scales^[2]. Tailored manipulation^[3-5] targeting specific wavelengths or bands can be achieved through the modification of material properties, thicknesses, geometric parameters and arrangements of meta-atoms. Compared to traditional optical devices, metasurfaces exhibit higher flexibility, compactness and multifunctionality. Therefore, numerous optical components based on metasurfaces have been numerically simulated and experimentally validated, including vortex beams^[6-8], holographic imaging^[9-10],

spectral filtering^[11-12], metalenses^[13-16] and polarization converters^[17-18].

However, in the fields such as optical communications, optical imaging and micro-optics systems, metasurfaces are typically designed to operate at a single wavelength. To achieve independent control of metasurfaces at different wavelengths, researchers have conducted extensive studies. Xu et al.^[19] optimized the structural parameters of the silicon nanorods by using a global optimization algorithm. They established a database covering all phase requirements for two wavelengths, allowing the reconstruction of different holograms for 532 nm *x*-linear-polarized light and 633 nm *y*-linear-polarized light. This method can greatly improve the design efficiency and minimize the cross-talk, but at the cost of time and computational resources. Arbabi et al.^[20] proposed and experimentally demonstrated two-photon fluorescence microscopy with a dual-wavelength metalens working as the objective lens, enabling simultaneous focusing of different wavelengths and improved compactness. Nevertheless, it is currently not feasible to achieve imaging of two wavelengths at arbitrary positions on the focal plane. Qu et al.^[21] demonstrated that, based on the principle of geometric phase modulation, two different types of meta-atoms could be arranged in different subregions to control the focusing performance of two wavelengths. Indeed, employing different types of meta-atoms to control the focusing of two wavelengths could result in inefficient use of design space.

In recent years, significant progress has been made in the field of acquiring target meta-atom structures by using deep learning^[22-26], particularly with the use of generative adversarial networks (GANs)^[27]. GANs consist of two mutually adversarial neural networks, known as the generator and the discriminator, respectively. Based on the original principles of GANs, researchers have proposed a number of GAN variants^[28-31] showing outstanding performance in the field of inverse

Received date: 2024-04-01

Foundation item: National Natural Science Foundation of China (No. 61975029)

* Correspondence should be addressed to WU Binhe, email: bhwu@dhu.edu.cn; SUN Hao, email: sh@mail.sim.ac.cn

Citation: LIU G C, WANG J K, LIN S, et al. Design of dual-wavelength bifocal metalens based on generative adversarial network model[J].

Journal of Donghua University (English Edition), 2025, 42(2): 168-176.

design for meta-atom structures. An et al.^[32] proposed an approach for designing free-form all-dielectric metasurface devices by combining conditional generative adversarial networks (CGANs) and Wasserstein generative adversarial networks (WGANs). Through the inverse networks, they successfully validated optical devices such as a bifocal lens, a polarization-multiplexed deflector, a polarization-multiplexed lens and a polarization-independent lens, demonstrating the versatility of the method.

In this work, we present a design approach based on conditional Wasserstein generative adversarial network-gradient penalty (CWGAN-GP)^[33-34] to achieve an efficient and precise design of a dual-wavelength bifocal metalens. The entire design process consists of a forward network and an inverse network. The forward network would rapidly predict the optical response of the meta-atom structure, while the inverse network would generate meta-atom structures that match the optical response. It is learned that current machine learning models perform well only for in-distribution inverse design, where the target optical response should align with the distribution of the training dataset^[35]. However, the reality is that the target optical responses often do not conform to the distribution of the dataset. To address this issue, a method is proposed to search for curves in an untrained dataset that closely matches the target optical response and input them into the inverse network. The method is compared to a traditional search method. It is expected that the method would solve the problem of in-distribution and enhance the stability of the network.

1 Theoretical Model

1.1 Training dataset

An et al.^[32] indicated that placing thin films with higher refractive indices on substrates with lower refractive indices would enhance the manipulation of light. Without loss of generality, to increase the phase freedom of the dual-wavelength bifocal metalens, the “needle-drop” approach is employed to generate various free-form structures of meta-atoms. The general structure of the meta-atom is shown in Fig. 1, which consists of a free-form silicon pattern and a silicon dioxide substrate, colored in cyan and gray, respectively. The thicknesses of the pattern and the substrate are 982.5 and 800.0 nm, respectively. Each meta-atom has a period of 1 280 nm. Images of free-form structural patterns and their corresponding optical responses are included within the dataset. The shapes of the meta-atoms are described by 32 pixel × 32 pixel images. In the 32 × 32 matrix representation, a pixel value of 0 represents the portion covered by vacuum, while a pixel value of 1 represents the absence of the silicon material. The selected optical response is the complex transmission coefficient S_{21} in the infrared wavelength range (2 400 to 3 000 nm), with 121 uniformly distributed wavelength points. Each

transmission coefficient has real and imaginary parts, resulting in a spectral response vector size of 242 × 1. The finite-difference time-domain (FDTD) methodology is employed for the numerical simulation. Periodic boundary conditions are applied in the x and y directions, while perfectly matched layers (PMLs) are used on the z boundary. A y -polarized plane wave is incident upon the metasurface from the + z direction.

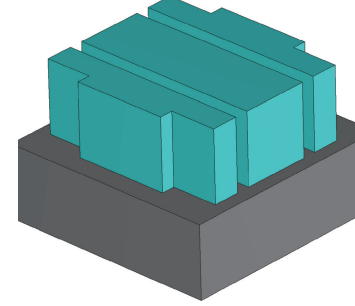


Fig. 1 General structural diagram of meta-atom

1.2 Forward network

The training dataset for the forward network consists of structural images of meta-atoms and their corresponding real and imaginary parts of the complex transmission coefficients. It is further divided into training, validation and test sets. This division enables robust model generalization and comprehensive performance evaluation. Moreover, a mean square error (MSE) serves as the loss function for the forward network, aiming to assess the difference between the target value and the predicted value.

$$L_{\text{pre}} = \frac{1}{N} \sum_{i=1}^N (Y_i - Y'_i)^2, \quad (1)$$

where L_{pre} is the loss function; Y_i is the target value; Y'_i is the predicted value; N is the number of data.

The loss function calculates the partial derivatives of the model parameters, and uses the gradient descent algorithm to update the model weights in the parameter space along the opposite direction of the gradient. As the number of training times increases, the loss function gradually decreases and the model gradually fits the training data. Continuously adjusting the model weight parameters to minimize the loss function or reduce the difference between the target value and the predicted value is the goal of the entire process. The whole architecture model of the forward network consists of eight convolutional layers, four pooling layers and three fully connected layers, as shown in Fig. 2. The model fits best when there are eleven layers in our model. There are batch normalization layers and ReLU activation functions with max-pooling layers interleaved between every other convolutional layer. These light yellow modules represent the convolutional and fully connected layers, yellow modules indicate the batch normalization layers, light blue modules signify the activation function layers, and the red modules represent the max-pooling layers.

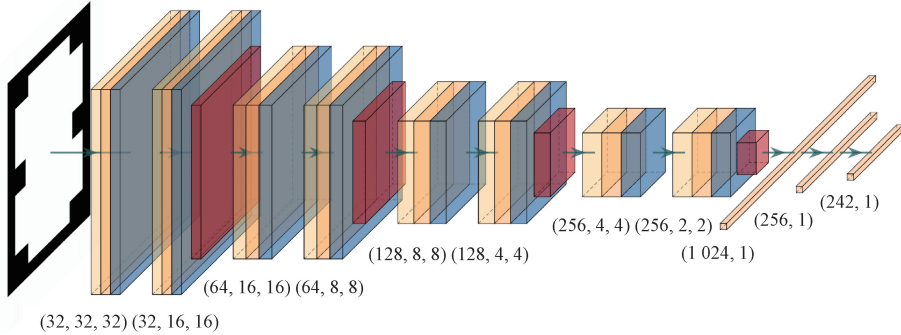


Fig. 2 Architecture of forward network

1.3 Inverse network

Using the CWGAN-GP method to reversely design the target spectrum has many advantages. On the one hand, compared with traditional GANs, CWGAN-GP uses the Wasserstein distance to distinguish images, resulting in more accurate results. On the other hand, the gradient penalty makes the entire inverse network more stable and can achieve outstanding convergence in a shorter training time. In terms of training methods, the discriminator is trained three times and the generator is trained once. It should be noted that the GAN model is trained on a dataset composed of 30 000 meta-atoms. The proposed inverse network trains a generator G that maps a set of design conditions, $\mathbf{x} = [\operatorname{Re}(S_{21}) \operatorname{Im}(S_{21})]$, combined with a noise vector \mathbf{z} to produce a target design \mathbf{y}' . Herein $\mathbf{y}' = G(\mathbf{z} | \mathbf{x})$. The discriminator D calculates the Wasserstein distance between the real samples \mathbf{y} and \mathbf{y}' , and it inversely tunes the parameters within the generator/discriminator network to minimize/maximize the Wasserstein distance by using a gradient algorithm. The optimization function is

$$(P_{\text{data}}, P_G) \approx \max_d \left\{ E_{\mathbf{y} \sim P_{\text{data}}} [D(\mathbf{y} | \mathbf{x})] - E_{\mathbf{y}' \sim P_G} [D(\mathbf{y}' | \mathbf{x})] - \lambda E_{\hat{\mathbf{R}} \sim P_{\hat{\mathbf{R}}}} [\max(0, \| \nabla_{\hat{\mathbf{R}}} D(\hat{\mathbf{R}} | \mathbf{x}) \| - 1)] \right\}, \quad (2)$$

$$\hat{\mathbf{R}} = \tau \times \mathbf{y} + (1 - \tau) \times \mathbf{y}', \quad (3)$$

where P_{data} is the distribution of real sample data; P_G is the distribution of generated sample data; $\hat{\mathbf{R}}$ is the interpolation between real and fake samples; τ is any real number between 0 and 1; $E_{\mathbf{y} \sim P_{\text{data}}} [D(\mathbf{y} | \mathbf{x})]$ denotes the discriminator's expectation over the real data distribution; $E_{\mathbf{y}' \sim P_G} [D(\mathbf{y}' | \mathbf{x})]$ denotes the discriminator's expectation over the fake data

distribution; $\lambda E_{\hat{\mathbf{R}} \sim P_{\hat{\mathbf{R}}}} [\max(0, \| \nabla_{\hat{\mathbf{R}}} D(\hat{\mathbf{R}} | \mathbf{x}) \| - 1)]$ is a gradient penalty term used to enforce the Lipschitz continuity condition on the discriminator and λ is a hyperparameter controlling the strength of the penalty.

It has been discerned from relevant studies that the current machine learning models can only work well for an in-distribution inverse design where the target optical

responses should follow a similar distribution of the training dataset. However, when designing the metasurface, target optical responses often do not conform to a similar distribution. One possible approach is to select the optical response closest to the target value from the untrained dataset and input it into the network to ensure a similar distribution. Subsequently, the inverse network generates multiple structures that meet the target optical response. There is a high probability that these structures will satisfy the phase information of the dual-wavelength bifocal metasurface. Figure 3 illustrates the entire design architecture.

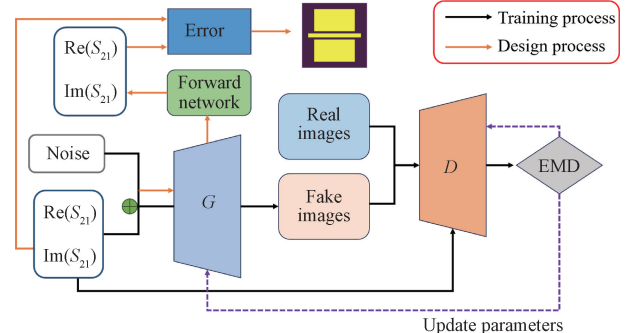


Fig. 3 Training process of neural network model and reverse design process of metasurface
EMD—earth mover's distance.

2 Design of Dual-Wavelength Bifocal Metalens

2.1 Forward network training and prediction results

In general, both the quantity and quality of training samples have a significant impact on the performance of deep learning models. When the number of training samples is either too small or too large, it can lead to inaccurate predictions. To highlight the predictive capability of the forward network, the training set consists of 60 000 samples, while the validation and test datasets each contain 4 000 samples. During the training process, numerous hyperparameters were evaluated. Ultimately, a batch size of 64 and a learning rate of 1×10^{-4} were selected, with the Adam optimizer being employed for weight training and optimization.

The training and validation loss curves during the training process of the forward network are displayed in Fig. 4. At 5 000 epochs, both curves converge smoothly, indicating the successful completion of the prediction task for the optical response of the meta-atom structures by the forward network.

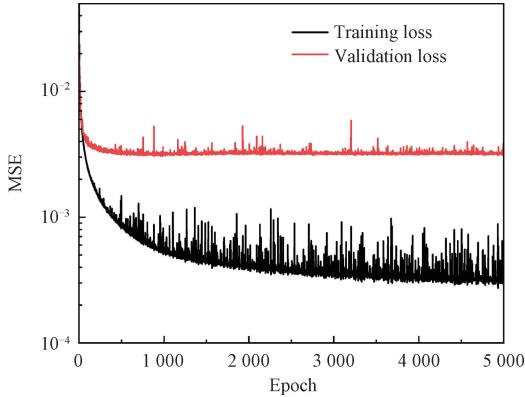


Fig. 4 Loss curves during training process of forward network

To demonstrate the model generalization ability to new data, the untrained test set was used for predictions. Since the real and imaginary parts of the complex transmission coefficients are contained in the output of the forward network, they are converted into amplitude and phase:

$$S_{\text{amp}} = \sqrt{\text{Im}(S_{21})^2 + \text{Re}(S_{21})^2}, \quad (4)$$

$$S_{\text{pha}} = \arctan \frac{\text{Im}(S_{21})}{\text{Re}(S_{21})}, \quad (5)$$

where S_{amp} is the amplitude; S_{pha} is the phase.

Figure 5 shows the comparison between the predicted results for the forward network and the numerically simulated results for four structures (shown in the insets). It can be clearly seen that the curves predicted by the forward network for the meta-atoms are almost identical to those of the simulated results. Hence, the excellent predictive performance of the forward network would contribute significantly to the design of a dual-wavelength bifocal metalens.

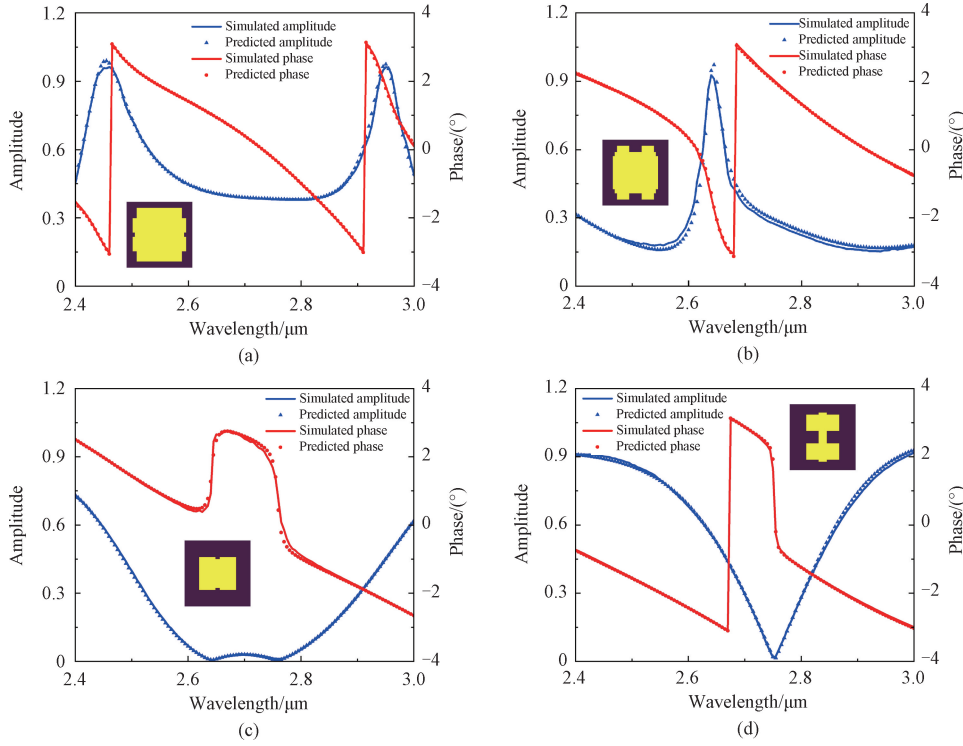


Fig. 5 Comparisons of predicted and numerically simulated amplitude-phase curves

2.2 Design results of dual-wavelength bifocal metalens

Our design goal is to achieve focusing at different positions on the focal plane with a focal length of 30 μm at two wavelengths. As shown in Fig. 6, the blue arrow indicates the propagation path of light at a wavelength of 2.4 μm . After modulation by the meta-atoms, the light

focuses on the first quadrant. Similarly, the orange arrow represents the propagation path of light at a wavelength of 2.8 μm , with its focal point located in the third quadrant. Depending on the focal position, we can clearly distinguish different wavelengths. In the initial design phase, it is critical to calculate the phase profiles

on the metalens, as they define the phase distribution across the surface. The theoretical phase profiles at different wavelengths are shown in Fig. 7, with a phase range from 0 to 2π . The theoretical phase profile is calculated by

$$\varphi_m(x, y) = \frac{2\pi}{\lambda_m} \left(f - \sqrt{(x - x_1)^2 + (y - y_1)^2 + f^2} \right), \\ m = 1, 2, \quad (6)$$

where $\varphi_m(x, y)$ is the theoretical phase profile; λ_m is the wavelength; f is the focal length; (x_1, y_1) is the coordinate position of the focus. According to the phase information, meta-atoms that meet the phase conditions are arranged into a 31×31 square matrix. The final size of the metalens is $39.68 \mu\text{m} \times 39.68 \mu\text{m}$.

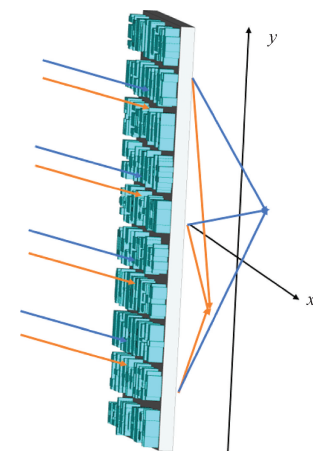


Fig. 6 Schematic diagram of dual-wavelength bifocal metalens

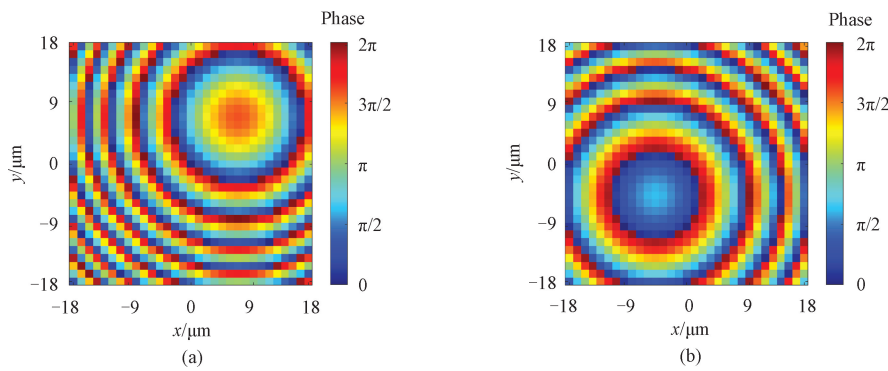


Fig. 7 Theoretical phase profiles of dual-wavelength bifocal metalens at different wavelengths: (a) $2.4 \mu\text{m}$; (b) $2.8 \mu\text{m}$

The workflow for designing the dual-wavelength bifocal metalens is as follows. Firstly, calculate the target phase profiles at two wavelengths. Secondly, select the optical response curve that is closest to the theoretical value from the untrained dataset, input it into the inverse network to generate multiple structural patterns, and perform symmetry processing. Thirdly, use the generated patterns as input to the forward network to obtain their optical responses in a short time. Finally, filter and array these meta-atoms to determine the structure of the metalens. The results of two examples are shown in Fig. 8. Figures 8(a) and 8(c) present 25 meta-atom structures generated to meet different target responses for examples 1 and 2, respectively. Figures 8(b) and 8(d) represent the amplitude and phase distributions of these structures at different wavelengths for examples 1 and 2, respectively, where the red solid line is the theoretically calculated phase at a wavelength of $2.4 \mu\text{m}$, and the blue solid line is the theoretically calculated phase at a wavelength of $2.8 \mu\text{m}$. In each polar plot, two red dots represent the amplitude and phase values of the input target curve at two wavelengths. Obviously, they are respectively close to the two target phase values. Near the red dots, the surrounding black dots represent the predicted amplitudes and phases at different wavelengths

for the meta-atom structures generated by the inverse network. Since we only consider phase information, the structure closest to the theoretical phase is selected as the component of the metalens from the structures corresponding to the black points.

To demonstrate the superiority of deep learning over the traditional search method, a comparative analysis was conducted. The traditional search method relies on the dataset to query target meta-atoms, which not only fails to generate new structures but also heavily depends on the diversity of the dataset for its search results. When the dataset lacks certain specific types of structures, this method may be unable to effectively explore and generate these structures. Therefore, the search process requires substantial computational resources and time, leading to high computational costs and low search efficiency. Figures 9(a) and 9(b) depict the normalized light intensity distribution of the dual-wavelength bifocal metalens at the focal plane generated by the traditional search method. Figures 9(c) and 9(d) depict the normalized light intensity distribution of the dual-wavelength bifocal metalens at the focal plane generated by deep learning. It is clearly observed that the metalens generated by deep learning has a better focusing effect and a more accurate focusing position.

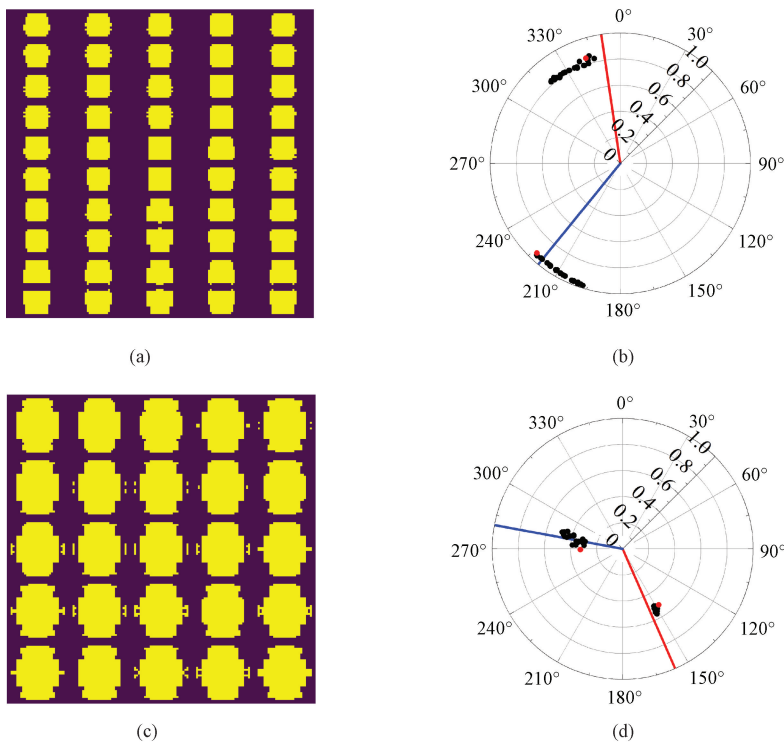


Fig. 8 Comparisons of predicted results and target values of meta-atoms generated by inverse network; (a) meta-atoms generated by inverse network of example 1; (b) amplitude and phase distributions at two wavelengths of example 1; (c) meta-atoms generated by inverse network of example 2; (d) amplitude and phase distributions at two wavelengths of example 2

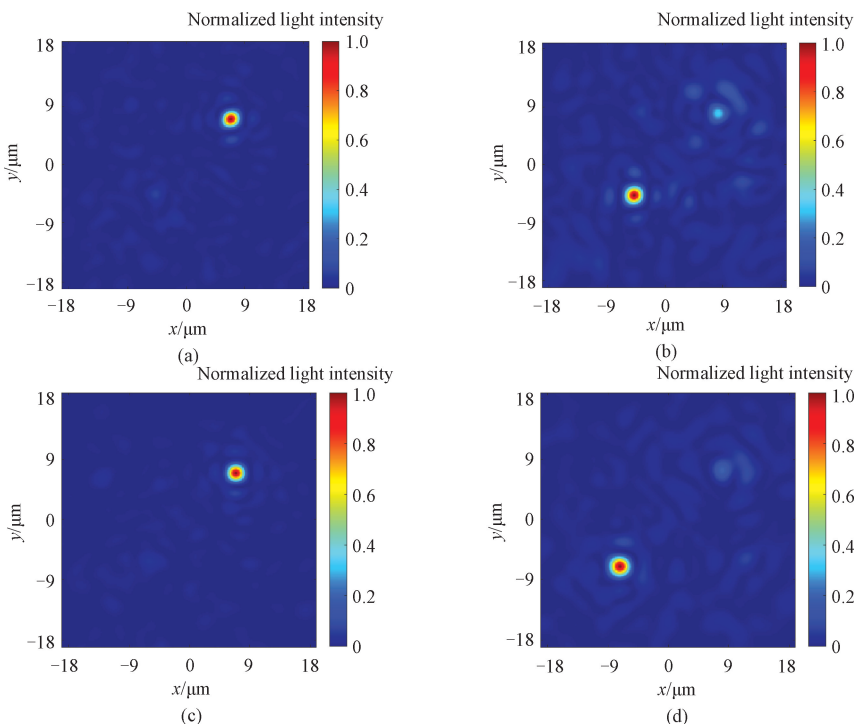


Fig. 9 Comparisons of normalized light intensity for dual-wavelength bifocal metalens designed; (a) 2.4 μm by traditional search method; (b) 2.8 μm by traditional search method; (c) 2.4 μm by deep learning; (d) 2.8 μm by deep learning

A clearer comparison method is to observe the focus intensity distribution along the x and z directions.

Figures 10(a) and 10(b) illustrate the normalized light intensity distribution along the x and z directions at

wavelengths of 2.4 μm and 2.8 μm . The result of the deep learning shows a higher light intensity and a higher accuracy. At both wavelengths, the dual-wavelength bifocal metalens generated by the inverse network exhibits a more pronounced and concentrated light intensity distribution, emphasizing the excellence of the inverse network. With the learning and

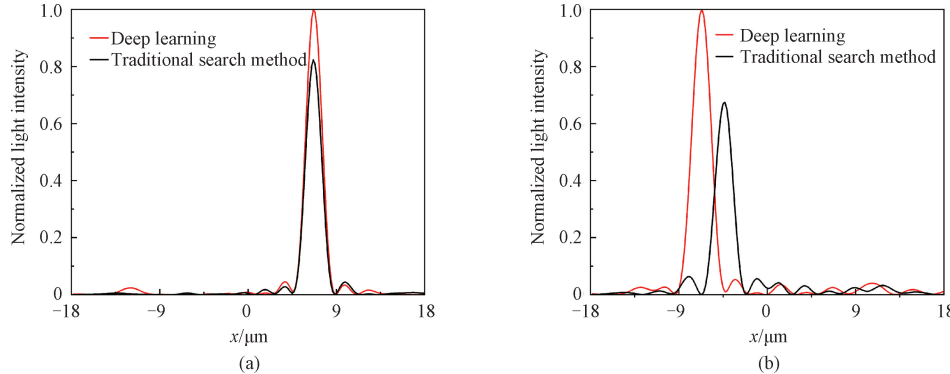


Fig. 10 Comparisons of normalized light intensity along x and z directions at different wavelengths: (a) 2.4 μm ; (b) 2.8 μm

3 Conclusions

A deep generative adversarial network composed of a forward network and an inverse network is proposed for designing a dual-wavelength bifocal metasurface, which is capable of rapidly generating meta-atoms to meet phase requirements at two wavelengths. Taking into account the advantages of current deep learning methods in in-distribution inverse design, the method that directly selects optical responses closest to the target values from the untrained dataset as inputs to the inverse network has been proposed. Compared with the traditional search method, the dual-wavelength bifocal metasurface designed by the reverse network has a better focusing effect in terms of light intensity and a more accurate design target position. To achieve the design goal, the method still needs to rely on the original dataset. In the future, we would further explore the application of deep generative models to optical design, focusing particularly on developing improved methods to address situations where inverse design models cannot be directly applied.

References

- [1] YU N F, GENEVET P, KATS M A, et al. Light propagation with phase discontinuities: generalized laws of reflection and refraction [J]. *Science*, 2011, 334(6054): 333-337.
- [2] KIM J, YANG Y, BADLOE T, et al. Geometric and physical configurations of meta-atoms for advanced metasurface holography [J]. *InfoMat*, 2021, 3(7): 739-754.
- [3] YU Y F, ZHU A Y, PANIAGUA-DOMÍNGUEZ R, et al. High-transmission dielectric metasurface optimization capabilities of neural networks, deep learning can not only automatically learn the relationship between complex meta-atom structures and optical responses but also improve the accuracy and efficiency of reverse design. Therefore, the deep learning exhibits greater flexibility and intelligence in optical device design.
- [4] OVERVIG A C, SHRESTHA S, MALEK S C, et al. Dielectric metasurfaces for complete and independent control of the optical amplitude and phase [J]. *Light: Science & Applications*, 2019, 8: 92.
- [5] WANG H L, MA H F, CHEN M, et al. A reconfigurable multifunctional metasurface for full-space control of electromagnetic waves [J]. *Advanced Functional Materials*, 2021, 31(25): 2100275.
- [6] YUE F Y, WEN D D, XIN J T, et al. Vector vortex beam generation with a single plasmonic metasurface [J]. *ACS Photonics*, 2016, 3(9): 1558-1563.
- [7] ZHANG L, LI J S. Vortex beam generator working in terahertz region based on transmissive metasurfaces [J]. *Optik*, 2021, 243: 167452.
- [8] AHMED H, KIM H, ZHANG Y B, et al. Optical metasurfaces for generating and manipulating optical vortex beams [J]. *Nanophotonics*, 2022, 11(5): 941-956.
- [9] HUANG L L, ZHANG S, ZENTGRAF T. Metasurface holography: from fundamentals to applications [J]. *Nanophotonics*, 2018, 7(6): 1169-1190.
- [10] NI X J, KILDISHEV A V, SHALAEV V M. Metasurface holograms for visible light [J]. *Nature Communications*, 2013, 4: 2807.
- [11] PARK C S, SHRESTHA V R, YUE W J, et al. Structural color filters enabled by a dielectric metasurface incorporating hydrogenated amorphous silicon nanodisks [J]. *Scientific*

- Reports*, 2017, 7: 2556.
- [12] HAN X, FAN Z Y, LIU Z Y, et al. Inverse design of metasurface optical filters using deep neural network with high degrees of freedom [J]. *InfoMat*, 2021, 3(4): 432-442.
- [13] KHORASANINEJAD M, CHEN W T, DEVLIN R C, et al. Metalenses at visible wavelengths: diffraction-limited focusing and subwavelength resolution imaging [J]. *Science*, 2016, 352 (6290): 1190-1194.
- [14] CHEN W T, ZHU A Y, SANJEEV V, et al. A broadband achromatic metalens for focusing and imaging in the visible [J]. *Nature Nanotechnology*, 2018, 13: 220-226.
- [15] ARBABI A, FARAOON A. Advances in optical metalenses[J]. *Nature Photonics*, 2023, 17: 16-25.
- [16] YANG M Y, SHEN X, LI Z P, et al. High focusing efficiency metalens with large numerical aperture at terahertz frequency [J]. *Optics Letters*, 2023, 48(17): 4677.
- [17] POUYANFAR N, NOURINIA J, GHOBADI C. Multiband and multifunctional polarization converter using an asymmetric metasurface [J]. *Scientific Reports*, 2021, 11: 9306.
- [18] WANG P, ZHANG Y, WANG Y, et al. Multifunctional polarization converter based on multilayer reconfigurable metasurface [J]. *Defence Technology*, 2023, 28: 136-145.
- [19] XU P, XIAO Y F, HUANG H X, et al. Dual-wavelength hologram of high transmittance metasurface[J]. *Optics Express*, 2023, 31(5): 8110.
- [20] ARBABI E, LI J Q, HUTCHINS R J, et al. Two-photon microscopy with a double-wavelength metasurface objective lens[J]. *Nano Letters*, 2018, 18(8): 4943-4948.
- [21] QU J Q, LUO H J, YU C Y. Dual-wavelength polarization-dependent bifocal metalens for achromatic optical imaging based on holographic principle [J]. *Sensors*, 2022, 22(5): 1889.
- [22] AN S S, FOWLER C, ZHENG B W, et al. A deep learning approach for objective-driven all-dielectric metasurface design [J]. *ACS Photonics*, 2019, 6(12): 3196-3207.
- [23] NOH J, NAM Y H, SO S, et al. Design of a transmissive metasurface antenna using deep neural networks[J]. *Optical Materials Express*, 2021, 11(7): 2310.
- [24] FOWLER C, AN S, ZHENG B, et al. Deep learning for metasurfaces and metasurfaces for deep learning[M]//Advances in Electromagnetics Empowered by Artificial Intelligence and Deep Learning. New York, USA: IEEE, 2023: 319-343.
- [25] AN S S, ZHENG B W, SHALAGINOV M Y, et al. Deep learning modeling approach for metasurfaces with high degrees of freedom [J]. *Optics Express*, 2020, 28(21): 31932.
- [26] NADELL C C, HUANG B H, MALOF J M, et al. Deep learning for accelerated all-dielectric metasurface design [J]. *Optics Express*, 2019, 27(20): 27523.
- [27] WANG J K, LIN S, LIU G C, et al. Reverse design of metasurface based on generative adversarial network model [J]. *Journal of Donghua University (Natural Science)*, 2024, 50(5): 61-68. (in Chinese)
- [28] YEUNG C, TSAI R, PHAM B, et al. Global inverse design across multiple photonic structure classes using generative deep learning [J]. *Advanced Optical Materials*, 2021, 9 (20): 2100548.
- [29] KIANI M, KIANI J, ZOLFAGHARI M. Conditional generative adversarial networks for inverse design of multifunctional metasurfaces [J]. *Advanced Photonics Research*, 2022, 3 (11): 2200110.
- [30] QIU Y H, CHEN S X, HOU Z Y, et al. Chiral metasurface for near-field imaging and far-field holography based on deep learning [J]. *Micromachines*, 2023, 14(4): 789.
- [31] WANG H P, CAO D M, et al. Inverse design of metasurfaces with customized transmission characteristics of frequency band based on generative adversarial networks [J]. *Optics Express*, 2023, 31(23): 37763.
- [32] AN S S, ZHENG B W, TANG H, et al. Multifunctional metasurface design with a generative adversarial network [J]. *Advanced Optical Materials*, 2021, 9(5): 2001433.
- [33] MIRZA M, OSINDERO S. Conditional generative adversarial nets[EB/OL]. (2014-11-06) [2024-02-05]. <https://arxiv.org/pdf/1411.1784.pdf>.
- [34] GULRAJANI I, AHMED F, ARJOVSKY M, et al. Improved training of Wasserstein GANs [EB/OL]. (2017-12-25) [2024-02-05]. <https://arxiv.org/pdf/1704.00028.pdf>.
- [35] MA T G, TOBAH M, WANG H Z, et al. Benchmarking deep learning-based models on nanophotonic inverse design problems[J]. *Opto-Electronic Science*, 2022, 1(1): 210012.

基于生成对抗网络模型的双波长双聚焦超透镜设计

刘港成¹, 王军凯¹, 林 森¹, 伍滨和^{1*}, 王春瑞¹, 周 健², 孙 浩^{2*}

1. 东华大学 物理学院, 上海 201620

2. 中国科学院 上海微系统与信息技术研究所, 上海 200050

摘要: 多焦点超透镜在光通信、光学成像和显微光学等领域具有重要价值, 然而其设计具有极大的挑战性。近年来, 深度学习方法为光学平面器件的设计提供了新的解决方案。该文提出了一种使用生成对抗网络 (generative adversarial network, GAN) 来实现双波长下不同聚焦位置的超透镜设计方法。该方法包括前向网络和逆向设计网络。前者用于快速预测超原子结构的光学响应, 后者自动生成符合需求的超原子结构。与传统搜索方法相比, 逆向设计网络在设计双波长双聚焦超透镜时具有更高的准确性和效率。这些结果将为可调波长超透镜的设计提供思路和方法, 突显了深度学习在光学器件设计中的潜力。

关键词: 生成对抗网络; 超透镜; 前向网络; 逆向设计

DOI: 10.19884/j.1672-5220.202403004

Context-Aware Visual Entailment Driven by Specific Instructions

HAN Yufeng^{1, 2}, HAO Kuangrong^{1, 2*}, TANG Xuesong^{1, 2}, WEI Bing^{1, 2}

1. College of Information Science and Technology, Donghua University, Shanghai 201620, China

2. Engineering Research Center of Digitized Textile and Apparel Technology, Ministry of Education, Donghua University, Shanghai 201620, China

Abstract: Visual entailment (VE) is a prototypical task in multimodal visual reasoning, where current methods frequently utilize large language models (LLMs) as the knowledge base to assist in answering questions. These methods heavily rely on the textual modality, which inherently cannot capture the full extent of information contained within images. We propose a context-aware visual entailment (CAVE) model, which introduces a novel aggregation module designed to extract high-level semantic features from images. This module integrates lower-level semantic image features into high-level visual tokens, formatting them similarly to text tokens so that they can serve as inputs for LLMs. The CAVE model compensates for the loss of image information and integrates it more effectively with textual comprehension. Additionally, the CAVE model incorporates a new input format and training methodology, which is rooted in instruction tuning and in-context learning techniques. The objective of this research is to maximize the inherent logical reasoning capabilities of LLMs. Experimental results on the E-SNLI-VE dataset show that the proposed CAVE model exhibits outstanding performance.

Keywords: visual entailment (VE); textual-visual integration; instruction tuning; in-context learning

CLC number: TP181

Document code: A

Article ID: 1672-5220(2025)02-0177-10

Open Science Identity
(OSID)



0 Introduction

Multimodal visual reasoning^[1-6] refers to a method that leverages multimodal information for answering visual questions. It aims to understand and reason about images by jointly encoding and learning the associations between visual and linguistic cues. Currently, there are three paradigms of multimodal visual reasoning models.

1) Explainer-based explicit models^[7-10]. These models utilize convolutional neural networks (CNNs)^[11] to extract prominent image features and incorporate attention mechanisms to prioritize the image features that

are pertinent to the question. They explicitly model the logical relationship between the image and the text question, and predict reasons using an explainer such as long short-term memory (LSTM)^[12] or generative pre-trained transformer 2 (GPT-2)^[13].

2) Two-stage pre-trained transformer models^[2,14-17]. These models consist of a pre-training stage followed by fine-tuning. Initially, they learn the joint semantic features of images and texts through contrastive learning on a large-scale and noisy dataset of image-text pairs. Then, they undergo fine-tuning using high-quality annotated data from specific downstream tasks. These models significantly improve performance and generalizability but remain close-set and domain-dependent, with limited answer diversity and a tendency to generate only short texts linked to predefined visual-textual tasks.

3) Fine-tuning large-scale language models^[3,18-21]. These models utilize powerful pre-trained language models (such as GPT-3^[22]) to adjust to different scenarios and needs in multimodal applications. Gui et al.^[18] and Lin et al.^[19] proposed novel architectures that utilized GPT-3 as a knowledge engine to assist in multimodal visual reasoning, even though they functioned solely in the domain of text-based question answering. However, relying only on captions without direct image analyses can lead to the model erroneously determining the entailment relationship between texts and images. Insufficient or misleading information within captions might cause the model to inappropriately classify a text as not entailing or irrelevant to an image. For example, this occurs when a crucial detail in the image is left out of the caption but is mentioned in the text. Consequently, the model may make judgments based solely on caption data, potentially misinterpreting the true visual-linguistic alignment.

To address this issue, we propose an aggregation module that extracts high-level semantic features from images as visual tokens, aligning the image and text domains. This implicit approach aims to alleviate the challenges posed by visual ambiguities and missing

Received date: 2024-03-12

Foundation items: Fundamental Research Funds for the Central Universities, China (No. 2232021A-10); Shanghai Pujiang Program, China (No. 22PJ1423400)

* Correspondence should be addressed to HAO Kuangrong, email: krhao@dhu.edu.cn

Citation: HAN Y F, HAO K R, TANG X S, et al. Context-aware visual entailment driven by specific instructions [J]. *Journal of Donghua University (English Edition)*, 2025, 42(2): 177-186.

semantic information, ensuring a more comprehensive understanding of the interplay between visual content and textual description. We enhance the model's logical reasoning ability by utilizing specific instructions and in-context learning techniques to leverage the text reasoning power of large language models (LLMs) in multimodal tasks. The contrastive language-image pre-training (CLIP)^[23] and the aggregation layer jointly operate as an image encoder, effectively transforming images into visual tokens. Vicuna^[24] is used as a text decoder, with inputs that include visual tokens, image captions, hypotheses and answers. These elements are meticulously adjusted according to specific instructions to construct coherent and comprehensive sentences. These sentences are then input into Vicuna to generate the predicted answer.

Overall, the contributions are as follows.

1) A novel context-aware visual entailment (CAVE) model is presented, which integrates CLIP and Vicuna,

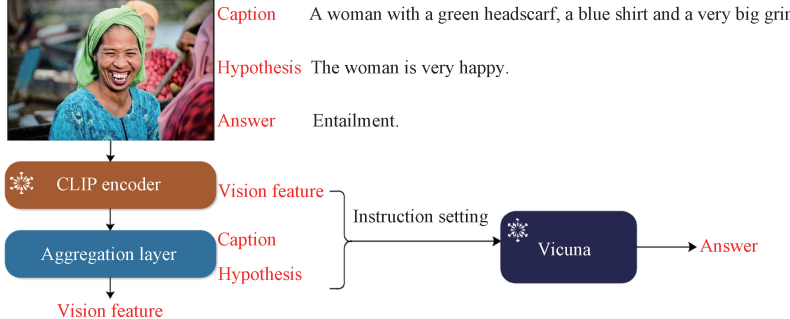


Fig. 1 An illustrative overview of the proposed CAVE model

Researchers encoded images and questions to obtain joint features, learned attentional characteristics from questions to images, and used LSTM to predict reasons^[7-8]. Thomas et al.^[9] employed multi-instance learning to make fine-grained predictions of the logical relationships between knowledge elements in images and texts. Although this method demonstrates the modeling of semantic relationships between images and texts, the explainable generator falls short in its ability to comprehend the global context and interact with it effectively, resulting in suboptimal integration of cross-modal information.

1.2 Two-stage pre-trained transformer models

Researchers have made significant advancements in recent years within the field of artificial intelligence, particularly at the intersection of natural language processing (NLP) and computer vision (CV)^[14-15, 17]. These models typically consist of two main stages: pre-training and fine-tuning. In the pre-training stage, the model is trained using large-scale unlabeled or weakly-labeled pairs of images and texts, often sourced from the Internet or other extensive datasets where there may be some association between the images and texts, but not always precise alignment. The primary goal during this stage is to enable the model to learn joint semantic features between images and texts. This is commonly achieved through contrastive learning, where the model learns to

and this model converts a classification task into a generation task.

2) An aggregation module is proposed, which extracts high-level semantic features from images, converting them into virtual tokens, thereby aligning the image and text modules.

3) An efficient instruction is designed for input samples, and in-context learning is utilized during the training process to optimize and enhance model performance.

4) The proposed model has been experimentally validated and its substantial performance on the E-SNLI-VE dataset^[25] has been demonstrated.

1 Related Works

1.1 Explainer-based explicit models

Figure 1 provides an illustrative overview of the proposed CAVE model.

distinguish between matching image-text pairs and non-matching pairs. To achieve this, the model creates an embedding space where corresponding image and text representations are brought closer together, while disparate ones are pushed apart. During the fine-tuning stage, the model is trained using high-quality annotated data for downstream tasks. These tasks usually relate to specific application scenarios such as image captioning, visual question answering (VQA), and image retrieval. At this stage, the model adjusts its parameters based on the task requirements to optimize performance on that particular dataset. While these models have shown improvements in both performance and generalization, they still have certain limitations. Notably, neural networks tend to be closed-set and domain-dependent. It means that they are good at new tasks which are similar to those encountered during training. However, their performance may deteriorate when faced with tasks that are substantially different from the distribution of the training data.

1.3 Fine-tuning large-scale language models

In the realm of multi-modal visual reasoning, several methods leveraging LLMs have emerged, such as in VQA tasks where Yang et al.^[26] used captions generated from images and questions directly inputted into the LLM to produce answers. Additionally, Gui et al.^[18] and Lin et al.^[19] utilized the knowledge about questions

and captions within the LLM to serve as candidate justifications for assisting in the training of VQA models. However, captions provide limited descriptions that fail to capture the full informational content of an image. Therefore, we propose a novel aggregation module to extract higher-level semantic features from images, compensating for the information gap in captions. Simultaneously, we explore a new input scheme and training strategy based on specific instructions and in-context learning to fully leverage the understanding and reasoning capabilities of LLMs in completing visual entailment (VE) tasks.

2 Methods

2.1 Problem description

Given an image I as the premise, a simple caption of

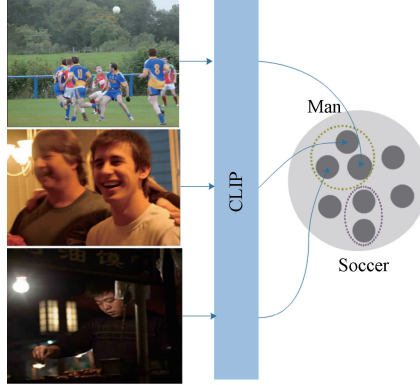


Fig. 2 Overall architecture of the proposed CAVE model

2.2.1 Aggregation-based image encoding

The model is built upon the foundation of CLIP's image encoder and an innovative aggregation network. CLIP, introduced by Radford et al.^[23] in 2021, is a self-supervised learning framework that excels particularly in image classification tasks. This model integrates an image encoder and a text decoder. Through large-scale training on aligned image-text pairs, it achieves instance-level cross-modal feature matching, demonstrating remarkable generalization capabilities. Within this module, we utilize the CLIP image encoder f_{CLIP} to extract visual features v , and mathematically express its application as

$$v = f_{\text{CLIP}}(I), \quad (1)$$

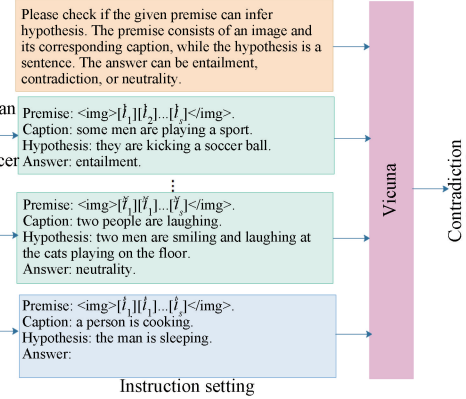
where $v \in \mathbf{R}^{N_1 \times D}$ represents the un-pooled features from the last layer of the CLIP image encoder that is flattened out; N_1 and D represent the dimensions of v . These patch-level features provide rich semantic information as input to the downstream aggregation project module.

VE tasks demand a more comprehensive set of image features to provide the necessary context for determining whether a hypothesis holds, necessitating further refinement of high-level semantic visual features and effective mapping of these into the textual feature space.

the image c , and a sentence h as the hypothesis, the goal is to determine whether the image semantically entails, neutral concerning or contradicts the hypothesis. There are three possible outcomes a : entailment, neutrality and contradiction. Consequently, each instance in the dataset can be denoted as a tuple $\{I, c, h, a\}$.

2.2 Model architecture

The proposed CAVE model consists of three key components: an aggregation-based image encoder which includes a CLIP encoder and an aggregation layer; a context-aware text decoder consisting of Vicuna and several contextual samples; an instruction-guided cross-modal information integration operation. The overall architecture of the proposed CAVE model is illustrated in Fig. 2, where $I_1^i, I_2^i, \dots, I_s^i$ ($i=1, 2, \dots, N$) denote the i th given image patch features, and $I_1^r, I_2^r, \dots, I_s^r$ denote the image patch features for inference.



We design an innovative aggregation mapping architecture, as depicted in Fig. 3, which incorporates two complementary pathways. On one pathway, a linear transformation layer $\text{FC}(\cdot)$, followed by a softmax function $\text{Softmax}(\cdot)$ and a transpose operation, is employed to perform the process of feature selection and aggregation, thereby yielding a feature selection matrix $m \in \mathbf{R}^{N_2 \times N_1}$, where N_1 and N_2 represent the dimensions of m .

$$m = \text{Softmax}(\text{FC}(v))^T. \quad (2)$$

This matrix effectively condenses the essential information from the image into a structured representation that can be more closely aligned with the textual modality. On the other pathway, the multi-layer perceptron is used to support the deep transformation of features, enhancing their expressive capacity and generating candidate features $v_{\text{can}} \in \mathbf{R}^{N_1 \times D}$.

$$v_{\text{can}} = \text{MLP}(v), \quad (3)$$

where MLP refers to a function that transforms the input features v into more expressive features v_{can} .

This component enhances the feature selection process by incorporating a non-linear mapping that can capture more intricate relationships within the visual data.

The multi-layer perceptron essentially refines these image features into semantically richer representations, ensuring that they carry sufficient information for accurate entailment judgment when integrated with textual information in the context of VE tasks. Ultimately, the outputs from both pathways are combined to produce a novel aggregated feature representation $v_a \in \mathbf{R}^{N_2 \times D}$.

$$v_a = m \cdot v_{\text{can}}. \quad (4)$$

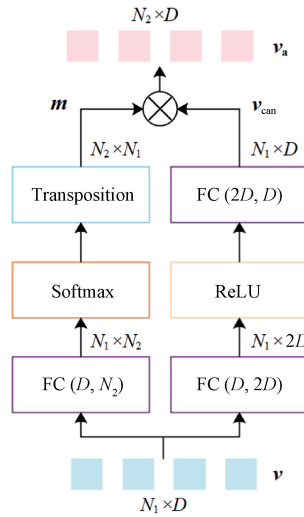


Fig. 3 Illustration of aggregation mapping module

2.2.2 Context-aware text decoding

With an extremely large number of parameters, the Vicuna model boasts an enhanced capacity for representation learning when tackling complex text understanding and generation tasks. The larger model capacity enables it to capture a broader range of linguistic rules, patterns and subtle semantic distinctions, thereby increasing the likelihood of generating high-quality text output. During its construction, the Vicuna model leverages vast amounts of diverse and heterogeneous textual data for pre-training, covering a wide array of topics and domains. This ensures that the model develops a profound understanding and broad adaptability to various types of textual content. Vicuna model is favored for its superior in-context learning ability and task adaptiveness. It can learn from just a few examples of input-output pairs without requiring fine-tuning when transferred to new tasks. The key to the LLM's performance lies in its attention layers, which facilitate an implicit parameter optimization process during inference, similar to explicit optimization through gradient descent during fine-tuning. Building upon this, the proposed model introduces in-context learning in two stages.

In the first stage, the aggregation network learns to infer a latent concept by utilizing the four components of

a prompt: input, output, format and input-output mapping. These latent concepts encompass lexical distributions, formats and syntactic relationships, which means premise \rightarrow hypothesis \rightarrow relationship. In the second stage, despite examples being concatenated in a non-continuous manner, the LLM can still make predictions by leveraging shared concepts (premise \rightarrow hypothesis \rightarrow relationship), indicating that in-context learning has occurred.

Let the Vicuna model be denoted as f_{dec} , and then the output is depicted as

$$y = f_{\text{dec}}(\text{format}(v_a, x_{11}, x_{12}, x_{13})), \quad (5)$$

where $\text{format}(\cdot)$ represents the input setting, the first stage involves tensor concatenation, and the second stage encompasses the instruction step; x_{11}, x_{12} and x_{13} denote textual embedding vectors for captions, hypotheses and answers, respectively; $y \in \mathbf{R}^{l_2 \times D_v}$ represents the prediction by the Vicuna language model, l_2 denotes the maximum length of the output tokens, and D_v refers to the size of the vocabulary.

2.2.3 Instruction-guided cross-modal information integration

In the cross-modal fusion phase, we incorporate principles of instruction learning by using a carefully designed set of instructions to guide Vicuna on how to dynamically combine features from both modalities based on task-specific requirements, as depicted in Fig. 4.

Here, [img1] [img2] ... [imgN] represent visual tokens extracted from image features, while X_{11}, X_{12} and X_{13} denote textual tokens for captions, hypotheses and answers, respectively. The black text represents fixed prompt information, whereas green-marked symbols such as <STOP> and , and double-hash symbol (##) serve as auxiliary indicators that signal the start and end of dialogues, the boundaries of image markers and the conclusion of answer sections. These instructions not only specify how the image and text features interact but also define the emphasis on one modality's information or how to harmonize the relationship between them in specific application scenarios. For example, when an instruction requires the model to determine entailment based on a text description, the system will prioritize guiding text features while also integrating image features in its assessment. During an image classification task, the model may rely more heavily on image features while still referring to text descriptions to improve accuracy. Operationally, Vicuna incorporates specific instructions as additional inputs. It then adjusts weight assignments within self-attention layers or cross-modal attention layers using these instruction signals to achieve a dynamic fusion of the visual and textual feature vectors.



Fig. 4 Diagram of instruction step

2.2.4 Objective function

The objective is to minimize the discrepancy between the predicted probability distribution and the true probability distribution. Concretely, the proposed model predicts a probability distribution $\mathbf{p}_{ij} = (\mathbf{p}_{i1}, \mathbf{p}_{i2}, \dots, \mathbf{p}_{il})$ for each sample \mathbf{p}_i , where $\mathbf{p}_{ij} \in \mathbf{R}^{D_v}$ denotes the prediction of the j th word. $\hat{\mathbf{y}}_i = (\mathbf{a}_{i1}, \mathbf{a}_{i2}, \dots, \mathbf{a}_{il})$ represents the label for the i th sample, where \mathbf{a}_{ij} denotes the one-hot vector of the j th word. N denotes the number of the dataset; l denotes the maximum length for each sample; $i \in 1, 2, \dots, N$; $j \in 1, 2, \dots, l$. The loss function L is defined as

$$L = -\frac{1}{N} \sum_{i=1}^N \sum_{j=1}^l \hat{\mathbf{y}}_j \log \mathbf{p}_{ij}. \quad (6)$$

2.3 Training details

We utilize original image inputs of size $224 \times 224 \times 3$ and extract high-level visual features using the ViT-Base model from CLIP. Concurrently, a seven billion-parameter Vicuna-7B language model is utilized for text comprehension and generation. The training process is executed on an NVIDIA TITAN RTX GPU with a batch size set to 4 to strike a balance between computational resources and memory efficiency. For optimizing model performance, we utilize the AdamW optimizer^[27] as the update strategy, initializing the learning rate at 3×10^{-5} . This value has been empirically determined through preliminary experimentation as the optimal starting point. Our training process consists of two periods. The initial training period allows the model to train the aggregation layer without instructions. During this period, we record and monitor performance metrics of the validation set at each iteration to identify the optimal model weights during the training process. After the initial training period, we enter the in-context learning period, during which we load the parameters from the optimal model and then freeze them for in-context learning. This enables the model to leverage its foundational knowledge to comprehend and adjust to contextual information unique to the task environment, thereby improving performance on VE tasks. Throughout the entire training regimen, techniques such as early stopping are also implemented to prevent overfitting and ensure the model's generalization capabilities.

3 Experimental Section

3.1 Dataset and metrics

E-SNLI-VE^[25], serving as a cutting-edge benchmark dataset for the VE task, not only extends and refines SNLI-VE^[28] by integrating image descriptions

from Flickr30k^[29] with VE principles but also, after rectifying annotation errors in the original dataset^[30], provides 401 700 training samples, 14 300 validation samples and 14 700 test samples to gauge models' cross-modal understanding capabilities between images and texts.

Three advanced automated evaluation metrics are employed to evaluate model performance: metric for evaluation of translation with explicit ordering (METEOR)^[31], bidirectional encoder representations from Transformers score (BERTScore)^[32] and accuracy (Acc). METEOR provides a holistic assessment of translation quality by considering word matches, phrase matches and semantic similarity. Additionally, it quantifies the degree of lexical overlap between the generated and reference texts. BERTScore, which leverages the pre-trained language model BERT, computes semantic similarity between sentences and is widely used in assessing outcomes in areas such as text generation and machine translations. Acc assesses the classification performance of the proposed model. In the VE task, there are three prediction classes: entailment, neutrality and contradiction.

3.2 Baseline models

We compared our proposed model with several advanced baseline models, including pointing and justification explanation (PJ-X)^[8], faithful multimodal explanation (FME)^[7], Rationale^{VT} Transformer (RVT)^[33], question-answering-only (QA-only)^[25], e-UG^[25], natural language explanations in vision and vision-language tasks (NLX-GPT)^[34] and one for all (OFA-X)^[16]. The performance of these models is evaluated in the E-SNLI-VE test dataset.

3.3 Quantitative analysis

Table 1 illustrates that CAVE achieves the highest scores across all evaluation metrics, indicating its ability in generating high-quality text that is semantically coherent and accurate. CAVE encompasses two variations: CAVE_ENC, where labels remain as the original text, entailment, neutrality and contradiction; CAVE_YNU, which modifies these labels to yes, unknown and no. CAVE_YNU outperforms CAVE_ENC by 1.5% in METEOR (M), 4.3% in BERTScore (BS), and 3.6% in Acc, respectively. Note that all percentage increases mentioned in this section are absolute improvements. The rationale behind this differentiation is that the original label format poses a greater challenge for generating the corresponding tokens in Vicuna. Words like "entailment" and "contradiction" are split into multiple tokens ("entail" and "ment", "contradict" and "tion", respectively). Assuming that each token predicts

the probability p_n , then the correct prediction of entailment or contradiction requires $p_1 \times p_2$, where p_1 is the probability of the first token and p_2 is the probability of the second token. Since CAVE_YNU only needs to predict the probability of one token (yes, unknown or no), it is simpler for the model.

Table 1 Comparative evaluation of model performance in E-SNLI-VE test dataset

Model	Metric score/%		
	M	BS	Acc
PJ-X ^[8]	14.7	79.1	69.2
FME ^[7]	15.6	79.7	73.7
RVT ^[33]	18.8	81.1	72.0
QA-only ^[25]	18.7	81.1	—
e-UG ^[25]	19.6	81.7	79.5
NLX-GPT ^[34]	18.8	80.8	73.9
OFA-X ^[16]	18.6	85.7	80.9
CAVE_ENC	19.0	86.3	83.2
CAVE_YNU	20.5	90.6	86.8

To further investigate the impact of the proposed individual components on the overall performance of the model, we conducted an ablation analysis, as illustrated in Table 2. The first row of data represents the proposed model as a baseline reference. Subsequently, one of the following components was removed (expressed as w/o in Table 2): image tokens, image captions, instructions or context learning (ICL) strategy. In the experiment involving the removal of image tokens, we trained the image features by replacing them with random vectors sampled from a normal distribution. It can be observed that all three metrics decrease, highlighting the significance of image tokens in model performance. After removing image captions, the accuracy drops significantly by 10.5%, while BERTScore and METEOR decrease by 5.8% and 2.8%, respectively. This shows that image captions are indispensable for modeling logical reasoning. After removing the ICL strategy, all three metrics decrease, but the decrease is not significant, and the impact on model performance is negligible. To summarize, image tokens and image captions contribute the most to the model's performance. The ICL strategy optimizes the model performance, demonstrating the effectiveness of our input sample settings.

Table 2 Ablation study

Model setting	Metric score/%		
	M	BS	Acc
CAVE_YNU	20.5	90.6	86.8
w/o image token	18.4	87.4	83.8
w/o image caption	17.7	84.8	76.3
w/o instruction	20.3	89.9	86.1
w/o ICL	20.4	90.1	85.9

Table 3 shows a comparison of the results of the mapping layer between image features and text features using different structures, including the linear layer, the self-attention layer, and the aggregation layer we designed. It can be seen that the aggregation layer achieves the highest accuracy, followed by the self-attention layer, with the linear layer performing the least effectively in terms of accuracy. In addition, the number of training parameters in the aggregation layer is lower than that in the self-attention layer, but higher than that in the linear layer. This proves that it is effective to introduce more complex nonlinear mapping when converting the original feature distribution of the image encoder and text decoder. The aggregation layer is superior to the self-attention layer, indicating that not all image candidate features are beneficial to downstream text feature alignment and inference. Our proposed aggregation layer is effective in this respect, and it can better fusion image information to extract high-level semantic features.

Table 3 Comparison results of mapping layer

Mapping layer	Training parameters	Metric score/%		
		M	BS	Acc
Linear	3.8×10⁷	19.1	87.3	83.5
Self-attention	1.17×10 ⁸	20.3	89.7	86.2
Aggregation (ours)	6.7×10 ⁷	20.5	90.6	86.8

Table 4 shows the comparative experimental results of the CAVE model with different aggregate token lengths under two label settings: CAVE_ENC and CAVE_YNU. The results indicate that the CAVE_YNU configuration outperforms CAVE_ENC in terms of overall performance metrics. Furthermore, an intriguing trend is observed in relation to the token length: there is a notable decrease in performance metrics as the length of input tokens grows, which is more pronounced than what was initially expected. This suggests that longer inputs may introduce additional complexity or noise, adversely affecting model performance.

Table 4 Comparative experiments of different aggregate token lengths

Model	Token length	Metric score/%		
		M	BS	Acc
CAVE_ENC	5	19.0	86.3	83.2
CAVE_YNU		20.5	90.6	86.8
CAVE_ENC	10	18.9	85.6	82.0
CAVE_YNU		20.1	89.5	84.7
CAVE_ENC	15	18.8	84.5	80.2
CAVE_YNU		20.1	87.1	83.9

Figure 5 shows the performance comparison across different training epochs for ICL samples. It can be seen that when the number of training epochs equals three, the model performance reaches its peak.

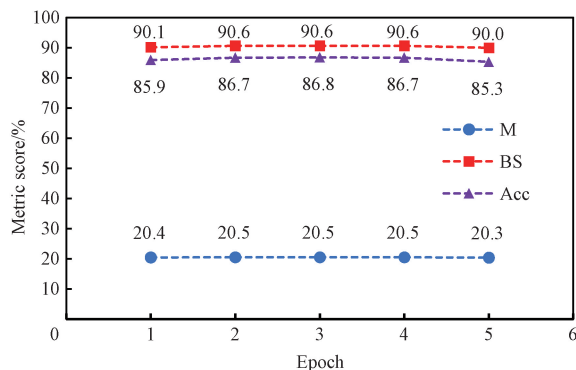


Fig. 5 Performance comparison for different ICL samples

3.4 Qualitative analysis

To visually show the results of converting image features into visual tokens, we select the five words that are most similar to visual tokens by calculating the cosine similarity between visual token vectors and all token vectors in the vocabulary. Then, these words are

arranged in descending order of the similarity score, and visualized in the form of a word cloud map, as shown in Fig. 6. In the four pairs of images shown, the word with the highest similarity in each image is the main semantic information in the image, such as “sitting” “woman” and “young child”. For example, in the first word cloud, we observe words such as “legs” “brown” “glass” and “hair”, which describe the various object concepts in the image. It is worth noting that these concepts are in the graph. The description or hypothesis of the image is not mentioned in the text, thus highlighting the effectiveness of the aggregation network for capturing image semantic features. In the second image, we see words related to “button” “holding” “taking”, etc., which further complement semantic information not fully covered in the caption description of the image. Overall, the visualizations in Fig. 6 once again validate that the aggregation network extracts effective and high-level semantic features.



Fig. 6 Word cloud visualization of visual tokens

In Fig. 7, we visualize the predicted answers. As can be seen, the first sentence of the predicted answer follows a template construction consistent with the template structure we provided in the training data.

The LLM Vicuna plays a key role in this process. It enables our model to go beyond the traditional three-category classification task, establish the connection between the image and the text based on the image

features provided by the aggregation layer. Furthermore, it explains the reason based on the

caption, demonstrating its ability in semantic understanding and logical reasoning.

	Hypothesis Caption Ground truth Prediction	The woman is very happy. A woman with a green headscarf, a blue shirt and a very big grin. Entailment. Answer: entailment. The premise describe a specific with details of a woman is laughing.
	Hypothesis Caption Ground truth Prediction	A tall human jumping. A bearded man jumps in the snow with the ocean in the background and an orange, recumbent bike parked near a road sign. Entailment. Answer: entailment. The premise describes a specific scenario involving a bearded man jumping.
	Hypothesis Caption Ground truth Prediction	A person is waiting for a train. A person in orange clothing rests above a metro entrance. Neutrality. Answer: neutral. The premise simply describes a person in orange clothing above a metro entrance, without explicitly stating that the person is waiting for a train.
	Hypothesis Caption Ground truth Prediction	A man getting ready to play golf. A man in a black tank top wearing a red plaid hat. Neutrality. Answer: neutral. The premise does not provide any direct information or implication about the man's activities or intentions related to playing golf.
	Hypothesis Caption Ground truth Prediction	The lioness is sleeping. A lioness closes in on its prey. Contradiction. Answer: contradiction. The premise indicates that the lioness is actively hunting its prey, which contradicts the hypothesis that the lioness is sleeping.
	Hypothesis Caption Ground truth Prediction	The car is yellow. A biker races. Contradiction. Answer: contradiction. The two statements are not logically connected, and both of them do not necessarily imply the hypothesis.

Fig. 7 Some qualitative examples from our model on the E-SNLI-VE test split

3.5 Strengths and limitations

3.5.1 Strengths

The main strengths of the proposed CAVE model are: the exploitation of cutting-edge pre-trained models (CLIP and Vicuna) to bolster cross-modal comprehension; the utilization of a tailored aggregation mechanism that facilitates smooth interaction and fusion of information across modalities; task specificity through instruction design, which guides and focuses the model's reasoning process for improved performance in targeted tasks.

3.5.2 Limitations

Despite these strengths, the proposed CAVE model is inherently constrained by its task-specificity, being primarily designed for logical reasoning in multimodal contexts. It does not readily generalize to other question-answering (QA) tasks without additional adaptation. More specifically, to broaden the model's applicability spectrum, there is a need to train a supplementary aggregation module capable of flexibly and effectively integrating various types of input data in different scenarios. This highlights the current limitation in terms of direct transferability to diverse QA tasks and represents a potential area for future improvement in the model's

versatility and adaptability.

4 Conclusions

In this paper, we propose a novel model named CAVE, which integrates an established CLIP image encoder with an LLM, Vicuna, serving as the decoder. To facilitate the integration, we introduce a streamlined aggregation network that acts as a transformative interface between the visual and textual modalities. It not only extracts high-level semantic features of images but also converts them into visual tokens to align texts effectively. Also, the proposed model combines instruction tuning and in-context learning in the training process to improve the training efficiency. The qualitative experiments show our significant results on the E-SNLI-VE dataset. Nevertheless, multimodal visual reasoning still faces many challenges, such as math reasoning capabilities, which we will explore further in the future.

References

- [1] DONG Q X, QIN Z W, XIA H M, et al. Premise-based multimodal reasoning: conditional

- [2] inference on joint textual and visual clues [C] // Proceedings of the 60th Annual Meeting of the Association for Computational Linguistics. Stroudsburg: ACL, 2022: 932-946.
- [3] CHEN Y C, LI L J, YU L C, et al. UNITER: universal image-text representation learning [M] // Lecture Notes in Computer Science. Cham: Springer International Publishing, 2020: 104-120.
- [4] SHAO Z W, YU Z, WANG M, et al. Prompting large language models with answer heuristics for knowledge-based visual question answering [C] // 2023 IEEE/CVF Conference on Computer Vision and Pattern Recognition (CVPR). New York: IEEE, 2023: 14974-14983.
- [5] SUZUKI R, YANAKA H, YOSHIKAWA M, et al. Multimodal logical inference system for visual-textual entailment [C] // Proceedings of the 57th Annual Meeting of the Association for Computational Linguistics: Student Research Workshop. Stroudsburg: ACL, 2019: 386-392.
- [6] YU S J, JIN X Q, WU G W, et al. Deep multi-module based language priors mitigation model for visual question answering [J]. *Journal of Donghua University (English Edition)*, 2023, 40 (6): 684-694.
- [7] LI Q, TAO Q Y, JOTY S, et al. VQA-E: explaining, elaborating, and enhancing your answers for visual questions [M] // Lecture Notes in Computer Science. Cham: Springer International Publishing, 2018: 570-586.
- [8] WU J L, MOONEY R. Faithful multimodal explanation for visual question answering [C] // Proceedings of the 2019 ACL Workshop BlackboxNLP: Analyzing and Interpreting Neural Networks for NLP. Stroudsburg: ACL, 2019: 103-112.
- [9] PARK D H, HENDRICKS L A, AKATA Z, et al. Multimodal explanations: justifying decisions and pointing to the evidence [C] // 2018 IEEE/CVF Conference on Computer Vision and Pattern Recognition. New York: IEEE, 2018: 8779-8788.
- [10] THOMAS C, ZHANG Y P, CHANG S F. Fine-grained visual entailment [M] // Lecture Notes in Computer Science. Cham: Springer Nature Switzerland, 2022: 398-416.
- [11] ANDERSON P, HE X D, BUEHLER C, et al. Bottom-up and top-down attention for image captioning and visual question answering [C] // 2018 IEEE/CVF Conference on Computer Vision and Pattern Recognition. New York: IEEE, 2018: 6077-6086.
- [12] HOCHREITER S, SCHMIDHUBER J. Long short-term memory [J]. *Neural Computation*, 1997, 9(8): 1735-1780.
- [13] RADFORD A, WU J, CHILD R, et al. Language models are unsupervised multitask learners [EB/OL]. (2019-02-14) [2024-03-15]. <https://openai.com/blog/better-language-models/>.
- [14] LI J N, SELVARAJU R R, GOTMARE A D, et al. Align before fuse: vision and language representation learning with momentum distillation [EB/OL]. (2021-10-07) [2024-03-15]. <https://arxiv.org/abs/2107.07651>.
- [15] ZENG Y, ZHANG X S, LI H. Multi-grained vision language pre-training: aligning texts with visual concepts [EB/OL]. (2022-06-01) [2024-03-15]. <https://arxiv.org/abs/2111.08276>.
- [16] PLÜSTER B, AMBSDORF J, BRAACH L, et al. Harnessing the power of multi-task pretraining for ground-truth level natural language explanations [EB/OL]. (2023-03-29) [2024-03-15]. <https://arxiv.org/abs/2212.04231>.
- [17] WANG P, YANG A, MEN R, et al. OFA: unifying architectures, tasks, and modalities through a simple sequence-to-sequence learning framework [EB/OL]. (2022-06-01) [2024-03-15]. <https://arxiv.org/abs/2202.03052>.
- [18] GUI L K, WANG B R, HUANG Q Y, et al. KAT: a knowledge augmented transformer for vision-and-language [C] // Proceedings of the 2022 Conference of the North American Chapter of the Association for Computational Linguistics: Human Language Technologies. Stroudsburg: ACL, 2022: 956-968.
- [19] LIN Y Z, XIE Y J, CHEN D D, et al. REVIVE: regional visual representation matters in knowledge-based visual question answering [EB/OL]. (2022-10-10) [2024-03-18]. <https://arxiv.org/abs/2206.01201>.
- [20] YANG H, LIN J Y, YANG A, et al. Prompt tuning for generative multimodal pretrained models [EB/OL]. (2022-08-04) [2024-03-15]. <https://arxiv.org/abs/2208.02532>.
- [21] LIU H T, LI C Y, WU Q Y, et al. Visual instruction tuning [EB/OL]. (2023-04-17) [2024-03-18]. <https://arxiv.org/abs/2304.08485>.
- [22] BROWN T B, MANN B, RYDER N, et al. Language models are few-shot learners [C] // Proceedings of the 34th International Conference on Neural Information Processing Systems (NeurIPS). New York: ACM, 2020: 1877-1901.
- [23] RADFORD A, KIM J W, HALLACY C, et al. Learning transferable visual models from natural language supervision [C] // International Conference on Machine Learning. Berlin: PMLR, 2021: 8748-8763.

- [24] TOUVRON H, LAVRIL T, IZACARD G, et al. LLaMA: open and efficient foundation language models [EB/OL]. (2023-02-27) [2024-03-30]. <https://arxiv.org/abs/2302.13971>.
- [25] KAYSER M, CAMBURU O M, SALEWSKI L, et al. E-ViL: a dataset and benchmark for natural language explanations in vision-language tasks [C]//2021 IEEE/CVF International Conference on Computer Vision (ICCV). New York: IEEE, 2021: 1224-1234.
- [26] YANG Z Y, GAN Z, WANG J F, et al. An empirical study of GPT-3 for few-shot knowledge-based VQA [J]. *Proceedings of the AAAI Conference on Artificial Intelligence*, 2022, 36(3): 3081-3089.
- [27] SCHROFF F, KALENICHENKO D, PHILBIN J. FaceNet: a unified embedding for face recognition and clustering [C]//2015 IEEE Conference on Computer Vision and Pattern Recognition (CVPR). New York: IEEE, 2015: 815-823.
- [28] XIE N, LAI F, DORAN D, et al. Visual entailment: a novel task for fine-grained image understanding [EB/OL]. (2019-01-20) [2024-03-30]. <https://arxiv.org/abs/1901.06706>.
- [29] PLUMMER B A, WANG L W, CERVANTES C M, et al. Flickr30k entities: collecting region-to-phrase correspondences for richer image-to-sentence models [C]//2015 IEEE International Conference on Computer Vision (ICCV). New York: IEEE, 2015: 1224-1234.
- [30] DO V, CAMBURU O M, AKATA Z, et al. E-SNLI-VE: corrected visual-textual entailment with natural language explanations [EB/OL]. (2021-08-19) [2024-03-15]. <https://arxiv.org/abs/2004.03744>.
- [31] BANERJEE S, LAVIE A. METEOR: an automatic metric for MT evaluation with improved correlation with human judgments [C]// Proceedings of the ACL Workshop on Intrinsic and Extrinsic Evaluation Measures for Machine Translation and/or Summarization. Stroudsburg: ACL, 2005: 65-72.
- [32] ZHANG T Y, KISHORE V, WU F, et al. BERTScore: evaluating text generation with BERT [EB/OL]. (2020-01-24) [2024-04-23]. <https://arxiv.org/abs/1904.09675>.
- [33] MARASOVIĆ A, BHAGAVATULA C, PARK J S, et al. Natural language rationales with full-stack visual reasoning: from pixels to semantic frames to commonsense graphs [C]//Findings of the Association for Computational Linguistics: EMNLP 2020. Stroudsburg: ACL, 2020: 2810-2829.
- [34] SAMMANI F, MUKHERJEE T, DELIGIANNIS N. NLX-GPT: a model for natural language explanations in vision and vision-language tasks [C]//2022 IEEE/CVF Conference on Computer Vision and Pattern Recognition (CVPR). New York: IEEE, 2022: 8312-8322.

基于特定指令驱动的上下文感知视觉蕴含

韩宇凤^{1, 2}, 郝矿荣^{1, 2*}, 唐雪嵩^{1, 2}, 隘 兵^{1, 2}

1. 东华大学 信息科学与技术学院, 上海 201620

2. 东华大学 数字化纺织服装技术教育部工程研究中心, 上海 201620

摘要: 视觉蕴含是多模态视觉推理中的一个典型任务, 当前的方法经常利用大型语言模型 (large language model, LLM) 作为知识库来协助回答问题。这些方法在很大程度上依赖于文本模态, 而文本模态本质上无法捕获图像中包含的全部信息。为此, 作者提出了一个上下文感知视觉蕴含 (context-aware visual entailment, CAVE) 模型。该模型引入了一种新的聚合模块, 用于从图像中提取高级语义特征, 将低级语义图像特征聚合为格式类似于文本标记的高级视觉标记, 作为 LLM 的输入。CAVE 模型弥补了图像信息的损失, 并更有效地将图像信息与文本理解相结合。同时, CAVE 模型采用了一种新的基于指令微调和上下文学习的输入格式和训练方法, 其目的在于最大化 LLM 固有的逻辑推理潜能。在 E-SNLI-VE 数据集上的实验结果表明, CAVE 模型表现出色。

关键词: 视觉蕴含; 文本-视觉融合; 指令微调; 上下文学习

DOI: 10.19884/j.1672-5220.202403011

An Efficient Temporal Decoding Module for Action Recognition

HUANG Qiubo*, MEI Jianmin, ZHAO Wupeng, LU Yiru, WANG Mei, CHEN Dehua

School of Computer Science and Technology, Donghua University, Shanghai 201620, China

Abstract: Action recognition, a fundamental task in the field of video understanding, has been extensively researched and applied. In contrast to an image, a video introduces an extra temporal dimension. However, many existing action recognition networks either perform simple temporal fusion through averaging or rely on pre-trained models from image recognition, resulting in limited temporal information extraction capabilities. This work proposes a highly efficient temporal decoding module that can be seamlessly integrated into any action recognition backbone network to enhance the focus on temporal relationships between video frames. Firstly, the decoder initializes a set of learnable queries, termed video-level action category prediction queries. Then, they are combined with the video frame features extracted by the backbone network after self-attention learning to extract video context information. Finally, these prediction queries with rich temporal features are used for category prediction. Experimental results on HMDB51, MSRDailyAct3D, Diving48 and Breakfast datasets show that using TokShift-Transformer and VideoMAE as encoders results in a significant improvement in Top-1 accuracy compared to the original models (TokShift-Transformer and VideoMAE), after introducing the proposed temporal decoder. The introduction of the temporal decoder results in an average performance increase exceeding 11% for TokShift-Transformer and nearly 5% for VideoMAE across the four datasets. Furthermore, the work explores the combination of the decoder with various action recognition networks, including Timesformer, as encoders. This results in an average accuracy improvement of more than 3.5% on the HMDB51 dataset. The code is available at <https://github.com/huangturbo/TempDecoder>.

Keywords: action recognition; video understanding; temporal relationship; temporal decoder; Transformer

CLC number: TP389.1

Document code: A

Article ID: 1672-5220(2025)02-0187-10

Open Science Identity
(OSID)



0 Introduction

Action recognition aims to identify and classify human actions within a video sequence. With the widespread development and dissemination of video

media, this field has attracted increasing research interest. As a fundamental area in computer vision, action recognition finds applications in various domains of video understanding, including video surveillance, retrieval and human activity detection. In contrast to static images, videos inherently contain temporal information. Therefore, for effective action recognition, models need to excel in feature extraction across both spatial and temporal dimensions. Spatial information represents the static details within each frame, including people, objects and backgrounds. Temporal information captures the contextual relationships between frames, requiring the integration of static information for a comprehensive understanding. Typically, the goal in action recognition tasks is to classify actions occurring between individuals, objects, or a combination of both.

For some datasets (e.g., UCF101^[1]) where many categories are less related to the action and only one or a few frames of static images are often needed to recognize the action, models with excellent static information extraction capabilities can achieve high recognition accuracy^[2]. However, in most real-life applications, relying solely on spatial information is insufficient. These video frames exhibit close correlations between actions over time. Enhancing the model ability to model temporal features becomes crucial for action recognition. Consequently, numerous studies have been conducted to address this issue. Early methods involved averaging the features extracted by convolutional neural networks (CNNs) for images across the temporal dimension, followed by classification^[3]. However, such simple fusion methods often result in the loss of significant temporal information, hindering action classification. Subsequently, researchers replaced two-dimensional (2D) convolutions with three-dimensional (3D) counterparts to simultaneously model the temporal dimension^[4], leading to improved performance. Nevertheless, the model parameters in this approach increase, resulting in substantial computational costs. To further enhance action classification accuracy, researchers incorporated optical flow^[5] into the model, forming two-stream networks. However, pre-extracting optical flow

Received date: 2024-03-22

Foundation item: Shanghai Municipal Commission of Economy and Information Technology, China (No. 202301054)

* Correspondence should be addressed to HUANG Qiubo, email: huangturbo@dh.edu.cn

Citation: HUANG Q B, MEI J M, ZHAO W P, et al. An efficient temporal decoding module for action recognition[J]. *Journal of Donghua University (English Edition)*, 2025, 42(2): 187-196.

incurs significant time and computational expenses, impeding the deployment of end-to-end models.

Following the remarkable success of the Transformer in natural language processing (NLP)^[6], attempts were made to transfer the Transformer into the computer vision (CV) domain. In action recognition tasks, researchers utilized the multi-head attention mechanism of the Transformer to globally model spatiotemporal information, achieving promising recognition results. However, many existing Transformer-based action recognition models simply perform average fusion on the final output features or add a classification token representing the entire video for action recognition. This simplistic approach hampers the exploration of temporal correlations between different actions, leading to the loss of some crucial temporal information.

Therefore, we propose a straightforward Transformer temporal decoding module to model the video frame features extracted by existing action recognition networks. This module aims to further extract temporal information, thereby improving action recognition performance. In contrast to introducing a singular classification token, we pre-introduce learnable queries, termed video-level action category prediction queries. Drawing inspiration from end-to-end object detection with the Transformer^[7], these prediction queries leverage the potent global modeling capabilities of the Transformer, enabling the decoder to autonomously learn spatiotemporal features within the video. Additionally, through the multi-head attention mechanism, the decoder can determine which temporal features are more critical, enhancing the overall spatiotemporal modeling capability of the entire model. We validate the effectiveness of the temporal decoder on HMDB51^[8], MSRDailyAct3D^[9], Diving48^[10] and Breakfast^[11] datasets.

1 Related Work

1.1 Video action recognition

Action recognition stands as a representative task in video understanding, and with the rise of deep learning, researchers have employed 3D CNNs to address video understanding challenges. Learning spatiotemporal features with 3D convolutional networks^[12] is notable. Extending ResNeXt into a 3D structure, ResNeXt3D^[13] further enhances the video understanding capabilities of 3D CNNs. However, due to limited receptive fields, 3D CNN approaches struggle to extract global spatiotemporal information, hindering the recognition of actions that span longer temporal ranges. To better describe temporal relationships between frames, Simonyan et al.^[14] proposed two-stream networks incorporating optical flow into action recognition tasks. Compared to using raw RGB images as input, optical flow efficiently eliminates non-motion backgrounds, simplifying the learning task. However, precomputing optical flow fields entails significant computational and storage requirements,

impeding large-scale training and real-time deployment.

In recent years, the tremendous success of the Transformers in handling sequential data has led to the exploration of Transformer-based^[15] methods in video action recognition. Timesformer^[16], the first Transformer-based video understanding network, employs a spatiotemporal attention mechanism to enable efficient and accurate video classification. The token shift module^[17] segments video sequences into multiple fragments for local processing, reducing computational complexity and memory consumption. Addressing the need for substantial training data for the Transformer, Tong et al.^[18] introduced VideoMAE, utilizing video self-supervised pretraining for efficient fine-tuning in downstream tasks like action recognition. These action recognition models, leveraging self-attention mechanisms, capture spatiotemporal dependencies across entire videos, extracting global and long-range temporal information to enhance the action recognition accuracy. However, these models primarily adopt an encoder structure, often performing simple fusion operations, such as averaging frame features and employing a single video action classification token for the action category prediction, resulting in the loss of some temporal action information. Additionally, compared to CNNs, Transformers generally lack local spatial awareness, impacting their static spatial modeling capabilities.

1.2 Temporal decoding modules

Recognizing the importance of modeling temporal features in video understanding, several temporal decoding modules have been proposed. Islam et al.^[19] introduced Vis4mer, incorporating structured state-space temporal layers to enhance long-range video modeling capabilities while reducing model computational complexity. However, due to a lack of fine-grained action expression capabilities, it may struggle to identify subtle actions in shorter videos. Lin et al.^[20] proposed an efficient video learner (EVL) decoder module that facilitated video action classification on the application to pre-trained image processing models. Yet, it requires the integration of multiple attention modules and imposes specific structural requirements on the backbone network, making it challenging to reuse in other models. Moreover, some work has migrated models from the NLP domain into video understanding networks to enhance temporal expression capabilities. Neimark et al.^[21] employed Longformer^[22] as a temporal decoding module for video action recognition. Kalfaoglu et al.^[23] directly appended the bidirectional encoder representation from the Transformer^[24] model to a 3D CNN-based action recognition network to boost temporal feature extraction capabilities of the 3D CNNs. While these decoding models exhibit strong temporal information extraction capabilities, their implementations are more complex, demanding larger computational resources. In contrast, our proposed model employs standard self-attention modules directly, making it simpler and more versatile,

capable of being appended to any action recognition or image classification backbone network.

2 Proposed Temporal Decoding Module

To construct a simple yet efficient video temporal decoder, we propose a module to introduce category prediction queries into the temporal decoder. Similar to the visual Transformer, we utilize a video action recognition Transformer as the encoder. The sampled video frames are converted into patches and fed into the encoder, yielding frame features with rich spatial semantics. Subsequently, our proposed temporal decoder, which efficiently incorporates action category prediction queries, is employed to further analyze the temporal information within the frame features extracted by the encoder.

2.1 Overall architecture

The fundamental framework for video action recognition in this work is depicted in Fig. 1, presenting an encoder-decoder architecture. The encoder is responsible

for extracting features from sampled RGB frames. Two video action recognition networks, TokShift-Transformer and VideoMAE, are used as encoders in experiments across multiple datasets. In TokShift-Transformer, we stack these frame features to construct spatiotemporal features, while VideoMAE uses the first frame feature as the spatiotemporal feature. To better leverage the encoded features, we do not directly use them for action category prediction. Instead, we feed these features into the proposed Transformer decoder to further explore temporal information and enhance the action recognition accuracy. This decoder initially performs self-attention operations on N_p learnable prediction queries, obtaining preliminary action learning information, where N_p is the number of query sequences. Subsequently, these N_p queries are combined with the previously encoded spatiotemporal features for a multi-head cross-attention operation. The resulting decoded feature vector contains rich temporal action information which is then fed into a linear layer to obtain action category predictions.

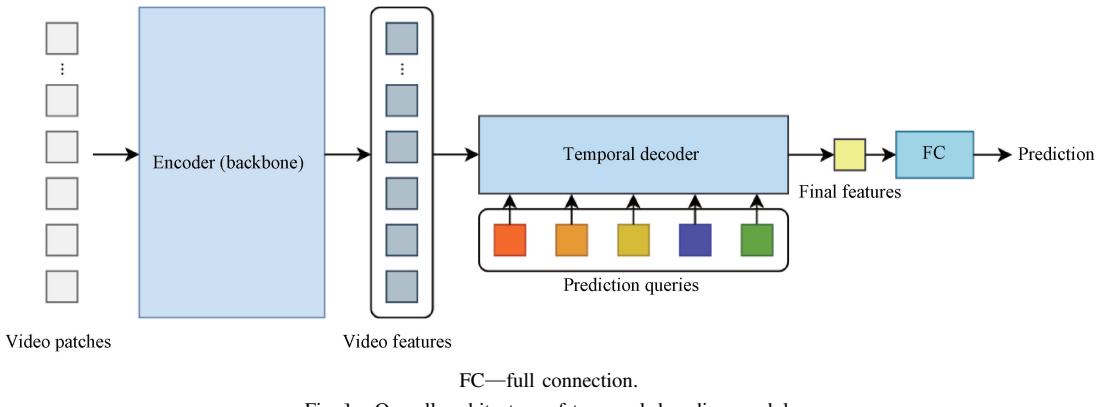


Fig. 1 Overall architecture of temporal decoding module

2.2 Encoder processing

Before performing action classification, we need to preprocess the input video frame sequence by using an encoder to extract rich temporal features. For this purpose, we can use the backbone network before the classification layer in any video action or image classification model as the encoder to extract features from video frames. Due to the powerful global modeling capabilities of Transformers, they have found widespread applications in video understanding domains like action recognition. We illustrate the encoding preprocessing of video frames using the TokShift-Transformer, a Transformer-based action recognition network.

Firstly, we have a video $V \in \mathbf{R}^{T \times H \times W \times 3}$, where T , H and W represent the number of sampled video frames and the height and width of the spatial resolution of each frame, respectively; 3 represents the three channels of RGB in the image. This video is reshaped into a sequential tensor $V^* \in \mathbf{R}^{T \times N \times d}$, where N represents the number of patches and $N = HW/P^2$, and P is the size of the patch; d denotes the number of RGB pixels in each patch, and $d = 3P^2$.

Next, a linear layer module $E \in \mathbf{R}^{d \times D}$ is applied to each patch $x_i \in \mathbf{R}^{T \times d}$ in V^* , where x_i indicates the i th patch, projecting the dimension of each patch to D . An additional classification token tensor $c \in \mathbf{R}^{T \times D}$ is concatenated to the patches, representing the global information for each frame. Simultaneously, a position encoding embedding $E_{\text{pos}} \in \mathbf{R}^{(N+1) \times D}$ is added to each patch, resulting in $z \in \mathbf{R}^{T \times (N+1) \times D}$:

$$z = [c, x_1 E, x_2 E, \dots, x_i E, \dots, x_N E] + E_{\text{pos}}. \quad (1)$$

This transforms the input video V^* into z . z is then input into multiple TokShift-MSA operations of the stacked TokShift-Transformer, resulting in \tilde{z} . \tilde{z} has the same dimensions as z :

$$\tilde{z} = \text{TokShift-MSA}(z), \quad (2)$$

where $\text{TokShift-MSA}(\cdot)$ is the multi-head self-attention operation inherent to the TokShift model itself.

Finally, $\tilde{z}[:, 0, :]$ is taken as the output of the encoder $z' \in \mathbf{R}^{T \times D}$, representing the video features for T frames:

$$z' = \tilde{z} [:, 0, :]. \quad (3)$$

2.3 Proposed temporal decoder

2.3.1 Decoder structure

The proposed structure of the temporal decoder is illustrated in Fig. 2. The decoder consists of L layers of decoding units, and the core of each decoding unit consists of two attention modules. The key operation in these attention modules is the multi-head attention (MHA) mechanism.

We construct queries for action category prediction. The queries are initialized to zero and represented as $\mathbf{q} \in \mathbf{R}^{N_p \times D}$. We add learnable position encodings $\mathbf{Q}_{\text{pos}} \in \mathbf{R}^{N_p \times D}$ to form \mathbf{q}' . Performing a multi-head self-attention operation on \mathbf{q}' facilitates initial learning among queries, resulting in a sequence $\mathbf{Q}_p \in \mathbf{R}^{N_p \times D}$ with certain temporal action representation capabilities:

$$\mathbf{q}' = \mathbf{q} + \mathbf{Q}_{\text{pos}}, \quad (4)$$

$$\mathbf{Q}_p = \text{MHSA}(\mathbf{q}'), \quad (5)$$

where $\text{MHSA}(\cdot)$ is the multi-head self-attention operation.

The video features z' extracted from the encoder undergo a cross-time spatial convolution module, aimed at enhancing the spatial modeling capability of the decoder. This process yields $z'' \in \mathbf{R}^{T \times D}$. Similar to the prediction queries, we add position encoding $\mathbf{P}_{KV} \in \mathbf{R}^{N_{\text{pos}} \times D}$ to z'' , obtaining frame features $\mathbf{K}_f \in \mathbf{R}^{T \times D}$ and $\mathbf{V}_f \in \mathbf{R}^{T \times D}$ with enhanced spatial expression capabilities:

$$z'' = \text{CTSC}(z'), \quad (6)$$

$$\mathbf{K}_f = \mathbf{V}_f = z'' + \mathbf{P}_{KV} [:, T], \quad (7)$$

where $\text{CTSC}(\cdot)$ is the cross-time spatial convolution operation. The position encoding uses trigonometric absolute position encoding, and N_{pos} represents the pre-set number of position encodings ($N_{\text{pos}} = 2048$ in this work).

$$\begin{cases} \mathbf{P}_{KV}(k, 2i) = \sin(k/10000^{2i/d}), \\ \mathbf{P}_{KV}(k, 2i+1) = \cos(k/10000^{2i/d}), \end{cases} \quad (8)$$

where $k=0, 1, \dots, N_{\text{pos}}-1$; $i=0, 1, \dots, D/2-1$.

Next, \mathbf{K}_f and \mathbf{V}_f are combined with \mathbf{Q}_p for a multi-head cross attention operation, enabling global perception of spatiotemporal information through attention mechanisms. The output is a vector $\mathbf{z}_{\text{cross}} \in \mathbf{R}^{N_{\text{pos}} \times D}$ with rich temporal features:

$$\mathbf{z}_{\text{cross}} = \text{MHCA}(\mathbf{Q}_p, \mathbf{K}_f, \mathbf{V}_f), \quad (9)$$

where $\text{MHCA}(\cdot)$ is the multi-head cross attention operation.

After multiple layers of stacking operations, the output $\mathbf{z}_{\text{cross}}$ undergoes further processing through the proposed temporal convolution module. This module performs convolution fusion on the temporal dimension, resulting in a feature $\mathbf{z}_{\text{out}} \in \mathbf{R}^D$ with rich spatial-temporal

semantic information for the final linear classification prediction.

$$\mathbf{z}_{\text{out}} = \text{Temp-Conv}(\mathbf{z}_{\text{cross}}). \quad (10)$$

where $\text{Temp-Conv}(\cdot)$ is the temporal convolution operation.

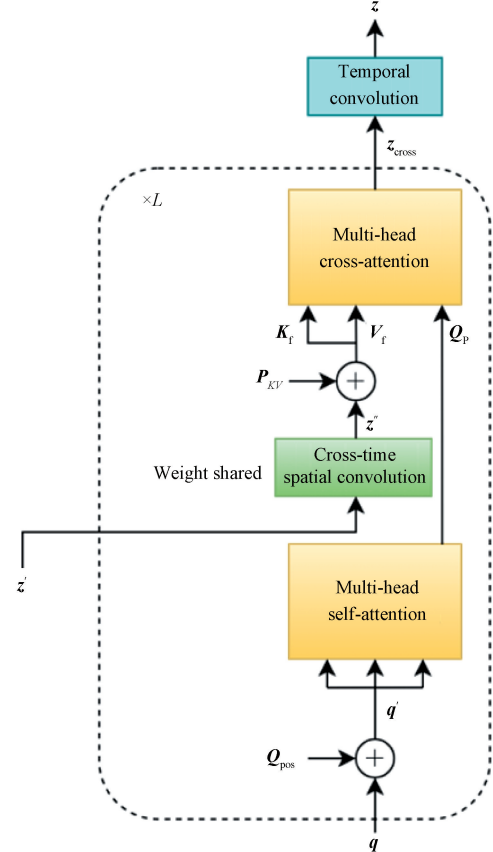


Fig. 2 Schematic diagram of temporal decoder structure

2.3.2 Cross-time spatial convolution and temporal convolution modules

Despite the powerful global temporal modeling capabilities of the Transformer attention mechanism, its ability for local spatial perception is relatively weak. To address this limitation, we introduce a weight-shared cross-time spatial convolution module. This module participates in convolutional operations on the frame features z' before entering the cross attention module, thereby enhancing the spatial modeling capability of the decoder. Generally, assuming that the input is $X_f \in \mathbf{R}^{T \times D}$ and the feature after convolution is $Y_{\text{cross}} \in \mathbf{R}^{T \times D}$, the operation is defined as follows.

$$Y_{\text{cross}}(t, d) = b_{\text{cross}} + \sum_{\Delta t, \Delta d} W_{\text{cross}}(\Delta t, \Delta d) X_f(t + \Delta t, d + \Delta d), \quad (11)$$

where b_{cross} and W_{cross} are the bias and weight parameters of cross-time spatial convolution, respectively; $\Delta t, \Delta d \in \{-1, 0, 1\}$. For $\Delta t, -1$ and 1 represent the neighboring frames before and after the current frame in the video,

respectively. For Δd , -1 and 1 represent the positions before and after the current position d , respectively. As shown in Fig. 3, to achieve spatial feature fusion across frames for the current temporal position, we convolve with the neighboring frames in the temporal and spatial dimensions, using zero-padding at the boundaries. The elements with the same color in Fig. 3 are multiplied and accumulated element-wise, and the result is added to obtain the instance corresponding to the above operation.

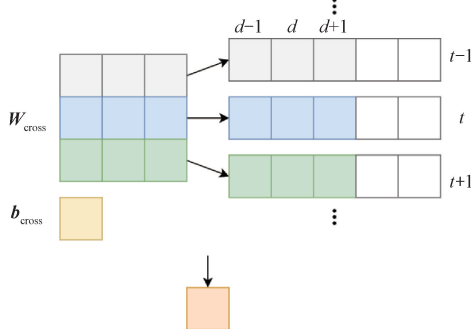


Fig. 3 Cross-time spatial convolution operation

To enhance the temporal fusion capability of the decoder, we also introduce a temporal convolution module, acting on the output feature of the last layer's multi-head cross attention operation. This module performs convolution fusion on the temporal dimension, producing the final output feature used for video action classification. Generally, assuming the input is $X_{\text{cross}} \in \mathbf{R}^{T \times D}$ and the feature after temporal convolution is $Y_{\text{temp}} \in \mathbf{R}^D$, the temporal convolution module's fusion operation is

$$Y_{\text{temp}}(d) = b_{\text{temp}} + \sum_{t=0}^{T-1} W_{\text{temp}}(t) X_{\text{cross}}(t, d), \quad (12)$$

where b_{temp} and W_{temp} are the bias and weight parameters of the temporal convolution module. The convolution weights learned by the network and the input features are multiplied and accumulated in the temporal dimension, resulting in an output feature with more temporal information.

3 Experiments

Extensive experiments were conducted on four representative datasets for video action recognition, and the accuracy was used as the evaluation metric.

3.1 Datasets

Four datasets are used for the experiments, namely HMDB51, MSRDailyAct3D, Diving48 and Breakfast.

The HMDB51 dataset comprises approximately 7 000 video clips, encompassing a total of 51 action categories. These video clips involve some similar actions, with a wealth of action information that cannot be identified solely through static frame images. The dataset defines three data splits, and split 1 is used in the experiment. The MSRDailyAct3D dataset consists of indoor video clips capturing human activities, featuring 16 action categories. Due to minimal background variation in this dataset, the model needs to exhibit robust action modeling capabilities. The Diving48 dataset is a fine-grained dataset of competitive diving videos, consisting of 48 precisely defined diving actions and approximately 18 000 video clips, and each diving action is divided into three sub-stages. As all videos are shot in the same setting with subtle differences between various diving actions, prolonged dynamic fine-grained modeling is necessary. The Breakfast dataset includes 10 complex actions related to breakfast preparation, executed by 52 different individuals across 18 distinct kitchens. This dataset comprises long-duration videos in a natural environment, with an average video duration exceeding 2 min, placing demands on the model ability for long-range modeling.

3.2 Implementation details

The AdamW optimizer was used for model training, and the initial learning rate was 1×10^{-4} . Additionally, ReduceLROnPlateau was used to dynamically adjust the learning rate based on the accuracy. For HMDB51 and Diving48 datasets, we randomly sampled 16 frames uniformly as input; for the MSRDailyAct3D dataset, we uniformly sampled eight frames; for the Breakfast dataset, we randomly sampled 32 frames as input video frames. All video frames from each dataset were cropped to 224 pixel \times 224 pixel before input. Random cropping, random horizontal flipping and normalization were employed as data augmentation techniques during training.

3.3 Main results

To validate the effectiveness of the proposed temporal decoding module, we employed the typical Transformer-based video action classification models (TokShift-Transformer and VideoMAE) which were pre-trained on the Kinetics-400 dataset. We integrated the temporal decoder before the classification layer of these models while keeping the rest of the architecture unchanged. The comparison of the Top-1 accuracy results with and without the temporal decoder for both models is presented in Table 1.

Table 1 Comparison of Top-1 accuracy with and without temporal decoder

Model	Top-1 accuracy/%			
	HMDB51	MSRDailyAct3D	Diving48	Breakfast
TokShift-Transformer	54. 64	73. 44	68. 93	69. 30
TokShift-Transformer with temporal decoder	67. 78	84. 50	76. 80	84. 23
VideoMAE	73. 30	90. 62	75. 33	74. 93
VideoMAE with temporal decoder	80. 52	98. 44	77. 26	77. 46

It is evident that the integration of the proposed temporal decoder into both encoder models significantly improves action classification accuracy. Specifically, on HMDB51, MSRDailyAct3D and Breakfast datasets, the accuracy improvement of TokShift-Transformer with the proposed temporal decoder exceeds 10% compared to that of the original model. Therefore, the proposed temporal decoder can effectively parse temporal dynamic information and enhance the discriminative ability of action classification. On the Diving48 dataset, both models show a performance improvement, indicating that the decoder enhances the overall models fine-grained recognition capability. Furthermore, the inclusion of the decoder also improves the classification performance on the long-range video dataset (Breakfast), demonstrating that the model can alleviate issues related to long-range temporal dependencies.

In addition, further comparisons were conducted by training these two networks for 20 epochs on the HMDB51 dataset, as shown in Fig. 4. The results indicate that the temporal decoder significantly enhances the model ability to extract temporally differentiated features. For the TokShift-Transformer, convergence is achieved in approximately three epochs with the temporal decoder, compared to around eight epochs without it. This improvement in the recognition capability, coupled with a reduction in training iterations, further validates the effectiveness of the proposed temporal decoder.

Table 2 Performance comparison with other temporal decoders on HMDB51 dataset

Temporal decoder	Top-1 accuracy/%		Computing performance/GFLOPs		Params/MB	
	TokShift-Transformer	VideoMAE	TokShift-Transformer	VideoMAE	TokShift-Transformer	VideoMAE
Vis4mer	61.11	78.95	270.09	103.56	87.13	66.46
BERT	66.80	79.54	270.43	101.89	106.94	86.27
Longformer	66.21	79.80	270.84	102.22	110.49	89.82
Proposed temporal decoder	67.78	80.52	270.19	101.97	108.15	87.47

We compared the proposed temporal decoder with Vis4mer, BERT and Longformer, three decoders known for their temporal feature extraction capabilities. The input frame number was 16 with a resolution of 224 pixel \times 224 pixel. As shown in Table 2, Vis4mer achieves lower parameters, but the proposed temporal decoder model, under the TokShift-Transformer baseline, exhibits a more significant improvement in the recognition accuracy compared to Vis4mer. Additionally, the proposed temporal decoder outperforms both BERT and Longformer when considering similar computational complexity and parameters. Notably, the proposed temporal decoder is simpler to implement, facilitating deployment and application. In summary, the temporal decoding module strikes a good balance between the computing performance and computational complexity.

To validate the scalability and generality of the proposed temporal decoder, experiments were conducted on the HMDB51 dataset by inserting the proposed

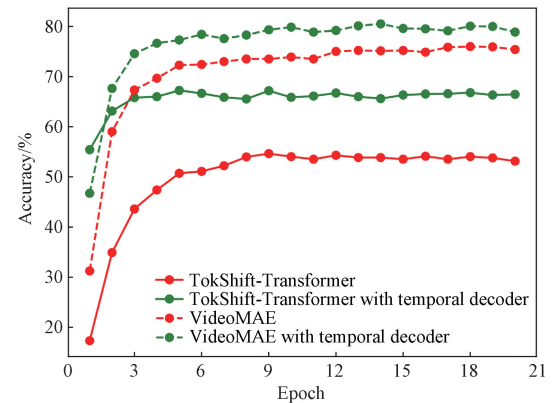


Fig. 4 Training results for different models on HMDB51 dataset

To further validate the effectiveness of the proposed temporal decoder, a performance comparison with other previously proposed efficient temporal decoders was conducted on the HMDB51 dataset. We used both TokShift-Transformer and VideoMAE as encoders for the encoding process. The results are presented in Table 2. The computing performance of a processor is measured in terms of billions of floating point operations it can perform in one second, namely Giga floating point operations per second (GFLOPs). Params refer to the parameters or variables that define the structure and behavior of a statistical or machine learning model.

temporal decoder into various action recognition encoders (backbones) in addition to TokShift-Transformer and VideoMAE. The results are summarized in Table 3. It is demonstrated that integrating the temporal decoder leads to varying degrees of improvement in the recognition accuracy on the HMDB51 dataset for all three backbone networks. This further validates the temporal feature extraction capabilities of the temporal decoder and indicates its versatility in extending to other domains of video understanding.

Table 3 Performance comparison with different encoders on HMDB51 dataset

Encoder	Top-1 accuracy/%	
	Without decoder	With decoder
Timesformer	63.59	69.54
ResNeXt3D-101	64.58	66.14
ViT-B	52.48	61.96

3.4 Ablation experiments

A series of ablation experiments were conducted based on TokShift-Transformer.

3.4.1 Number of queries for video-level action category prediction

To investigate the impact of different query quantities for action category prediction on model performance, various sizes of N_p were used in the experiment. The results are presented in Table 4. It is evident that N_p has varying effects on the experimental results. Initially, as the number of queries increases, the model incorporates richer action information, leading to a continuous improvement in the action recognition accuracy. However, as the number of queries continues to increase, it exhibits a declining trend. Based on the experimental results, a query number of six achieves the best results. Therefore, in subsequent experiments, unless otherwise specified, we set the number of queries to six.

Table 4 Ablation experiment on different numbers of queries for action category prediction on HMDB51 dataset

Number of queries	Top-1 accuracy/%
1	65.29
3	66.14
6	67.78
10	66.80
16	65.42

3.4.2 Number of decoder layers

To assess the impact of different numbers of stacked attention modules in the temporal decoder on the model, various numbers of decoder layers L were used in the experiments. The model performance is presented in Table 5.

Table 5 Ablation experiment on different numbers of decoder layers on HMDB51 dataset

Number of decoder layers	Top-1 accuracy/%
1	65.36
3	66.34
6	67.78
12	66.21

Similar to the impact of the number of queries for action category prediction, the model accuracy on the HMDB51 dataset shows an increasing trend followed by a decline as the number of decoder layers increases. Comparative analyses of the results reveal that the optimal performance is achieved when L is six. As L continues to increase, the accuracy does not improve. This may be attributed to the fact that excessively deep stacking of attention modules can lead to the extraction of overly consistent spatiotemporal features, weakening the model ability to represent differences between various actions and consequently reducing its action recognition

capability.

3.4.3 Cross-time spatial convolution module

We compared the impact of the cross-time spatial convolution module on the accuracy on the HMDB51 dataset. The results are shown in Table 6. Additionally, the effect of a single weight-shared convolution or multiple layers of non-weight-shared convolution was also analyzed when incorporating the cross-time spatial convolution module.

Table 6 Impact of cross-time spatial convolution module on accuracy on HMDB51 dataset

Model	Cross-time spatial convolution	Shared weight	Top-1 accuracy/%
TokShift-Transformer	✗	—	66.27
TokShift-Transformer	✓	✗	66.14
TokShift-Transformer	✓	✓	67.78

The introduction of the cross-time spatial convolution module leads to an improvement in the accuracy by more than 1%. This module models spatial relationships between adjacent temporal regions and integrates with the attention mechanism of the Transformer, aiding in a more comprehensive extraction of spatiotemporal information and thereby enhancing the overall model performance. Additionally, compared to using a single weight-shared convolution, employing multiple layers of non-weight-shared convolution leads to a decline in the model performance. This suggests that an excessive introduction of this module is detrimental to network optimization and increases parameters, adding a burden to the network. Therefore, the decoder is constructed with a single weight-shared convolution.

4 Model Visualization

4.1 Visualization of cross-attention feature maps in decoder

A video clip from the HMDB51 dataset was randomly selected as input to the model and visualized the cross-attention feature maps for each layer of the temporal decoder, as shown in Fig. 5. The horizontal axis represents the temporal locations of video frame features, indicating the time dimension, while the vertical axis represents the sequence in the action category prediction queries.

From Fig. 5, it can be observed that in the first layer of the decoder, the features between action states are relatively chaotic, and the boundaries are not clearly defined. From the second layer to the fifth layer, the temporal information is gradually learned by the network, and corresponding features for each time period are gradually formed, presenting a pattern of vertical lines. By the sixth layer, the model assigns different weights based on the importance of different states within the entire action, aiding the model in better distinguishing

action categories. Furthermore, compared to those of the fourth layer, the feature map weights in the sixth layer tend to be mostly towards zero, reducing the weights of more video frame features and filtering out a significant

amount of redundant information. The attention mechanism segregates the most important parts, further assisting the model in more accurately identifying and determining video actions.

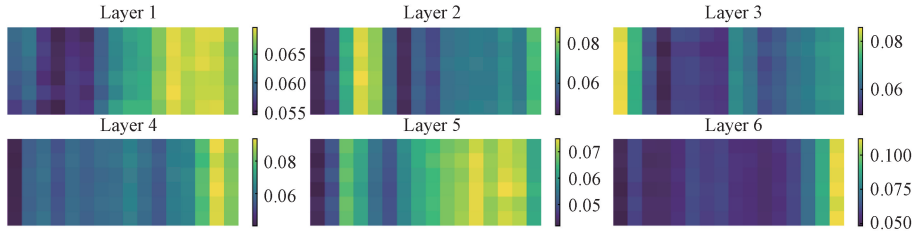


Fig. 5 Visualization of cross-attention feature maps in decoder

4.2 Qualitative analysis

We selected several video clips from the HMDB51 dataset and compared action category predictions between the TokShift-Transformer and the model with the proposed temporal decoder, as shown in Fig. 6. In each case, the odd-numbered rows represent the original video frames, while the even-numbered rows represent

the corresponding attention feature maps from the TokShift-Transformer encoder with the proposed temporal decoder. The entries within parentheses represent the predicted action categories by TokShift-Transformer, while those preceding the parentheses indicate the actual categories predicted after incorporating the proposed decoder.

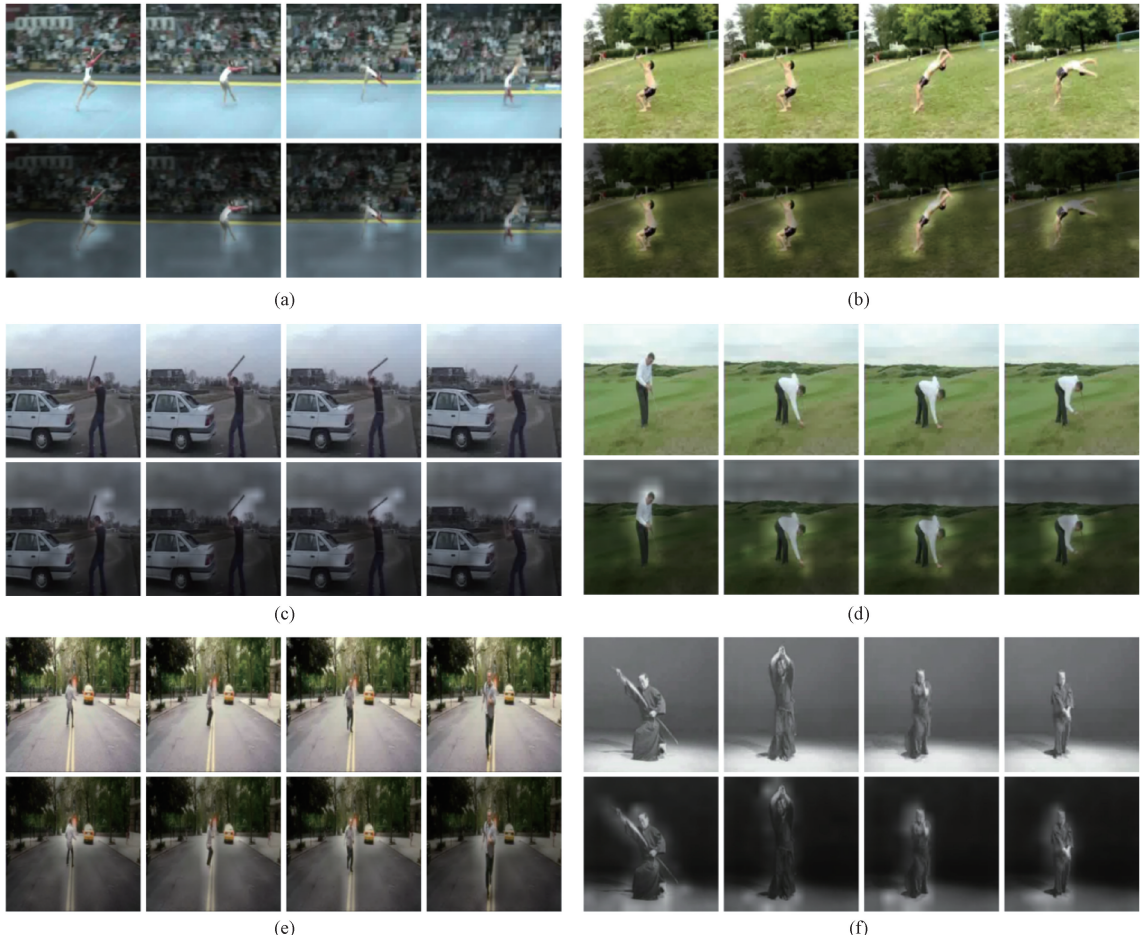


Fig. 6 Qualitative comparisons of samples on HMDB51 dataset: (a) cartwheel (flic_flac); (b) flic_flac (cartwheel); (c) hit (swing_baseball); (d) pick (golf); (e) run (dribble); (f) sword_exercise (draw_sword)

Upon comparison, it is evident that when faced with highly similar actions such as “cartwheel” and “flic_

flac”, misclassifications occur in these video clips by using the original model, whereas the model with the

temporal decoder correctly identifies them. This suggests that the temporal decoder can further extract spatiotemporal features and effectively capture subtle differences in actions. Additionally, comparing the prediction results for the last two clips, it is observed that with the temporal decoder, the model not only focuses on local state information but also expresses global temporal dynamics. This further illustrates that the proposed temporal decoder can analyze contextual information in videos, enhancing the overall temporal modeling capability of the model. Moreover, by examining the attention feature maps, it is apparent that the model emphasizes key parts where actions occur, aiding in the model ability to determine action categories.

5 Conclusions

We have proposed an efficient temporal decoding module for video action recognition based on action classification prediction queries. This module, by pre-constructing a certain number of prediction queries and leveraging the powerful global temporal modeling capability of Transformer attention mechanisms, autonomously learns to classify different actions. The temporal decoder is conceptually and implementation-wise straightforward, making it easily extensible to other action recognition models with relatively low additional cost for efficient temporal modeling, thus improving the action classification accuracy. Moreover, incorporating this temporal decoder enhances the discriminative ability for subtle actions, particularly helpful in scenarios involving similar action sequences. Our experiments demonstrate that the constructed decoder improves the recognition of actions in longer-duration videos, effectively addressing issues related to long-range dependencies. This study may contribute to similar tasks in the field of video understanding in the future.

References

- [1] SOOMRO K, ZAMIR A R, SHAH M. UCF101: a dataset of 101 human actions classes from videos in the wild [EB/OL]. (2012-12-03) [2024-03-01]. <https://arxiv.org/pdf/1212.0402v1.pdf>.
- [2] ZHU Y, LI X Y, LIU C H, et al. A comprehensive study of deep video action recognition [EB/OL]. (2020-12-11) [2024-03-01]. <https://arxiv.org/pdf/2012.06567.pdf>.
- [3] KARPATHY A, TODERICI G, SHETTY S, et al. Large-scale video classification with convolutional neural networks [C]//Proceedings of the IEEE Conference on Computer Vision and Pattern Recognition. New York, USA: IEEE, 2014: 1725-1732.
- [4] JI S W, XU W, YANG M, et al. 3D convolutional neural networks for human action recognition [J]. *IEEE Transactions on Pattern Analysis and Machine Intelligence*, 2013, 35 (1): 221-231.
- [5] HORN B K P, SCHUNCK B G. Determining optical flow [J]. *Artificial Intelligence*, 1981, 17 (1/2/3): 185-203.
- [6] VASWANI A, SHAZER N, PARMAR N, et al. Attention is all you need [EB/OL]. (2023-08-02) [2024-03-01]. <https://arxiv.org/pdf/1212.0402v1.pdf>.
- [7] CARION N, MASSA F, SYNNAEVE G, et al. End-to-end object detection with transformers [M]//Lecture Notes in Computer Science. Cham, Switzerland: Springer International Publishing AG, 2020: 213-229.
- [8] KUEHNE H, JHUANG H, GARROTE E, et al. HMDB: a large video database for human motion recognition [C]//2011 International Conference on Computer Vision. New York, USA: IEEE, 2011: 2556-2563.
- [9] WANG J, LIU Z C, WU Y, et al. Mining actionlet ensemble for action recognition with depth cameras [C]//2012 IEEE Conference on Computer Vision and Pattern Recognition. New York, USA: IEEE, 2012: 1290-1297.
- [10] LI Y W, LI Y, VASCONCELOS N. RESOUND: towards action recognition without representation bias [M]//Lecture Notes in Computer Science. Cham, Switzerland: Springer International Publishing AG, 2018: 520-535.
- [11] KUEHNE H, GALL J, SERRE T. An end-to-end generative framework for video segmentation and recognition [C]//2016 IEEE Winter Conference on Applications of Computer Vision (WACV). New York, USA: IEEE, 2016: 1-8.
- [12] TRAN D, BOURDEV L, FERGUS R, et al. Learning spatiotemporal features with 3D convolutional networks [C]//Proceedings of the IEEE International Conference on Computer Vision. New York, USA: IEEE, 2015: 4489-4497.
- [13] GESSERT N, SCHLÜTER M, SCHLAEFER A. A deep learning approach for pose estimation from volumetric OCT data [J]. *Medical Image Analysis*, 2018, 46: 162-179.
- [14] SIMONYAN K, ZISSERMAN A. Two-stream convolutional networks for action recognition in videos [J]. *Advances in Neural Information Processing Systems*, 2014, 1: 568-576.
- [15] DOSOVITSKIY A, BEYER L, KOLESNIKOV A, et al. An image is worth 16×16 words: Transformers for image recognition at scale [EB/OL]. (2020-10-22) [2024-03-01]. <https://arxiv.org/pdf/2010.11929v1.pdf>.
- [16] BERTASIUS G, WANG H, TORRESANI L. Is space-time attention all you need for video understanding? [EB/OL]. (2021-06-09) [2024-

- [17] 03-01]. <https://arxiv.org/pdf/2102.05095.pdf>.
 ZHANG H, HAO Y B, NGO C W. Token shift transformer for video classification [C]// Proceedings of the 29th ACM International Conference on Multimedia. New York, USA: ACM, 2021: 917-925.
- [18] TONG Z, SONG Y B, WANG J, et al. VideoMAE: masked autoencoders are data-efficient learners for self-supervised video pre-training[EB/OL]. (2022-10-18) [2024-03-01]. <https://arxiv.org/pdf/2203.12602v3.pdf>.
- [19] ISLAM M M, BERTASIUS G. Long movie clip classification with state-space video models [M]//Lecture Notes in Computer Science. Cham, Switzerland: Springer Nature Switzerland AG, 2022: 87-104.
- [20] LIN Z Y, GENG S J, ZHANG R R, et al. Frozen CLIP models are efficient video learners [M]//Lecture Notes in Computer Science. Cham, Switzerland: Springer Nature Switzerland AG, 2022: 388-404.
- [21] NEIMARK D, BAR O, ZOHAR M, et al. Video transformer network[EB/OL]. (2021-08-17) [2024-03-01]. <https://arxiv.org/pdf/2102.00719.pdf>.
- [22] BELTAGY I, PETERS M E, COHAN A. Longformer: the long-document transformer[EB/OL]. (2020-12-02) [2024-03-01]. <https://arxiv.org/pdf/2004.05150.pdf>.
- [23] KALFAOGLU M E, KALKAN S, ALATAN A A. Late temporal modeling in 3D CNN architectures with BERT for action recognition [M]//BARTOLI A, FUSIELLO A, eds. Lecture Notes in Computer Science. Cham, Switzerland: Springer International Publishing AG, 2020: 731-747.
- [24] DEVLIN J, CHANG M W, LEE K, et al. BERT: pre-training of deep bidirectional transformers for language understanding [EB/OL]. (2020-12-02) [2024-03-01]. <https://arxiv.org/pdf/1810.04805.pdf>.

用于动作识别的高效时序解码模块

黄秋波*, 梅建敏, 赵武鹏, 卢怡如, 王梅, 陈德华
 东华大学 计算机科学与技术学院, 上海 201620

摘要: 动作识别作为视频理解领域的基础性任务, 得到了广泛研究和应用。相比图像, 视频媒介增加了时间维度。然而, 目前许多动作识别网络只是对时序信息进行简单平均融合, 或者是由图像的预训练模型迁移而来, 对时序信息的抽取能力较弱。该文提出了一个可拼接在任意动作识别骨干网络上的高效时序解码模块, 以进一步关注视频帧之间的时序关系。该解码器首先初始化一定数量的可学习查询张量, 即视频级的动作类别预测查询张量, 进行自注意力学习后与骨干网络得到的视频帧特征相结合来提取视频上下文信息, 最后再使用这些具有丰富时序特征的预测查询张量作分类预测。在 HMDB51、MSRDailyAct3D、Diving48 及 Breakfast 数据集上将 TokShift-Transformer 和 VideoMAE 作为编码器进行实验。实验结果显示, 与原始模型 TokShift-Transformer 和 VideoMAE 相比, 引入所提出的时序解码器后, Top-1 准确率得到明显提升。在这四个数据集上, TokShift-Transformer 的性能提高超过 11%, 在 VideoMAE 上的准确率也平均提高了近 5%。该工作还将包括 Timesformer 在内的其他动作识别网络作为编码器, 使其与解码器进一步结合。实验结果表明, 在 HMDB51 数据集上, 准确率平均提高 3.5% 以上。代码见 <https://github.com/huangturbo/TempDecoder>。

关键词: 动作识别; 视频理解; 时序关系; 时序解码器; Transformer

DOI: 10.19884/j.1672-5220.202310002

Calculating Sound Absorption Coefficients of Sound-Absorbing Materials Using Flow Resistivity

ZHU Congyun*, SHAO Zhenya, DING Guofang

School of Intelligent Mechatronics Engineering (School of Industrial Design), Zhongyuan University of Technology, Zhengzhou 450007, China

Abstract: To minimize the calculation errors in the sound absorption coefficient resulting from inaccurate measurements of flow resistivity, a simple method for determining the sound absorption coefficient of sound-absorbing materials is proposed. Firstly, the sound absorption coefficients of a fibrous sound-absorbing material are measured at two different frequencies using the impedance tube method. Secondly, utilizing the empirical formulas for the wavenumber and acoustic impedance in the fibrous material, the flow resistivity and porosity of the sound-absorbing materials are calculated using the MATLAB cycle program. Thirdly, based on the values obtained through reverse calculations, the sound absorption coefficient, the real and the imaginary parts of the acoustic impedance of the sound-absorbing material at different frequencies are theoretically computed. Finally, the accuracy of these theoretical calculations is verified through experiments. The experimental results indicate that the calculated values are basically consistent with the measured values, demonstrating the feasibility and reliability of this method.

Keywords: sound-absorbing material; sound absorption coefficient; flow resistivity; acoustic impedance

CLC number: TB527

Document code: A

Article ID: 1672-5220(2025)02-0197-07

Open Science Identity
(OSID)



0 Introduction

Porous materials contain a large number of interconnected pores inside and play a crucial role in sound absorption. As sound waves propagate through the material, the viscosity of the air and the thermal conductivity of the material contribute to a gradual loss of sound energy. Research indicates a strong correlation between porosity and sound absorption performance^[1-3]. If the porosity is too low, the material becomes dense, hindering sound waves from penetrating its interior, and resulting in poor sound absorption. Conversely, if the porosity is excessively high, the material becomes too

loose, allowing sound waves to pass through the pores without sufficient friction, which diminishes sound absorption performance. Additionally, the size of the pore reflects the magnitude of the resistivity encountered by air as the sound wave moves through the material, i.e. the flow resistivity^[4-5]. Therefore, we can assess the acoustic performance of porous sound-absorbing materials by measuring their flow resistivity and conducting acoustic calculations and analyses.

Wang^[6] proposed a method for measuring the flow resistivity of materials in an impedance tube that could measure the sound absorption coefficient of materials using the existing transfer function method. He analyzed the accuracy of measuring the flow resistivity using this method and verified its feasibility through experiments. Li^[7] measured the flow resistivity of porous materials using the direct current method, as well as their sound absorption coefficients using the transfer function method. He found that there was an optimal flow resistivity that enabled the porous sound-absorbing material to achieve its maximum sound absorption coefficient. Wang^[8] designed a device to measure the flow resistivity of different porous materials and employed impedance tubes to measure their sound absorption coefficients. Ma^[9] measured the sound absorption coefficients and flow resistivity of four types of sound-absorbing materials and subsequently performed inverse operations on other parameters of the materials through a differential evolution algorithm. The reliability of the inverse operation results was also verified by experiments. Xiong^[10] added a sealing ring, applied petroleum jelly, and polished the surface of sound-absorbing material samples during flow resistivity measurements, successfully reducing significant errors in the measurements.

The flow resistivity of porous sound-absorbing materials is generally measured by experiments, but due to the interference of the sample preparation effect and environmental factors, the actual measurement results are

Received date: 2023-10-06

Foundation item: National Natural Science Foundation of China (No. 51705545)

* Correspondence should be addressed to ZHU Congyun, email: zcy711126@163.com

Citation: ZHU C Y, SHAO Z Y, DING G F. Calculating sound absorption coefficients of sound-absorbing materials using flow resistivity [J].

Journal of Donghua University (English Edition), 2025, 42(2): 197-203.

often inaccurate^[11]. To avoid calculation errors in sound absorption coefficients resulting from inaccurate experimental measurements of flow resistivity, this study bypasses the experimental measurement process and instead employs theoretical inversion for calculations. The overview of the approach is as follows. Firstly, the sound absorption coefficients of a fibrous sound-absorbing material are measured at two frequencies using the impedance tube method. Secondly, a MATLAB program based on empirical formulas is employed to reverse-calculate the material's flow resistivity and porosity. Thirdly, these parameters are utilized to theoretically predict the sound absorption coefficient and acoustic impedance at other frequencies. Finally, the accuracy of these theoretical predictions is experimentally validated to assess the feasibility of the method.

1 Establishment of Mathematical Model for Calculating Sound Absorption Coefficient

Figure 1 shows the acoustic impedance layout of the sound-absorbing material, in which l is the thickness of the sound-absorbing material; x is the sound path length.

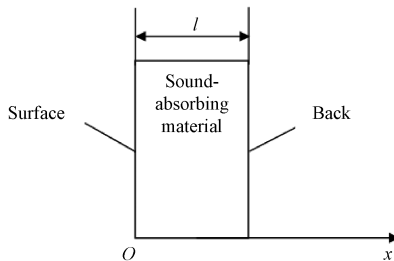


Fig. 1 Acoustic impedance layout of sound-absorbing material

The acoustic impedance at the surface of the sound-absorbing material Z_s at $x=0$ is expressed as^[12]

$$Z_s = \rho c \frac{Z_b \cosh(\gamma l) + \rho c \sinh(\gamma l)}{Z_b \sinh(\gamma l) + \rho c \cosh(\gamma l)}, \quad (1)$$

where Z_b is the acoustic impedance at the back of the sound-absorbing material; ρ is the density of the sound-absorbing material; c is the sound speed in the sound-absorbing material; γ is the wavenumber of the sound.

$$\begin{cases} \rho_1(\omega) = 1.2 + [-0.0364(\rho_0 f_1 / \sigma)^{-2} - j0.1144(\rho_0 f_1 / \sigma)^{-1}]^{\frac{1}{2}}, \\ K_1(\omega) = 101320 \times \frac{j29.64 + [2.82(\rho_0 f_1 / \sigma)^{-2} + j24.9(\rho_0 f_1 / \sigma)^{-1}]^{\frac{1}{2}}}{j21.17 + [2.82(\rho_0 f_1 / \sigma)^{-2} + j24.9(\rho_0 f_1 / \sigma)^{-1}]^{\frac{1}{2}}}, \end{cases} \quad (8)$$

$$\begin{cases} \rho_2(\omega) = 1.2 + [-0.0364(\rho_0 f_2 / \sigma)^{-2} - j0.1144(\rho_0 f_2 / \sigma)^{-1}]^{\frac{1}{2}}, \\ K_2(\omega) = 101320 \times \frac{j29.64 + [2.82(\rho_0 f_2 / \sigma)^{-2} + j24.9(\rho_0 f_2 / \sigma)^{-1}]^{\frac{1}{2}}}{j21.17 + [2.82(\rho_0 f_2 / \sigma)^{-2} + j24.9(\rho_0 f_2 / \sigma)^{-1}]^{\frac{1}{2}}}, \end{cases} \quad (9)$$

When the sound-absorbing material is backed by a rigid wall, i.e., $Z_b=0$, then the acoustic impedance Z_s at $x=0$ is

$$Z_s = Z_0 \coth(\gamma l), \quad (2)$$

where Z_0 is the acoustic impedance of the sound-absorbing material, and $Z_0 = \rho c$.

In this paper, the glass fiber is used as the sound-absorbing material, whose bulk elastic modulus $K(\omega)$ and density $\rho(\omega)$ can be expressed as^[13]

$$\begin{aligned} K(\omega) &= 101320 \times \\ &j29.64 + [2.82(\rho_0 f / \sigma)^{-2} + j24.9(\rho_0 f / \sigma)^{-1}]^{\frac{1}{2}}, \\ &j21.17 + [2.82(\rho_0 f / \sigma)^{-2} + j24.9(\rho_0 f / \sigma)^{-1}]^{\frac{1}{2}}, \end{aligned} \quad (3)$$

$$\begin{aligned} \rho(\omega) &= 1.2 + [-0.0364(\rho_0 f / \sigma)^{-2} - \\ &j0.1144(\rho_0 f / \sigma)^{-1}]^{\frac{1}{2}}, \end{aligned} \quad (4)$$

where ρ_0 is the air density, kg/m^3 ; f is the acoustic frequency, Hz; σ is the flow resistivity, $\text{N}\cdot\text{s}/\text{m}^4$; ω is the angular frequency.

The wavenumber $\gamma(\omega)$ and acoustic impedance $Z_0(\omega)$ of the sound wave propagating in sound-absorbing materials are^[14]

$$\gamma(\omega) = \omega \left[\frac{\rho(\omega)}{K(\omega)} \right]^{\frac{1}{2}}, \quad (5)$$

$$Z_0(\omega) = \frac{1}{\phi} [\rho(\omega) K(\omega)]^{\frac{1}{2}}, \quad (6)$$

$$\alpha = 1 - \left(\frac{Z_s - \rho_0 c_0}{Z_s + \rho_0 c_0} \right)^2, \quad (7)$$

where ϕ is the porosity; α is the sound absorption coefficient; c_0 is the sound speed in air.

2 MATLAB Cycle Program Calculation Method

The sound absorption coefficient was measured at two different frequencies. The sound absorption coefficient at frequency f_1 is α_1 ; the sound absorption coefficient at frequency f_2 is α_2 . Therefore, according to Eqs. (3) and (4), the density and bulk elastic modulus of the sound-absorbing material at two frequencies are as follows:

where $\rho_i(\omega)$ ($i=1, 2$) and $K_{0i}(\omega)$ ($i=1, 2$) represent the density and the bulk elastic modulus at two frequencies, respectively.

By substituting Eqs. (8) and (9) into Eqs. (5)

and (6), respectively, the wavenumbers and acoustic impedance of sound waves propagating in the sound-absorbing material at two frequencies were obtained:

$$\left\{ \begin{array}{l} \gamma_1(\omega) = \omega \left[\frac{\rho_1(\omega)}{K_1(\omega)} \right]^{\frac{1}{2}} = \omega \left\{ \frac{1.2 + [-0.0364(\rho_0 f_1/\sigma)^{-2} - j0.1144(\rho_0 f_1/\sigma)^{-1}]^{\frac{1}{2}}}{101320 \times \frac{j29.64 + [2.82(\rho_0 f_1/\sigma)^{-2} + j24.9(\rho_0 f_1/\sigma)^{-1}]^{\frac{1}{2}}}{j21.17 + [2.82(\rho_0 f_1/\sigma)^{-2} + j24.9(\rho_0 f_1/\sigma)^{-1}]^{\frac{1}{2}}}} \right\}^{\frac{1}{2}}, \\ Z_{01}(\omega) = \frac{1}{\phi} [\rho_1(\omega) K_1(\omega)]^{\frac{1}{2}} = \frac{1}{\phi} \left\{ 1.2 + [-0.0364(\rho_0 f_1/\sigma)^{-2} - j0.1144(\rho_0 f_1/\sigma)^{-1}]^{\frac{1}{2}} \right\}^{\frac{1}{2}} \times \\ \left\{ 101320 \times \frac{j29.64 + [2.82(\rho_0 f_1/\sigma)^{-2} + j24.9(\rho_0 f_1/\sigma)^{-1}]^{\frac{1}{2}}}{j21.17 + [2.82(\rho_0 f_1/\sigma)^{-2} + j24.9(\rho_0 f_1/\sigma)^{-1}]^{\frac{1}{2}}} \right\}^{\frac{1}{2}}, \end{array} \right. \quad (10)$$

$$\left\{ \begin{array}{l} \gamma_2(\omega) = \omega \left[\frac{\rho_2(\omega)}{K_2(\omega)} \right]^{\frac{1}{2}} = \omega \left\{ \frac{1.2 + [-0.0364(\rho_0 f_2/\sigma)^{-2} - j0.1144(\rho_0 f_2/\sigma)^{-1}]^{\frac{1}{2}}}{101320 \times \frac{j29.64 + [2.82(\rho_0 f_2/\sigma)^{-2} + j24.9(\rho_0 f_2/\sigma)^{-1}]^{\frac{1}{2}}}{j21.17 + [2.82(\rho_0 f_2/\sigma)^{-2} + j24.9(\rho_0 f_2/\sigma)^{-1}]^{\frac{1}{2}}}} \right\}^{\frac{1}{2}}, \\ Z_{02}(\omega) = \frac{1}{\phi} [\rho_2(\omega) K_2(\omega)]^{\frac{1}{2}} = \frac{1}{\phi} \left\{ 1.2 + [-0.0364(\rho_0 f_2/\sigma)^{-2} - j0.1144(\rho_0 f_2/\sigma)^{-1}]^{\frac{1}{2}} \right\}^{\frac{1}{2}} \times \\ \left\{ 101320 \times \frac{j29.64 + [2.82(\rho_0 f_2/\sigma)^{-2} + j24.9(\rho_0 f_2/\sigma)^{-1}]^{\frac{1}{2}}}{j21.17 + [2.82(\rho_0 f_2/\sigma)^{-2} + j24.9(\rho_0 f_2/\sigma)^{-1}]^{\frac{1}{2}}} \right\}^{\frac{1}{2}}, \end{array} \right. \quad (11)$$

where $\gamma_i(\omega)$ ($i=1, 2$) and $Z_{0i}(\omega)$ ($i=1, 2$) represent the wavenumbers and acoustic impedance at two frequencies, respectively.

If the back of the sound-absorbing material is a rigid wall, the surface acoustic impedance of the sound-absorbing material at two frequencies respectively are

$$\begin{aligned} Z_{s1} &= Z_{01} \coth(\gamma_1 l) = \frac{1}{\phi} \left\{ 1.2 + [-0.0364(\rho_0 f_1/\sigma)^{-2} - j0.1144(\rho_0 f_1/\sigma)^{-1}]^{\frac{1}{2}} \right\}^{\frac{1}{2}} \times \\ &\quad \left\{ 101320 \times \frac{j29.64 + [2.82(\rho_0 f_1/\sigma)^{-2} + j24.9(\rho_0 f_1/\sigma)^{-1}]^{\frac{1}{2}}}{j21.17 + [2.82(\rho_0 f_1/\sigma)^{-2} + j24.9(\rho_0 f_1/\sigma)^{-1}]^{\frac{1}{2}}} \right\}^{\frac{1}{2}} \times \\ &\quad \coth \left(\omega \left\{ \frac{1.2 + [-0.0364(\rho_0 f_1/\sigma)^{-2} - j0.1144(\rho_0 f_1/\sigma)^{-1}]^{\frac{1}{2}}}{101320 \times \frac{j29.64 + [2.82(\rho_0 f_1/\sigma)^{-2} + j24.9(\rho_0 f_1/\sigma)^{-1}]^{\frac{1}{2}}}{j21.17 + [2.82(\rho_0 f_1/\sigma)^{-2} + j24.9(\rho_0 f_1/\sigma)^{-1}]^{\frac{1}{2}}}} \right\}^{\frac{1}{2}} l \right), \end{aligned} \quad (12)$$

$$\begin{aligned} Z_{s2} &= Z_{02} \coth(\gamma_2 l) = \frac{1}{\phi} \left\{ 1.2 + [-0.0364(\rho_0 f_2/\sigma)^{-2} - j0.1144(\rho_0 f_2/\sigma)^{-1}]^{\frac{1}{2}} \right\}^{\frac{1}{2}} \times \\ &\quad \left\{ 101320 \times \frac{j29.64 + [2.82(\rho_0 f_2/\sigma)^{-2} + j24.9(\rho_0 f_2/\sigma)^{-1}]^{\frac{1}{2}}}{j21.17 + [2.82(\rho_0 f_2/\sigma)^{-2} + j24.9(\rho_0 f_2/\sigma)^{-1}]^{\frac{1}{2}}} \right\}^{\frac{1}{2}} \times \\ &\quad \coth \left(\omega \left\{ \frac{1.2 + [-0.0364(\rho_0 f_2/\sigma)^{-2} - j0.1144(\rho_0 f_2/\sigma)^{-1}]^{\frac{1}{2}}}{101320 \times \frac{j29.64 + [2.82(\rho_0 f_2/\sigma)^{-2} + j24.9(\rho_0 f_2/\sigma)^{-1}]^{\frac{1}{2}}}{j21.17 + [2.82(\rho_0 f_2/\sigma)^{-2} + j24.9(\rho_0 f_2/\sigma)^{-1}]^{\frac{1}{2}}}} \right\}^{\frac{1}{2}} l \right). \end{aligned} \quad (13)$$

The sound absorption coefficients at two frequencies are

$$\alpha_1 = 1 - \left(\frac{Z_1 - \rho_0 c_0}{Z_1 + \rho_0 c_0} \right)^2, \quad (14)$$

$$\alpha_2 = 1 - \left(\frac{Z_2 - \rho_0 c_0}{Z_2 + \rho_0 c_0} \right)^2. \quad (15)$$

From Eqs. (12)–(15), it can be seen that the flow resistivity σ and porosity ϕ are unknown. Solving these two unknowns using general methods is relatively difficult, so it is necessary to use a MATLAB cyclic program to solve this problem.

3 Theoretical Calculation and Experimental Verification

3.1 Experimental measurement of sound absorption coefficient

The impedance tube method, also known as the standing wave ratio method, is a method to measure the absorption coefficient of sound-absorbing materials utilizing an impedance tube^[15–16]. Figure 2 presents a schematic diagram of the impedance tube method.

The testing steps are outlined below.

- 1) Place the tested material sample at the end of the impedance tube and ensure that it is sealed tightly.
- 2) Use a speaker to emit a single-frequency sound signal that propagates through the pipeline and creates standing waves.
- 3) Use sensors to measure the sound pressures at different positions within the pipeline, and obtain the locations and amplitudes of the maximum and minimum sound pressure values.
- 4) Calculate the standing wave ratio using the measured sound pressures, and subsequently determine

the sound absorption coefficient at that frequency.

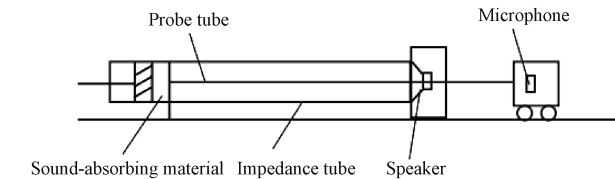


Fig. 2 Schematic diagram of impedance tube method

It is assumed that the sound wave in the impedance tube is positive along the negative direction of x ; the incident sound pressure, the reflected sound pressure and the reflection coefficient are denoted as P_i , P_r and r , respectively.

When P_i and P_r are in phase, the maximum measured pressure P_{\max} is described by

$$|P_{\max}| = |P_0| \times (1 + |r|), \quad (16)$$

where P_0 is the pressure of the air.

When P_i and P_r are in reverse phase, the minimum measured pressure P_{\min} is described by

$$|P_{\min}| = |P_0| \times (1 - |r|). \quad (17)$$

The standing wave ratio G is expressed as

$$G = \frac{|P_{\max}|}{|P_{\min}|} = \frac{1 + |r|}{1 - |r|}. \quad (18)$$

The absorption coefficient α is expressed as

$$\alpha = 1 - |r|^2 = \frac{4G}{(G + 1)^2}. \quad (19)$$

The flowchart illustrating the measurement of the sound absorption coefficient is presented in Fig. 3. The corresponding experimental setup is identical to that used in our previous work^[17].

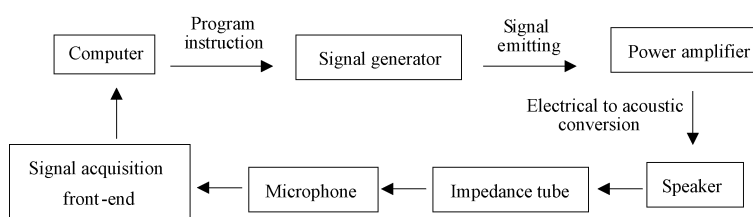


Fig. 3 Flowchart for measuring sound absorption coefficient

3.2 Theoretical calculation and verification

The sound absorption coefficients of the sound-absorbing materials with different thicknesses at 500 Hz and 1 000 Hz were measured, respectively. Then, the flow resistivity and porosity at different thicknesses were derived using the MATLAB cycle program. The experimentally measured and the theoretically calculated acoustic properties of the sound-absorbing materials are presented in Table 1.

Table 1 illustrates that the porosity of the sound-

absorbing material remains constant, even as the thickness increases. This consistency is attributed to the porosity being inherently defined by the material's structural characteristics. However, the flow resistivity increases with increasing the thickness. This increase is due to the greater number of pores and the longer pathways that air must travel through within the thicker material, leading to the heightened flow resistivity. This behavior is consistent with the sound-absorbing properties of the material.

Table 1 Experimentally measured and theoretically calculated acoustic properties of sound-absorbing materials

Thickness/mm (measured)	Absorption coefficient (measured)		Porosity/% (calculated)	Flow resistivity/(N·s/m ⁴) (calculated)
	500 Hz	1 000 Hz		
50	0.91	0.87	2	15 905
100	0.90	0.85	2	20 688
150	0.93	0.87	2	24 048
200	0.94	0.89	2	26 829
250	0.95	0.91	2	28 912
300	0.96	0.93	2	30 830

After calculating the flow resistivity using the MATLAB cycle program, the sound absorption coefficient, as well as the real and imaginary parts of the acoustic impedance, was measured at frequencies of 200, 500, 1 000, 1 500, 2 000, 2 500, 3 000, 3 500 and 4 000 Hz. The experimentally measured values were then compared with the theoretically calculated values for the corresponding frequencies (Figs. 4–6). These comparisons were conducted using sound-absorbing materials with different thicknesses, each with a porosity of 2% and a rigid back wall.

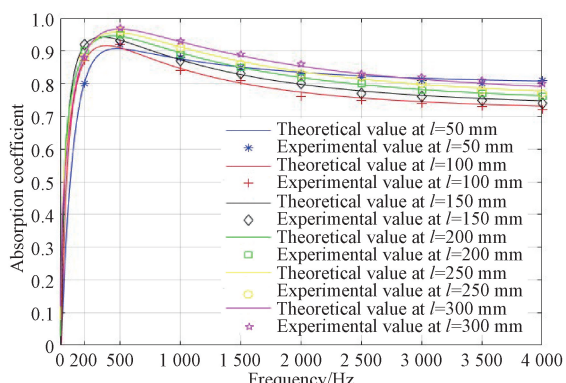


Fig. 4 Comparison of theoretical and experimental sound absorption coefficients versus frequency for sound-absorbing materials at different thicknesses

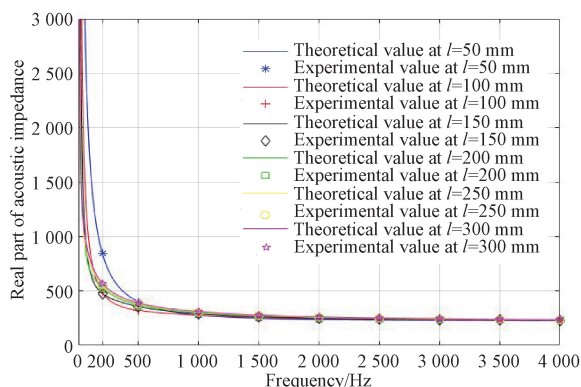


Fig. 5 Comparison of theoretical and experimental real part of acoustic impedance versus frequency for sound-absorbing materials at different thicknesses

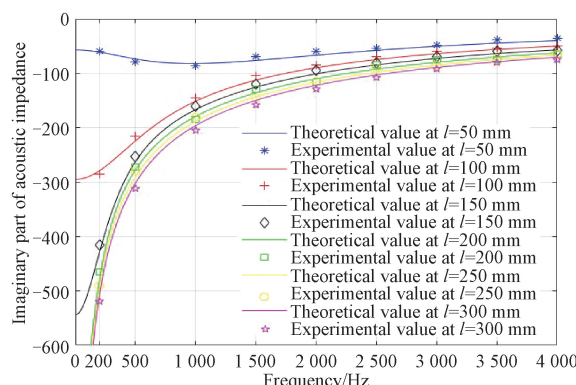


Fig. 6 Comparison of theoretical and experimental imaginary part of acoustic impedance versus frequency for sound-absorbing materials at different thicknesses

From Figs. 4–6, it is evident that the theoretically calculated values are basically consistent with the experimentally measured values.

4 Conclusions

In this study, a simple method for calculating the sound absorption coefficient of the sound-absorbing material theoretically was provided. Firstly, the sound absorption coefficient of the sound-absorbing material at two frequencies was measured in the sound-absorbing material by the impedance tube method. Then, according to the empirical formulas of wavenumber and acoustic impedance in the fibrous material, the flow resistivity of the sound-absorbing material was calculated by using the MATLAB cycle program. Secondly, by changing the thickness of the sound-absorbing material and using the flow resistivity obtained by the reverse operation, the absorption coefficient, the real part of the acoustic impedance and the imaginary part of the acoustic impedance of the sound-absorbing material at different frequencies were calculated, and the relationship between the frequency and them was investigated. Finally, the calculated sound absorption coefficient, as well as the real and imaginary parts of the acoustic impedance was compared with the measured values. The results show that the theoretically calculated values are basically

consistent with the experimentally measured values, which verifies the feasibility and reliability of calculating the sound absorption coefficient by using the flow resistivity obtained by the reverse operation.

References

- [1] ZHU R X, LI J, BI W L, et al. Study on inorganic porous sound absorption materials [J]. *Journal of University of Science and Technology Liaoning*, 2017, 40(3) : 194-199. (in Chinese)
- [2] WU L, LIU M, LIU X W, et al. Optimal design of structural parameters of multi-layer porous sound-absorbing materials [J]. *Journal of Applied Acoustics*, 2021, 40(3) : 449-456. (in Chinese)
- [3] YANG M L, FENG T, JIA Y Q, et al. Hybrid calculation method for normal absorption coefficient of foam material under air backing [J]. *Noise and Vibration Control*, 2018, 38 (2) : 42-44, 76. (in Chinese)
- [4] XIANG J H, LIAO R D, PU D Y. Performance of sound-absorbing material based on flow resistivity [J]. *Transactions of Beijing Institute of Technology*, 2009, 29(11) : 1018-1021, 1034. (in Chinese)
- [5] BI Y Z. Development and experimental study of steady state airflow resistivity measurement system for ultra-thin porous materials [D]. Hefei: Hefei University of Technology, 2022. (in Chinese)
- [6] WANG P. A study on the acoustic measurement methods of static flow resistivity [D]. Nanjing: Nanjing University, 2013. (in Chinese)
- [7] LI Y C. Study on sound absorption properties of porous materials [D]. Qinhuangdao: Yanshan University, 2021. (in Chinese)
- [8] WANG L H. Analysis and optimization of sound absorption performance of porous material used in automobile [D]. Changchun: Jilin University, 2017. (in Chinese)
- [9] MA W T. Analysis and optimization of sound absorption and insulation properties of acoustic materials for vehicle high frequency noise [D]. Changchun: Jilin University, 2021. (in Chinese)
- [10] XIONG X Z. Research on measurement for acoustic performance of automotive porous sound absorbing materials [D]. Shanghai: Shanghai University of Engineering Science, 2021. (in Chinese)
- [11] National Standardization Administration of the People's Republic of China. Acoustics – materials for acoustical applications – determination of airflow resistance: GB/T 25077—2010 [S]. Beijing: Standards Press of China, 2010. (in Chinese)
- [12] YU C S, LUO Z, LUO H T, et al. Research progress on acoustic model of porous sound absorbing materials and measurement method of its characteristic parameters [J]. *Materials Reports*, 2002, 36(4) : 226-236. (in Chinese)
- [13] ZHU C Y. Research on theories and methods of active sound absorption [D]. Wuhan: Huazhong University of Science and Technology, 2005. (in Chinese)
- [14] ZHANG R Q, ZHU C Y, DING G F, et al. Active absorption of perforated plate based on airflow [J]. *Journal of Donghua University (English Edition)*, 2022, 39(6) : 590-596.
- [15] National Standardization Administration of the People's Republic of China. Acoustic—determination of sound absorption coefficient and impedance in impedance tubes – part 1: method using standing wave ratio: GB/T 18696.1—2004 [S]. Beijing: Standards Press of China, 2004. (in Chinese)
- [16] WANG X L, LIU B L, YANG J, et al. Utilizing vector hydrophones to achieve an active anechoic terminal in an acoustic tube [J]. *Chinese Journal of Acoustics*, 2019, 38(2) : 201-214.
- [17] ZHU C Y, ZHANG S Q, DING G F. Semi-active sound absorption method with acoustic impedance matching [J]. *Journal of Donghua University (English Edition)*, 2025, 42(1) : 64-70.

用流阻率计算吸声材料吸声系数

朱从云^{*}, 邵镇亚, 丁国芳

中原工学院 智能机电工程学院(工业设计学院), 河南 郑州 450007

摘要:为了降低由于流阻率测量不准确而引起的吸声系数计算误差,提出了一种计算吸声材料吸声系数的简便方法。首先,通过阻抗管法测量出吸声材料的两个频率的吸声系数,根据纤维材料的波数和声阻抗的经验公式,利用 MATLAB 循环程序逆算出吸声材料的流阻率。其次,计算出不同频率下吸声材料的理论吸声系数、阻抗实部和阻抗虚部。最后,通过试验验证理论计算值的正确性。多组试验结果表明,理论计算值与试验测量值基本一致,验证了此方法的可行性和可靠性。

关键词:吸声材料; 吸声系数; 流阻率; 声阻抗

Corneal Topographic Restoration Imaging Based on Placido Disc

WAN Xuanrun¹, WANG Chaoxing¹, HU Jun^{2, 3}, JIANG Jian^{4, 5*}, LI Kangmei^{1*}

1. College of Mechanical Engineering, Donghua University, Shanghai 201620, China

2. Institute of Artificial Intelligence, Donghua University, Shanghai 201620, China

3. Shanghai Industrial Big Data Engineering Technology Research Center, Shanghai 201620, China

4. Eye Hospital, Wenzhou Medical University, Wenzhou 325000, China

5. Zhejiang Eye Hospital, Wenzhou 325000, China

Abstract: Corneal topography serves as an essential reference for diagnostic treatment in ophthalmology. Accurate corneal topography is crucial for clinical practice. In this study, the refractive power calculation was performed based on the initial corneal information collected using the Placido disc. A corneal point cloud model was established in polar coordinates, and an interpolation algorithm was proposed to fill missing points of the local bicubic B-spline by searching control points in the self-defined interpolation matrix. The grid interpolation of the point cloud information and the smooth imaging of the final topographic map were achieved by Delaunay triangulation and Gaussian kernel function smoothing. Experiment results show that the proposed interpolation algorithm has higher accuracy than previous algorithms. The mean absolute error between the measured diopter of the original detection and the reconstructed is less than 0.300 D, indicating that this algorithm is feasible.

Keywords: corneal topography; Placido disc; point cloud model; bicubic B-spline; Gaussian kernel function

CLC number: R778

Article ID: 1672-5220(2025)02-0204-09

Document code: A

Open Science Identity
(OSID)



0 Introduction

The cornea is the most important refractive physiological structure before light enters the retina, and its susceptibility to deformation is a significant factor contributing to ocular diseases such as myopia and keratoconus^[1-3]. Corneal topography provides a quantitative, color-coded representation of corneal surface refraction and other information displayed in layers. It reflects the true three-dimensional shape of the cornea and serves as an essential reference in the field of ophthalmology for keratomileusis fitting, pre-operative and post-operative keratomileusis examinations and other

ophthalmic treatments^[4-6]. The Placido disc is an important instrument for collecting information from various points on the cornea^[7-8]. By processing the reflected light from the corneal surface, it is possible to obtain preliminary information about the corneal surface, which is the basis for computerized corneal topography generation.

In the field of computerized corneal topography, Xu et al.^[9] used ray inverse tracking with edge detection to extract subpixel data from the Placido disc ring for corneal topography imaging. However, this method relies on the assumption of an ellipsoidal corneal surface, resulting in a correction to the standard ellipsoidal surface. Zhou et al.^[10] proposed an improved Shepard corneal surface interpolation method. It exhibited slightly poor accuracy due to the limitation of the principles of the interpolation algorithm, and it was computationally intensive and time-consuming when dealing with a large number of missing points. Florindo et al.^[11] performed image boundary segmentation and reconstruction based on the Mumford-Shah algorithm. However, the whole process was cumbersome and complicated, which made it difficult to meet the practical application requirements.

The point cloud model is one of the best ways to describe the corneal surface. In response to the challenges posed by limited accuracy and computational complexity in the previously mentioned restoration algorithm, this study introduces a corneal surface missing-point filling algorithm based on bicubic B-spline. Building on the established polar coordinate corneal point cloud model, the algorithm employs Delaunay triangulation for mesh interpolation and incorporates a Gaussian kernel function for data point convolution smoothing. This approach is expected to achieve the high-precision reconstruction of computer-generated corneal topographic images.

Received date: 2024-01-05

Foundation item: Shanghai Science and Technology Program, China (No. 20DZ2251400)

* Correspondence should be addressed to JIANG Jian, email: jiangjianwmu@wmu.edu.cn; LI Kangmei, email: lkm718@126.com

Citation: WAN X R, WANG C X, HU J, et al. Corneal topographic restoration imaging based on Placido disc [J]. *Journal of Donghua University (English Edition)*, 2025, 42(2): 204-212.

1 Acquisition and Transformation of Placido Disk Detection Images

1.1 Image acquisition of Placido disc

The Placido disc is composed of a series of black and white concentric rings centered on the optic axis to detect the cornea of the instrument^[12], as shown in Fig. 1. For the Placido disc image acquisition to the imaging process, the acquisition system consists of the Placido disc, the projector and the charge-coupled

device (CCD) image acquisition system. Light is transmitted through the white concentric rings projected onto the corneal surface from the center to the peripheral region in turn, the entire cornea light is reflected to the CCD, and the individual pixels reflected from each point are converted into digital signals by the CCD. At the same time, the imaging digital signal is analyzed and processed by the image acquisition system to calculate the characteristic information of each collected point, and the final corneal imaging is processed by the computer.

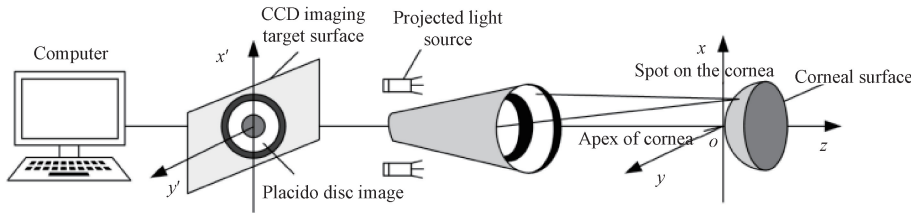


Fig. 1 Placido disc image acquisition to imaging procedure

1.2 Diopter conversion

The corneal information collected as described above is processed mainly as the curvature information of corneal points. The diopter reflects the ability of the eye to refract light and is one of the most important indicators for physicians in clinical practice, as well as the main corneal diagnostic outcome data used to present corneal topography.

The axial diopter provides a good representation of the overall shape of the cornea, and it is generally used to outline the overall shape of the corneal surface^[13]. The schematic diagram of the axial refraction is shown in Fig. 2. The corneal vertex is used as the reference point, and the center of all light is placed in the axial direction of the diopter. In Fig. 2, A represents a point on the cornea, and its coordinates are (x_A, y_A) . The dashed line indicates the normal direction at point A and intersects the coordinate axis at A' . The distance between point A and A' is denoted as r_A and the slope angle is represented by α .

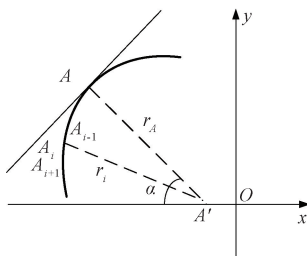


Fig. 2 Schematic diagram of axial refraction

r_A can be depicted as follows:

$$r_A = \frac{y_A}{\sin \alpha}. \quad (1)$$

Thus, the axial diopter D_A can be obtained from the relationship between the diopter and curvature transformation:

$$D_A = \frac{n - 1}{r_A}, \quad (2)$$

where n is the corneal refractive index and $n=1.3375$.

An instantaneous diopter is used to characterize the features of the corneal surface and corresponds to the local radius of the cornea curvature^[14]. Considering the aspheric nature of the cornea, the instantaneous diopter can better describe the true curvature radius of the cornea. Assuming that three adjacent points on the same corneal meridian can be approximated as an arc of a circle, each point is the same distance from the center of the circle. If the coordinates of the three adjacent points on the same meridian are (x_{i-1}, y_{i-1}) , (x_i, y_i) and (x_{i+1}, y_{i+1}) , the center of the arc is represented by the coordinates (x_A, y_A) , and the radius of curvature is denoted as r_i , the following equations can be set out:

$$\begin{cases} (x_{i-1}-x_A)^2 + (y_{i-1}-y_A)^2 = r_i^2, \\ (x_i-x_A)^2 + (y_i-y_A)^2 = r_i^2, \\ (x_{i+1}-x_A)^2 + (y_{i+1}-y_A)^2 = r_i^2. \end{cases} \quad (3)$$

The relationship between (x_A, y_A) and r_i can be found according to Eq. (3) :

$$x_A = \frac{(x_i^2+y_i^2)(y_{i-1}-y_{i+1})+(x_{i-1}^2+y_{i-1}^2)(y_{i+1}-y_i)+(x_{i+1}^2+y_{i+1}^2)(y_i-y_{i-1})}{2[(x_i-x_{i-1})(y_i-y_{i+1})-(x_i-x_{i+1})(y_i-y_{i-1})]}, \quad (4)$$

$$y_A = \frac{[y_{i-1} + y_i + (x_i + x_{i-1} - 2x_A)(x_i - x_{i-1})]}{2(y_i - y_{i-1})}, \quad (5)$$

$$r_i = \sqrt{(x_i - x_A)^2 + (y_i - y_A)^2}. \quad (6)$$

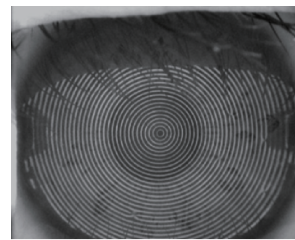
The instantaneous diopter can be obtained from the relationship between the diopter and curvature transformation:

$$D_i = \frac{n - 1}{r_i} = \frac{0.3375}{r_i}. \quad (7)$$

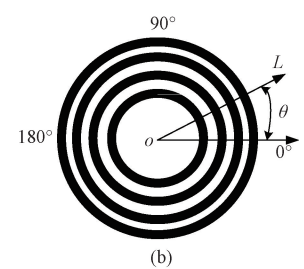
2 Corneal Point Cloud Model Analysis Imaging

2.1 Polarization of coordinates

Due to the large number of corneal data points collected, it is difficult to determine the coordinates for the establishment of the point cloud model in a rectangular coordinate system. Given the characteristics of the images acquired by the Placido disc, the point cloud coordinate system is established in polar coordinates in this study. This can be seen in Fig. 3 (a) which represents a schematic diagram of the Placido disc projected onto the human eye. Figure 3 (b) shows a schematic of the resulting polar coordinate system, where L is the distance from the point on the image to the center of the cornea, and θ is the angle of the point away from the polar axis.



(a)



(b)

Fig. 3 Schematic of resulting polar coordinate system: (a) Placido disc projected onto human eye; (b) polar coordinate system

2.2 Missing-point filling based on bicubic B-splines

Ideally, the Placido disc can collect all the reflected corneal data points. However, eyelash blockage and other reasons cause a large number of missing data points during the actual collection process. The missing data points lead to a pronounced discontinuity in the point cloud model, as shown in Fig. 4, which affects the subsequent corneal three-dimensional imaging thereby affecting the accuracy of the topographic map. The idea of B-splines is to use a flexible strip that is tough enough to pass through the selected interpolated data points under stresses to form a smooth curve or surface, thus enabling the interpolation of unknown points^[15-16]. In this study, the missing data points are interpolated and filled by fitting a local bicubic B-spline surface.

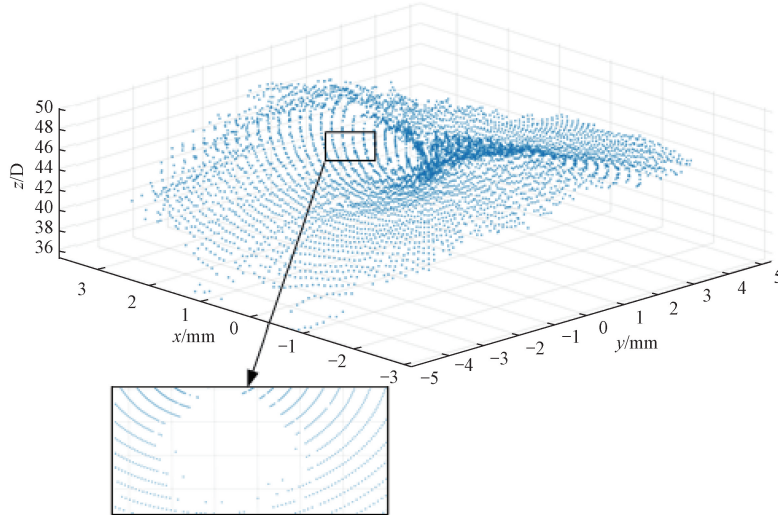


Fig. 4 Schematic of missing points in point cloud

Let the set of discrete points in three-dimensional space be $T = \{(x, y, D_i)\}$ and T is approximated by $m \times n$ bicubic B-spline surface slices. These $m \times n$ bicubic B-spline surface patches are represented by the control mesh volume $F_{(i+p)(j+l)}$, which is composed of the surrounding 16 control points. The resulting bicubic B-spline interpolation function is

$$F(x, y) = \sum_{p=0}^3 \sum_{l=0}^3 B_p(s) B_l(\alpha) F_{(i+p)(j+l)}, \quad (8)$$

where the double summation $\sum_{p=0}^3 \sum_{l=0}^3$ iterates over the 4×4 control points and computes the weighted contribution of each; B_p and B_l are the B-spline basis functions that determine the influence of the control points in the x - and y -directions; s and α are normalized parameters indicating the relative position of x and y within the grid cell; $F_{(i+p)(j+l)}$ represents the known function values at the control grid points $(i+p, j+l)$, and contributes to the

value of $F(x, y)$. The bicubic B-spline interpolation formula represents the function value at position (x, y) . Equation (8) calculates the value at any point (x, y) by performing a weighted average of these control points and basis functions, thus achieving bicubic B-spline interpolation. The basis function of the bicubic B-spline for this study is

$$\begin{cases} B_0(u) = (1 - 3u + 3u^2 - u^3)/6, \\ B_1(u) = (4 - 6u^2 + 3u^3)/6, \\ B_2(u) = (1 + 3u + 3u^2 - 3u^3)/6, \\ B_3(u) = u^3/6, \end{cases} \quad (9)$$

where u represents the parameter value and defines the position of the current calculated point in the node interval. Specifically, u is a normalized parameter that typically takes on values in a node interval, typically in the range $[0, 1]$. As a point moves along a curve from one node to another, u represents the relative position of the point on the curve within this interval between nodes.

The problem of finding the partitioned small mesh surface is to find the interpolation problem of bicubic B-splines. In the case of fully considering the selection of influence points, this study established a 5×5 interpolation matrix to reduce the program complexity and calculation amount. The closest 16 points surrounding the point to be interpolated (that is, the sixteen points with the smallest radial distance from the point to be interpolated) are selected as the control points that affect the interpolated data. As shown in Fig. 5, the red circle points are the points to be interpolated; the triangles are the sample points; B_{pl} represents the sampling point involved in bicubic B-spline interpolation. Due to the lack of sample points, there may be blank points in the interpolation matrix. When searching for the control points, the radial distance between the points existing in the 5×5 interpolation matrix and the points to be interpolated is calculated, and the grid is generated by using the 16 control points. The 16 control points are

substituted into the basis function Eq. (9) in turn to calculate their respective basis function values. The calculated basis function values of each point and the data value of each control point are substituted into Eq. (8) to obtain $F(x, y)$ to be interpolated.

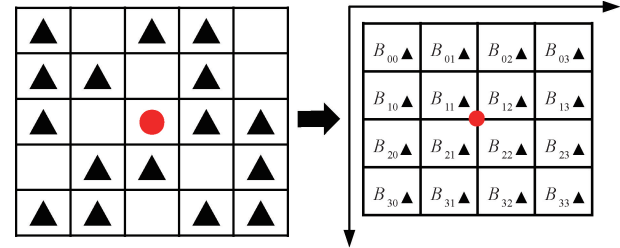


Fig. 5 Schematic diagram of bicubic B-spline interpolation implementation

2.3 Corneal topography

Gridding is the process of dividing the discrete point cloud data into a grid of regular features. The maximum number of point clouds actually processed in this study is $300 \times 32 = 9600$, here the plot data domain is divided into 200 parts by polar coordinates, and the radian of each angle is $\pi/200$. The data domain is divided into a grid of $200 \times 200 = 40000$, and the known point cloud data are converted into grid point data. Delaunay triangular dissection is a special kind of triangle dissection. If there are two points in the set of points V where the outer circle of the two points does not contain any other points in V , then the line connecting these two points is the Delaunay edge^[17-18]. In this study, the entire point cloud collection is subjected to a two-dimensional Delaunay triangulation process to create a Delaunay triangular mesh, as depicted in Fig. 6 for the local region generated in this study. The red points denote the centers of the Delaunay triangles, and the grid points located within the Delaunay triangles (the Voronoi diagram region) are interpolated into the mesh using a natural neighborhood approach. The mesh is interpolated, and the values are replaced by 0 if the mesh is not within the Voronoi diagram region.

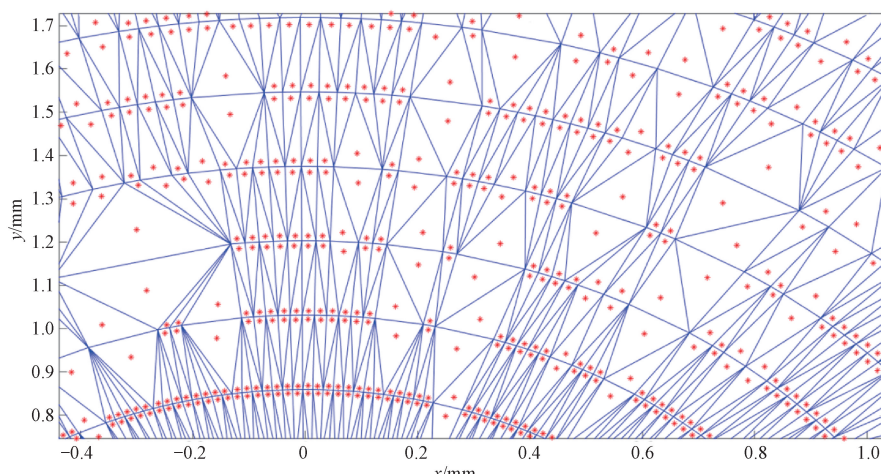


Fig. 6 Localized areas of Delaunay triangular mesh

The initial modeling and imaging of the cornea's three-dimensional image and topography are shown in Figs. 7(a) and 7(b). In Fig. 7, warm colors correspond to higher values in the diopter, indicating relatively steep areas on the cornea; cool colors represent lower values in the diopter, denoting relatively flat areas; D is the unit of diopter, and $1 \text{ D} = 1 \text{ m}^{-1}$. A clear discontinuity in the graphical features of the topography requires image smoothing. Gaussian kernel function is an effective tool for image smoothing, and the smoothing based on the two-dimensional Gaussian function^[19] is used in this study. The expression of the two-dimensional Gaussian function is

$$G(x,y) = \frac{1}{2\pi\sigma^2} \exp\left[\frac{-(x^2+y^2)}{2\sigma^2}\right], \quad (10)$$

where σ is the standard deviation and determines the smoothing degree of the image. When σ is high, the more dispersed the distribution of weights, the smaller the difference between the weights of each part, and thus the transition is more rounded; when σ is low, the more centralized the distribution of weights, the larger the difference between the weights of each part, and thus the transition is rougher. Given the magnitude of the local influence, σ is set as five to smooth the initial three-dimensional modeled corneal image and complete the final corneal topography image (Fig. 7(c)).

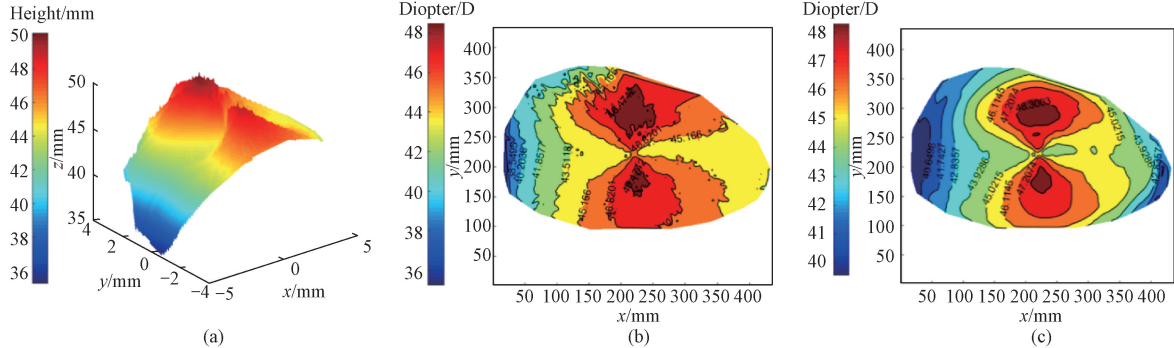


Fig. 7 Modelling of corneal: (a) initial modeling of corneal three-dimensional image; (b) initial modeling of corneal topography; (c) final modeling of corneal topography

3 Experiments and Analyses

3.1 Analysis of missing-point filling algorithms

To verify the effectiveness of the missing-point filling algorithm proposed in this study, the interpolation algorithm based on bicubic B-splines is used to interpolate the known 3 000-point cloud data, and the interpolated

results are compared with the inverse distance interpolation algorithm proposed in Ref. [20] as well as the true value.

Due to the huge amount of experimental data, this study only shows the interpolation results of part of the point cloud data, as shown in Table 1. For 3 000-point cloud data, the relative error distribution of the interpolation methods is shown in Fig. 8.

Table 1 Comparison of 3 000-point cloud data and interpolated data

Coordinate value		True value	Diopter/D		
x/mm	y/mm		Bicubic B-spline interpolation	Inverse distance-weighted interpolation	
0.153 8	0.076 7	43.91	43.83	44.58	
-4.462 6	0.234 7	39.78	39.88	40.34	
-3.207 7	1.235 8	42.52	42.71	42.09	
-1.778 1	0.642 5	44.34	44.23	44.43	
5.298 7	-0.558 8	37.21	37.47	37.43	
⋮	⋮	⋮	⋮	⋮	
2.109 3	-0.737 2	42.25	42.09	41.69	
1.298 4	-1.126 2	47.54	47.53	48.25	
-2.459 4	0.773 5	43.78	43.59	43.41	
-0.104 9	-0.136 1	45.63	45.27	45.72	
-3.952 9	-0.041 5	41.34	41.09	41.93	

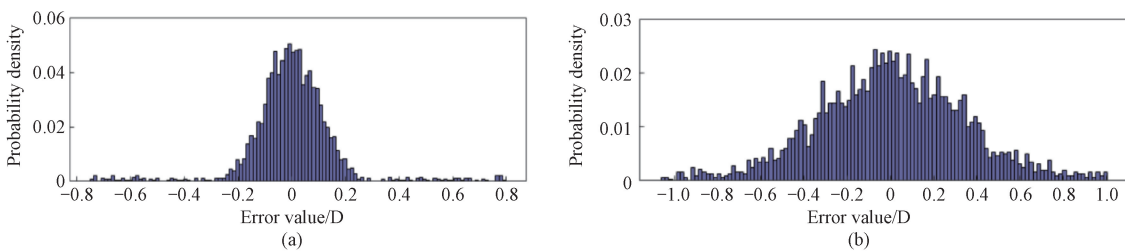


Fig. 8 Histogram of error distribution of interpolation method; (a) bicubic B-spline interpolation error distribution; (b) inverse distance-weighted interpolation error distribution

From the data and the histograms, it can be concluded that the bicubic B-spline interpolation method is more accurate, with a tighter error distribution around zero and generally smaller deviations from the true values. The inverse distance interpolation method shows larger errors and a broader error distribution, which may make it less reliable for precise applications.

The specific evaluation metrics of the error

distribution histograms are shown in Table 2, and the three error evaluation metrics corresponding to the local bicubic B-spline interpolation method proposed are smaller than those corresponding to the inverse distance-weighted interpolation method, which suggests that this algorithm is more suitable for the corneal point cloud missing-point filling interpolation.

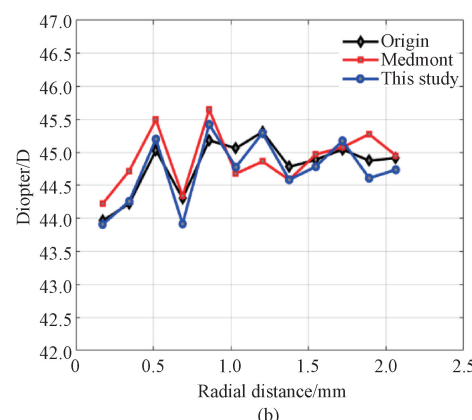
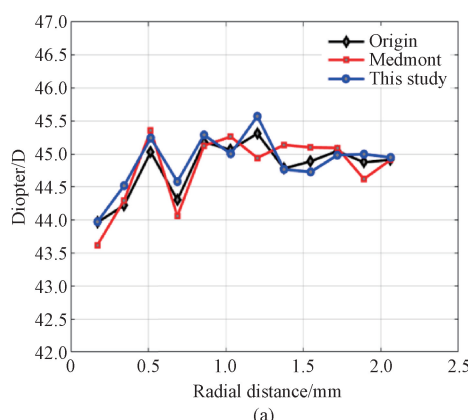
Table 2 Statistical analysis of interpolated data by different interpolation methods

Interpolation method	Mean absolute error/D	Mean squared error/D ²	Standard deviation/D
Bicubic B-spline interpolation	0.109	0.002	0.173
Inverse distance-weighted interpolation	0.267	0.005	0.341

3.2 Corneal topography imaging analysis

In order to verify the feasibility of the restoration algorithm in this study, the accuracy of the corneal topographies recovered was compared and analyzed to determine the superiority of the algorithm. The results from the Medmont (E300U, Australia) corneal topography restoration software were chosen as the reference for comparison in this study. The same patient was selected for examination, and the initial data from the Placido disc examination were collected.

Subsequently, the axial and tangential corneal maps of the patients' recovered corneas were compared respectively. The corneal data on the 0°, 90°, 180° and 270° half meridian of the recovered topographic maps, axial maps, and tangential maps were selected and compared with the original corneal data acquired by the Placido disc. The restoration results of axial maps evaluated along distinct meridians are presented in Fig. 9 and Table 3. The restoration results of tangent plots are presented in Fig. 10 and Table 4.



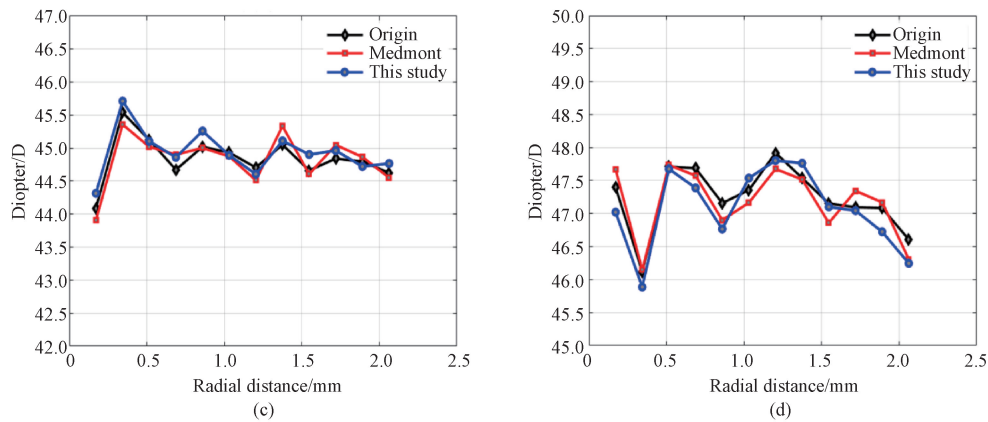


Fig. 9 Comparison of axial map along distinct meridians: (a) 0° ; (b) 90° ; (c) 180° ; (d) 270°

Table 3 Difference between each meridian and original data in axial map

Method	Mean absolute error/D			
	0°	90°	180°	270°
Medmont	0.207	0.138	0.173	0.275
This study	0.135	0.135	0.223	0.172

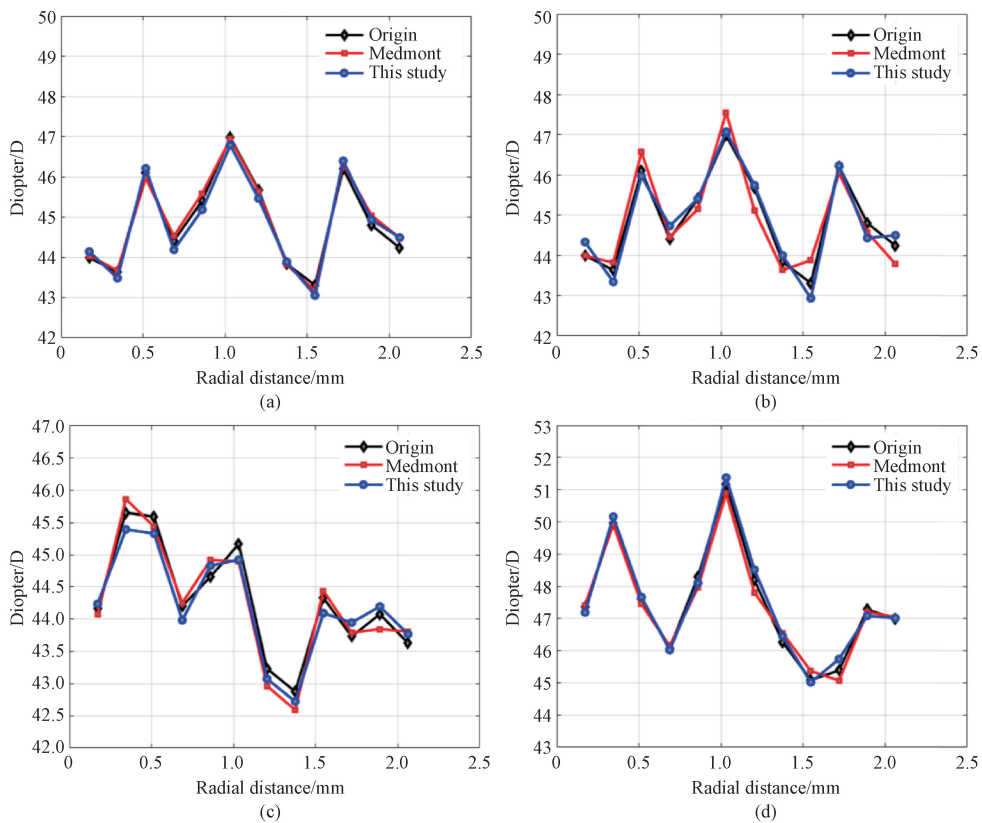


Fig. 10 Comparison of tangent plot along distinct meridians: (a) 0° ; (b) 90° ; (c) 180° ; (d) 270°

Table 4 Difference between each meridian and original data in tangent plot

Method	Mean absolute error/D			
	0°	90°	180°	270°
Medmont	0.211	0.181	0.194	0.310
This study	0.178	0.187	0.168	0.202

The computerized corneal topography restoration algorithm proposed in this study shows comparable performance to the method used in the Medmont corneal topography restoration software. The error between the restored topography and the original corneal examination data remains relatively stable. Additionally, the mean absolute error is generally less than 0.300 D, which is within the permissible error range. This indicates that the method proposed in this study is feasible.

4 Conclusions

In this study, a corneal topography restoration method based on initial information from Placido disc detection is proposed. The problem of difficult coordinate determination during corneal point cloud modeling is solved by using polar coordinate modeling. An algorithm based on filling missing points in the bicubic B-spline point cloud is proposed. The algorithm automatically searches for control points within the established interpolation matrix, which reduces the complexity of procedure implementation and achieves a higher accuracy compared with the widely used inverse distance-weighted interpolation. The application of the Gaussian kernel function addresses the issue of image feature discontinuity and completes the smoothing of topographic maps. The entire reconstruction process demonstrates a high level of accuracy and feasibility, with minimal discrepancies between the reconstructed results and the original corneal examination data. The mean absolute error remains below 0.300 D, thereby satisfying the medical requirements.

References

- [1] ESPANA E M, BIRK D E. Composition, structure and function of the corneal stroma [J]. *Experimental Eye Research*, 2020, 198: 108137.
- [2] MOBARAKI M, ABBASI R, VANDCHALI S O, et al. Corneal repair and regeneration: current concepts and future directions [J]. *Frontiers in Bioengineering and Biotechnology*, 2019, 7: 135.
- [3] WEI Z Y, ZHENG P P, CHEN Q K, et al. Correlation of corneal nerve innervation and ocular surface inflammationin in meibomian gland dysfunction [J]. *Chinese Journal of Ophthalmologic Medicine (Electronic Edition)*, 2021, 11(4): 205-210. (in Chinese)
- [4] KANCLERZ P, KHORAMNIA R, WANG X G. Current developments in corneal topography and tomography [J]. *Diagnostics*, 2021, 11 (8) : 1466.
- [5] KANDEL S, CHAUDHARY M, MISHRA S K, et al. Evaluation of corneal topography, pachymetry and higher order aberrations for detecting subclinical keratoconus[J]. *Ophthalmic and Physiological Optics*, 2022, 42 (3) : 594-608.
- [6] SHEN Y, XIAN Y Y, HAN T, et al. Bilateral differential topography: a novel topographic algorithm for keratoconus and ectatic disease screening [J]. *Frontiers in Bioengineering and Biotechnology*, 2021, 9: 772982.
- [7] DE ROJAS SILVA M V, TOBÍO RUIBAL A, SUANZES HERNÁNDEZ J. Corneal power measurements by ray tracing in eyes after small incision lenticule extraction for myopia with a combined Scheimpflug camera-Placido disk topographer [J]. *International Ophthalmology*, 2022, 42(3): 921-931.
- [8] JIN Y L, MCALINDEN C, SUN Y, et al. Sirius Scheimpflug: Placido versus ultrasound pachymetry for central corneal thickness: meta-analysis[J]. *Eye and Vision*, 2021, 8(1): 5.
- [9] XU D Y, GAO J X, SUI C H, et al. Image edge detection and shape reconstruction in corneal topography [J]. *Laser & Optoelectronics Progress*, 2017, 54 (10) : 209-214. (in Chinese)
- [10] ZHOU H Y, SHEN J X, GAO S L, et al. Research and application of interpolation algorithm in corneal topography system [J]. *Manufacture Information Engineering of China*, 2011, 40(1): 54-56, 60. (in Chinese)
- [11] FLORINDO J B, SOARES S H M, DE CARVALHO L A V, et al. Mumford-Shah algorithm applied to videokeratography image processing and consequences to refractive power values[J]. *Computer Methods and Programs in Biomedicine*, 2007, 87(1): 61-67.
- [12] SUI C H, WO S J, XU D Y, et al. Design and implementation of Placido disk and projection lighting system for corneal topography [J]. *Optics and Precision Engineering*, 2017, 25(3): 603-610. (in Chinese)
- [13] SONG L B, HE L B, HUO S J, et al. Comparison of refraction before and after pupil dilation in adolescents with initial myopia [J]. *China Glasses Science-Technology Magazine*, 2022(9):138-141. (in Chinese)
- [14] ZHANG Z H, ZENG S, CAI J J, et al. Control effect of corneal plastic lens in children with myopia different diopters [J]. *Contemporary Medicine*, 2022, 28(13): 35-38. (in Chinese)
- [15] YU Y C, JI X G, YAN C, et al. Research on multi-resolution fairing for non-uniform rational B-spline curves [J]. *Machine Design & Research*, 2019, 35(2): 1-5, 11. (in Chinese)
- [16] ZHANG Y W. Research on B-spline fitting algorithm based on dense point cloud data[D]. Shanghai: Shanghai Institute of Technology, 2021. (in Chinese)
- [17] WANG Z S, CHEN G L, WANG H, et al. A study on precision design of parallel mechanisms

- based on mapping of error space [J]. *Machine Design & Research*, 2016, 32 (4): 10-14. (in Chinese)
- [18] JIANG S, JIANG W S. Reliable image matching via photometric and geometric constraints structured by Delaunay triangulation [J]. *ISPRS Journal of Photogrammetry and Remote Sensing*, 2019, 153: 1-20.
- [19] MAFI M, MARTIN H, CABRERIZO M, et al.
- [20] ZHOU H Y. Research on the reconstruction algorithms in corneal topography system and their applications [D]. Nanjing: Nanjing University of Aeronautics and Astronautics, 2010. (in Chinese)

基于 Placido 盘的角膜地形图成像

万烜润¹, 王超星¹, 胡俊^{2, 3}, 姜俭^{4, 5*}, 李康妹^{1*}

1. 东华大学 机械工程学院, 上海 201620

2. 东华大学 人工智能研究院, 上海 201620

3. 上海市工业大数据工程技术研究中心, 上海 201620

4. 温州医科大学 眼科医院, 浙江 温州 325000

5. 浙江省眼科医院, 浙江 温州 325000

摘要: 在眼科领域, 角膜地形图是进行诊断治疗的重要参考依据。复原度高的角膜地形图对临床实践有重要意义。该研究基于 Placido 盘采集到的角膜初始信息进行屈光度计算。以极坐标的方式建立角膜点云模型, 提出了一种在自定义插值矩阵中自寻控制点的方式下的局部双三次 B 样条缺失点填充插值算法。通过 Delaunay 三角剖分算法和高斯核函数平滑, 实现了点云信息的网格化插值和地形图平滑成像。试验表明, 该插值算法与之前算法相比具有更好的精度, 从最终成像的地形图得到的屈光度与检测得到的屈光度的平均误差在 0.300 D 以内。该算法具有较好的可行性。

关键词: 角膜地形图; Placido 盘; 点云模型; 双三次 B 样条; 高斯核函数

DOI: 10.19884/j.1672-5220.202402008

Leader-Following Consensus for a Class of Nonlinear Cascaded Multi-Agent Systems

LI Xianda, KANG Jianling*

School of Mathematics and Statistics, Donghua University, Shanghai 201620, China

Abstract: This paper focuses on the problem of leader-following consensus for nonlinear cascaded multi-agent systems. The control strategies for these systems are transformed into successive control problem schemes for lower-order error subsystems. A distributed consensus analysis for the corresponding error systems is conducted by employing recursive methods and virtual controllers, accompanied by a series of Lyapunov functions devised throughout the iterative process, which solves the leader-following consensus problem of a class of nonlinear cascaded multi-agent systems. Specific simulation examples illustrate the effectiveness of the proposed control algorithm.

Keywords: cascaded multi-agent system; distributed control; consensus; recursive method

CLC number: O231; TP18

Article ID: 1672-5220(2025)02-0213-06

Document code: A

Open Science Identity
(OSID)



0 Introduction

The research on multi-agent systems, as a comprehensive interdisciplinary field, has important theoretical value and broad application prospects in industrial and military fields. It can be applied to formation control such as multi-robot, drone, military vehicle and satellite formation control, as well as air traffic control and military searching^[1-4]. The consensus is the foundation of collaborative control. The goal of achieving consensus among multi-agent systems is to design appropriate control protocols that enable all agents to reach certain quantities of interest.

Generally speaking, cascaded systems can be roughly classified into two types: linear cascaded systems and nonlinear cascaded systems. We are mainly interested in nonlinear cascaded systems. The global asymptotic stability of a class of nonlinear cascaded systems was achieved by using the method of state feedback^[5]. The uniform global finite-time stability was discussed for the cascaded time-varying system consisting of two uniformly finite-time stable subsystems^[6]. The output feedback

control was investigated for nonlinear cascaded systems with external disturbance and asymmetric constraints^[7].

Based on the count of leaders in multi-agent systems, the consensus issue can be divided into three types: leaderless consensus, leader-following consensus and containment consensus with multiple leaders. The ultimate states of the followers can reach the trajectories of the leader labeled as the 0th agent. The leader agent can be physical or virtual, and all other agents are referred to as followers.

The majority of research on multi-agent consensus focuses on individual dynamics as first-order integrators and second-order integrators^[8-13]. However, when applying the aforementioned theoretical results to real-world applications, such as the coordination of multi-wheeled mobile robots with non-holonomic constraints and consensus of multiple satellite rigid body attitudes, the multi-agent systems could not achieve the desired control effects. The fundamental reason is that the low-order linearized models adopted in the theoretical research are too simplistic and overlook the high-order, nonlinear and non-holonomic characteristics of the systems.

In recent years, there has been increasing attention on the research of collaborative control problems for high-order multi-agent systems. To solve the bipartite consensus problem in high-order multi-agent systems, a new distributed controller was proposed based on the output information from neighboring agents^[14]. It was considered that the fixed-time consensus of the high-order chained-form multi-agent systems was subject to non-holonomic constraints by employing the backstepping structure^[15]. The finite-time leader-following consensus problem was investigated for a class of high-order multi-agent systems characterized by uncertain nonlinear dynamics^[16]. However, there is currently limited research on distributed collaborative control of nonlinear cascaded multi-agent systems. Therefore, it is worthwhile to investigate the consensus of cascaded multi-agent systems for their broad prospects and application value.

The main purpose of this paper is to discuss the consensus problem for nonlinear cascaded multi-agent

Received date: 2024-02-24

Foundation item: National Natural Science Foundation of China (No. 12071370)

* Correspondence should be addressed to KANG Jianling, email: kangjl@dhu.edu.cn

Citation: LI X D, KANG J L. Leader-following consensus for a class of nonlinear cascaded multi-agent systems [J]. *Journal of Donghua University (English Edition)*, 2025, 42(2): 213-218.

systems. The main contributions are as follows. Firstly, a distributed control strategy based on recursive methods is proposed. The neighbor state information and virtual controllers are utilized. Secondly, it is demonstrated that the nonlinear cascaded multi-agent systems can achieve consensus by providing a proof of the inductive step based on the Lyapunov stability theorem.

The remainder of this paper is arranged as follows. Some preliminaries on graph theory, communication topology, and the necessary definitions and lemmas are given in Section 1. The consensus protocols and the stability analysis of the nonlinear cascaded multi-agent systems are presented in Section 2. Simulation examples are provided in Section 3 to demonstrate the effectiveness of the proposed results. A summary is presented in Section 4.

1 Preliminaries and Problem Formulations

1.1 Preliminaries

The network associated with a multi-agent system can be represented by an undirected graph G . It is represented by a triple, i.e. $G = \{V, E, A\}$, where V is the set of nodes and $V = \{v_1, v_2, \dots, v_n\}$; E is the set of edges and $E \subseteq V \times V$; A describes the adjacency matrix of G with $a_{ij} = 0$ ($i = 1, 2, \dots, N; j = 1, 2, \dots, n$) and $A = [a_{ij}]_{n \times n}$. If the agent i can directly receive information from the agent j , $a_{ij} \neq 0$; otherwise $a_{ij} = 0$. The edge weights between the leader and the followers are denoted by a_{i0} . $D = \text{diag}(d_1, d_2, \dots, d_n)$ is defined as the in-degree matrix of the graph with $d_i = \sum_{j=1}^n |a_{ij}|$, and the Laplacian matrix $L_s := [l_{ij}] \in \mathbf{R}^{n \times n}$ of the graph is presented as $L_s = D - A$, where $l_{ij} = -a_{ij}, i \neq j$; $\mathbf{R}^{n \times n}$ is Euclidean space with $n \times n$ dimension. If there is a path between any two vertices in the graph, the undirected graph G is connected.

Assumption 1 The communication topology between followers is an undirected connected graph.

Assumption 2 The communication graph, i.e. the undirected graph G , contains a directed spanning tree in which the leader acts as the root node.

Assumption 3 The nonlinear function $f(t, x(t))$ satisfies the following inequality

$$|f(t, x) - f(t, y)| \leq \rho |x - y|, \quad \forall x, y \in \mathbf{R}, t \geq 0, \quad (1)$$

where ρ is a positive constant.

Assumption 4 The input of the leader u_0 is zero, i.e., $u_0(t) = 0$.

Definition 1 Define a matrix $B = \text{diag}(a_{10}, a_{20}, \dots, a_{N0})$, where $a_{i0} > 0$ if the leader is a neighbor of an agent i ; otherwise, $a_{i0} = 0$. The matrix L is defined as $L = L_s + B$.

Lemma 1^[17] (Barbalat's Lemma) Let $f: \mathbf{R} \rightarrow \mathbf{R}$ be a uniformly continuous function on $[0, \infty)$.

Supposing that $\lim_{t \rightarrow \infty} \int_0^t f(\tau) d\tau$ exists and is finite, then $\lim_{t \rightarrow \infty} f(t) = 0$, where $f(\cdot)$ is a nonlinear function.

Lemma 2^[18] Under Assumption 1 and Assumption 2, the matrix L is symmetric positive definite.

1.2 Problem formulation

Considering a nonlinear cascaded multi-agent system consisting of a leader labeled as 0, and N followers labeled as $i = 1, 2, \dots, N$, the dynamic of the i th ($i = 0, 1, 2, \dots, N$) agent is described as follows:

$$\begin{cases} \dot{x}_{i1} = f(t, x_{i1}) + x_{i2}, \\ \dot{x}_{i2} = x_{i3}, \\ \vdots \\ \dot{x}_{in} = u_i, \end{cases} \quad (2)$$

where $x_i = [x_{i1}, x_{i2}, \dots, x_{in}]^T \in \mathbf{R}^n$ and $u_i \in \mathbf{R}^m$, which are the states of the i th agent and control input, respectively.

The objective of this paper is to make all agents achieve consensus for the nonlinear cascaded multi-agent systems (Eq. (2)). In other words, if the above assumption conditions are satisfied, a distributed controller that only relies on local information can be designed, ensuring that the state of each agent satisfies:

$$\lim_{t \rightarrow \infty} |x_{ij}(t) - x_{0j}| = 0, \quad i = 1, 2, \dots, N; \quad j = 1, 2, \dots, n. \quad (3)$$

2 Main Results

Based on the local information of the agents, a distributed controller is designed by using a recursive method, and a series of Lyapunov functions are proposed during the iterative process.

Theorem 1 Consider the nonlinear cascaded multi-agent system (Eq. (2)). If **Assumptions 1–4** are satisfied, there exist distributed protocols that solve the consensus tracking problem.

Proof Define the tracking error as $e_i = x_i - x_0$, then the error system can be written as

$$\begin{cases} \dot{e}_{i1} = \Delta f_{i1} + e_{i2}, \\ \dot{e}_{i2} = e_{i3}, \\ \vdots \\ \dot{e}_{in} = u_i, \quad i = 1, 2, \dots, N, \end{cases} \quad (4)$$

where $\Delta f_{i1} = f(t, x_{i1}) - f(t, x_{01})$; $e = [e_{1m}, e_{2m}, \dots, e_{Nm}]^T \in \mathbf{R}^n, m = 1, 2, \dots, n$.

Define a new set of variables

$$\begin{cases} z_{i1} = e_{i1}, \\ z_{ij} = e_{ij} - \alpha_{ij}, \quad i = 1, 2, \dots, N; \quad j = 2, 3, \dots, n, \end{cases} \quad (5)$$

where α_{ij} represents the virtual controller to be designed during the iterative process.

Step 1 Consider the first-order subsystem in the error system (Eq. (4)), i.e.,

$$\dot{e}_{i1} = \Delta f_{i1} + e_{i2},$$

where the error variable is defined as $z_{ii} = e_{ii}$. We choose the following Lyapunov function V_1 :

$$\dot{V}_1 = \frac{1}{2} z_1^T \mathbf{L} z_1, \quad (6)$$

where $\mathbf{z}_1 = [z_{11}, z_{21}, \dots, z_{N1}]^T$.

The first distributed virtual controller is defined as

$$\alpha_{i2} = -\beta \sum_{j=1}^N [a_{ij}(x_{i1} - x_{j1}) + a_{i0}(x_{i1} - x_{01})], \quad (7)$$

which can be also written as

$$\alpha_{i2} = -\beta \sum_{j=1}^N [a_{ij}(e_{i1} - e_{j1}) + a_{i0}(e_{i1} - e_{01})], \quad (8)$$

where $\beta > 0$; $e_{i2} = \alpha_{i2}$, $i = 1, 2, \dots, N$. Taking the derivative of the Lyapunov function V_1 with respect to Eq. (2) yields

$$\begin{aligned} \dot{V}_1 &= \mathbf{e}_1^T \mathbf{L} \dot{\mathbf{e}}_1 = \mathbf{e}_1^T \mathbf{L} (-\beta \mathbf{L} \mathbf{e}_1 + \Delta f_1) \\ &\leq -\beta \|\mathbf{L} \mathbf{e}_1\|_2^2 + \frac{1}{2} \mathbf{e}_1^T \mathbf{L}^2 \mathbf{e}_1 + \frac{1}{2} \Delta f_1^T \Delta f_1 \\ &\leq -\beta \|\mathbf{L} \mathbf{e}_1\|_2^2 + \frac{1}{2} \|\mathbf{L}_1\|_2^2 + \frac{1}{2} \rho^2 \mathbf{e}_1^T \frac{\mathbf{L}^2}{\lambda_{\min}^2(\mathbf{L})} \mathbf{e}_1 \\ &\leq -\beta \|\mathbf{L} \mathbf{e}_1\|_2^2 + \frac{1}{2} \|\mathbf{L} \mathbf{e}_1\|_2^2 + \frac{1}{2} \rho^2 \mathbf{e}_1^T \frac{\mathbf{L}^2}{\lambda_{\min}^2(\mathbf{L})} \mathbf{e}_1 \\ &\leq \|\mathbf{L} \mathbf{e}_1\|_2^2 \left(-\beta + \frac{1}{2} + \frac{\rho^2}{2\lambda_{\min}^2(\mathbf{L})} \right), \end{aligned} \quad (9)$$

where $\Delta f_1 = [\Delta f_{11}, \Delta f_{21}, \dots, \Delta f_{N1}]^T$; $\lambda_{\min}(\mathbf{L})$ is the minimum eigenvalue of \mathbf{L} .

Remark 1 According to Lemma 2, \mathbf{L} is a positive definite matrix, then $\lambda_{\min}(\mathbf{L}) > 0$.

Choose $\beta = \frac{3}{2} + \frac{\rho^2}{2\lambda_{\min}^2(\mathbf{L})}$, and then we can

obtain $\dot{V}_1 \leq -\|\mathbf{L} \mathbf{e}_1\|_2^2$. Integrating both sides of the above inequality, we have that

$$V_1(\mathbf{e}_1(t)) - V_1(\mathbf{e}_1(0)) \leq - \int_0^t \|\mathbf{L} \mathbf{e}_1(\tau)\|_2^2 d\tau. \quad (10)$$

It follows that

$$\int_0^t \|\mathbf{L} \mathbf{e}_1(\tau)\|_2^2 d\tau \leq V_1(\mathbf{e}_1(0)) - V_1(\mathbf{e}_1(t)) \leq V_1(\mathbf{e}_1(0)). \quad (11)$$

By Lemma 1, we have $\lim_{t \rightarrow \infty} \|\mathbf{L} \mathbf{e}_1(t)\|_2^2 = 0$, i.e., $\lim_{t \rightarrow \infty} \mathbf{e}_1(t) = 0$, which implies that the tracking error asymptotically converges to 0.

Step 2 Consider the second-order subsystem in the error system (Eq. (4)), i.e.,

$$\begin{aligned} \dot{e}_{i1} &= \Delta f_{i1} + e_{i2}, \\ \dot{e}_{i2} &= e_{i3}, \end{aligned}$$

and choose the Lyapunov function $V_2 = V_1 + \frac{1}{2} z_2^T \mathbf{L} z_2$,

where $\mathbf{z}_2 = [z_{12}, z_{22}, \dots, z_{N2}]^T$. The derivative of the Lyapunov function V_2 yields

$$\begin{aligned} \dot{V}_2 &\leq -\|\mathbf{L} \mathbf{e}_1\|_2^2 + z_2^T \mathbf{L} \dot{z}_2 \\ &= -\|\mathbf{L} z_1\|_2^2 + z_2^T \mathbf{L} (\dot{e}_2 - \alpha_{i2}) \\ &= -\|\mathbf{L} z_1\|_2^2 + z_2^T \mathbf{L} [\mathbf{e}_3 + \beta \mathbf{L} (\mathbf{e}_2 + \Delta f_1)], \end{aligned} \quad (12)$$

where $\mathbf{e}_2 = [e_{12}, e_{22}, \dots, e_{N2}]^T$.

Define $\alpha_3 = \mathbf{e}_3 = -\mathbf{L} \mathbf{e}_2 - \beta \mathbf{L} \rho \|\mathbf{z}_1\|_2 - \mathbf{L} z_2$, where $\alpha_3 = [\alpha_{13}, \alpha_{23}, \dots, \alpha_{N3}]^T$, $\|\mathbf{z}_1\|_2 = \sqrt{\sum_{i=1}^N z_{ii}^2}$, $\alpha_{i3} = -l_{i2} z_{i2} - \beta \sum_{j=1}^N l_{ij} e_{i2} - \beta \rho \sum_{j=1}^N l_{ij} \|\mathbf{z}_1\|_2$. So we have

$$\dot{V}_2 \leq -\|\mathbf{L} z_1\|_2^2 - \|\mathbf{L} z_2\|_2^2. \quad (13)$$

By the inductive method, Formulas (9) and (12) can be recursively extended as follows.

Step k Consider the k th-order subsystem in the error system, where $2 \leq k \leq n-1$, i.e.,

$$\begin{aligned} \dot{e}_{i1} &= \Delta f_{i1} + e_{i2}, \\ \dot{e}_{i2} &= e_{i3}, \\ &\vdots \\ \dot{e}_{ik} &= e_{i,k+1}, \quad i = 1, 2, \dots, N. \end{aligned}$$

Assume the Lyapunov function V_{k-1} exists,

$$V_{k-1} = V_1 + \frac{1}{2} \sum_{\mu=2}^{k-1} z_\mu^T \mathbf{L} z_\mu \geq 0, \quad (14)$$

which satisfies $\dot{V}_{k-1} \leq -\sum_{\mu=1}^{k-1} \|\mathbf{L} z_\mu\|_2^2$. To prove that when $n = k$, the following results hold, we choose the Lyapunov function $V_k = V_{k-1} + \frac{1}{2} z_k^T \mathbf{L} z_k$, where $\mathbf{z}_k = [z_{1k}, z_{2k}, \dots, z_{Nk}]^T$.

Taking the derivative of the Lyapunov function V_k , we have

$$\begin{aligned} \dot{V}_k &\leq \dot{V}_{k-1} + z_k^T \mathbf{L} z_k \\ &\leq -\sum_{\mu=1}^{k-1} \|\mathbf{L} z_\mu\|_2^2 + z_k^T \mathbf{L} (\dot{e}_k - \alpha_k) \\ &\leq -\sum_{\mu=1}^{k-1} \|\mathbf{L} z_\mu\|_2^2 + z_k^T \mathbf{L} e_{k+1} - z_k^T \mathbf{L} \dot{\alpha}_k, \end{aligned} \quad (15)$$

where $\alpha_k = [\alpha_{1k}, \alpha_{2k}, \dots, \alpha_{Nk}]^T$;

$$\dot{\alpha}_{ik} = -\beta l_{ii} \sum_{\mu=2}^{k-1} \frac{\partial \alpha_{ik}}{\partial e_{i,\mu-1}} e_{i\mu} - \beta \sum_{\mu=2}^{k-1} \sum_{j=1}^n l_{ij} \frac{\partial \alpha_{ik}}{\partial e_{j,\mu-1}} e_{j\mu} - \beta \sum_{j=1}^n l_{ij} \Delta f_{j1};$$

$$\mathbf{z}_k = \mathbf{e}_k - \alpha_k, \quad k = 2, 3, \dots, n.$$

If $\alpha_{i,k+1} = e_{i,k+1} = -l_{ik} z_{ik} + \dot{\alpha}_{ik}$, then $\dot{V}_k \leq -\sum_{\mu=1}^k \|\mathbf{L} z_\mu\|_2^2$.

Furthermore, the inductive argument guarantees that for the Lyapunov function $V_n = V_{n-1} + \frac{1}{2} z_n^T \mathbf{L} z_n$, and thus

$$\begin{aligned} \dot{V}_n &\leq -\sum_{\mu=1}^{n-1} \|\mathbf{L} z_\mu\|_2^2 + z_n^T \mathbf{L} \dot{z}_n \\ &\leq -\sum_{\mu=1}^{n-1} \|\mathbf{L} z_\mu\|_2^2 + z_n^T \mathbf{L} (\dot{e}_n - \alpha_n) \end{aligned}$$

$$\leq - \sum_{\mu=1}^{n-1} \|Lz_\mu\|_2^2 + z_n^T Lu - z_n^T L\dot{\alpha}_n, \quad (16)$$

where $\mathbf{u} = [u_1, u_2, \dots, u_N]^T$; $u_i = -l_{in}z_{in} - \beta l_{ii} \times \sum_{\mu=2}^{n-1} \frac{\partial \alpha_{in}}{\partial e_{j,\mu-1}} e_{j\mu} - \beta \sum_{\mu=2}^{n-1} \sum_{j=1}^n l_{ij} \frac{\partial \alpha_{ik}}{\partial e_{j,\mu-1}} \frac{\partial \alpha_{ik}}{\partial e_{j,\mu-1}} e_{j\mu} - \beta \sum_{j=1}^n l_{ij} \Delta f_{ji}$; $\dot{\alpha}_n = [\alpha_{1n}, \alpha_{2n}, \dots, \alpha_{Nn}]^T$.

The distributed controller is designed as

$$\mathbf{u} = -Lz_n + \dot{\alpha}_n.$$

Based on Formula (16), further deduction yields:

$$\dot{V}_n \leq - \sum_{\mu=1}^n \|Lz_\mu\|_2^2.$$

By **Lemma 1**, we have $\lim_{t \rightarrow \infty} \|Lz_i\| = 0$, $i = 1, 2, \dots, n$. Due to $\lim_{t \rightarrow \infty} z_1 = 0$, then $\lim_{t \rightarrow \infty} e_1 = 0$ and $\lim_{t \rightarrow \infty} \alpha_2 = 0$. According to Eq. (5), $e_2 = z_2 + \alpha_2$, so $\lim_{t \rightarrow \infty} e_2 = 0$. Based on the inductive discussion, it can be further obtained that for $i = 2, 3, \dots, n$, $\lim_{t \rightarrow \infty} e_i = 0$, and then, $x_i - x_0 = 0$, as $t \rightarrow \infty$, which means the leader-following consensus problem is solved.

3 Simulation Example

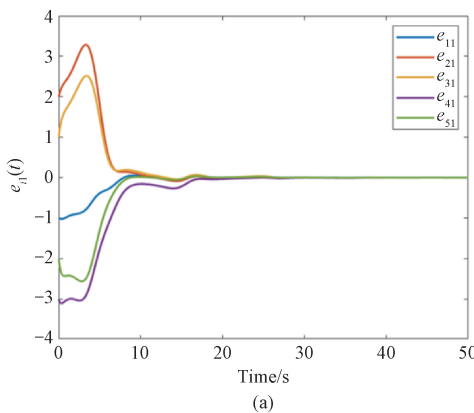
In this section, a specific numerical example is utilized to validate the effectiveness of the proposed theoretical results.

Considering the multi-agent system consisting of a second-order integrator with one leader and five followers, the dynamic of the i th agent is described as follows:

$$\begin{cases} \dot{x}_{i1} = x_{ii} \sin(0.6t) + x_{i2}, \\ \dot{x}_{i2} = u_i, \end{cases} \quad i = 0, 1, \dots, 5. \quad (17)$$

According to **Assumption 4**, $u_0(t) = 0$, the error system for the above Eq. (17) can be written as

$$\begin{cases} \dot{e}_{i1} = e_{ii} \sin(0.6t) + e_{i2}, \\ \dot{e}_{i2} = u_i, \end{cases} \quad i = 0, 1, \dots, 5. \quad (18)$$



(a)

According to **Theorem 1**, we can obtain $\beta = 7.4659$ and design $\mathbf{u} = [u_1, u_2, u_3, u_4, u_5]^T$ as $-\beta L e_2 - \beta L \rho \|e_1\|_2 - L(e_2 - \alpha_2)$.

The corresponding communication topology among agents is described in Fig. 1

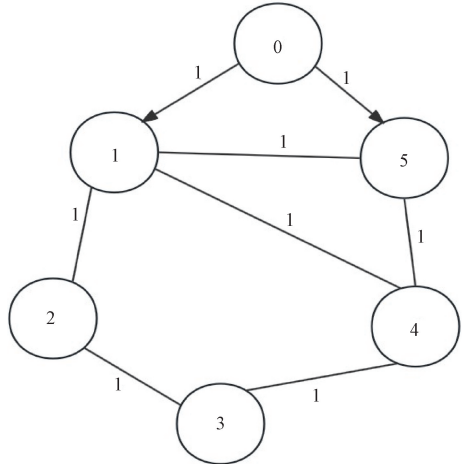


Fig. 1 Communication topology

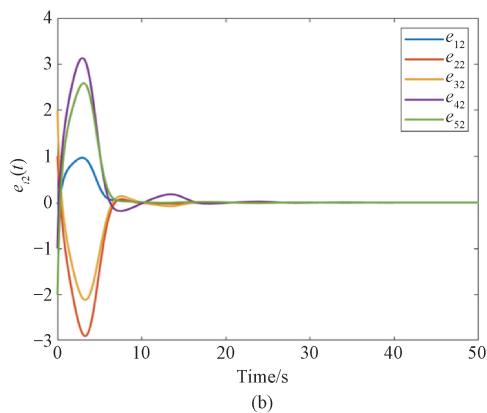
The Laplacian matrix is expressed as

$$\mathbf{L} = \begin{bmatrix} 4 & -1 & 0 & -1 & -1 \\ -1 & 2 & -1 & 0 & 0 \\ 0 & -1 & 2 & -1 & 0 \\ -1 & 0 & -1 & 3 & -1 \\ -1 & 0 & 0 & -1 & 3 \end{bmatrix}.$$

The initial states of followers are given as $[x_{11}(0), x_{21}(0), x_{31}(0), x_{41}(0), x_{51}(0)]^T = [-2, 3, 2, -2, -1]^T$ and $[x_{12}(0), x_{22}(0), x_{32}(0), x_{42}(0), x_{52}(0)]^T = [-1, 0, 1, -2, -3]^T$.

The initial states of the leader are given as $x_{01}(0) = 1$ and $x_{02}(0) = -1$.

The tracking errors of the multi-agent system (Eq. (18)) are shown in Fig. 2. It indicates the achievement of leader-following consensus.



(b)

Fig. 2 Trajectories of tracking error: (a) first component; (b) second component

4 Conclusions

In this paper, we considered the leader-following consensus problem for nonlinear cascaded multi-agent systems. The distributed consensus protocols are designed with the aid of virtual controllers in a recursive manner, which can guarantee leader-following consensus. A specific numerical example illustrates the effectiveness of the proposed control strategy. Future work will focus on the bipartite consensus problem for nonlinear cascaded multi-agent systems, with further attention to the consensus for nonlinear cascaded multi-agent systems with time-varying delays.

References

- [1] LEONARD N E, FIORELLI E. Virtual leaders, artificial potentials and coordinated control of groups [C]//Proceedings of the 40th IEEE Conference on Decision and Control. New York: IEEE, 2001, 3: 2968-2973.
- [2] OLFATI-SABER R. Flocking for multi-agent dynamic systems: algorithms and theory [J]. *IEEE Transactions on Automatic Control*, 2006, 51(3): 401-420.
- [3] KRISTIANSEN R, NICKLASSON P J. Spacecraft formation flying: a review and new results on state feedback control [J]. *Acta Astronautica*, 2009, 65(11/12): 1537-1552.
- [4] AHN H S. Leader-follower type relative position keeping in satellite formation flying via robust exponential stabilization [J]. *International Journal of Robust and Nonlinear Control*, 2012, 22(18): 2084-2099.
- [5] JANKOVIC M, SEPULCHRE R, KOKOTOVIC P V. Constructive Lyapunov stabilization of nonlinear cascade systems [J]. *IEEE Transactions on Automatic Control*, 1996, 41(12): 1723-1735.
- [6] LI S, TIAN Y P. Finite-time stability of cascaded time-varying systems [J]. *International Journal of Control*, 2007, 80(4): 646-657.
- [7] ZHANG J, YANG J, ZHANG Z C, et al. Output feedback control of nonlinear cascaded systems with external disturbance and asymmetric constraints [J]. *Nonlinear Dynamics*, 2022, 108(4): 3727-3743.
- [8] LIU X Y, CAO J D, XIE C L. Finite-time and fixed-time bipartite consensus of multi-agent systems under a unified discontinuous control protocol [J]. *Journal of the Franklin Institute*, 2019, 356(2): 734-751.
- [9] GAO S, WEN G G, ZHAI X Q, et al. Finite-/fixed-time bipartite consensus for first-order multi-agent systems via impulsive control [J]. *Applied Mathematics and Computation*, 2023, 442: 127740.
- [10] CONG Y Z, DU H B, LIU B B, et al. Distributed constrained finite-time consensus algorithm for second-order multi-agent systems [J]. *Information Sciences*, 2023, 626: 773-786.
- [11] ZUO Z Q, JI J W, ZHANG Z C, et al. Consensus of double-integrator multi-agent systems with asymmetric input saturation [J]. *Systems & Control Letters*, 2023, 172: 105440.
- [12] LU M Y, WU J, ZHAN X S, et al. Consensus of second-order heterogeneous multi-agent systems with and without input saturation [J]. *ISA Transactions*, 2022, 126: 14-20.
- [13] CAO M T, ZHOU Q, CHENG Y H. Scaled consensus of second-order multi-agent systems based on edge-event driven control [J]. *Journal of the Franklin Institute*, 2022, 359(14): 7319-7336.
- [14] WU Y Z, HU J P. Bipartite consensus control of high-order multi-agent systems [J]. *IFAC-PapersOnline*, 2019, 52(24): 201-206.
- [15] CHEN Y Y, ZHU B. Distributed fixed-time control of high-order multi-agent systems with non-holonomic constraints [J]. *Journal of the Franklin Institute*, 2021, 358(6): 2948-2963.
- [16] HUA C C, YOU X, GUAN X P. Leader-following consensus for a class of high-order nonlinear multi-agent systems [J]. *Automatica*, 2016, 73: 138-144.
- [17] KHALIL H K. Nonlinear systems [M]. 3rd ed. Upper Saddle River, USA: Prentice Hall, 2002.
- [18] CAO W J, ZHANG J H, REN W. Leader-follower consensus of linear multi-agent systems with unknown external disturbances [J]. *Systems & Control Letters*, 2015, 82: 64-70.

一类非线性级联多智能体系统的领导跟随一致性

李显达, 康剑灵*

东华大学 数学与统计学院, 上海 201620

摘要: 研究了非线性级联多智能体系统的领导跟随一致性问题。将非线性级联多智能体系统的控制策略转化为对低阶误差子系统的系列控制。采用递归方法和虚拟控制器, 在迭代过程中设计一系列的李雅普诺夫函数, 并对相应误差系统的分布式一致性进行分析, 解决了一类非线性级联多智能体系统的领导跟随一致性问题。仿真实例验证了所设计控制算法的有效性。

关键词: 级联多智能体系统; 分布式控制; 一致性; 递归方法